A BIO-INSPIRED MULTI-AGENT SYSTEM FRAMEWORK FOR REAL-TIME LOAD MANAGEMENT IN ALL-ELECTRIC SHIP POWER SYSTEMS

A Dissertation

by

XIANYONG FENG

Submitted to the Office of Graduate Studies of
Texas A&M University
in partial fulfillment of the requirements for the degree of

DOCTOR OF PHILOSOPHY

May 2012

Major Subject: Electrical Engineering

A Bio-Inspired Multi-Agent System Framework for Real-Time

Load Management in All-Electric Ship Power Systems

A BIO-INSPIRED MULTI-AGENT SYSTEM FRAMEWORK FOR REAL-TIME LOAD MANAGEMENT IN ALL-ELECTRIC SHIP POWER SYSTEMS

A Dissertation

by

XIANYONG FENG

Submitted to the Office of Graduate Studies of
Texas A&M University
in partial fulfillment of the requirements for the degree of

DOCTOR OF PHILOSOPHY

Approved by:

Chair of Committee,	Karen L. Butler-Purry
Committee Members,	Takis Zourntos
	Le Xie
	Sergiy Butenko
Head of Department,	Costas N. Georghiades

May 2012

Major Subject: Electrical Engineering

ABSTRACT

A Bio-Inspired Multi-Agent System Framework for Real-Time Load Management in All-Electric Ship Power Systems. (May 2012)

Xianyong Feng, B.S., Harbin Institute of Technology;

M.S., University of Science and Technology of China

Chair of Advisory Committee: Dr. Karen L. Butler-Purry

All-electric ship power systems have limited generation capacity and finite rotating inertia compared with large power systems. Moreover, all-electric ship power systems include large portions of nonlinear loads and dynamic loads relative to the total power capacity, which may significantly reduce the stability margin. Pulse loads and other high-energy weapon loads in the system draw a large amount of power intermittently, which may cause significant frequency and voltage oscillations in the system. Thus, an effective real-time load management technique is needed to dynamically balance the load and generation to operate the system normally.

Multi-agent systems, inspired by biological phenomena, aim to cooperatively achieve system objectives that are difficult to reach by a single agent or centralized controller. Since power systems include various electrical components with different dynamical systems, conventional homogeneous multi-agent system cooperative controllers have difficulties solving the real-time load management problem with heterogeneous agents. In this dissertation, a novel heterogeneous multi-agent system

cooperative control methodology is presented based on artificial potential functions and reduced-order agent models to cooperatively achieve real-time load management for all-electric ship power systems. The technique integrates high-order system dynamics and various kinds of operational constraints into the multi-agent system, which improves the accuracy of the cooperative controller. The multi-agent system includes a MVAC multi-agent system and a DC zone multi-agent, which are coordinated by an AC-DC communication agent.

The developed multi-agent system framework and the notional all-electric ship power system model were simulated in PSCAD software. Case studies and performance analysis of the MVAC multi-agent system and the DC zone multi-agent system were performed. The simulation results indicated that propulsion loads and pulse loads can be successfully coordinated to reduce the impact of pulse loads on the power quality of all-electric ship power systems. Further, the switch status or power set-point of loads in DC zones can be optimally determined to dynamically balance the generation and load while satisfying the operational constraints of the system and considering load priorities.

The method has great potential to be extended to other isolated power systems, such as microgrids.

DEDICATION

To my family

ACKNOWLEDGEMENTS

First and foremost, I would like to thank my advisor, Dr. Karen L. Butler-Purry, for her guidance, support, and encouragement throughout my Ph.D. study. Working with Dr. Butler-Purry has been a great experience in my life. The guidance and encouragement from Dr. Butler-Purry always drive me to achieve excellence in the research work.

I would like to thank my committee members, Dr. Takis Zourntos, Dr. Le Xie, and Dr. Sergiy Butenko, for investing their time on my committee. Thanks to Dr. Zourntos for leading me to the bio-inspired multi-agent system world.

Thanks also go to my friends and colleagues at Power System Automation Laboratory for their support and friendships. I greatly acknowledge Office of Naval Research for their support of this research work.

Finally, I would like to thank my lovely wife, Kehua You, for her patience and love throughout my Ph.D. study and thank to my mother and father for their patience, encouragement, and love.

TABLE OF CONTENTS

LIST OF FIGURES

FIGURE Page

FIGURE Page

FIGURE Page

FIGURE Page

FIGURE Page

FIGURE Page

FIGURE Page

FIGURE Page

FIGURE Page

FIGURE Page

FIGURE Page

FIGURE Page

FIGURE Page

FIGURE Page

LIST OF TABLES

TABLE Page

TABLE Page

1. INTRODUCTION

1.1 Introduction

Some isolated power systems are located in rural or remote areas [1], [2], such as offshore oil exploration areas, remote mining districts, islands, ships, etc. They can operate autonomously without connecting to bulk power systems. However, because isolated power systems have limited generation capacity and finite rotating inertia compared with large power systems, a sudden load increase can easily overload generators. Some isolated power systems include large portions of dynamic loads and nonlinear loads, moreover, which may significantly reduce the stability margin of the system. In addition, the various operational constraints of the system, such as frequency, current, and voltage constraints, and power capacity constraints of electrical devices, need to be satisfied in operational real time. Otherwise, the system may not operate normally to supply power to loads. Therefore, an effective real-time load management technique needs to be developed for isolated power systems to dynamically balance the generation and load while satisfying operating constraints of the system.

The all-electric ship power system is an isolated power system, which consists of gas turbine generators, electric propulsion loads, service loads, high-energy weapon loads, and power electronics devices. The all-electric ship power system helps ships accomplish cruising and military functions using electric propulsion loads and high-energy weapon loads, respectively. The system supplies power to propulsion loads

---

This dissertation follows the style of *IEEE Transactions on Power Systems*.

to drive the ship speed to its cruising speed and supplies power to high-energy weapon loads, such as electromagnetic, radar, and sonar guns, to attack its targets and protect itself from battle damage. This dissertation discusses a novel real-time load management methodology developed for all-electric ship power systems and potential applications of the methodology for microgrids.

The all-electric ship power system includes four gas turbine generators – two main turbine generators (MTGs) and two auxiliary turbine generators (ATGs). The total generation capacity of the system is 80 MW. The inertia constants of MTG and ATG are 1.49 MW-sec/MVA and 1.06 MW-sec/MVA, respectively. The typical inertia values of H for thermal units and hydraulic units are shown in Table 1.1 [3]. Since these gas turbine generators have smaller inertia constants, they have faster mechanical dynamics than steam turbine and hydro turbine generators.

Since isolated power systems are small-scale power systems and electrical components are tightly coupled, it is realistic to assume that the system frequency is approximately the same at different locations in the system. The collective behavior of the generation system is used to analyze the dynamic behavior of the system frequency, so the system frequency decline [4] rate can be expressed as (1-1).

$$\frac{d\bar{f}}{dt} = -\frac{f_{rated}\Delta P_L}{2\sum_{i=1}^{n} H_i} \tag{1-1}$$

where, $d\bar{f}/dt$ (Hz/sec) is the average frequency decline rate; f_{rated} is the rated system frequency (60 Hz); ΔP_L (pu) is the magnitude of generation and load mismatch; $\sum_{i=1}^{n} H_i$ is the total inertia of the system. The frequency decline rate at the first few seconds of a

disturbance directly depends on the total system inertia and the magnitude of the generation and load mismatch because the turbine governors take several seconds to respond to system disturbances. For the same magnitude of the generation and load mismatch, the smaller the total system inertia, the larger the system frequency deviation. Since isolated power systems have much smaller inertia compared with large power systems, the frequency deviation of isolated power systems after certain disturbances will be much larger than that of larger inertia power systems, as shown in Figure 1.1. Thus, real-time load management is needed to balance the generation and load of the system to reduce the frequency oscillation and deviation.

Table 1.1 Typical value of generator inertia [3]

Type of generating unit	H (MW·sec/MVA)
Thermal unit	
(a) 3600 r/min (2-pole)	2.5 – 6.0
(b) 1800 r/min (4-pole)	4.0 – 10.0
Hydraulic unit	2.0 – 4.0

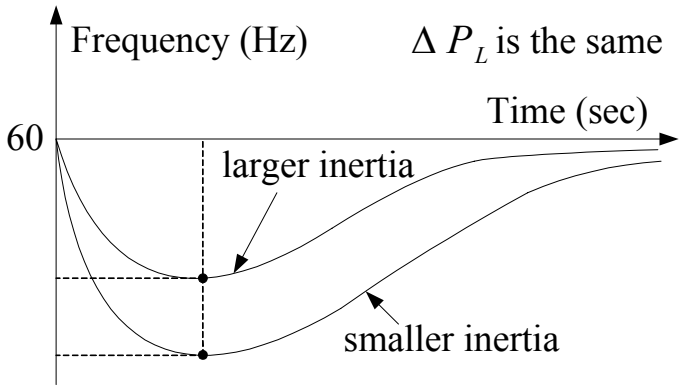

Figure 1.1 Power system frequency behavior after a system disturbance

In the all-electric ship power system, battle damage or a sudden increase in load demand, such as a pulse load or other high-energy weapon loads, can easily overload the generators. For instance, a pulse load has a very high-rated power with a short pulse width. When pulse loads are served in the system, the total load demand may exceed the generation capacity quickly, as shown in Figure 1.2(a). In this case, for a simplified notional all-electric ship power system model, the total generation capacity of the power system was only 36 MW (only one MTG was in service); the pulse load was served at 10 sec with a 12 MW magnitude and 0.3 sec pulse width [5]. When the pulse load was served at 10 sec, the total load demand was 44 MW, which greatly exceeded the generation capacity and caused the system frequency to decline very quickly. The maximum frequency deviation was 0.8 Hz, which is shown in Figure 1.2(b). Therefore, a real-time load management technique needs to be used to reduce the impact of pulse loads on the power system.

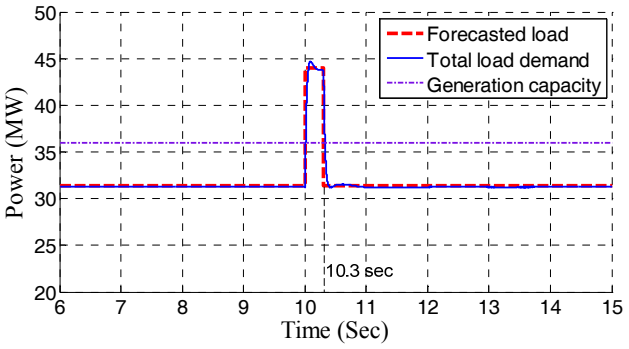

(a)

Figure 1.2 Dynamic performance of components of a notional all-electric ship power system with a pulse load. **(a)** Total load demand and generation capacity of a notional all-electric ship power system model, **(b)** Frequency dynamic behavior of the MTG generator

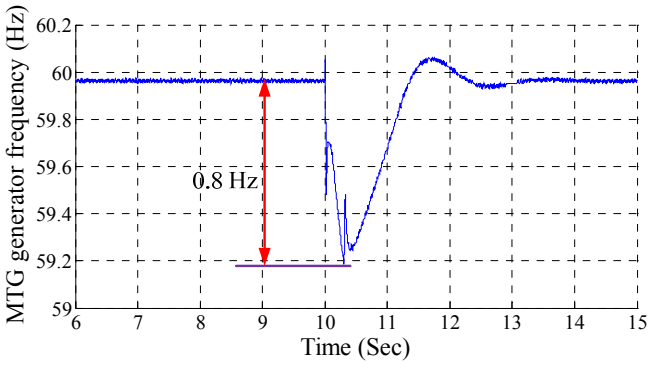

(b)

Figure 1.2 Continued

The all-electric ship power system includes loads with various priorities such as vital loads, semi-vital loads, and non-vital loads. Non-vital loads, such as lighting loads, heater loads, and air conditioners, receive only a single power feed, and can be immediately shed without affecting the ship's survivability. Semi-vital loads can be shed to prevent total loss of ship's power. In contrast, vital loads, such as radar, sonar, and electromagnetic weapons, are required to maintain the military effectiveness of the ship [6], [7]. The vital loads have a normal path and an alternate path, as shown in Figure 1.3, which improves their reliability. For instance, in Figure 1.3, if the port side DC distribution bus is damaged in DC zone 1, loads in DC zone 1 cannot be served by the port side bus; thus, vital loads served by the port side bus should be immediately switched to the alternate path to be continuously served.

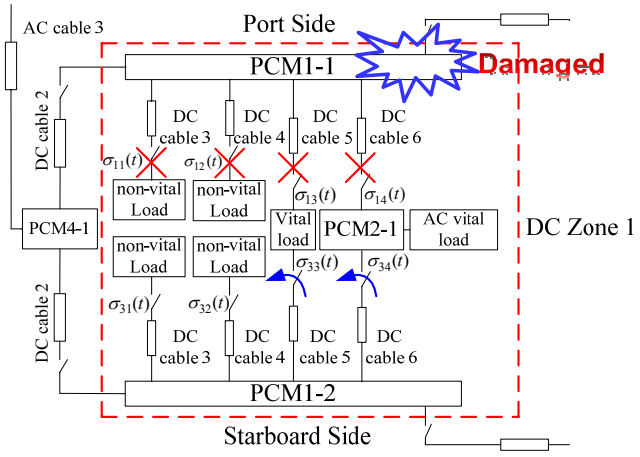

Figure 1.3 Diagram of vital loads in the DC zone system of a portion of a notional all-electric ship power system model

Moreover, the system serves a large number of dynamic and nonlinear loads, such as propulsion loads driven by a 36.5 MW advanced induction motor, DC loads interfaced with the MVAC system based on power electronics devices, etc. The power demand of the propulsion load can be changed from no-load to its rated power in a few seconds, which introduces large transients into the power system. For example, if the propulsion load power set-point was changed instantaneously, frequency oscillations would be introduced by the load changes. In this case, for a simplified notional all-electric ship power system model with one MTG and one ATG in service, the total generation capacity was 40 MW. A propulsion load was also served in the system, and the power set-point of the propulsion load was changed from 0 to 32 MW at 0 sec, reduced to 16 MW at 10 sec, increased to 26 MW at 20 sec, and then reduced to 7 MW at 30 sec, as shown in Figure 1.4(a). The system frequency deviation was more than 1 Hz when the propulsion load power set-point was changed, as shown in Figure 1.4(b).

If the propulsion load power set-point could be regulated slowly based on the system frequency deviation, the frequency deviation of the system would be reduced significantly, which would improve the dynamic performance of the system. Therefore, the dynamic loads and nonlinear loads should be regulated dynamically to balance the generation and load in real time. Otherwise, the system may not operate normally, and the failure of the all-electric ship power system would reduce the ability of the ship to perform cruising and military functions.

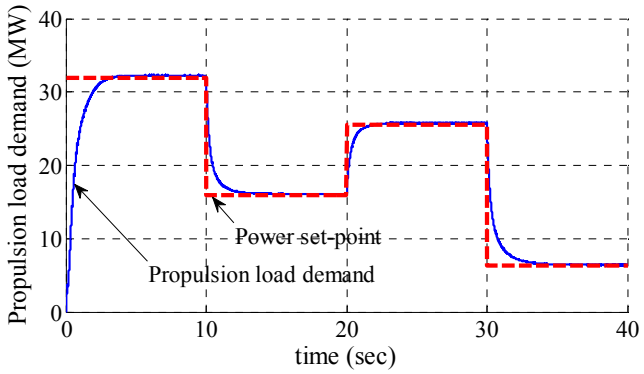

(a)

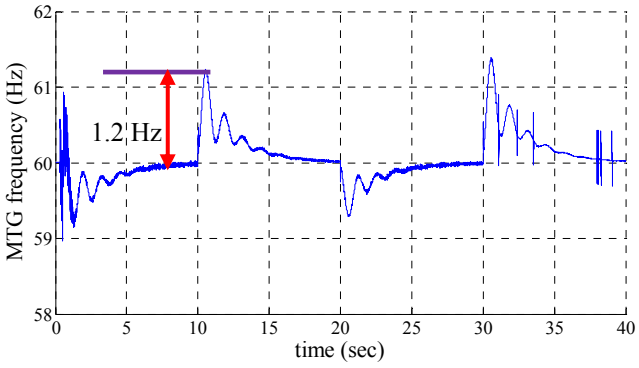

(b)

Figure 1.4 Dynamic performance of a simplified notional all-electric ship power system with propulsion load changes. **(a)** Propulsion load demand, **(b)** Frequency behavior of the MTG generator with propulsion load changes

In the all-electric ship power system, load priorities should be taken into consideration because vital loads need to be served before non-vital and semi-vital loads when the system does not have enough available power. The priority of loads may be different for various ship operation modes. When the system operates in battle mode, pulse loads and high-energy weapon loads have the highest priority to achieve ship's military functions; when the system operates in cruise mode, propulsion loads have the highest priority to drive a ship at the desired cruising speed. When a ship's operation mode is changed, a load management technique needs to be used to regulate individual loads to achieve certain objectives. For instance, when the operation mode is changed from cruise mode to battle mode, pulse loads would be served and the propulsion load demand would be regulated to compensate for the impact of pulse loads on the power quality of the power system.

All operational constraints of the power system should be satisfied in real time to operate the system normally. Some significant constraints for the research include: 1) available power source capacity constraint; 2) bus voltage, system frequency, and cable constraints; 3) dynamic system constraints, 4) the power capacity constraints of individual power electronics components; and 5) rated power constraints for individual loads.

For these reasons, an effective real-time load management technique needs to be developed to balance the generation and load of all-electric ship power systems while satisfying the operational constraints of the system and considering load priorities. The developed real-time load management technique can not only be used for all-electric

ship power systems, but also has great potential to be extended to other isolated power systems, such as microgrids and islanded power systems in oil fields.

The objective of this research was to develop a bio-inspired multi-agent system framework to achieve the real-time load management objective for all-electric ship power systems. The new multi-agent system framework determines the optimum switch status or power set-points for individual loads using autonomous agents based on local communication and coordination to maximize the served loads in the system. This solution must satisfy the operational constraints of the system, considering load priorities in operational real time.

The bio-inspired multi-agent system framework was implemented and applied to all-electric ship power system model in PSCAD/EMTDC® software to study the dynamic performance of the framework. Various pulse loads and operating conditions were used to evaluate the dynamic performance of the system. Various operational constraints of all-electric ship power systems were also illustrated to show the effectiveness of the new method.

1.2 Organization

The dissertation includes six chapters. In chapter 2, a notional all-electric ship power system model is introduced, and a time-frame analysis of various loads, such as pulse loads, propulsion loads, and motors, is also provided. Chapter 3 discusses isolated power system operations, a literature review of load management methods, a proof-of-concept for a real-time load management method for all-electric ship power systems, and

the problem formulation for the new real-time load management method. In addition, the decision time step for the real-time load management method is discussed. The new bio-inspired multi-agent system methodology for real-time load management in the all-electric ship power system is presented in chapter 4. The implementation of the multi-agent system framework for real-time load management in an all-electric ship power system and the performance analysis for the method are discussed in chapter 5. Finally, chapter 6 presents conclusions and contributions of the research and discusses potential applications of the developed methodology in microgids.

2. NOTIONAL ALL-ELECTRIC SHIP POWER SYSTEM MODEL

2.1 Introduction

This chapter discusses the various component models and system behavior for a notional all-electric ship power system. The outline of this chapter is as follows. In section 2.2, the MVAC and DC zone subsystems of the notional all-electric ship power system model are introduced; the propulsion load model, pulse load model, and motor load model are also discussed. In section 2.3, the dynamic time-frame of various types of loads in all-electric ship power systems was analyzed using the PSCAD/EMTDC® transient simulation software to determine a feasible decision time step to use for the real-time load management method. A summary is given in section 2.4.

2.2 Notional All-Electric Ship Power System Model

The one-line diagram of a notional all-electric ship power system is shown in Figure 2.1. The system includes four gas turbine generators – two main turbine generators (MTGs) and two auxiliary turbine generators (ATGs). Four transformers are used to convert the 13.8 kV AC into 4.16 kV AC to supply power to propulsion loads and service loads. Rectifiers are used to convert 4.16 kV AC voltage into 1000 V DC voltage to supply power to loads in DC zones. The system includes two propulsion loads, and each one has a 36.5 MW rated power. A pulse load is served by a MTG bus, which has a 13.8 kV input voltage. The system consists of four DC zones, which

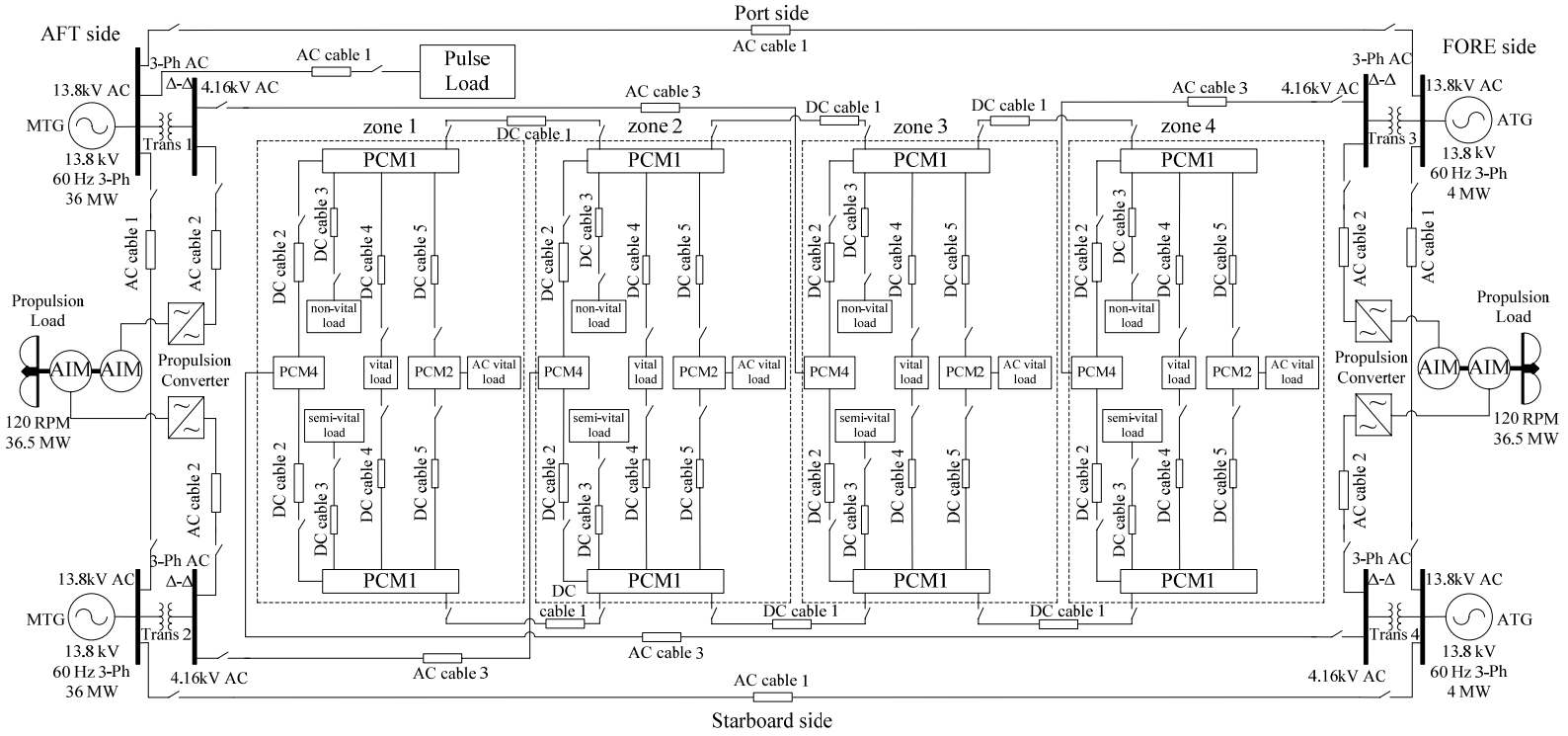

Figure 2.1 One-line diagram of a notional all-electric ship power system model for navy ships

construct the DC zone system. The DC zone system includes various power electronics devices to supply power to AC motor loads, DC motor loads, and constant power loads, which may have different priorities. The electrical component definitions are shown in Table 2.1.

Table 2.1 Component definitions for the all-electric ship power system model

No.	Component Name	Component Description
1	MTG	3 ph, 13.8 kV, 36 MW generator, 60 Hz
2	ATG	3 ph, 13.8 kV, 4 MW generator, 60 Hz
3	Transformer	3 ph, Δ-Δ connected, 13.8/4.16 kV
4	Propulsion load	36.5 MW (rating), 4.16 kV, AC
5	Propulsion converter	Variable frequency drive (VFD)
6	PCM1	1000 V DC to 375, 650, and 800 V DC power converters
7	PCM2	800 V DC to 3-ph, 450 V AC power converter
8	PCM4	3-ph, 4.16 kV AC to 1000 V DC rectifier (2 MW power capacity)
9	AC cable 1	3 ph, 13.8 kV AC cable
10	AC cable 2	3 ph, 4.16 kV AC cable
11	AC cable 3	3 ph, 4.16 kV AC cable
12	DC cable 1	1 kV DC cable
13	DC cable 2	1 kV DC cable
14	DC cable 3	375 V DC cable
15	DC cable 4	650 V DC cable
16	DC cable 5	800 V DC cable
17	Vital load	Vital loads should be served all the time
18	Semi-vital load	Loads can be shed to prevent total loss of ship's power
19	Non-vital load	Non-vital loads can be shed without affecting ship operations

2.2.1 MVAC system model

The MVAC system consists of 13.8 kV AC voltage level and 4.16 kV AC voltage level systems. The system includes two MTGs and two ATGs with 13.8 kV voltage level. MTG capacity is 36 MW and ATG capacity is 4 MW, so the total generation capacity of the system is 80 MW. A pulse load is connected to a MTG bus with 13.8 kV AC voltage. Four transformers convert 13.8 kV AC voltage into 4.16 kV AC voltage to supply power to propulsion loads and services loads. Each propulsion

load is driven by an advanced induction motor (AIM), and a propulsion converter is used to drive an AIM to accomplish the cruising function of ships.

2.2.1.1 Generation system model

Each gas turbine generator consists of an exciter, a gas turbine governor, and a synchronous generator. The exciter is used to maintain the output voltage of the generator at the desired value. The gas turbine governor is used to control the gas turbine to convert mechanical power to electrical power using the synchronous generator. The gas turbine generator has smaller inertia compared with steam or hydro turbine generators. The mismatch between the generation and load may result in significant frequency oscillations in all-electric ship power systems. Thus, the gas turbine governor needs to respond fast to make the system frequency converge to 60 Hz quickly.

The gas turbine governor model, as shown in Figure 2.2(a), includes a temperature control loop and a speed control loop [8], [9], which is a commonly used dynamic model for gas turbine governors. A low value selector is used to select a smaller value from outputs of speed controller and temperature controller. Two first-order inertia elements are used to model fuel valve and fuel system, respectively. D_{Turb} is the damping coefficient of the gas turbine. During system operation, the gas turbine generator should be set as droop mode or isochronous (isoch) mode. The parameters of the gas turbine governor are shown in Table 2.2.

For a droop mode generator, a load reference should be designated to control the power output of the generator; the model for the droop mode generator is shown in Figure 2.2(b). As shown in the diagram, the temperature control loop is neglected to

simplify the system analysis. R is the droop of the speed governor, which is usually chosen as 4% or 5%. When the speed equals the reference speed, the output power equals the load reference.

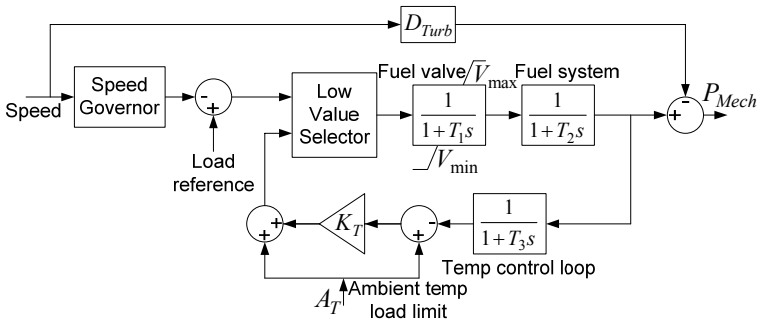

(a) Diagram of the actual gas turbine governor model

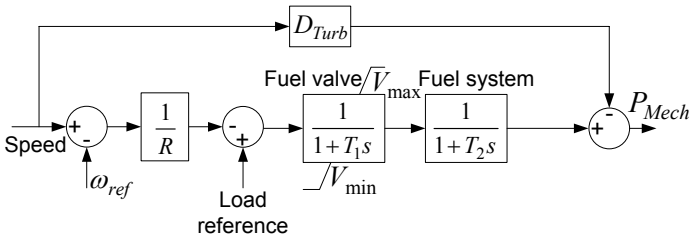

(b) Diagram of gas turbine governor model in droop mode

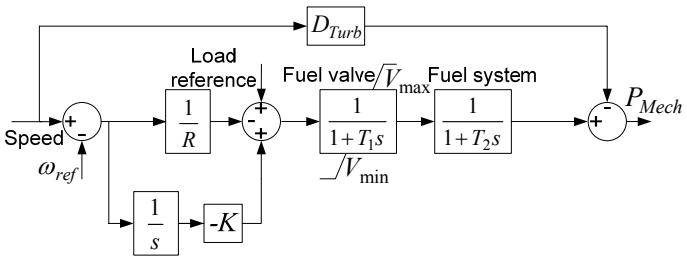

(c) Diagram of gas turbine governor model in isoch mode

Figure 2.2 Diagrams of gas turbine governor model for the all-electric ship power system

When load changes occur, there will be a mismatch between the generation and load in the system. Consequently, the system frequency will deviate from 60 Hz. In this

situation, an isoch generator can pick up the load change to restore the system frequency to approximately 60 Hz. For the isoch generator, the synchronous speed should be designated to ensure that the system frequency is maintained at 60 Hz; the model for the isoch generator is shown in Figure 2.2(c). K is the gain of the integral controller, which determines the response speed of the isoch generator.

Table 2.2 Parameters of the gas turbine governor model

Parameter	Value
Time constant of fuel valve T_1	0.1 sec
Time constant of fuel system T_2	0.4 sec
Droop coefficient R	4%
Damping coefficient D_{Turb}	0
Gain of integral controller K	5

2.2.1.2 Propulsion load model

The diagram of the marine propulsion system model is shown in Figure 2.3. An advanced induction motor is driven by a propulsion converter, which includes a rectifier, a DC link, and an inverter. The rectifier converts 4.16 kV AC into DC voltage, and a space vector PWM inverter is used to convert the DC voltage into AC voltage to serve the advanced induction motor. The marine propulsion controller has two operation modes – speed control mode and power control mode. In the speed control mode, the speed controller is used to drive the ship speed to the desired value. In the power control mode, the power controller is used to regulate the power demand of the advanced induction motor to the desired value. The propulsion system and the hydrodynamics for

the marine propulsion system have been discussed in detail in [10]. The parameters of the advanced induction motor are shown in Table 2.3 [11].

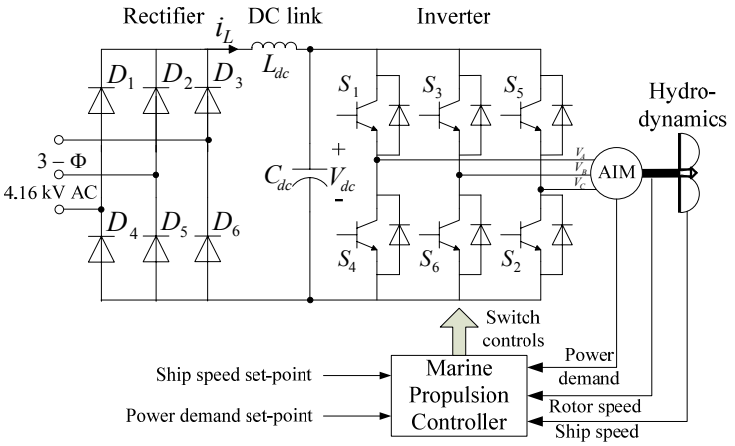

Figure 2.3 Diagram of the marine propulsion system model

Table 2.3 Parameters of the advanced induction motor model [11]

Parameter	Value
Rated power	45 MVA
Rated voltage	12 kV
Base angular frequency	377 rad/s
Stator / rotor turns ratio	2.637687
Angular moment of inertia (J = 2H)	1 sec
Mechanical damping	0.01 pu
Stator resistance	0.0034 pu
Wound rotor resistance	0.00607 pu
Magnetizing inductance	0.9 pu
Stator leakage inductance	0.0102 pu
Wound rotor leakage inductance	0.011 pu

The diagram of the power controller of the marine propulsion system is shown in Figure 2.4. The power controller includes the power control loop and rotor speed control loop. The output of the power controller is the set-point of the rotor speed controller; the output of the rotor speed controller is the torque command, which is used to control the

dq currents of the inverter; and the switch control component is used to control the status of switches in the inverter.

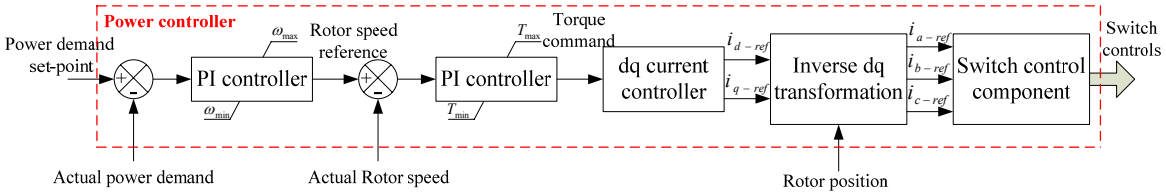

Figure 2.4 Diagram of the power controller for the marine propulsion system

The power controller can be expressed as (2-1).

$$G(s) = k_P + k_I / s \tag{2-1}$$

where, the proportional gain k_P and integral gain k_I of the power controller were chosen as 0.1 and 0.5, respectively. The maximum and minimum limits of the power controller were chosen as 1.5 and 0 (p.u.), respectively. The rotor speed controller used the same kind of PI controller as shown in (2-1), and the proportional gain k_P and integral gain k_I of the rotor speed controller were chosen as 40 and 2.5, respectively. The maximum and minimum limits of the rotor speed controller were chosen as 20 and -5 (p.u.), respectively.

The main function of the propulsion system is to drive the ship speed to a user desired value; the speed controller of the marine propulsion system is shown in Figure 2.5. The ship speed controller has maximum and minimum limits to constrain the maximum and minimum power demand of the propulsion system. The speed controller also used (2-1). The proportional gain k_P and integral gain k_I of the speed controller

were chosen as 1 and 500, respectively; the maximum and minimum limits of the speed controller were chosen as 1.1 and 0 (p.u.), respectively.

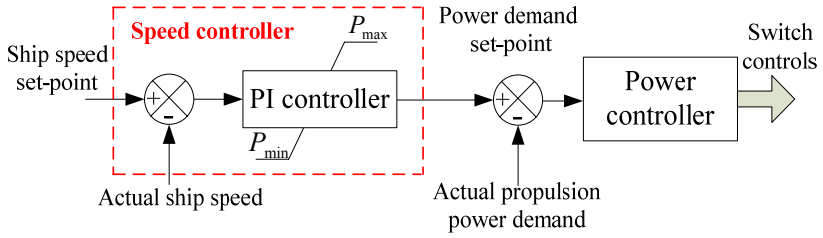

Figure 2.5 Diagram of the speed controller for the marine propulsion system model

When the speed set-point of the marine propulsion system is increased, the PI controller operates in the saturation region immediately, which means that output value of the controller reaches the maximum limit. The ship is accelerated using the maximum power of the propulsion load. When the ship speed reaches the desired speed, the PI controller returns to the linear region, which reduces the power demand of the propulsion load to steady state. Due to this reason, the ship can be accelerated to its desired speed quickly. For the same reason, when the ship speed set-point is decreased, the speed controller hits its minimum limit, which decelerates the ship using its minimum power. When the ship speed decreases to its desired value, the PI controller returns to the linear region, which also decreases the ship speed to the desired value quickly.

2.2.1.3 Pulse load model

The pulse load was modeled using a pulse charging circuit, as shown in Figure 2.6. A rectifier was used to convert AC voltage into DC voltage to supply power to the

pulse load, which was modeled as a resistor. This pulse load model is used in [12], [13] to study the impact of pulse loads on all-electric ship power systems. It was assumed that the discharging time was much smaller than the charging time, so the discharging pulse was almost instantaneous compared with the charging duration. When the charging circuit was charging, it produced a pulse in the power system. A small value was chosen for the resistor in the charging circuit to emulate the charging process of the pulse load; in contrast, a very large value was chosen for the resistor to emulate the disconnection of the charging circuit from the power system. The inductor L_P and capacitor C_P in the charging circuit were chosen as 1 mH and 10 mF, respectively.

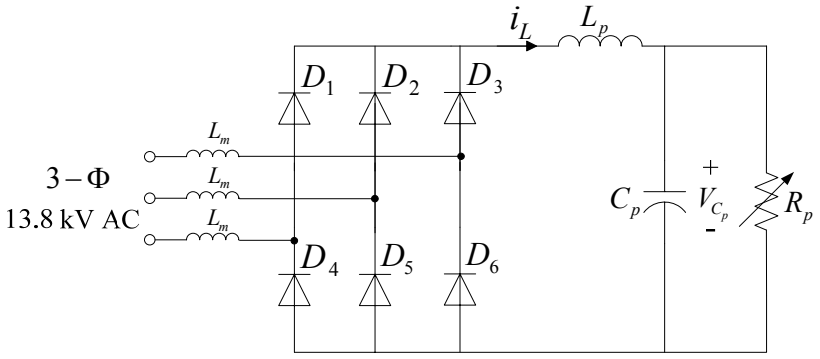

Figure 2.6 Diagram of the pulse load charging circuit model [12], [13]

A pulse load can draw a large amount of power in a short period of time. A typical power demand waveform of a pulse load is shown in Figure 2.7. The pulse load was served from 10 to 11 seconds. The pulse magnitude was 10 MW; the pulse length was 1 second.

The priorities of pulse loads, propulsion loads, and service loads are varied based on the operation mode of ships [14]. In battle mode, pulse loads have the highest priority

to serve weapon loads; in cruise mode, propulsion loads have the highest priority to drive the ship to its cruising speed. In battle mode, when a pulse load needs to be served, the propulsion load demand can be decreased temporarily to compensate for the impact of the pulse load on the power quality of the all-electric ship power system. Due to the inertia of the ship, the disturbance would not decrease the ship speed significantly.

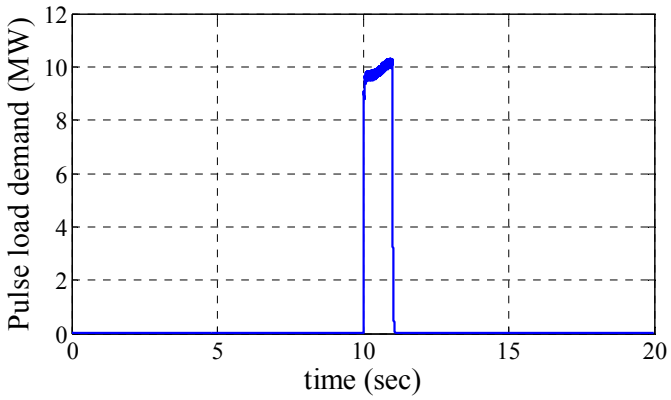

Figure 2.7 The power demand waveform of a pulse load with 10 MW magnitude and 1 second pulse width

2.2.2 DC zone system model

The DC zone system consists of four DC zones, as shown in Figure 2.1. A detail diagram of a DC zone is shown in Figure 2.8. Each DC zone has two DC distribution buses – a starboard side bus and a port side bus (port and starboard are nautical terms which refer to the left and right sides of a ship). The DC distribution buses are served by PCM4 modules (rectifiers) which convert 4.16 kV 3-ph AC voltage to 1000 V DC voltage. A PCM4 does not serve the starboard side bus and the port side bus at the same time. The power capacity of each PCM4 is 2 MW. Each DC distribution bus is

connected to a PCM1 which converts the 1000 V DC voltage into three voltage levels, 375 V DC, 650 V DC, and 800 V DC. PCM2 modules (inverters) are served by 800 V DC-DC converters and invert the 800 V DC to 3-ph 450 V AC to serve AC loads, such as induction motors.

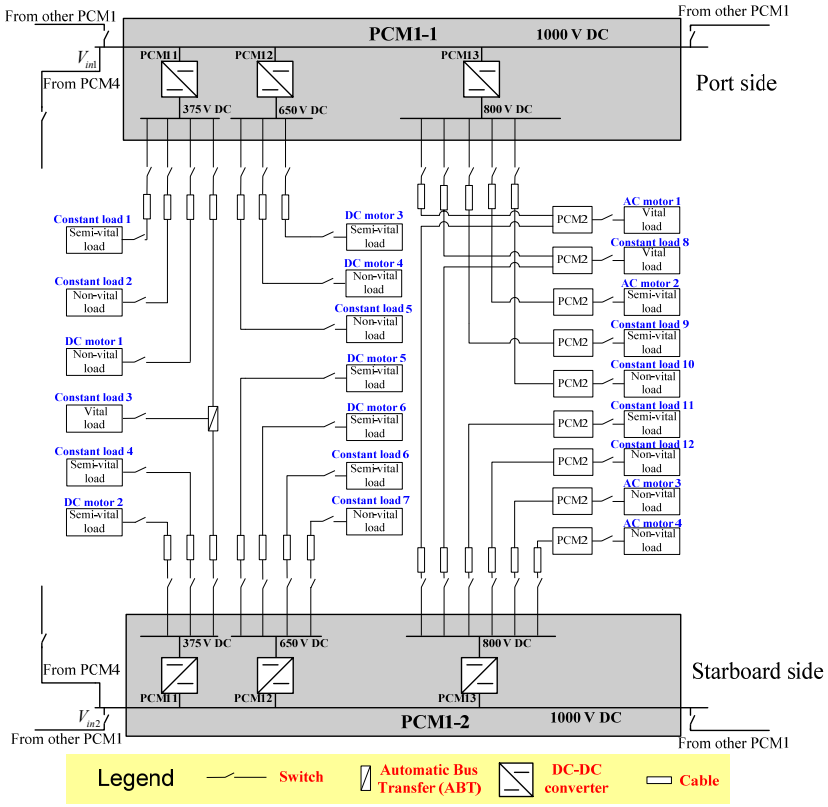

Figure 2.8 Diagram of a DC zone model in the notional all-electric ship power system

2.2.2.1 DC-DC converter model

Each DC zone consists of a starboard side DC distribution bus and a port side DC distribution bus. Each DC distribution bus supplies power to three DC-DC converters at 375 V, 650 V, and 800 V DC voltage levels. A diagram of the DC-DC converter model

is shown in Figure 2.9. The DC-DC converter includes a switch, an inductor, and a capacitor. A PI controller is used to regulate the output power of the DC-DC converter to the desired value. The averaged model of the DC-DC converter is expressed in (2-2).

$$\begin{aligned}
&\dot{i}_L(t) = 1/L \cdot \left(D + \hat{d}\right) \cdot V_{in} - v_C(t)/L \\
&\dot{v}_C(t) = i_L(t)/C - v_C(t)/RC \\
&\dot{\hat{d}}(t) = -k_i i_L(t)/C + \left(k_i/RC - k_p\right) \cdot v_C(t) + k_p \cdot v_{ref} \\
&i_{in}(t) = \left(D + \hat{d}\right) \cdot i_L(t)
\end{aligned} \tag{2-2}$$

where, i_L and v_C are the inductor current and capacitor voltage, respectively; V_{in} and i_{in} are the input voltage and current, respectively; d is the duty ratio of the switch in the converter; $\hat{d}$ is the output signal of the PI controller; D is the feed-forward term of the converter; v_{ref} is the output voltage reference; R is the equivalent resistor of the load; k_p and k_i are the proportional and integral coefficients of the PI controller. The averaged model neglects the high-frequency switching of the power electronic device in the converter. This model can be used to study dynamic behaviors of the control system.

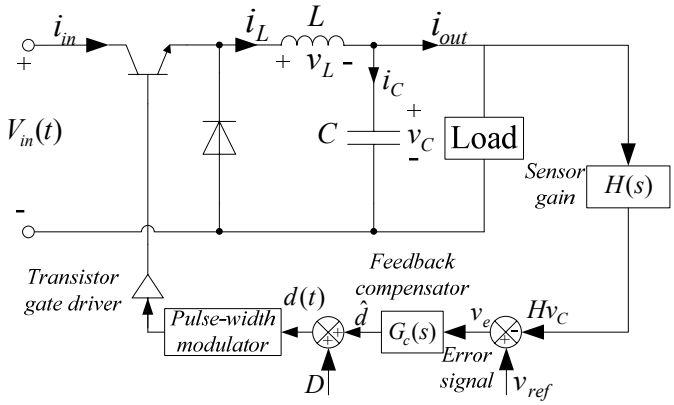

Figure 2.9 Diagram of DC-DC converter model with a voltage controller

2.2.2.2 DC motor model

In the DC zone system, DC motors are used to drive mechanical loads. A diagram of a DC motor model is shown in Figure 2.10. The DC motor model includes the electrical part and mechanical part. The DC motor is connected to a DC voltage bus. The mechanical torque of the DC motor is proportional to the square of the rotor speed of the DC motor. The model also includes the damping effect of the DC motor. The DC motor model can be expressed as (2-3).

$$\begin{aligned} \dot{i}_{motor}(t) &= \left(v_{motor}(t) - K_1 \cdot \omega_{motor}(t) - R_a \cdot i_{motor}(t)\right)/L_a \\ \dot{\omega}_{motor}(t) &= \left(-T_M(t) - B \cdot \omega_{motor}(t) + K_2 \cdot i_{motor}(t)\right)/J \\ T_M(t) &= k_M \omega_{motor}^2(t) \end{aligned} \tag{2-3}$$

where, ω_{motor} is the rotor speed; B is the damping coefficient; T_M is the mechanical torque; k_M is a positive constant; L_a is the equivalent armature inductance; R_a is the equivalent armature resistance; J is the inertia of the DC motor; K_1 and K_2 are coefficients of the DC motor model; v_{motor} and i_{motor} are the input voltage and current to the DC motor model, respectively.

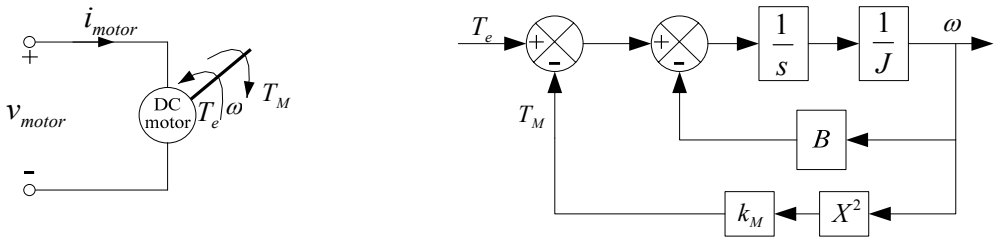

(a) Diagram of electrical part for DC motor **(b)** Diagram of mechanical part for DC motor

Figure 2.10 Diagram of a DC motor model

2.2.2.3 AC motor model

In the DC zone system, 800 V DC-DC converters supply power to induction motors. PCM2 is used to invert the 800 V DC voltage into 450 V AC voltage. A variable frequency drive was designed to drive the induction motor. The power demand of the induction motor was regulated using the machine drive system. The total power demand of the induction motor was controlled by regulating the set-point of the machine drive system. The block diagram of the induction motor and the machine drive system is expressed in Figure 2.11. The AC motor model includes a power converter and an induction motor. The power converter consists of a rectifier, a DC link, and an inverter. The power controller was designed to regulate dq currents to drive the power demand of the induction motor to track the power demand set-point.

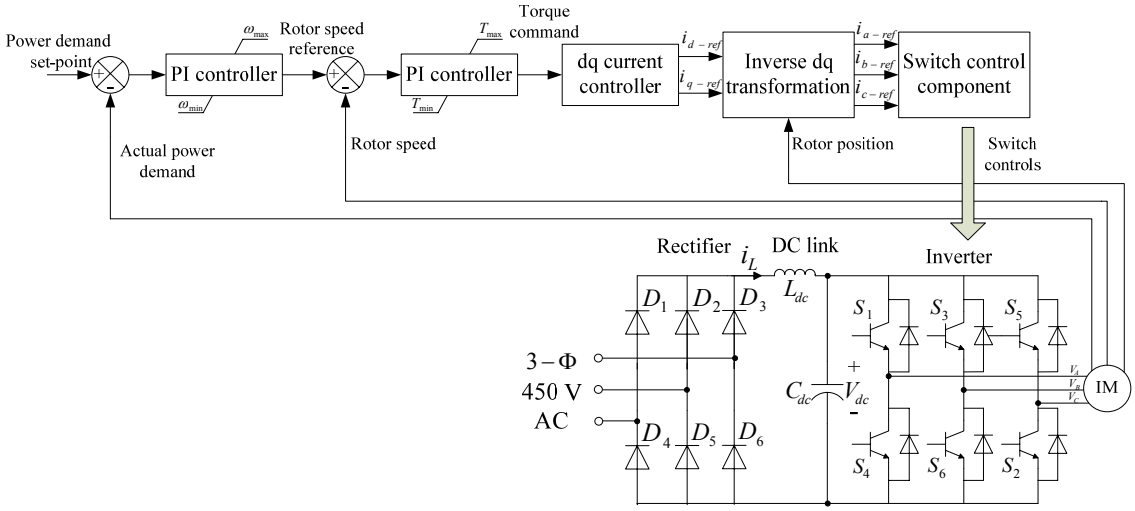

Figure 2.11 Diagram of an induction motor model and a variable frequency drive

2.3 Time-Frame Analysis of Loads in the Notional All-Electric Ship Power System

Since the notional all-electric ship power system consists of large portions of nonlinear loads and dynamic loads with fast dynamics, load dynamics need to be carefully studied to determine an appropriate decision time step for real-time load management. In the MVAC system, the power set-point of the propulsion load needs to be regulated when the pulse load is served. In the DC zone system, the load demand of each load needs to be regulated when the available power to the DC zone system is changed. Thus, an appropriate decision time step for real-time load management needs to be determined to achieve these objectives.

2.3.1 Time-frame analysis for pulse load

In future all-electric warships, high-energy weapon loads, such as electromagnetic guns, electromagnetic launch systems, free-electron lasers, pulse radar, aircraft launch, and high power microwave, will be integrated into all-electric ship power systems. These pulse loads draw very large short-time power in an intermittent way and may cause significant voltage and frequency oscillations in the system, which deteriorate the power quality of the all-electric ship power system. The dynamic and transient stabilities of the all-electric ship power system, when pulse loads were served, were analyzed using PSCAD simulation studies.

2.3.1.1 Literature review for pulse loads in all-electric ship power systems

Pulse loads can be classified as kinetic energy weapons, direct energy weapons, and high power sensors [15]. Kinetic energy weapons use electric power to accelerate a projectile, such as electromagnetic guns, coil guns, electrothermal guns, and

electrothermal-chemical guns [15], [16]. Direct energy weapons emit a high power electromagnetic wave to the target, such as high energy laser, high power microwave, [15]. High power sensors include pulse sonar and pulse radar.

MIL-STD-1399, IEEE-STD-45 [17], and STANAG 1008 [18] provide specifications for voltage and frequency modulations for navy shipboard power systems. The frequency and voltage modulations are defined in (2-4).

$$\begin{aligned} m_{freq} &= \frac{f_{\max} - f_{\min}}{2 f_{nom}} \\ m_{voltage} &= \frac{V_{\max} - V_{\min}}{2 V_{nom}} \end{aligned} \tag{2-4}$$

where m_{freq} and $m_{voltage}$ are the frequency and voltage modulation, respectively; f_{nom} and V_{nom} are the nominal frequency and RMS or peak line-to-line voltage, respectively. To meet the IEEE-STD-45 requirement, the frequency and voltage modulations should be less than 0.5% and 2%; to meet STANAG 1008 requirement, the frequency and voltage modulations should be less than 0.5% and 5%. The frequency modulation of the two standards is the same, but the voltage modulation is different.

Based on the requirements for voltage and frequency modulations, STANAG 1008 [18] provides specifications of the power constraints for pulse loads in all-electric ship power systems, which are shown in (2-5).

$$\begin{aligned} P_{pulse} &< 0.25 S_{supply} \\ Q_{pulse} &< 0.065 S_{supply} \end{aligned} \tag{2-5}$$

where, P_{pulse} and Q_{pulse} are pulse load active and reactive power demand, and S_{supply} is the full rated apparent power of the supply at the occurrence of the pulse load. The

power quality requirements for shipboard power systems defined by IEEE-STD-45 [17] are summarized in Table 2.4.

Table 2.4 IEEE-STD-45 power quality requirements for shipboard power systems

Characteristics	Frequency	Voltage
Tolerance	±3%	±5%
Modulation	0.5%	2%
Transient tolerance	±4%	±16%
Transient recovery time	2 sec	2 sec

Various kinds of pulse loads have been studied in the literature. These pulse loads have different energy demand, power demand, pulse width, and pulse frequency. The magnitudes of various pulse loads are summarized in Table 2.5. The durations of various pulse loads are summarized in Table 2.6. The power requirements for typical pulse loads are shown in Table 2.7.

Table 2.5 Summary of pulse load magnitudes

Pulse load magnitude	Reference #
5 MW – 20 MW	[12], [13]
20 MW – 70 MW	[19], [20], [21], [22], [23]
20 kW – 200 kW	[24], [25], [26]

Table 2.6 Summary of pulse load durations

Pulse load duration	Reference #
1 sec – 25 sec	[12], [13], [24], [26]
0.1 sec – 1 sec	[19], [25], [20], [21], [22], [23]

Table 2.7 Summary of power requirements for typical pulse loads

Pulse load type	Energy	Pulse length	Average power (Charging power)	Peak power
EM rail-gun [16], [27]	30-40 MJ	4-6 ms	2 MW	15-28 GW
Radar [15], [27]	0.2 kJ	0.2 μs	2 MW	20 GW
Coil gun [15]	8.6 MJ	100 ms	0.09 MW	0.086 GW
ETC igniter [16]	0.3-0.5 MJ	1-2 ms	25 kW	100-500 kW
ETC gun [16]	3-5 MJ	3-4 ms	0.25 MW	0.36-0.9 GW
Pure ET gun [16]	60-90 MJ	3-4 ms	4.5 MW	0.11-8 GW
Electromagnetic aircraft launch system (EMALS) [27], [28]	550-2250 MJ	Several seconds	≤6 MW	150 MW

2.3.1.2 Dynamic studies for pulse loads in the notional all-electric ship power system

To study the dynamic behaviors of pulse loads in the notional all-electric ship power system, a simplified notional system was designed to demonstrate the dynamic behavior of the system, when a pulse load was served. The one-line diagram of the simplified notional all-electric ship power system model is shown in Figure 2.12. The system consists of one MTG with 36 MW/45 MVA capacity, one auxiliary turbine generator (ATG) with 4 MW/5 MVA capacity, one propulsion load with 36.5 MW rated power, two DC zones with 2 MW rated power for each zone, and one pulse load connected to the MTG bus.

It was assumed that MTG and ATG were in service, so the total generation capacity of the system was 40 MW. An automatic generation control (AGC) was used to regulate set-points of generators to maintain the system frequency at 60 Hz. Each gas turbine generator included a gas turbine governor, an exciter, and one synchronous generator. Droop control was used to dynamically regulate the output mechanical power of the gas turbine based on the generator frequency. If the total load demand exceeded the generation capacity, the system frequency would decline quickly from 60 Hz.

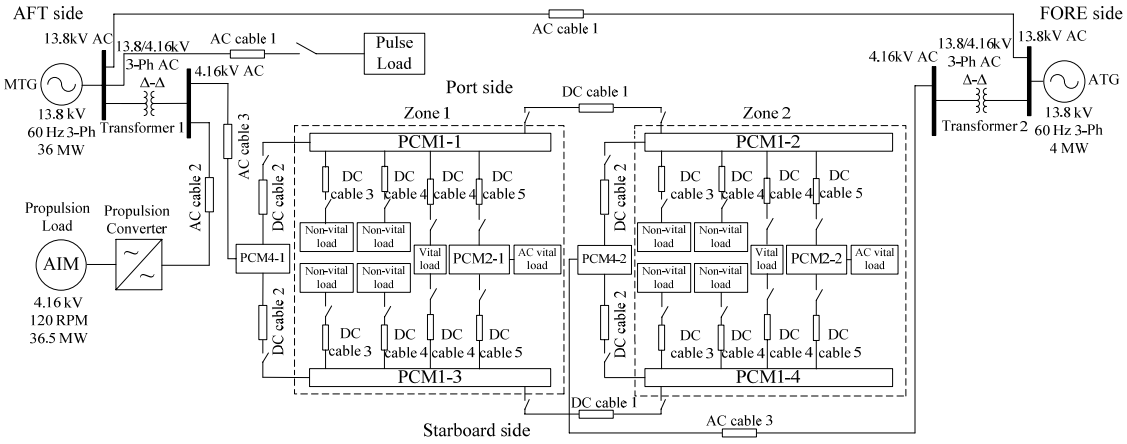

Figure 2.12 One-line diagram of a simplified notional all-electric ship power system model

Ten case studies were conducted to study the dynamic behavior of two types of pulse loads – single-pulse load and multiple-pulse load. The pulse loads used in the ten case studies are summarized in Table 2.8. The magnitude of pulse loads was chosen as 10 MW, which was 25% of the generation capacity. The pulse lengths were chosen between 0.1 and 1 second, which were widely used in the literature.

Table 2.8 Summary of pulse loads for case studies

Case No.	Pulse magnitude (MW)	Pulse length (sec) & duty ratio	Number of pulses	Propulsion load demand (MW)	DC zone load demand (MW)
1	10	0.1 – NA	1	16	4
2	10	0.5 – NA	1	16	4
3	10	1.0 – NA	1	16	4
4	10	0.1 – NA	1	32	4
5	10	0.5 – NA	1	32	4
6	10	1.0 – NA	1	32	4
7	10	0.1 – 10%	10	16	4
8	10	0.1 – 50%	10	16	4
9	10	0.1 – 10%	10	32	4
10	10	0.1 – 50%	10	32	4

The pulse load in case studies was served at 10 seconds. In case studies 1-3, three pulse loads had different pulse lengths and the same magnitude (10 MW), and the propulsion load demand was 16 MW. The RMS voltage drop of the MTG generator was almost the same in case studies 1-3, as shown in Figure 2.13. The frequency behavior of the MTG generator in case studies 1-3 is shown in Figure 2.14. The frequency behavior was different when the pulse duration was different. When the pulse length was increased from 0.1 second to 0.5 second, the maximum frequency deviation of the MTG generator was increased from 0.4 Hz to 1.1 Hz, as shown in Figure 2.14. However, when the pulse duration was increased from 0.5 sec to 1 sec, the maximum frequency deviation was not increased because the system included enough generation capacity to supply all the loads and the prime movers of generators picked up the load changes in 0.5 second to restore the system frequency. If the generation capacity was less than load demand, the system frequency decreased significantly, which was illustrated in case studies 4-6.

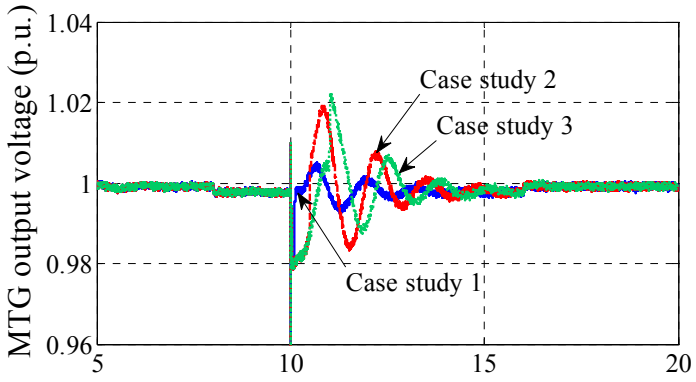

Figure 2.13 RMS voltage of the MTG generator for case studies 1-3

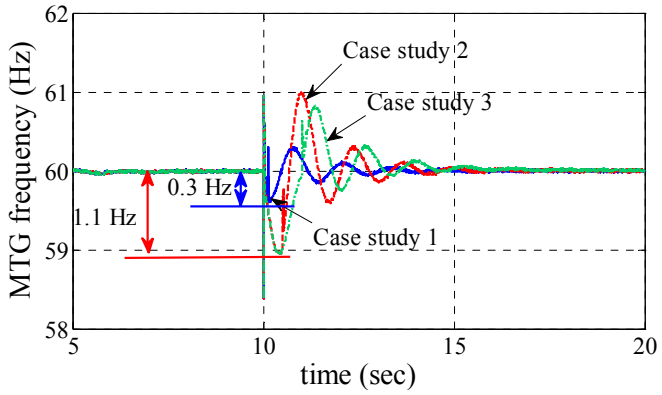

Figure 2.14 Frequency dynamic behavior of the MTG generator for case studies 1-3

In case studies 4-6, the pulse load had a different pulse length and the same magnitude (10 MW) for each case. The propulsion load demand was 32 MW for each case. The frequency behavior of the MTG generator in case studies 4-6 is shown in Figure 2.15. As the pulse length was increased from 0.1 second to 1.0 second for each case, the maximum frequency deviation of the MTG generator increased significantly. Since the total generation capacity was 40 MW, the available power source capacity constraint was violated when the pulse load was served in case studies 4-6. When the pulse length was larger than 1 second, the maximum frequency deviation of the MTG generator was more than 2 Hz, which might trip generators and sensitive loads in the all-electric ship power system. Comparing the MTG frequency behavior of case studies 2 and 5, as shown in Figure 2.16, the pulse load characteristics in the two cases were the same, but the maximum frequency deviation in case study 5 was larger than case study 2 because the available power source capacity constraint was violated in case study 5. For the same reason, the maximum frequency deviation in case study 6 was much larger than

case study 3, as shown in Figure 2.17, even though they used the same pulse load characteristics.

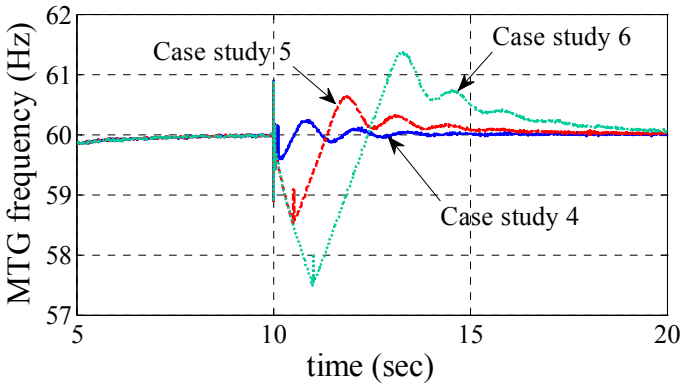

Figure 2.15 Frequency dynamic behavior of the MTG generator for case studies 4-6

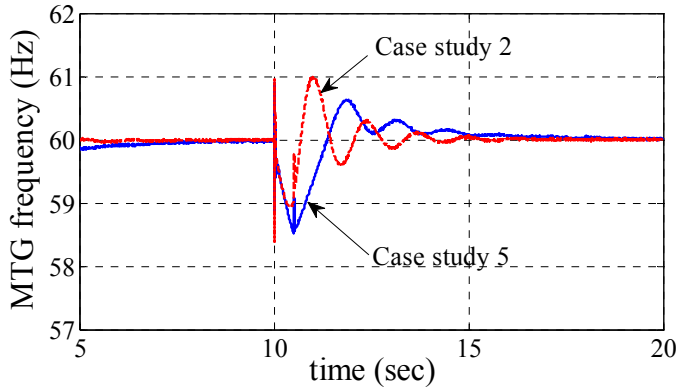

Figure 2.16 Frequency dynamic behavior of the MTG generator for case studies 2 and 5

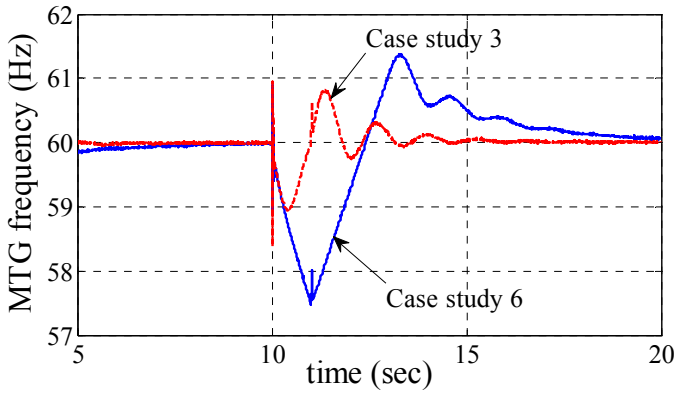

Figure 2.17 Frequency dynamic behavior of the MTG generator for case studies 3 and 6

Since the notional all-electric ship power system will serve pulse train loads in which several pulses occur periodically such as rail gun [24], [19] and radar [25], the system frequency behavior will be impacted by the repetition period of the pulse loads. In case studies 7-10, multiple-pulse loads were used to study the dynamic performance of the notional all-electric ship power system with repetition pulses. The pulse load characteristics were the same in case studies 8 and 10, and the propulsion load demand was 16 MW in case study 8 and 32 MW in case study 10. The maximum frequency deviation of the MTG generator in case study 10 was larger than case 8, as shown in Figure 2.18, because the load demand exceeded the generation capacity in case study 10. Comparing frequency behaviors of pulse loads with 10% and 50% duty ratios, the maximum frequency deviation of case study 10 was larger than case study 9, as shown in Figure 2.19. Thus, the duty ratio of the pulse load also affected the frequency behavior of the notional all-electric ship power system.

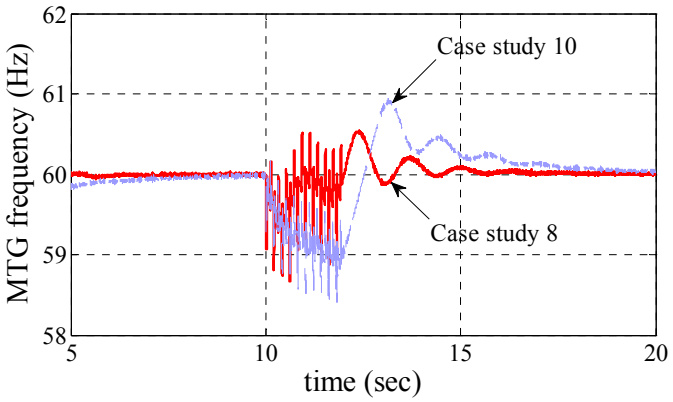

Figure 2.18 Frequency dynamic behavior of the MTG generator for case studies 8 and 10

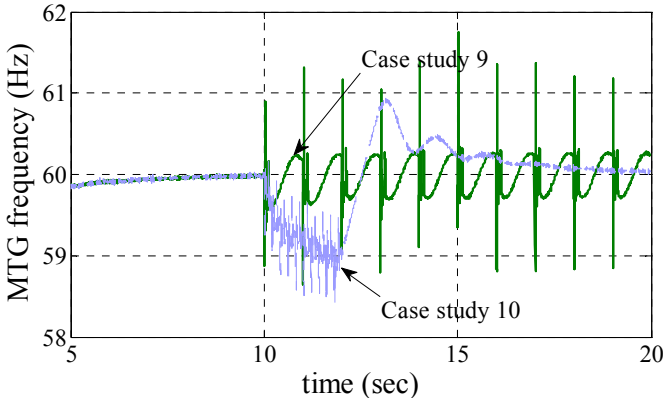

Figure 2.19 Frequency dynamic behavior of the MTG generator for case studies 9 and 10

The case studies indicated that the impact of pulse loads on the dynamics of the all-electric ship power system depended on the pulse magnitude, pulse length, generation capacity, total load demand, number of pulses, and duty ratio of pulses. Especially when the total load demand was close to the generation capacity, the frequency oscillation was significant after a pulse load was served. It was because after the pulse load was served, the available power source capacity constraint was violated, which resulted in a significant frequency decline.

2.3.2 Time-frame analysis for propulsion load

In the notional all-electric ship power system, propulsion loads consume 90% of the total generation capacity, which has great impact on the finite inertia power system. When the power demand of propulsion loads increases or decreases quickly, the frequency and voltage may deviate from the nominal values. The navy ship has a large inertia, so the ship speed does not change quickly after the power demand of propulsion loads is changed. Due to this reason, propulsion loads can be temporarily regulated to compensate for the load changes in the system when other higher priority loads need to be served [29]. For instance, pulse loads have higher priority and propulsion loads have lower priority in battle mode [14]. When a pulse load is served, the propulsion load demand can be reduced immediately to keep the total load demand constant and reduce the frequency deviation. Similar ideas have been implemented in [13], [24], [30], [31].

2.3.2.1 Literature review for propulsion loads in all-electric ship power systems

In [32], typical time constants of a marine propulsion system based on a 20-MW propulsion motor and rapid-response ship are given to show the diversity of the time constant in the marine drive system. The time constant of hydrodynamics is on the order of hundred seconds; the time constants of the variable frequency drive and motor dynamics are on the order of milliseconds to seconds; and the time constant of power electronics devices is on the order of microseconds. If the simulation step size is chosen based on the time constant of power electronics devices, the computation complexity of the simulation would be high for the mechanical transient duration. In order to increase

the simulation efficiency, the authors developed averages models to model the rectifier and inverters in the marine drive system, which allowed a larger simulation step size.

In [24], [29], [33], the propulsion system was driven by a 37 kW, 180 rpm, 460 V line-line voltage induction motor in the reduced-scale naval combat survivability generation and propulsion test-bed. In [24], [33], the propulsion load was coordinated with a pulse load to reduce the impact of pulse loads on the power quality of all-electric ship power systems. In battle mode, when a pulse load was served in the system, the power demand of the propulsion load was immediately reduced to compensate for the impact of the pulse load on the dynamics of the system. After the pulse load was disconnected from the system, the power demand of the propulsion load was gradually regulated to the nominal value.

Another pulse load and propulsion load coordination method is discussed in [30]. When the ship operates at full speed, the system does not have enough power to recharge energy storage systems. In order to recharge the energy storage system quickly, the ship speed was reduced to decrease the propulsion load demand. After the ship reached a lower cruising speed, energy storage systems were recharged quickly to serve pulse loads. The simulation results indicated that, if necessary, the electromagnetic launcher and free electron laser could both be served using the energy storage systems, while using the full generation power to accelerate the ship.

2.3.2.2 Dynamic studies for propulsion loads in the notional all-electric ship power system

A simplified notional all-electric ship power system model, as shown in Figure 2.12, was used to study the dynamic behavior of propulsion loads. The simplified system consisted of one MTG, one ATG, one propulsion load, one pulse load, and two DC zones. In the case studies, it was assumed that the navy ship operated in cruise mode and the pulse load was out of service. The rated power of the propulsion load was 36.5 MW, and the load demand in the DC zone system was 4 MW. Two case studies were used to study the dynamic behavior of the power demand of the propulsion load and the ship speed, respectively. The decision time step for the propulsion load power set-point was chosen as 10 milliseconds in the case studies.

In case study 1, the propulsion load operated in power control mode to study the dynamic behavior of the power demand of the propulsion load. The power set-point and actual load demand of the propulsion load are shown in Figure 2.20. The power set-point of the propulsion load was decreased from 32 MW to 16 MW at 10 seconds, increased to 25.6 MW at 20 seconds, and decreased to 6.4 MW at 30 seconds. The simulation results indicated that the propulsion load demand reached the new desired value in 5 sec for each set-point change. The output power signals of the MTG and ATG generators are shown in Figure 2.21. After the power demand of the propulsion load was changed, the output power of each generator was also changed to balance the generation and load in the system.

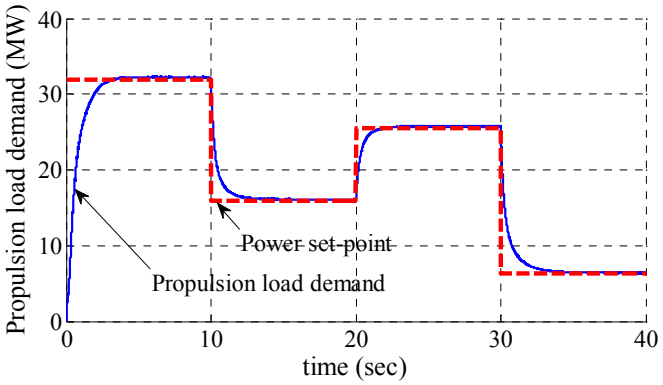

Figure 2.20 Power set-point and actual power demand of the propulsion load for case study 1

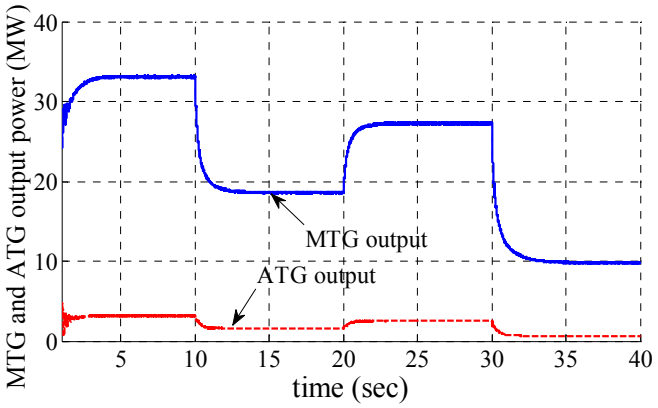

Figure 2.21 MTG and ATG output power for case study 1

The MTG generator frequency is shown in Figure 2.22. When the propulsion load demand was decreased from 32 MW to 16 MW at 10 seconds, the maximum frequency deviation was 1.2 Hz; when the propulsion load demand was increased from 16 MW to 25.6 MW at 20 seconds, the maximum frequency deviation was 0.7 Hz; and when the propulsion load demand was decreased from 25.6 MW to 6.4 MW, the maximum frequency deviation was 1.3 Hz. The propulsion load demand changed from one level to another level in a few seconds, and the prime mover could not response

quickly enough to pick up the load change, which resulted in the frequency oscillations. The output voltages of MTG and ATG generators are shown in Figure 2.23. When the power demand of the propulsion load changed, the maximum voltage deviation was around 2%. When the power demand of the propulsion load was increased, the output voltages of generators were decreased from the normal value; and when the power demand of the propulsion load was decreased, the output voltages of generators were increased from the nominal value.

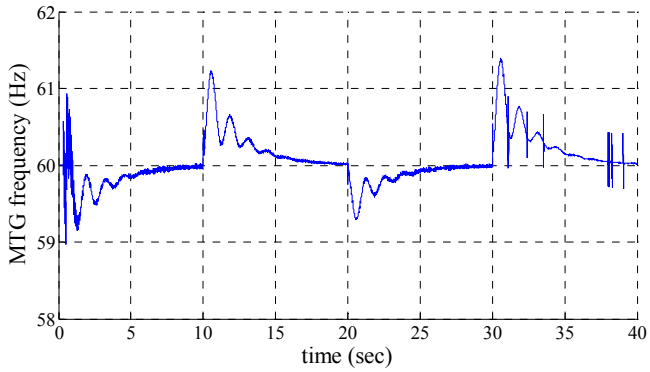

Figure 2.22 Frequency behavior of the MTG generator for propulsion load changes in case study 1

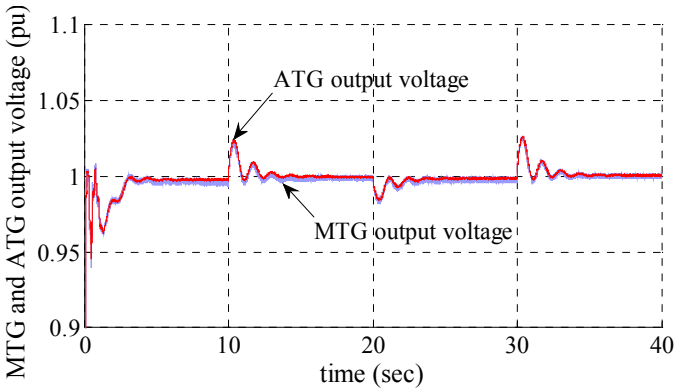

Figure 2.23 MTG and ATG output voltages for propulsion load changes in case study 1

In case study 2, the propulsion load operated in speed control mode to study dynamic behavior of the ship speed. The decision time step of the speed controller was chosen as 10 milliseconds in the case study. The ship speed set-point was increased from 20 to 30 knots at 30 seconds, reduced to 20 knots at 60 seconds, and increased to 25 knots at 80 seconds. The ship speed dynamic behavior is shown in Figure 2.24. The ship speed was increased from 0 knot to 20 knots in 15 seconds. The ship was accelerated from 20 knots to 28 knots in 12 seconds.

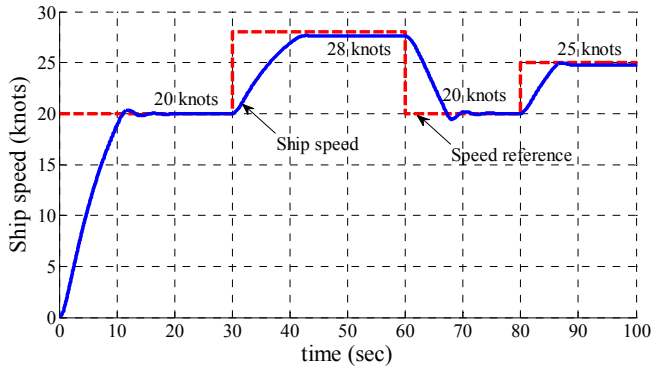

Figure 2.24 Ship speed set-point and actual ship speed for case study 2

When the ship speed was increased, the propulsion load used its maximum power to accelerate the ship to its desired speed, as shown in Figure 2.25. When the ship speed reached the desired value, the speed controller returned to the linear region of the controller. The ship was accelerated using its maximum power and decelerated using its minimum power, which could drive the ship to its desired speed quickly. The system frequency behavior is shown in Figure 2.26. When the ship was accelerated, the maximum frequency deviation was around 2.2 Hz. When the ship was decelerated, the

maximum frequency deviation was around 1.8 Hz. MTG and ATG output voltages are shown in Figure 2.27. When the ship was accelerated, the voltage drop was 5% of the nominal value, and the voltage returned to the normal value in 2 seconds; when the ship speed was decreased, the voltage increased by 3% and then returned to the nominal value in 2 seconds.

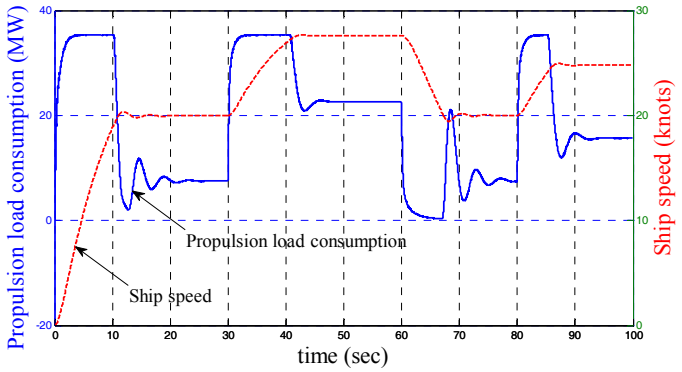

Figure 2.25 Propulsion load demand for ship speed changes in case study 2

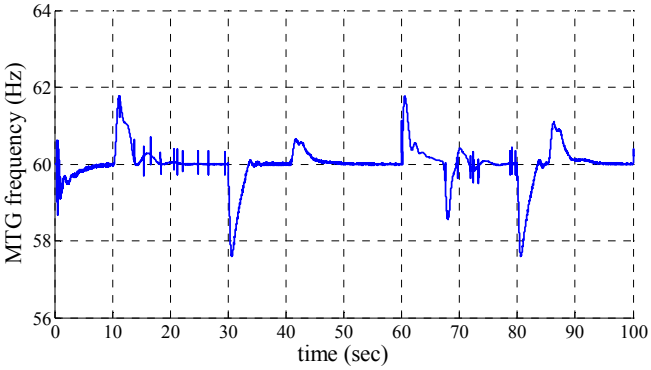

Figure 2.26 MTG frequency signal for ship speed changes in case study 2

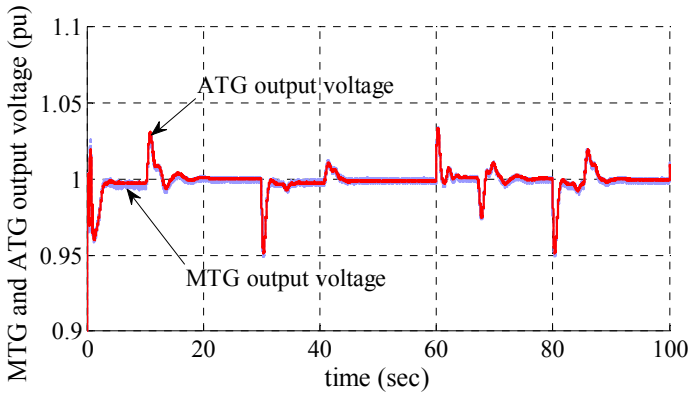

Figure 2.27 MTG and ATG output voltages for ship speed changes in case study 2

In power control mode, the propulsion load reached the steady state in 5 seconds when the load reference changed. The decision time step for the power set-point of the propulsion load was chosen as 10 milliseconds. When a pulse load was served in the notional all-electric ship power system, the power set-point of the propulsion load could be regulated immediately to compensate for the impact of the pulse load based on the system frequency signal. The 10 ms decision time step of the propulsion load power controller could successfully accomplish this task.

In speed control mode, the ship speed could reach the steady state in 15 seconds when the speed reference changed. When the ship speed set-point was increased, the speed controller immediately operated in saturation region to accelerate the ship using the full propulsion power. After the ship speed reached to the desired speed, the speed controller returned to linear region to maintain the ship speed at the desired value. The decision time step of the speed controller was also chosen as 10 milliseconds in the case study 2, which successfully achieved the cruising function of the propulsion load.

2.3.3 Time-frame analysis for motor loads in DC zones

The data for the motor loads in a DC zone are shown in Table 2.9. The rated power of DC and AC motors in DC zones are in the range of 36 kW to 192.6 kW. DC motor loads are served by DC-DC converters in PCM1s directly, and AC motor loads are served by inverters (PCM2s).

Table 2.9 Motor load definitions in one DC zone

Component name	Priority	Rating (kW)	Voltage (V)	Switch Board
DC motor load 1	Non-vital	115.4	650	Port
DC motor load 2	Non-vital	36	650	Port
DC motor load 3	Non-vital	115.4	650	Starboard
DC motor load 4	Non-vital	47.6	650	Starboard
DC motor load 5	Non-vital	36	375	Port
DC motor load 6	Non-vital	115.4	375	Starboard
AC motor load 1	Vital	181	450	Port
AC motor load 2	Non-vital	79.4	450	Port
AC motor load 3	Non-vital	115.4	450	Starboard
AC motor load 4	Vital	192.6	450	Starboard

2.3.3.1 Dynamic studies for DC motor loads in the DC zone system

The simulation diagram of a DC motor in PSCAD software is shown in Figure 2.28. The DC motor model consists of the DC motor, excitation system, mechanical load, and power controller. The DC motor model discussed in section 2.2.2.2 does not include the machine drive system. In this section, a torque control method was designed to control the power demand of the DC motor. The power controller is used to drive the DC motor power demand to the desired value. To study the dynamic performance of the DC motor model, the dynamic behavior of the DC motor and machine drive system was modeled using a second-order linear system, which is shown in (2-6).

$$P_{\mathrm{DC}}(s)=\frac{K_{\mathrm{DC}}}{T_2 s^2+T_1 s+1}P_{\mathrm{set-point}}(s) \tag{2-6}$$

where, K_{DC}, T_1, and T_2 are the coefficients of the model; $P_{\mathrm{set-point}}$ is the power demand set-point of the DC motor; P_{DC} is the actual power demand of the motor. The state space equation for the DC motor model can be shown as (2-7).

$$\begin{aligned}
&\dot{x}_1(t)=x_2\\
&\dot{x}_2(t)=-(1/T_2)x_1(t)-(T_1/T_2)x_2(t)-(K_{DC}/T_2)u(t)\\
&y(t)=x_1(t)=P_{DC}(t)\\
&u(t)=P_{\mathrm{set-point}}(t)
\end{aligned} \tag{2-7}$$

where, x_1 is equal to the power demand of the DC motor; x_2 is the first derivative of state variable x_1; u is the input variable of the linear system, which is equal to $P_{\mathrm{set-point}}(t)$; y is the output signal of the system, which is equal to $P_{DC}(t)$. The unknown parameters T_1, T_2, and K_{DC} were identified using a system identification method. The diagram of the identification procedure is shown in Figure 2.29.

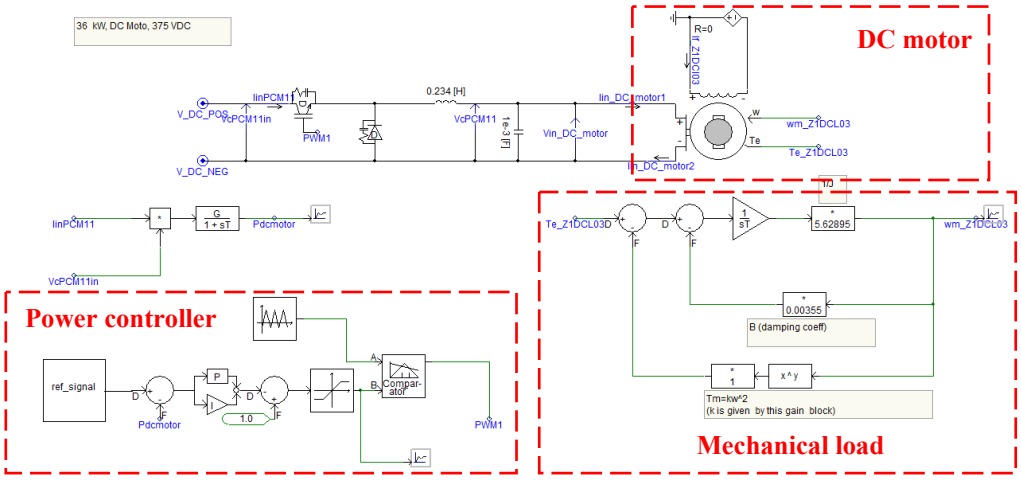

Figure 2.28 Diagram of DC motor simulation model in PSCAD software

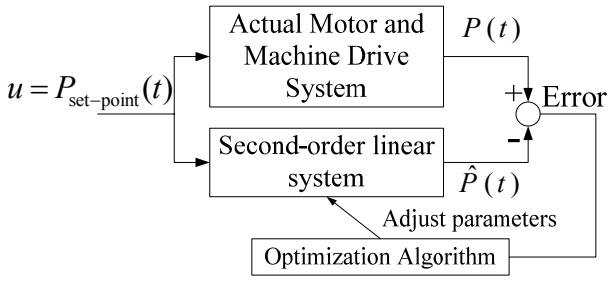

Figure 2.29 Diagram of system identification for motor load model

To model the DC motor using (2-7), a system identification technique was used to identify the unknown parameters of the system model. DC motors were simulated in PSCAD software. Based on the DC motor dynamic model (2-7) and data from the PSCAD simulation, the unknown parameters of the dynamic model were identified using the simplex method.

The identification results of 36 kW 375 V DC motor are shown in Figure 2.30. The identification results of 115.4 kW 375 V DC motor are shown in Figure 2.31. The identification results of 115.4 kW 650 V DC motor are shown in Figure 2.32. The identification results of 47.6 kW 650 V DC motor are shown in Figure 2.33. The simulation results indicated that the estimated system followed the PSCAD model very well. The identified parameters of DC motors are summarized in Table 2.10.

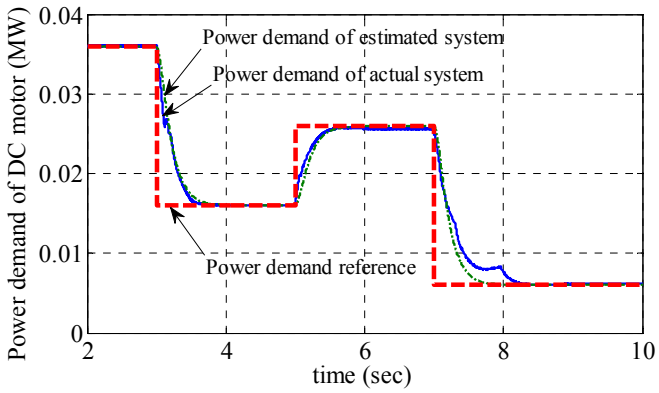

Figure 2.30 Power demands of estimated system and actual system for 375 V 36 kW DC motor

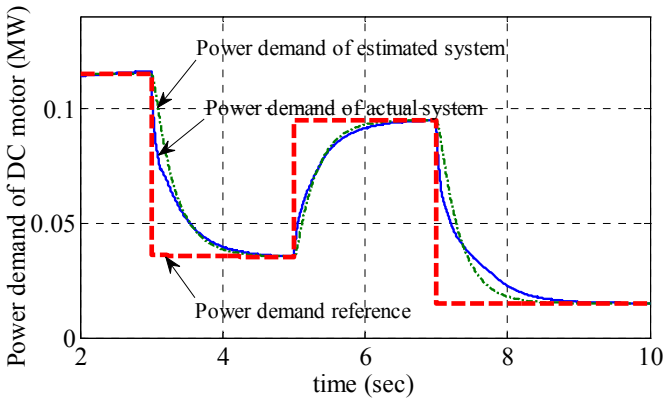

Figure 2.31 Power demands of estimated system and actual system for 375 V 115.4 kW DC motor

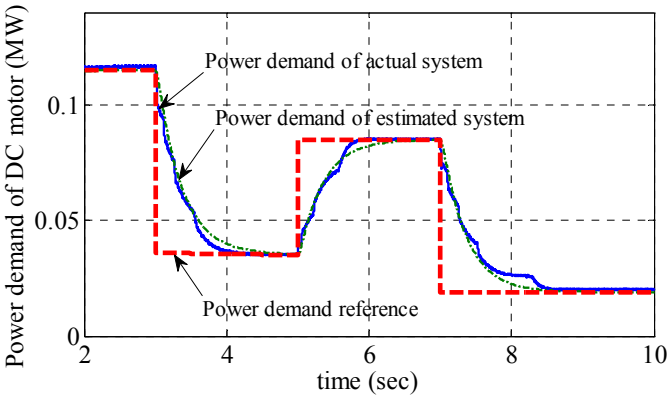

Figure 2.32 Power demands of estimated system and actual system for 650 V 115.4 kW DC motor

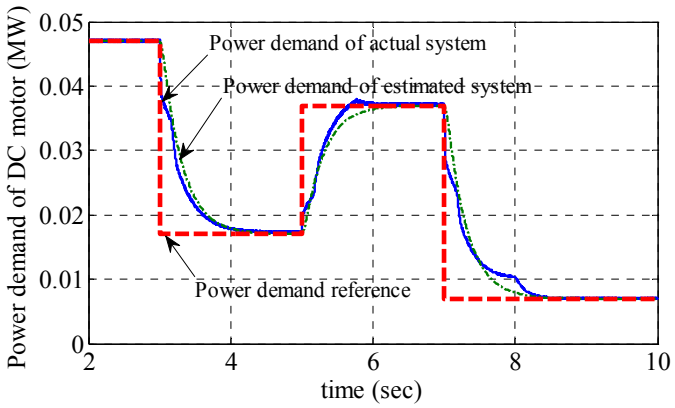

Figure 2.33 Power demands of estimated system and actual system for 650 V 47.6 kW DC motor

Table 2.10 Identified parameters of DC motors

Component name	K_{DC}	T_1	T_2
36 kW 375 V DC motor	1	0.2203	0.01
115 kW 375 V DC motor	1	0.3289	0.01
115 kW 650 V DC motor	1	0.3648	0.01
47.6 kW 650 V DC motor	1	0.3123	0.01

When the power set-point of a DC motor load was changed from one value to another, the system reached the new steady state in a second. When the available power to the DC zone system was reduced, load demand of non-vital DC motor loads could be immediately decreased to rebalance the generation and load.

2.3.3.2 Dynamic studies for AC motor loads in the DC zone system

The AC motor load used in this section to study the load dynamic behavior is shown in Figure 2.11 in section 2.2.2.3, which includes an induction motor and a machine drive system. The dynamic behavior of the induction motor and machine drive system can be modeled using a second-order linear system, which is shown in (2-8).

$$P_{AC}(s) = \frac{K_{AC}}{T_2 s^2 + T_1 s + 1} P_{set-point}(s) \tag{2-8}$$

where, K_{AC}, T_1, and T_2 are the coefficients of the model; $P_{\mathrm{set-point}}$ is the power set-point of the AC motor; P_{AC} is the actual power demand of the induction motor. The state space equation for the AC motor load model can be expressed in (2-9).

$$\begin{aligned}
&\dot{x}_1(t) = x_2(t) \\
&\dot{x}_2(t) = -(1/T_2)x_1(t) - (T_1/T_2)x_2(t) - (K_{AC}/T_2)u(t) \\
&y(t) = x_1(t) = P_{AC}(t) \\
&u(t) = P_{\mathrm{set-point}}(t)
\end{aligned} \tag{2-9}$$

where, x_1 is equal to the power demand of the AC motor; x_2 is the first derivative of state variable x_1; u is the input variable of the system, which is equal to $P_{\mathrm{set-point}}(t)$; y is the system output, which is equal to $P_{AC}(t)$. The unknown parameters T_1, T_2, and K_{AC} were identified using the identification method, as shown in Figure 2.29.

The simplex method was used to identify unknown parameters of the AC motors. The identification results of 192 kW AC motor are shown in Figure 2.34. The identification results of 115 kW AC motor are shown in Figure 2.35. The identification results of 181 kW AC motor are shown in Figure 2.36. The identification results of 79 kW AC motor are shown in Figure 2.37. The simulation results indicated that the estimated system tracked the actual system very well. The identified parameters of the AC motors are summarized in Table 2.11.

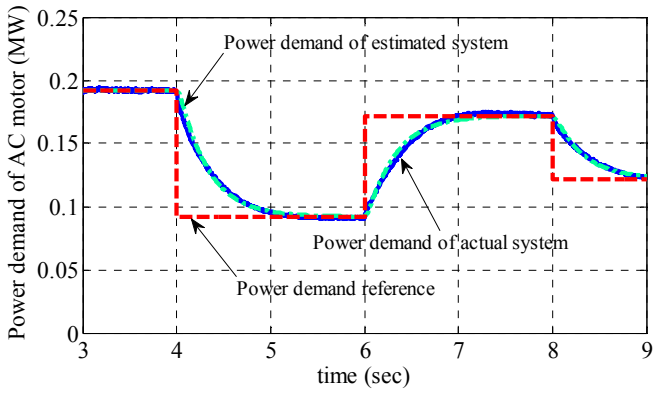

Figure 2.34 Power demands of estimated system and actual system for 192 kW AC motor

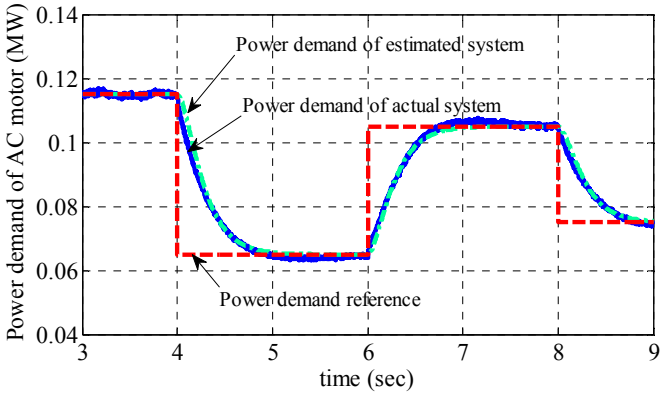

Figure 2.35 Power demands of estimated system and actual system for 115 kW AC motor

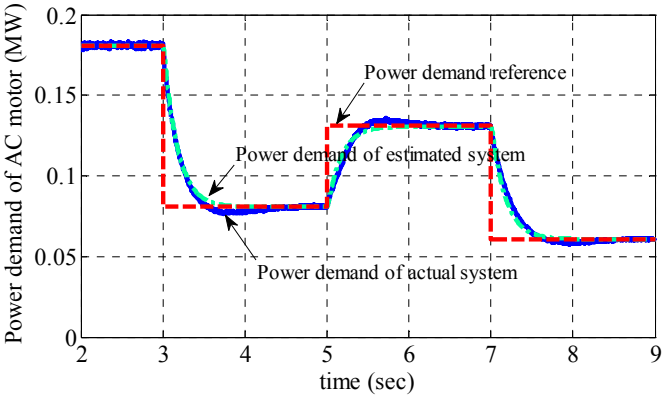

Figure 2.36 Power demands of estimated system and actual system for 181 kW AC motor

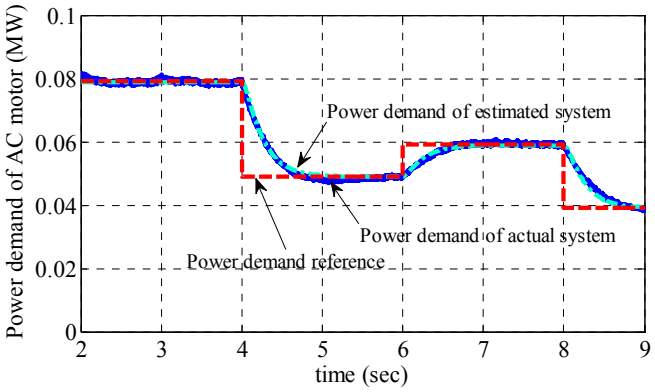

Figure 2.37 Power demands of estimated system and actual system for 79.4 kW AC motor

Table 2.11 Identified parameters of AC motors

Component name	K_{AC}	T_1	T_2
192 kW AC motor	1	0.3394	0.0105
115 kW AC motor	1	0.3	0.02
181 kW AC motor	1	0.1789	0.002
79 kW AC motor	1	0.2763	0.0116

2.4 Summary

In this chapter, a notional all-electric ship power system model for ships was discussed. The MVAC system and DC zone system models were discussed, separately. The propulsion load model, pulse load model and motor load models in DC zones were discussed in details. The dynamic behaviors of propulsion loads, pulse loads, and motor loads in DC zones were studied to analyze the time-frame of these loads. The dynamic performances of these loads were studied in PSCAD simulation.

The decision time step of the propulsion load was chosen as 10 milliseconds in the case studies. The simulation results indicated that the propulsion load successfully achieved the cruising function and power control function by using this decision time

step. The case studies for pulse loads indicated that the dynamic behaviors of the system were determined by the pulse magnitude, pulse length, generation capacity, total load demand, number of pulses, and duty ratio of pulses, when pulse loads were served. The case studies for AC and DC motors in DC zones indicated that these dynamics loads had smaller time constants than the propulsion load. When the available power to the DC zone system was changed, the loads in DC zones could be immediately regulated to track the available power signal. The time-frame analysis for loads in the all-electric ship power system would be used to determine the decision time step for real-time load management in the next chapter.

3. LITERATURE REVIEW AND PROBLEM FORMULATION

3.1 Introduction

This chapter discusses the operations of isolated power systems, which include three levels – primary control, secondary control, and tertiary control. The real-time load management is defined as a secondary control problem. The load management methods for large power systems are reviewed. Most of existing methods aims to balance the generation and load while achieving certain objectives. The decision time step for these methods is on the order of minutes to hours, and the detail load and system dynamics are not included in the load management problem. However, all-electric ship power systems have faster dynamics and include large portions of nonlinear loads and dynamics loads, which require a smaller decision time step. Moreover, pulse loads in all-electric ship power systems draw a large amount of power in an intermittent way. Thus, the loads in the system need to be dynamically regulated to achieve the generation and load balancing in real time while satisfying various operational constraints of the system. Otherwise, pulse loads may cause significant frequency and voltage oscillations in all-electric ship power systems.

Due to these reasons, a real-time load management problem was formulated for all-electric ship power systems to achieve dynamic balancing while satisfying various operational constraints of the system. The objective of real-time load management is to optimally determine the switch status or set-point of each load while satisfying the operational constraints of the system and considering load priorities. In the problem

formulation, various system operational constraints were included, such as available power source capacity constraints, voltage constraints for motor loads, steady state and dynamic state cable constraints, and load bus power capacity constraints. The decision time step of real-time load management for all-electric ship power systems chosen as 10 milliseconds based on the time-frame analysis of loads is also discussed. The real-time load management problem was illustrated in three scenarios, which indicated that the dynamic performance of the system with real-time load management was much better than that without real-time load management.

The outline of this chapter is as follows. In section 3.2, operations of isolated power systems are introduced. In section 3.3, the literature review of load management is discussed. The shortcomings of existing methods are also given in this section. A proof-of-concept for the real-time load management approach is shown in section 3.4. Section 3.5 states the problem formulation of real-time load management and defines the decision time step for the real-time load management approach based on the time-frame of loads in all-electric ship power systems. At last, a summary is given in section 3.6.

3.2 Operations of Isolated Power Systems

The operation of isolated power systems can be classified as primary control, secondary control, and tertiary control [34], [35]. A diagram of the operation of isolated power systems is shown in Figure 3.1 [34]. The system state information flows from primary level to tertiary level, and the decision signals flow from tertiary level to primary level to achieve overall operation objectives of isolated power systems. The

primary controller has the smallest decision time step to regulate the voltage and frequency to desired values. On the other hand, tertiary controller collects state information of the system through the communication infrastructure and makes decisions to improve the overall performances of isolated power systems, which has a longer decision time step.

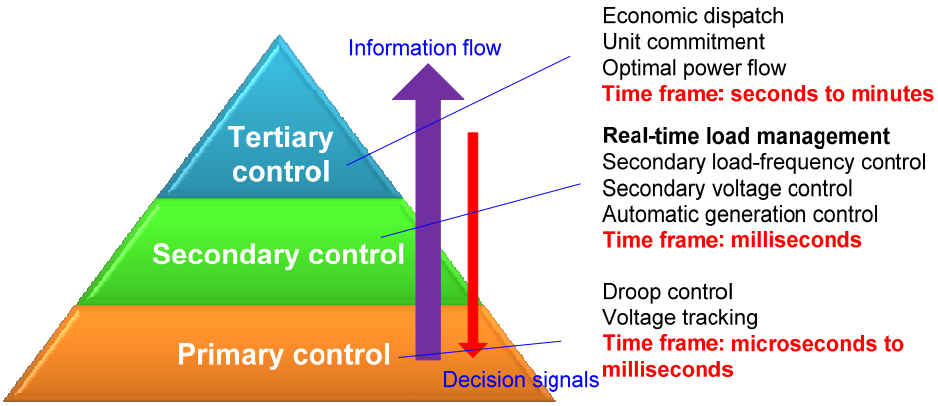

Figure 3.1 Diagram of isolated power system control operations [34]

The primary control has the smallest decision time step, which ensures that the frequency and voltage of a power system can track their reference signals, such as droop control and voltage tracking control. For instant, a microgrid operating in islanded mode has difficulties to maintain the system frequency using a single distributed generator (DG) due to the limited generation capacity of the DG unit. The frequency-droop characteristics for microgrids [36], [37], [38], [39], [40] are introduced to control the output active power of each DC unit to dynamically balance the generation and load. The voltage-droop characteristics for microgrids [37], [38], [39], [40] are introduced to maintain bus voltages of microgrids by regulating the reactive power set-point of each

DG unit. In all-electric ship power systems, the droop control and isochronous control of gas turbine generators are discussed in [41]. These droop-based controllers can make local decision based on the local measurements and the set-points to achieve local objectives. The decision time step of the primary controller can be changed from microseconds to milliseconds.

The secondary control [35], [40] is responsible for balancing the active and reactive power of isolated power systems through communication infrastructures by determining the set-points for primary controllers. The secondary control includes automatic generation control (AGC), secondary load-frequency control [40], [42], secondary voltage control [35], [43], [44], real-time load management [5], etc. In this level, the secondary controller is used to determine set-points for local controllers to achieve the overall objectives of isolated power systems. For example, one objective of AGC is to maintain the system frequency at the nominal value for isolated power systems [3], [45]. The AGC can adjust set-points of dispatchable generators in the system to regulate the power outputs of these generators when the system frequency deviates from the nominal value. The power set-point signals are sent from the control center to individual generation units through communication infrastructures. For the secondary voltage control problem, the pre-specified voltage signals are sent to the dispatchable generation units to maintain bus voltages at desired values [35]. In the all-electric ship power system, the real-time load management and secondary voltage control have been studied in [5], [46], [43], [44]. The time-frame of the secondary control is on the order of milliseconds to seconds.

The tertiary control determines the optimal steady state set-points based on marketing signals [47] or other system requirements. Economic dispatch (ED), unit commitment (UC), and optimal power flow (OPF) are used to operate the system normally and economically. For instance, the optimal set-points for generators are determined by economic dispatch, which has a slower time-frame on the order of seconds to minutes. Due to the larger decision time step of tertiary control, optimization techniques are used to solve the problems in this level.

3.3 Literature Review for Load Management

This section discusses the literature review for load management in large power systems. Since all-electric ship power systems include pulse loads and large portions of nonlinear loads and dynamic loads, the traditional methods have difficulties to solve the load management problem for all-electric ship power systems. The shortcomings of existing methods are also discussed to indicate that a novel real-time load management approach needs to be developed for all-electric ship power systems.

3.3.1 Load management literature review

The concept of load management was first introduced in the 1970s. It was aimed to control and modify the patterns of demands of various consumers of a power utility in order to reduce the operating cost and maintain the reliability of the electric power network [48]. Load management can be categorized as direct load control (DLC), indirect load control, and local energy storage. DLC mainly focuses on shedding loads directly to satisfy certain objectives; indirect load control allows customers to control

their loads independently according to the price signal sent by utilities; local energy storage allows both utilities and customers to store energy in off-peak periods and use the stored energy during times of great demand. DLC mainly focuses on matching the generation power and the consumed loads in real time while achieving certain objectives, such as reducing the operating cost [49], maximizing the profit margin [48], and reducing the peak load [49]. Since the control status and the load profile of the system can be accessed by the control center almost instantaneously, real-time load management techniques can be developed to optimally coordinate suitable customers for DLC [50].

In [49], the objective of load management was to minimize production cost and peak load over a period of time. The constraints of load management included the maximum disturbed time constraint of controllable loads and the minimum connected time constraint of controllable loads. The energy demand constraints of controllable loads were also considered. The maximum disturbed time of controllable loads was chosen as 4 hours and the minimum connected time of controllable loads was chosen as 2 hours. The controllable load was formulated as a dynamic load. The decision time step was chosen as 1 hour. Forward dynamic programming method was used to solve the load management problem. This approach was applied to a residential power system with water heater loads. The controllable loads were divided into nine control groups of equal size. This method needed more computation complexity when the decision time step was reduced.

In [48], the objective of the load management approach was to maximize the profit margin over a period of time while satisfying the maximum disturbed time

constraint, minimum connected time constraint, and maximum disturbed power constraint of controllable loads. Linear programming was used to solve the load management problem. The objective function of load management was linearized to use the linear programming approach. The decision time step was chosen as 1 hour. The load management approach was applied to a utility power system to maximize profit margin.

In [50], a real-time two-way direct load control algorithm was proposed to coordinate suitable loads in power systems based on monitored air conditioning loads to minimize the difference between the load planned to be shed and actual load shedding. Integer programming was used to solve the direct load control problem. The proposed approach was applied to a utility grid with base load groups planned by control center and 100 controllable load groups. The decision time step was chosen as 15 minutes.

Many researchers have developed approaches to generate load control schemes to achieve certain objectives. Several successful direct load control examples and feasibility studies were illustrated in the literature [51], [52], [53], [54]. The DLC dispatch coordinated with unit commitment was discussed in [55], [56], [57]. Dynamic programming was the most commonly used method to solve load management problems [49], [57], [58]. Linear programming methods were also used to solve load management problems [48], [59] for reducing the peak load or maximizing the profit margin.

In [55], the benefit accrued from using DLC capacity as a part of system spinning reserve was illustrated, and the load management was formulated as an optimization problem, which included a load control objective and several operational constraints of the system, such as load balanced constraint, maximum disturbed time constraint of

controllable loads, minimum connected time constraint of controllable loads, etc. A binary flow network model was proposed to solve the direct load control problem, and performance of the proposed technique d was better than that of dynamic programming as illustrated in [49]. The proposed method was applied to utility power systems with multiple controllable load groups and 6000 MW of thermal capacity over a summer week. The decision time step was chosen as 1 hour.

In [57], a direct load control method was developed to coordinate with unit commitment to reduce the total production cost over a period of time. The operational constraints included generation-load balanced constraint, spinning reserve constraint, and maximum disturbed time constraint and minimum connected time constraint of controllable loads. Dynamic programming approach was used to solve the load management problem. The proposed approach was applied to Taiwan power system, which included 5 nuclear units, 48 hydro units, 25 thermal units, and multiple groups of controllable loads. The decision time step was chosen as 30 minutes.

In [60], a multi-pass dynamic programming method was developed to improve the efficiency to solve the direct load control problem in Taiwan power system for air conditioning loads. The proposed approach was also applied to a Taiwan power system in summer period of 1991, which included 5 nuclear units, 48 hydro units, 25 thermal units, and multiple groups of controllable loads.

A novel adaptive control strategy for integrating DLC and interruptible load management to provide instantaneous reserves for ancillary services in deregulated power system was discussed in [61]. A fuzzy-dynamic-programming approach was used

to minimize operational costs and reduce peak loading while satisfying customers' requirements. The proposed fuzzy dynamic programming approach was applied to a Taiwan power system with 38 units, 20 air conditioning loads, and 15 interruptable loads. The decision time step was chosen as 10 minutes.

In [62], a modified genetic algorithm (GA) called iterative deepening GA was developed to optimize the scheduling of DLC strategies. This strategy minimized the amount of load shedding so that the utility company's revenue loss due to DLC was minimized. The proposed approach was applied in a utility power system with 60 controllable load groups. The decision time step was chosen as 7.5 minutes. However, the genetic algorithm needs more iterations to determine the optimal or sub-optimal solution, which has some difficulties to be extended for real time applications.

Even though load management problems have been studied for more than 30 years, the techniques are mainly applied to solve the load control problem in bulk power systems. When applied to bulk systems, load management is integrated with the unit commitment or economic dispatch to achieve certain economic and security objectives. The decision time step of load management is from 7.5 minutes to 1 hour. Thus, the load management problem in large power systems is classified as a tertiary control problem, which ensures that power systems operate normally and economically.

Since isolated power systems have much faster transients and include large portions of dynamic loads and nonlinear loads, it is necessary to take the dynamic characteristics of the system into consideration. Moreover, individual loads need to be regulated in real time to maintain the power quality of the system. Fortunately, concepts

of real-time direct load control can be extended to isolated power systems by including system dynamics. When the system does not have enough power generation to serve all its loads, only higher priority loads are energized and some non-vital loads are shed to avoid overloading generators. When the system has more available power, the non-vital loads are restored immediately. Thus, the objective of real-time load management for isolated power systems is to balance the generation and load of the system while satisfying operational constraints of the system and considering load priorities.

In the field of all-electric ship power systems, researchers have studied dynamic load shedding problem and the coordination of propulsion loads and pulse loads using load control schemes. The research on dynamic load shedding for all-electric ship power systems has been studied in [63], [64], [65], [66]. This research mainly focused on the load shedding problem for navy shipboard power systems considering load priorities, when the total load demand exceeded the generation capacity. However, the dynamic load restoration method was not considered, when more generation power is available in ship power systems.

In [63], [64], [65], a new load shedding scheme was developed for islanded power systems. The objective of the developed load shedding scheme was to maximize system benefits, minimize load curtailment, and optimize the number of circuit breaker switching actions. The constraint of the load shedding scheme included the available power capacity constraint. The loads in the system were classified as vital loads, semi-vital loads, and non-vital loads. Moreover, loads had dynamic priorities, which could change based on missions of the power system. A rule-based expert system was

developed to find the optimal control actions to shed loads using the knowledge-tree approach. The developed method was used in a 10-load zone of a shipboard power system. However, this method did not consider load restoration when more power was available, and the load dynamics were not included in the developed approach.

In [66], a dynamic load shedding scheme was developed for shipboard power systems using a non-intrusive load monitor. The objective of the load shedding scheme was to minimize the amount of load shed while considering available power capacity constraint and dynamic load priorities. This scheme was applied in a shipboard power system with 450 V voltage level and 3.125 MW power capacity. However, the load dynamics and system dynamics of the ship power system were not considered in the developed approach.

The coordination of propulsion loads and pulse loads for all-electric ship power systems have been studied in [12], [13]. Pulse loads were used to accomplish the military functions of navy ships; propulsion loads were used to drive the navy ship to its cruising speed. In battle mode, pulse loads had the highest priority; propulsion loads and other service loads could be disturbed to maintain the power quality of the system. When a pulse load was served, propulsion loads were disturbed temporarily to compensate for the impact of the pulse load on the all-electric ship power system. Due to the inertia of the ship, the cruising speed would not be disturbed significantly after the disturbance caused by the pulse load.

In [12], [13], a propulsion load was used to compensate the impact of pulse loads on the power quality of shipboard power system. When the pulse load was connected to

the system, the demand of propulsion load was reduced; on the other hand, when the pulse load is disconnected from the system, the demand of propulsion load was increased. The developed approach was used in a ship power system. However, this method only considered the coordination of pulse loads and propulsion loads, and the impact of service loads on the power quality of the system was not considered.

3.3.2 Shortcomings of existing methods

The shortcomings of existing methods can be summarized as follows:

1) Decision time step of traditional methods for load management is on the order of minutes to hours [49], [48], [50], [62], which have difficulties to consider fast system and load dynamics in all-electric ship power systems.
2) The detail load and system dynamics were not included in the existing load management methods [48], [59], [63], [64], [65], [66].
3) The dynamic state operational constraints of the system were not considered in the existing load management methods [49], [57], [60].
4) The traditional load management methods have difficulties to reduce the impact of the pulse load on the power quality of all-electric ship power systems due to large decision time step [60], [62].
5) Exisitng load management methods for all-electric ship power systems only considered the coordination of propulsion loads and pulse loads, but did not study the impact of service loads on the power quality of all-electric ship power systems [12], [13].

6) Centralized methods take longer time to make decisions [49], [57], [58], [61], [62], which have difficulties to solve the real-time load management problem for all-electric ship power systems.

Due to these reasons, a real-time load management method for all-electric ship power systems needs to be developed to include system and load dynamics and integrate steady state and dynamic state system operational constraints. A distributed control method is also needed to solve the real-time load management problem for all-electric ship power systems because centralized methods have difficulties to solve the real-time load management problem with small decision time step.

3.4 Real-Time Load Management Concept

The real-time load management concept is illustrated in Figure 3.2. The two curves in the figure represent power demands of loads with and without real-time load management. At certain time, the power demand exceeds the generation capacity. When the real-time load management is available, some non-vital loads would be shed to make the available power source capacity constraint satisfied.

The generation capacity of a power system is approximately constant for a period of time. Since all-electric ship power systems serve pulse loads and nonlinear loads, the power demand of loads in the system may exceed the generation capacity if real-time load management is not available. When the power demand exceeds the generation capacity, the system frequency decreases quickly from 60 Hz. Real-time load management is used to disconnect some non-vital loads in the system when the load

demand exceeds the generation capacity to achieve the generation and load balancing in operational real-time. Moreover, various operational constraints of the system are satisfied in operational real time by using real-time load management.

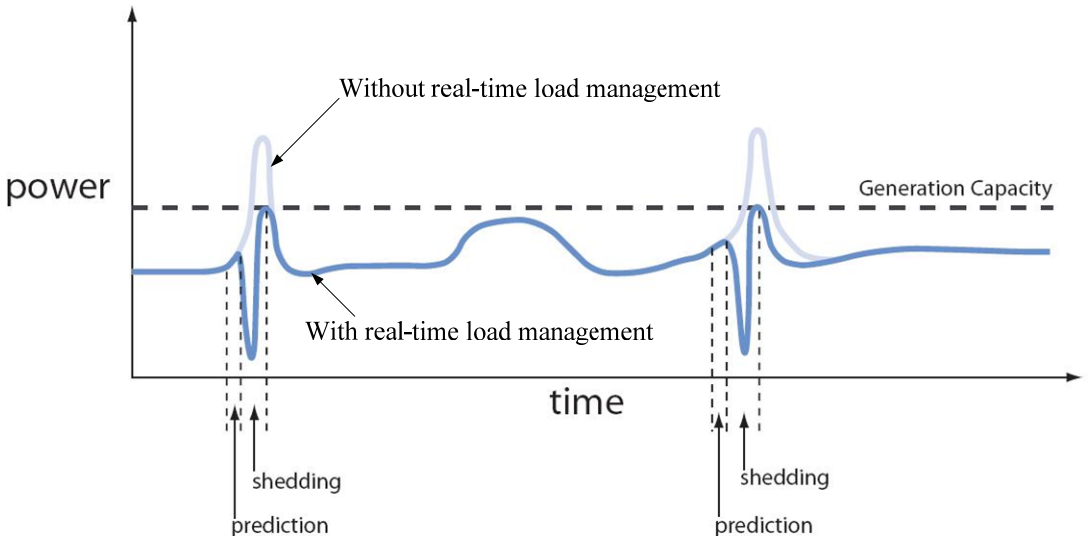

Figure 3.2 Diagram of the real-time load management concept [67]

To illustrate the potential of the real-time load management approach, a simple real-time load management concept with only available power source capacity constraint was applied to a simplified all-electric ship power system model that was simulated in PSCAD software [5]. Three scenarios were implemented to illustrate the real-time load management approach. A one-line diagram of the system is shown in Figure 3.3. The priorities of the loads in DC zones are shown in Table 3.1. The objective of the real-time load management approach was to maximize the served loads in the all-electric ship power system without violating available power source capacity constraint and PCM4 capacity constraints. The PCM4 capacity constraints ensured that the total loads

connected to starboard (or port) side DC distribution buses in zones should not exceed 2 MW. The simple real-time load management approach is shown in (3-1), which is to maximize the total power demand considering load priorities subject to PCM4 capacity constraints and available power source capacity constraint.

$$\begin{aligned} \max \quad & \sum_{k\in L}\left[P_k(\Delta t_i)\cdot s_k(\Delta t_i)\cdot W_k\right] \\ s.t. \quad & \sum_{l\in Starboard} P_l(\Delta t_i) \le 2 \text{ MW} \\ & \sum_{j\in Port} P_j(\Delta t_i) \le 2 \text{ MW} \\ & \sum_{k\in L} P_k(\Delta t_i) \le \sum_{m\in S} P_{G_m} \\ & P_k(\Delta t_i) = V_k^2(\Delta t_i)/R_k \end{aligned} \tag{3-1}$$

where, L is the load set in the all-electric ship power system, Δt_i is the decision time step of the real-time load management, $s_k(\Delta t_i)$ is the switch status of load k (if the load switch is open, $s_k(\Delta t_i)=0$; otherwise, $s_k(\Delta t_i)=1$), $P_k(\Delta t_i)$ is the load demand of load k, R_k is the equivalent resistance of load k, $V_k(\Delta t_i)$ is the input voltage of load k, P_{G_m} is the generation capacity of generator m, *Starboard* is the set of loads served by starboard side DC distribution buses, *Port* is the set of loads served by port side DC distribution buses, and S is the set of all the available generators in the system.

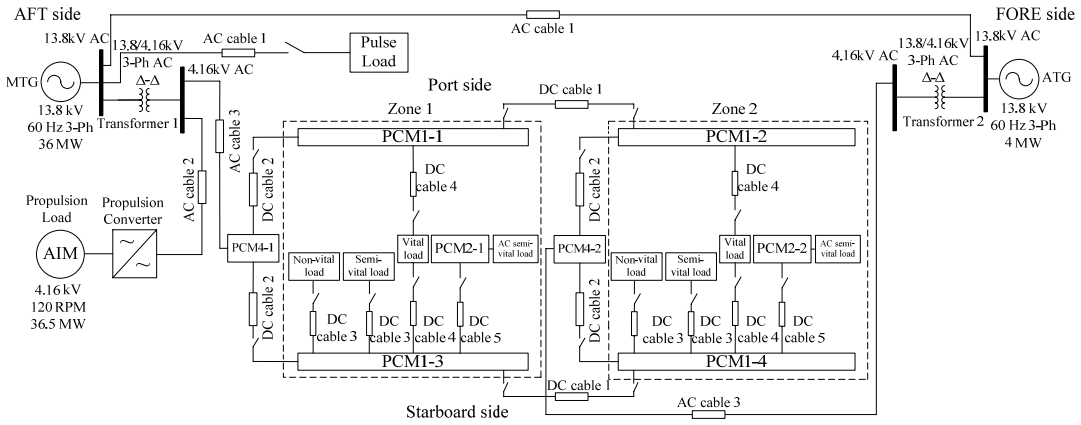

Figure 3.3 One-line diagram of a simplified all-electric ship power system model to illustrate real-time load management concept

Table 3.1 Definitions of loads in DC zones of the simplified all-electric ship power system model

Load	Weight Factor	Priority	Rating
Load L_{DC12}	1.7	Vital	0.95 MW, 0.65 kV DC
Load L_{DC22}	1.7	Vital	0.95 MW, 0.65 kV DC
Load L_{DC11}	1.5	Semi-vital	0.4 MW, 0.375 kV DC
Load L_{DC21}	1.5	Semi-vital	0.4 MW, 0.375 kV DC
Load L_{AC13}	1.4	Semi-vital	0.5 MW, 0.45 kV AC
Load L_{AC23}	1.4	Semi-vital	0.5 MW, 0.45 kV AC
Load L_{DC14}	1.0	Non-vital	0.2 MW, 0.375kV DC
Load L_{DC24}	1.0	Non-vital	0.2 MW, 0.375kV DC

3.4.1 Scenario I

In this scenario, the available power source capacity constraint was studied based on the real-time load management. The system dynamic performance without load management was studied first, and the available power source capacity constraint might be violated. Then the system with real-time load management was studied to show that the available power source capacity constraint was always satisfied. The decision time step of the real-time load management in this scenario was chosen as 0.2 second.

It was assumed that the MTG generator was in service and the ATG generator was out of service. Thus, the generation capacity of the system was 36 MW. The power demand of propulsion load was increased from 31.5 MW to 33.5 MW at 8 seconds, and decreased from 33.5 MW to 31.5 MW at 11 seconds. In zones, $L_{DC_{24}}$ was not served, and $L_{DC_{11}}$, $L_{DC_{12}}$, $L_{DC_{21}}$, $L_{DC_{22}}$, $L_{AC_{13}}$, $L_{AC_{23}}$, and $L_{DC_{14}}$ were served, where, $L_{DC_{12}}$ and $L_{DC_{22}}$ were served by port side DC distribution buses, and the other loads were served by starboard side DC distribution buses. The load demand in the two zones was 3.9 MW. Therefore, the load demand of the system was changed from 35.4 MW to 37.4 MW at 8 seconds, and the demand was returned to 35.4 MW at 11 seconds. The total losses of the system were 0.6 MW. The total load demand of the system included the power consumed by loads and losses of the system. The load status is shown in Table 3.2.

Table 3.2 Load status without load management in Scenario I

Time	0~8 s	8~11 s	11~15 s
Load L_{DC11}	served	served	served
Load L_{DC12}	served	served	served
Load L_{AC13}	served	served	served
Load L_{DC14}	served	served	served
Load L_{DC21}	served	served	served
Load L_{DC22}	served	served	served
Load L_{AC23}	served	served	served
Load L_{DC24}	not served	not served	not served
Pulse Load	not served	not served	not served
Propulsion Load	31.5 MW	33.5 MW	31.5 MW

From 8 to 11 seconds, the load demand exceeded the generation capacity. If the load management method was not applied, the available power source capacity constraint was violated between 8 and 11 seconds, as shown in Figure 3.4(a). The

frequency of MTG generator was decreased from 60 Hz to 58.7 Hz at 8 seconds due to the increased load, and the frequency gradually returned to 60 Hz after the load demand decreased at 11 seconds, as shown in Figure 3.4(b).

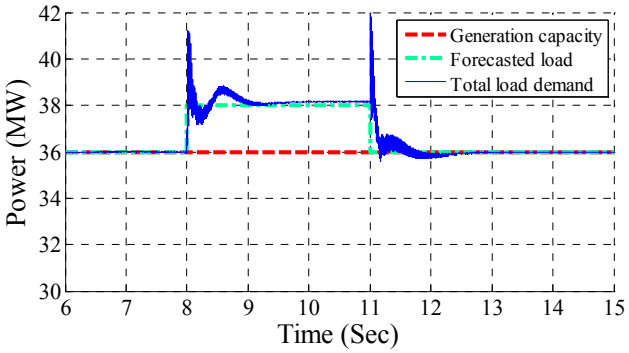

(a) Total load demand in Scenario I

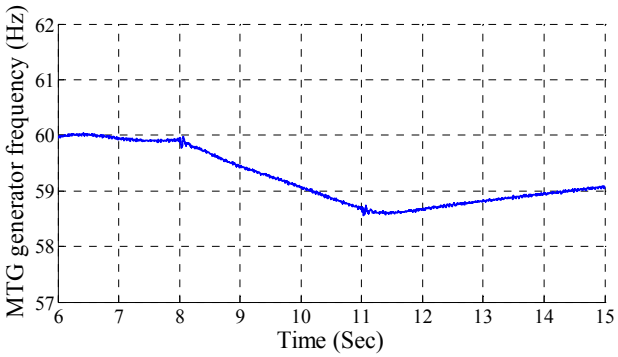

(b) MTG frequency in Scenario I

Figure 3.4 Dynamic performance of the all-electric ship power system without load management in Scenario I

To improve the dynamic performance of the system, the real-time load management approach shown in (3-1) was applied to the simplified all-electric ship power system to maximize the served loads without violating the operating constraints of the system. In order to ensure that the total consumed power was less than the

generation capacity, the load management approach was applied at 7.8 seconds to shed some lower priority loads in zones. The loads were shed based on the load priority to make the objective function optimal. In this case, all non-vital and semi-vital loads $L_{DC_{11}}$, $L_{DC_{14}}$, $L_{DC_{21}}$, $L_{AC_{13}}$, and $L_{AC_{23}}$ were shed which total 2 MW. Only the two vital loads $L_{DC_{12}}$ and $L_{DC_{22}}$ were served, which made the objective function optimal. Therefore, the total load demand was decreased from 38 MW to 36 MW. After 11 seconds, the power demand of the propulsion load was decreased from 33.5 MW to 31.5 MW. At 11.2 seconds, the load management approach was applied to restore loads $L_{DC_{11}}$, $L_{DC_{14}}$, $L_{DC_{21}}$, $L_{AC_{13}}$, and $L_{AC_{23}}$, which were shed at 7.8 seconds. The load status of the system is shown in Table 3.3. Figure 3.5(a) indicates that the generation power does not exceed the generation capacity except some transient times.

After 2 MW of loads were shed at 7.8 seconds, the frequency began to increase slowly, and then the propulsion load increased to 33.5 MW, so the frequency was maintained at 60 Hz in steady state, which is shown in Figure 3.5(b). At 11 seconds, the total load demand was decreased to 34 MW, and the loads were restored after 0.2 second. In this period, the frequency changed in the range of 59.9 Hz to 60.0 Hz. The load management method began to work before the total load demand exceeded the generation capacity, which prevented the frequency of MTG from dropping. After shedding 2 MW of loads in zones, the total load demand in the system was decreased to about 36 MW, which satisfied the available power source capacity constraint.

Table 3.3 Load status with load management in Scenario I

Time	0~7.8 s	7.8~8 s	8~11 s	11~11.2 s	11.2~15 s
Load L_{DC11}	served	shed	shed	shed	served
Load L_{DC12}	served	served	served	served	served
Load L_{AC13}	served	shed	shed	shed	served
Load L_{DC14}	served	shed	shed	shed	served
Load L_{DC21}	served	shed	shed	shed	served
Load L_{DC22}	served	served	served	served	served
Load L_{AC23}	served	shed	shed	shed	served
Load L_{DC24}	not served	not served	not served	not served	not served
Pulse Load	not served	not served	not served	not served	not served
Propulsion Load	31.5 MW	31.5 MW	33.5 MW	31.5 MW	31.5 MW

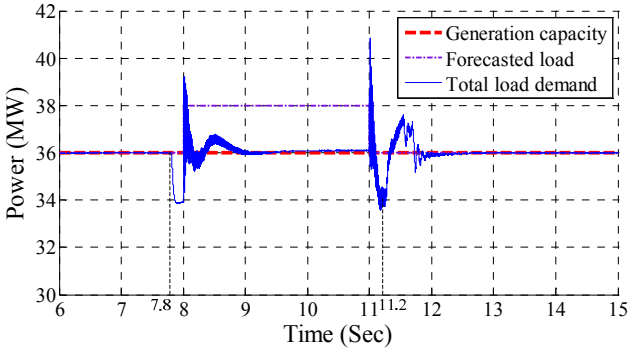

(a) Total load demand in Scenario I

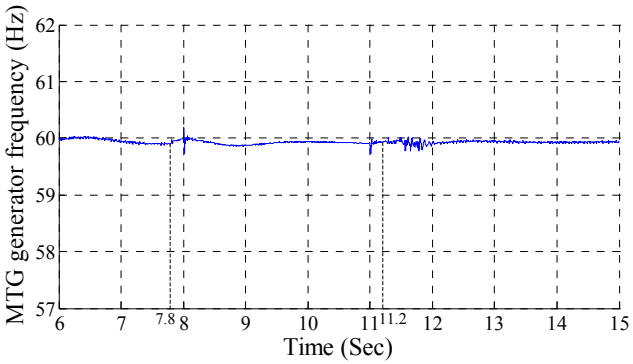

(b) MTG frequency in Scenario I

Figure 3.5 Dynamic performance of the all-electric ship power system with load management in Scenario I

3.4.2 Scenario II

In this scenario, the PCM4 capacity constraint was studied to show that the real-time load management approach ensured that PCM4 capacity constraints were satisfied. The decision time step was chosen as 0.2 second. It was assumed that the propulsion load demand was 25 MW. The total capacity of the system was 40 MW by assuming that the MTG generator and the ATG generator were both available. Thus, the system could serve another 15 MW of loads without violating the available power source capacity constraint. If the PCM4 capacity constraint was not considered, all loads in the zones could be served, since the total power demand in zones was 4.1 MW.

If the real-time load management was not used, all loads in zones were connected to the system. The two vital loads were connected to the port side DC distribution buses, and other loads were connected to the starboard side DC distribution buses. The load status of the system is shown in Table 3.4. The input powers to PCM4-1 and PCM4-2 are shown in Figure 3.6(a) and Figure 3.6(b), respectively. The input power to PCM4-1 did not exceed the capacity of PCM4. On the other hand, the input power to PCM4-2 exceeded the capacity of PCM4, which means that the PCM4 capacity constraint was violated.

Table 3.4 Load status without load management in Scenario II

Time	0~2 s	2~5s
Load L_{DC11}	served	served
Load L_{DC12}	served	served
Load L_{AC13}	served	served
Load L_{DC14}	served	served
Load L_{DC21}	served	served
Load L_{DC22}	served	served
Load L_{AC23}	served	served
Load L_{DC24}	served	served
Pulse Load	not served	not served
Propulsion Load	25 MW	25 MW

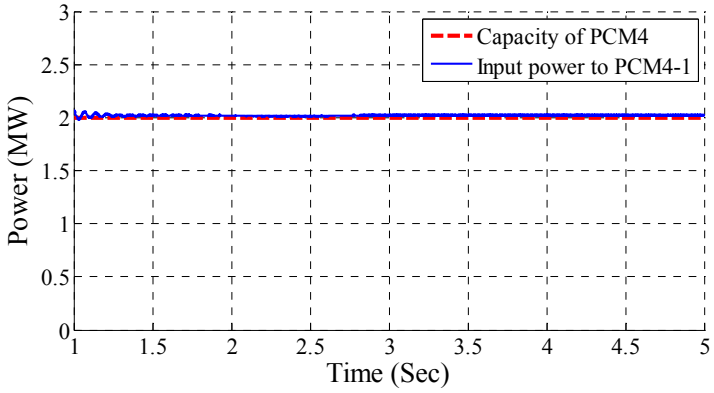

(a) Input power to PCM4-1 in Scenario II

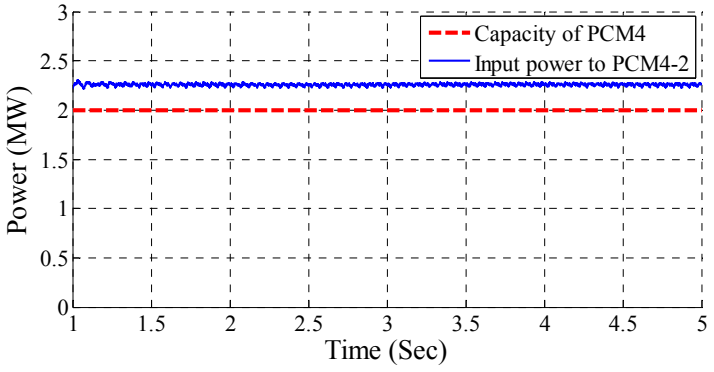

(b) Input power to PCM4-2 in Scenario II

Figure 3.6 Power inputs to PCM4s without load management in Scenario II

In order to handle this problem, the load management approach was applied to the system. $L_{DC_{24}}$ was a non-vital load and had the lowest priority. Thus, $L_{DC_{24}}$ was shed at 2 seconds to reduce the input power to PCM4-2 and to make the objective function optimal. The load status of the system is shown in Table 3.5. Figure 3.7 shows that the PCM4 capacity constraint is satisfied after shedding $L_{DC_{24}}$. The nonlinear dynamics of the DC-DC converter in PCM1 caused the transients from 2 to 2.5 seconds.

Table 3.5 Load status with load management in Scenario II

Time	0~2 s	2~5s
Load L_{DC11}	served	served
Load L_{DC12}	served	served
Load L_{AC13}	served	served
Load L_{DC14}	served	served
Load L_{DC21}	served	served
Load L_{DC22}	served	served
Load L_{AC23}	served	served
Load L_{DC24}	served	shed
Pulse Load	not served	not served
Propulsion Load	25 MW	25 MW

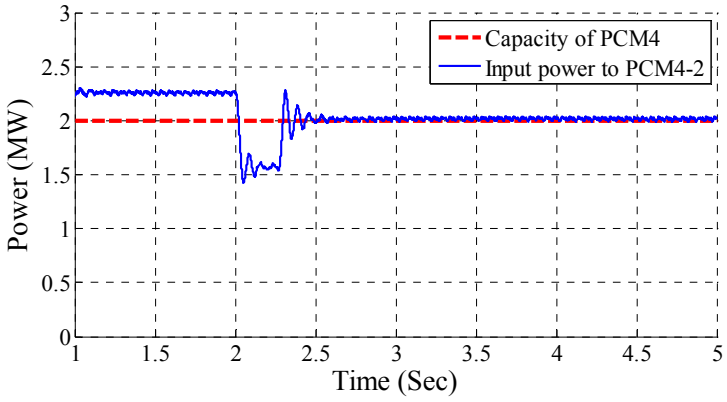

Figure 3.7 Input power to PCM4-2 with load management in Scenario II

3.4.3 Scenario III

In the last scenario, the impact of a pulse load on the power quality of the all-electric ship power system was studied. The real-time load management concept was applied to regulate the power demand of a propulsion load to compensate for the impact of the pulse load on the dynamics of the all-electric ship power system. It was assumed that the pulse load was connected to the MTG bus and had a 10 MW magnitude with a 2 seconds pulse width. The load demand in the DC zone system was 3.9 MW. The propulsion load was driven by the propulsion converter, and the power demand of the propulsion load could be regulated by the power controller of the marine propulsion system. The decision time step of the propulsion load was chosen as 10 milliseconds. Both the MTG and ATG generators were in service, so the generation capacity was 40 MW.

Initially, the ship was operated in cruise mode. Then the operating mode was changed from cruise mode to battle mode at 30 sec. In the battle mode, the pulse load has a higher priority than the propulsion load. At 30 sec, the marine propulsion system controller was switched from speed control mode to power control mode to reduce the impact of the pulse load on the power quality of the all-electric ship power system. The ship speed and the propulsion load demand could not be controlled at the same time by the marine propulsion controller; thus, the marine propulsion system could only operate in speed control mode or power control mode.

The ship speed was increased from 0 to 27 knots in 20 seconds, as shown in Figure 3.8. When the pulse load was served at 40 seconds as shown in Figure 3.9, the

load demand of the propulsion load was regulated to compensate for the impact of the pulse load by using the real-time load management approach. The propulsion load demand is shown in Figure 3.10. When the pulse load was served, the propulsion load demand was decreased quickly to maintain the total load demand at certain value to reduce the frequency oscillation. When the propulsion load was disturbed, the ship speed decreased slowly, as shown in Figure 3.11. Due to the large inertia and mass of the ship, the ship speed drop during this disturbance was small, which was around 0.7 knots. The total generation power of the system is shown in Figure 3.12. When the pulse load was served, the total generation power was nearly constant except two spikes caused by sudden load changes. The dynamic behaviors of the MTG generator frequency with and without the application of the real-time load management approach are shown in Figure 3.13. Without real-time load management, the maximum frequency deviation of the MTG generator was more than 1 Hz, which was much larger than the frequency deviation with real-time load management.

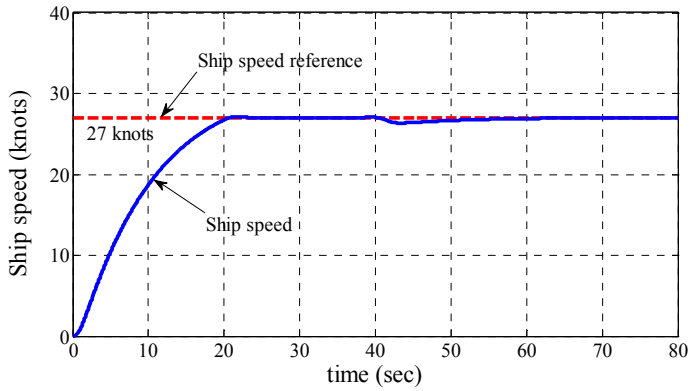

Figure 3.8 Ship speed for Scenario III

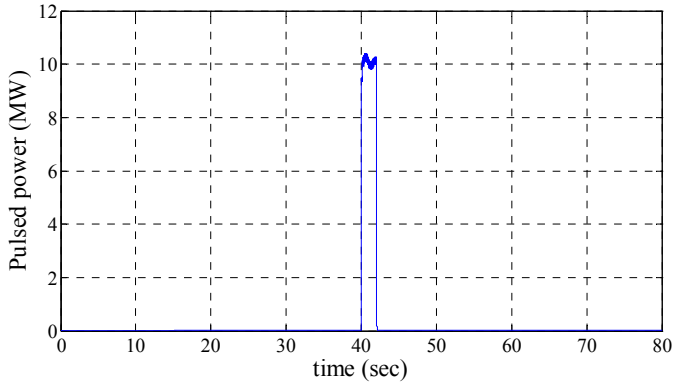

Figure 3.9 Pulse load demand for Scenario III

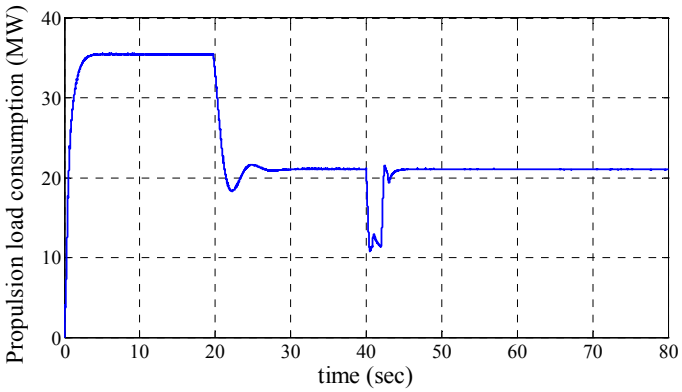

Figure 3.10 Propulsion load demand for Scenario III

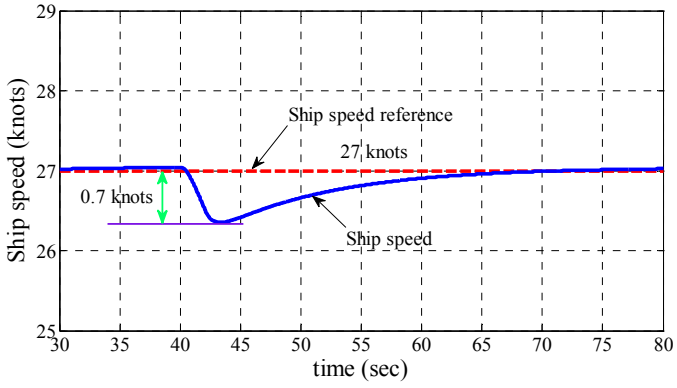

Figure 3.11 Ship speed when pulse load is served for Scenario III

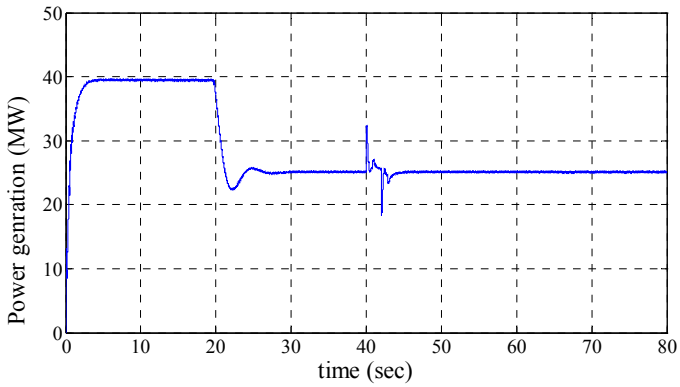

Figure 3.12 Total power generation with the disturbance of the pulse load in scenario III

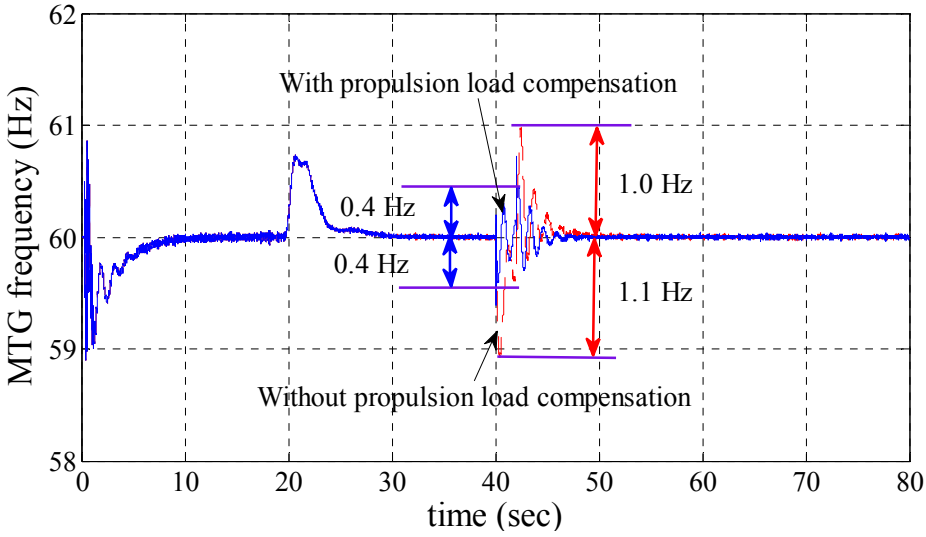

Figure 3.13 Frequency behavior of the MTG generator with and without the application of real-time load management approach in Scenario III

3.4.4 Summary real-time load management concept

In Scenario I, if the real-time load management was not applied in the system, the total load demand exceeded the generation capacity and the MTG generator frequency decreased from 60 Hz. After integrating the real-time load management approach, several lower priority loads were shed to satisfy the available power source

capacity constraint. The simulation results indicated that the system dynamic performance with load management was much better than its performance without load management. In Scenario II, the PCM4 capacity constraint was studied. If a PCM4 served more than 2 MW loads, the PCM4 capacity constraint was violated. The real-time load management approach was applied and some non-vital load was shed to satisfy the constraint. In Scenario III, a pulse load was integrated into the system. When the pulse load was served, the total load demand was increased quickly, which caused significant system frequency oscillations. In order to serve the load demand, the real-time load management approach was applied and the power demand of the propulsion load was regulated to reduce the frequency oscillation caused by the pulse load. Simulation results indicated that the MTG frequency drop of the system with the application of the load management approach was much less than that without load management.

3.5 Real-Time Load Management Problem Formulation

In this section, the real-time load management problem is formulated for all-electric ship power systems to achieve real-time matching of load to generation while considering load priorities and system constraints in all-electric ship power systems. The real-time load management approach explores optimal switch status or set-point of each load in the all-electric ship power system while satisfying various operational constraints of the system, such as available power source capacity constraint, bus voltage constraints, steady state and dynamic state cable constraints, and load bus capacity constraints. Since the all-electric ship power system has faster dynamics and includes

large portions of dynamic loads and nonlinear loads, detail load and system dynamics also need to be included in the problem formulation.

In this dissertation, the multi-agent system technique is used to achieve the real-time load management for all-electric ship power systems. The high-level diagram of the multi-agent system-based real-time load management approach is shown in Figure 3.14. The diagram consists of the multi-agent system-based real-time load management component and the all-electric ship power system model. The multi-agent system-based real-time load management component obtains real-time measurement from the all-electric ship power system and makes decisions to control individual loads in the power system. The decision and measurement intervals are chosen as Δt_i, which is on the order of milliseconds. Δt_i is determined based on the time-frame analysis of loads in all-electric ship power systems. The simulation step size of the multi-agent system is chosen as Δt_i, and the simulation step size of the all-electric ship power system model is chosen as $\Delta \tau$, which is on the order of microseconds to promise the accuracy of the multi-agent system and the power system simulation.

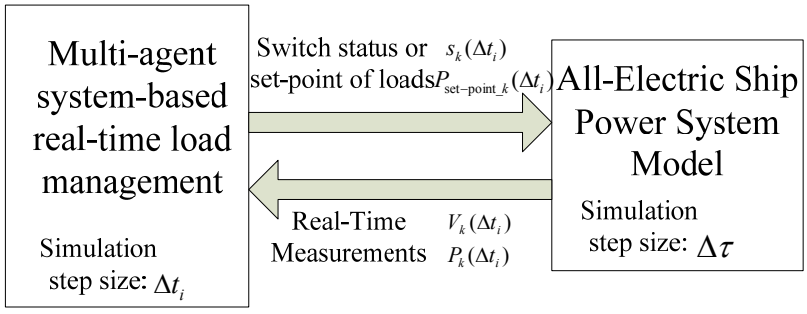

Figure 3.14 High-level diagram of the multi-agent system-based real-time load management approach

3.5.1 Problem formulation

The real-time load management problem formulation for all-electric ship power systems is shown in (3-2)-(3-14).

$$\text{Objective:} \quad \max \quad \sum_{k\in L}\left[P_k(\Delta t_i)\cdot s_k(\Delta t_i)\cdot W_k\right] \tag{3-2}$$

s.t. Available power source capacity constraint:

$$\sum_{k\in L}\left[P_k(\Delta t_i)\cdot s_k(\Delta t_i)\right]+P_{losses}(\Delta t_i)\le\sum_{j\in S}P_{G_j}(\Delta t_i) \tag{3-3}$$

Motor load voltage constraints:

$$V_m^{\min}\le\left|V_m(\Delta t_i)\right|,\ \forall m\in\left\{1,2,\cdots,N_{motor}\right\} \tag{3-4}$$

Cable constraints:

$$I_l(\Delta t_i)\le I_l^{Ampacity},\ l\in B_1 \tag{3-5}$$

Dynamic cable constraints:

$$\int_{t-T}^{t}0.5\cdot\left[1+\text{sgn}(I_q(\Delta t_i)-I_q^{Ampacity})\right]dt\le T_1,\ q\in B_2 \tag{3-6}$$

Load bus capacity constraints:

$$P_{L_p}(\Delta t_i)\le C_{L_p}^{\max} \tag{3-7}$$

Load dynamic constraints:

$$I_l(\Delta t_i)=P_k(\Delta t_i)/V_{in\_k}(\Delta t_i) \tag{3-8}$$

$$P_k(\Delta t_i)=V_{in\_k}(\Delta t_i)\cdot p_k(t) \tag{3-9}$$

$$\dot{p}_k(t)=q_k(t) \tag{3-10}$$

$$\dot{q}_k(t)=u_{Lk}(t) \tag{3-11}$$

$$u_{Lk}(t) = -(1/T_{k2})p_k(t) - (T_{k1}/T_{k2})q_k(t) + (K_k/T_{k2})u_k(\Delta t_i) \tag{3-12}$$

$$u_k(\Delta t_i) = P_{\text{set-point\_}k}(\Delta t_i)\big/V_{in\_k}(\Delta t_i) \tag{3-13}$$

$$\begin{aligned} &\text{Vital load: } W_k = \left(\frac{P_{Non}^{\max} + P_{Semi}^{\max}}{P_k}\right) + 1 \\ &\text{Semi-vital load: } W_k = \left(\frac{P_{Non}^{\max}}{P_k}\right) + 1 \\ &\text{Non-vital load: } W_k = 1 \end{aligned} \tag{3-14}$$

The variables in the problem formulation are defined as follows.

L – load set in the power system

$s_k(\Delta t_i)$ – switch status of load k ($s_k = 0$, disconnected; $s_k = 1$, served)

$P_k(\Delta t_i)$ – power demand of load k

W_k – weight factor of load k

Δt_i – decision time step for real-time load management

$P_{losses}(\Delta t_i)$ – total losses in the power system

$P_{G_j}(\Delta t_i)$ – capacity of generator j

S – set of generators in the power system

N_{motor} – total number of motor load buses

$I_l^{Ampacity}$ – amapacity of cable l

$I_l(\Delta t_i)$ – current through cable l

T_1 – constraint time for dynamic cable constraint

B_1, B_2 – sets of cables in the power system

$P_{L_p}(\Delta t_i)$ – consumed power by load bus p

$C_{L_p}^{\max}$ – power capacity of load bus p

T_{k1}, T_{k2}, K_k – coefficients of load k

p_k, q_k – state variables of load k

$P_{\text{set-point\_}k}(\Delta t_i)$ – power set-point of load k

$V_{in\_k}(\Delta t_i)$ – input voltage of load k

$P_{Non}^{\max}$ – the largest non-vital load

$P_{Semi}^{\max}$ – the largest semi-vital load

In this problem formulation, the objective is to maximize the served loads in the all-electric ship power system considering load priorities, as shown in (3-2). the decision variables include the load switch status $s_k(\Delta t_i)$ or power set-point of individual load $P_{\text{set-point\_}k}(\Delta t_i)$. The loads in the all-electric ship power system are classified into two types – fixed load and variable load. The fixed load can only be connected or disconnected from the power system, which means that the load can only operate with rated power or without power, such as some motor loads in the DC zone system of the all-electric ship power system; the variable load can be partially served based on the quantization method, which means that the consumed power of variable load can be changed from 0 to its rated power, such as propulsion loads.

In order to serve as many higher priority loads as possible during the system's current operating mode, loads are designated as vital loads, semi-vital loads, and non-

vital loads for specific operating modes. In the all-electric ship power system, vital loads include combat, mobility, fire, navigation, and communication systems. Semi-vital loads are important to ship operation and survivability but can be shed to prevent total loss of ship's power. Non-vital loads are those that can be shed during an electrical casualty [7]. A technique was developed in earlier work [6], [7] for determining the weight factor of loads in shipboard power systems, as shown in (3-14).

In addition to achieve real-time matching of load to generation while considering load priorities, various operational constraints of the system should be satisfied in operational real time, such as available power source capacity constraint, voltage constraints, cable constraints, and load bus capacity constraints.

The first constraint is available power source capacity constraint, which is shown in (3-3). The sum of the total load demand and system losses of the power system should not be larger than the available power source capacity. If this constraint is violated, the total load demand will exceed the generation capacity, which will result in a frequency decline in the system. When the frequency drops below certain thresholds, the protection system begins to trip sensitive loads or generators in the system, which may cause system blackout. The system losses of the power system can be calculated using steady state method [68], which can be expressed as (3-15).

$$P_{losses}(\Delta t_i) = \left(\boldsymbol{P}_G(\Delta t_i) - \boldsymbol{P}_D(\Delta t_i)\right)^T \boldsymbol{B}^{-1}\boldsymbol{M}^T\boldsymbol{G}\boldsymbol{M}\boldsymbol{B}^{-1}\left(\boldsymbol{P}_G(\Delta t_i) - \boldsymbol{P}_D(\Delta t_i)\right) \tag{3-15}$$

where, $\boldsymbol{P}_G(\Delta t_i)$ and $\boldsymbol{P}_D(\Delta t_i)$ are the generation and load vector on each bus of the system, $\boldsymbol{G}$ is the diagonal matrix of line conductances of the system, $\boldsymbol{B}$ is obtained from

the ***Y*** matrix of the system, and ***M*** is determined by the system topology. This method has been discussed in details in [68].

The voltage constraints are used to operate some motor loads within certain voltage limits, as shown in (3-4). Certain motor loads are sensitive to their input voltage levels. If the input voltage is too low, the load may not be able to operate normally. In this case, the load should be disconnected from the load bus or, if possible, the power demand of the load should be decreased to make the voltage constraint satisfied.

The cable constraints include steady state [6] and dynamic state constraints. Ampacity is the RMS current that a cable can continuously carry while remaining within its temperature rating. Thus, the line current should be less than or equal to its ampacity in steady state, as shown in $I_l(\Delta t_i) \le I_l^{Ampacity}$. The all-electric ship power system serves pulse loads, which draw a large amount of power in an intermittent way. When a pulse load is served, it draws a large current from the system for a short period of time, which may violate the cable ampacity constraint. In this case, the dynamic cable constraint, as shown in $\int_{t-T}^{t} 0.5 \cdot \left[1 + \mathrm{sgn}(I_q(\Delta t_i) - I_q^{Ampacity})\right] dt \le T_1$, is considered. Due to the thermal dynamics of cables, the temperature of the cable takes several seconds to minutes to exceed its temperature rating. Thus, the cable ampacity constraint can be violated for a certain amount of time before the cable temperature exceeds its rating.

The load bus capacity constraint is shown in (3-7), which means that the total loads on certain bus *k* should not exceed the power capacity of the bus.

The operating constraints for load dynamics are shown in (3-8)-(3-13). A dynamic load is modeled using a second-order dynamic system as shown in (3-10)-(3-

13). The input current of the dynamic load can be determined using load dynamics, input voltage measurement, and switch status or set-point of the load. (3-10)-(3-11) are double integrator system, which model the load dynamics. (3-12) represents the transformation of the dynamic load model. (3-13) determines the set-point of the load model.

3.5.2 Opertional decision time step of real-time load management

The time constants for various loads in all-electric ship power systems have been studied in chapter 2. To determine the decision time step of real-time load management for all-electric ship power systems, the time constants of various electrical components are summarized in Table 3.6. The DC-DC converter in PCM1 has the smallest time constant due to the local voltage regulator. The output voltage of each converter can reach steady state in half a second. The DC and AC motor loads in DC zones can reach the steady state in one second, after the power set-point of each load is regulated. The available power to the DC zone system may change significantly due to the load changes in the MVAC system, the load demand in the DC zone system needs to be regulated immediately to smoothly achieve the load and generation balancing. Thus, the decision time step of loads should be much smaller than the time constant of DC-DC converters and individual motor loads in DC zones.

Table 3.6 Component time constant in all-electric ship power systems

Component	Time constant (sec)
DC-DC converter	0.1-0.5
AC motor in DC zones	0.5-1
DC motor in DC zones	0.5-1
Pulse load duration	0.1-25
Propulsion load	1-5
Ship run-up time	20-100
Gas turbine generator	5-10

Pulse load durations are in the range of 0.1 to 25 seconds [12], [13], [19], [24], [26]. When a pulse load is served in the system, the propulsion load needs to be regulated to reduce the impact of the pulse load on the power quality of the system. The time constants of propulsion loads are in the range of 1 to 5 seconds. In order to compensate the impact of the pulse load, the power set-point of the propulsion load should be regulated immediately when the pulse load is served. Thus, the decision time step should be small enough to achieve the coordination of the pulse load and propulsion load.

In this work, the operational decision time step of real-time load management for all-electric ship power systems was chosen as 10 milliseconds, which is much smaller than the time constant of electrical components in DC zones. Moreover, this decision time step is small enough to successfully coordinate the pulse load and propulsion load during the real-time load management for all-electric ship power systems.

3.6 Summary

In this chapter, the operations of isolated power systems were discussed. The system operation was classified as primary control, secondary control, and tertiary control. The decision time step of primary controllers is on the order of microseconds to milliseconds, which ensures that system states can track their set-points quickly based on the local controller and local measurements. The secondary control is responsible for determining the set-points of primary controllers based on communication infrastructures to improve the dynamic performance of the system. The decision time

step of secondary controller is on the order of milliseconds to seconds. The tertiary control determines the optimal set-points for local controllers in steady state to operate the system normally and economically. The decision time step of tertiary controllers is on the order of seconds to minutes.

A literature review was also provided to discuss some existing load management methods for large power systems. Since the all-electric ship power system has fast dynamics and includes large portions of nonlinear loads and dynamics loads, the existing methods have difficulties in solving the real-time load management problem for all-electric ship power systems. The shortcomings of existing methods were discussed to indicate that a new real-time load management approach is needed for all-electric ship power systems. The real-time load management concept was also illustrated to show advantages of a real-time load management approach.

Real-time load management should optimally determine the switch status or set-point of each load in the system based on communication infrastructures to achieve the balance of load with generation while satisfying the operational constraints of the system and considering load priorities. In section 3.5, real-time load management for all-electric ship power systems was formulated to achieve the real-time matching of load to generation while considering load priorities and system constraints. The decision time step of real-time load management for the all-electric ship power system was also determined based on the time-frame analysis of individual electrical components in the system.

4. MULTI-AGENT SYSTEM FRAMEWORK FOR REAL-TIME LOAD MANAGEMENT IN ALL-ELECTRIC SHIP POWER SYSTEMS

4.1 Introduction

This chapter discusses the multi-agent system framework for real-time load management in the all-electric ship power system. Three partitioning strategies for the DC zone system were studied to determine the multi-agent system topology required to represent the all-electric ship power system. The advantages and disadvantages of each partitioning strategy are discussed. Partitioning Strategy I partitioned the system based on the DC zone system topology and modeled each half of a zone as a homogeneous agent. For this strategy, the multi-agent system topology was very simple. Thus, it was easy to design cooperative controllers to achieve real-time load management for all-electric ship power systems. However, the accuracy of the reduced-order model for each agent was low, since all loads in each agent were modeled as constant resistive loads and aggregated together. On the other hand, Partitioning Strategy III partitioned the system based on individual electrical components and modeled each electrical component in the DC zone system as a heterogeneous agent. Even though the heterogeneous multi-agent system topology was very complex, the detailed load and system dynamics were easily integrated into the multi-agent system, which significantly improved the accuracy of agent models. Moreover, various kinds of operational constraints of the system were integrated into the multi-agent system. Due to these reasons, a novel heterogeneous

multi-agent system framework was developed based on Partitioning Strategy III to achieve real-time load management for all-electric ship power systems.

Since the all-electric ship power system consists of the MVAC and DC zone systems, the heterogeneous multi-agent system was first designed for these two systems, respectively. Then the MVAC and DC zone multi-agent systems were coordinated by an AC-DC communication agent. In the MVAC multi-agent system, generator agents, propulsion load agents, pulse load agents, and a system losses agent were designed to coordinate propulsion loads and pulse loads while satisfying the operational constraints of the system. In the DC zone system, the converter-layer and load-layer multi-agent systems were developed to coordinate various priority loads and converters to achieve dynamic load balancing while satisfying the operational constraints of the system and considering load priorities. The AC-DC communication agent obtains information from the MVAC multi-agent system to calculate the available power to the DC zone system and provides the DC zone load demand information to the system losses agent to estimate total losses in the MVAC system.

The outline of this chapter is as follows. The bio-inspired multi-agent system concept and some applications are introduced in section 4.2. Three partitioning strategies with their advantages and disadvantages are discussed in section 4.3. In section 4.4, the heterogeneous multi-agent system framework for real-time load management in the all-electric ship power system based on Partitioning Strategy III is presented. The heterogeneous multi-agent system cooperative controllers were developed based on

artificial potential functions and reduced-order agent models to achieve real-time load management. A summary is given in section 4.5.

4.2 Applications of Bio-Inspired Multi-Agent Systems in Power Systems

A multi-agent system, inspired by biological phenomena, such as bird flocking [69], fish schooling [70], and bacteria foraging, aims to cooperatively achieve group objectives that are difficult to reach by a single agent or centralized controller [71]. The multi-agent system cooperative controller is a decentralized controller, which has many advantages over a centralized controller. The design complexity of the cooperative controller for the multi-agent system is proportionally increased with an increase in the number of agents. On the other hand, the computation complexity of a centralized controller is increased exponentially with an increase in the number of agents.

The multi-agent dynamic system has been modeled as a single integrator system [72], double integrator system [73], coupled-phase oscillator system [74], and non-holonomic agent system [75], for various system applications. The multi-agent system cooperative controller can coordinate a group of agents and cooperatively achieve their group goals in real time. The multi-agent system cooperative control techniques have been widely used in many engineering areas, such as formation control [76] and multi-robotic system [77], as shown in Figure 4.1. Moreover, multi-agent systems are used to study the collective behaviors of biological systems, such as bird flocking, fish schooling, bacteria foraging, and synchronization of fire flies, as shown in Figure 4.2.

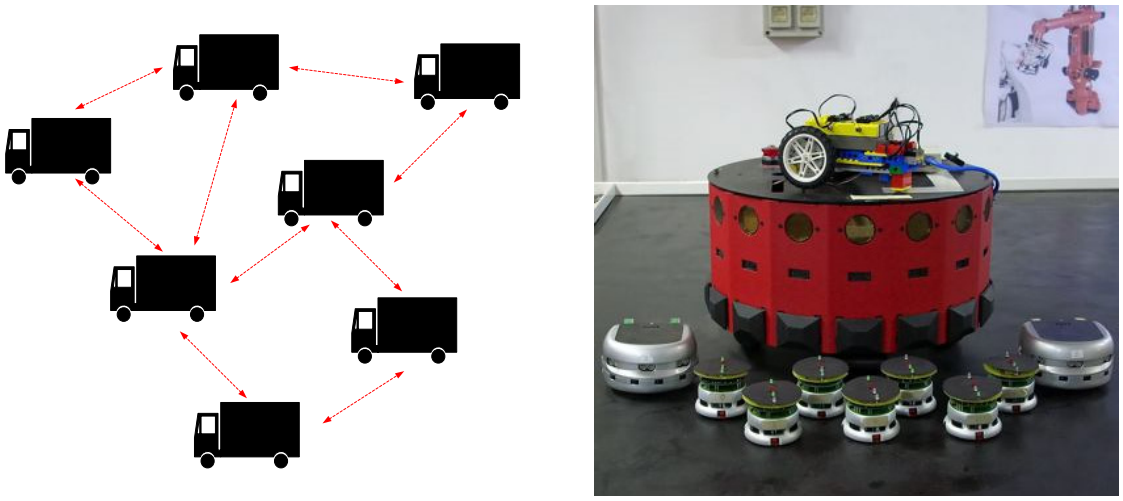

(a) Formation control **(b)** Multi-robotic system [78]

Figure 4.1 Applications of the multi-agent dynamic system cooperative controller

(a) Bird flocking **(b)** Fish schooling **(c)** Synchronization of fire flies

Figure 4.2 Biological phenomena of swarms

Most existing cooperative controllers have been used for homogeneous multi-agent systems, which means that each agent has an identical dynamic model. A widely used cooperative controller [73] for homogeneous multi-agent systems is shown as (4-1).

$$\overline{\boldsymbol{u}}(t) = -\nabla E_p(\boldsymbol{x}(t)) - L \cdot \boldsymbol{v}(t) - k(\boldsymbol{v}(t) - \boldsymbol{v}^{ref}) \tag{4-1}$$

where, $\overline{\boldsymbol{u}}(t)$ is the control vector of the multi-agent system; E_p is the artificial potential function of the multi-agent system; $\boldsymbol{x}(t)$ and $\boldsymbol{v}(t)$ are the state variable vectors of agents; $\boldsymbol{v}^{ref}$ is the speed reference vector; k is a positive constant; and L is the graph Laplacian, which is determined by the communication topology of the multi-agent system.

Since power systems include various electrical components modeled by different dynamic systems, traditional homogeneous multi-agent system cooperative controllers have difficulties solving the real-time load management problem with heterogeneous component models. Researchers have proposed a cooperative controller for heterogeneous multi-agent systems [79], but this method is mainly used to solve problems in multi-vehicle systems. To solve the real-time load management problem for all-electric ship power systems, a heterogeneous multi-agent system cooperative controller is needed because the all-electric ship power system includes various electrical components with different dynamic models.

Multi-agent system techniques have been developed to solve challenging problems [80], [81] in power engineering over the past decade. Many of these research efforts have applied the multi-agent system technique to power system restoration [82], diagnosis [83], secondary voltage control [84], wide area control [85], and protection [86]. For all-electric ship power systems, multi-agent system techniques have been developed for applications including system restoration [87], and fault detection [88]. Since the multi-agent system technology has great potential for solving challenging

problems, this dissertation explores its utilization in real-time load management for all-electric ship power systems.

4.3 Three Partitioning Strategies for the DC Zone System of Notional All-Electric Ship Power Systems

The all-electric ship power system is a very complex dynamic system which is a very high-order nonlinear system, so it is difficult to solve the real-time load management problem using a single controller or traditional optimization methods. A multi-agent system aims to cooperatively achieve the group objectives which are difficult to reach by a single agent or centralized controller [71], [73]. Thus, a multi-agent system cooperative controller was developed to cooperatively achieve the real-time load management objective based on a group of dynamic agents. In order to apply the multi-agent system technique in a power system, the DC zone system needs to be first partitioned into smaller subsystems, which can be controlled using dynamic autonomous agents. The nature of the system, such as the system's topology, indicates a logical way to partition the system which makes the multi-agent system more effective.

The three partitioning strategies studied to explore different multi-agent system cooperative controller design procedures are discussed in this section. In Partitioning Strategy I, two zones of the DC zone system of a notional all-electric ship power system were partitioned based on the topology of the system. The partitioned system included four agents, and each agent modeled half a zone, which included three DC-DC converters, switches, and a group of loads. In Partitioning Strategy II, the DC zone

system of a notional all-electric ship power system model was partitioned based on the DC-DC converters in PCM1s. Each agent included one DC-DC converter, switches, and various priority loads. In Partitioning Strategy III, the DC zone system of a notional all-electric ship power system was partitioned based on its individual electrical components such as loads and power converters. The advantages and disadvantages of each partitioning strategy are also discussed.

4.3.1 Partitioning Strategy I

In Partitioning Strategy I, each DC zone was partitioned into two agents as shown in Figure 4.3. Zones have similar topologies, and three voltage levels, 375 V DC, 650 V DC, and 800 V DC, are available to serve various priority loads. The two zones of the DC zone system of the notional all-electric ship power system were partitioned into four agents. Each individual agent included one PCM1, cables, switches, and various priority loads as shown in Figure 4.4.

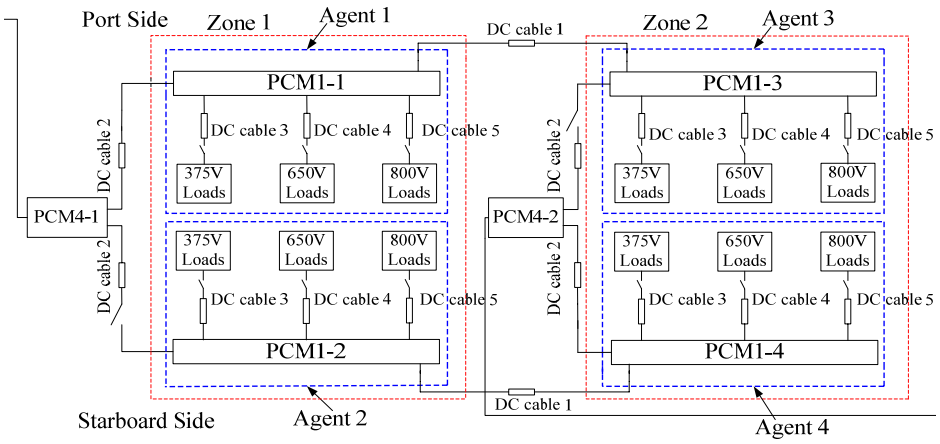

Figure 4.3 Diagram of Partitioning Strategy I for two zones of the DC zone system of the notional all-electric ship power system model

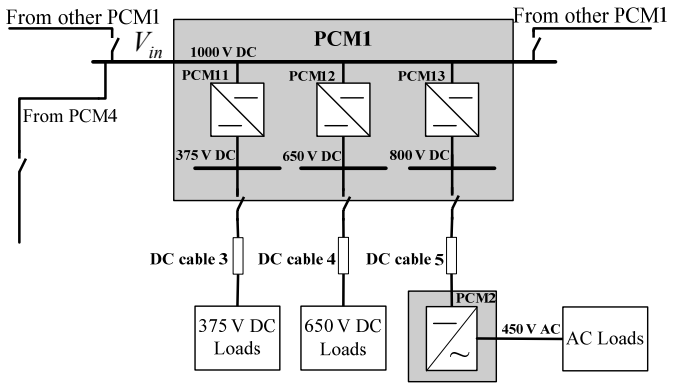

Figure 4.4 Single agent diagram for Partitioning Strategy I

The topology of the multi-agent system for Partitioning Strategy I is shown in Figure 4.5. The communication links and electrical couplings of the system were both available in the multi-agent system. The four agents in the multi-agent system constructed an all-to-all communication network. The partitioned system included four agents which had the same topology. Thus, each dynamic agent was modeled using an identical second-order nonlinear system. Moreover, only constant resistive loads were considered in the agent model. A group of load switches in the agent were aggregated into the control variable of the agent model. Through regulating the control variable of each agent based on the distributed controller, the load switch configuration was optimally adjusted to achieve the real-time load management objective.

In Partitioning Strategy I, the alternate supply paths of vital loads were not taken into consideration, which means that a vital load had only one supply path and the alternate supply path of the vital load was neglected. Vital loads are required to maintain the military effectiveness of navy ships. Loss of vital loads is unacceptable for all-electric ship power systems. In this partitioning strategy, the alternate path of the vital

load was integrated into the multi-agent system by adding switch constraints on vital loads.

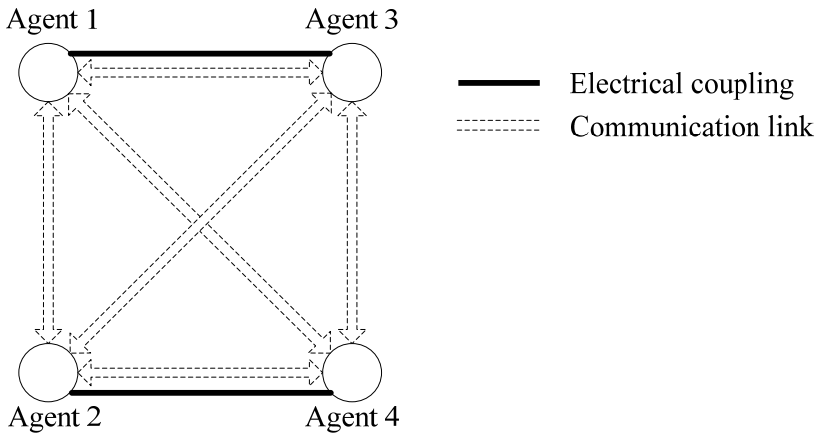

Figure 4.5 Topology of the multi-agent system for Partition Strategy I

Advantages of Partitioning Strategy I:

1) Partitioning Strategy I was based on the architecture of the notional all-electric ship power system model. Each agent modeled half a zone, which included one PCM1 and a group of loads. This partitioning strategy made the topology of the multi-agent system simple.
2) Using the partitioning strategy, all the agents were modeled using an identical dynamic agent model. The identical agent model simplified the cooperative controller design to achieve the real-time load management objective. Various cooperative controllers were systematically studied and used in vehicle formation [76], multi-robotic system [77], flocking [73], fish schooling [74], etc. These developed techniques can be easily extended to the

multi-agent system-based real-time load management for all-electric ship power systems.

3) The propulsion load could be easily integrated into the multi-agent system through adding communication links between the propulsion load and other agents. Since the propulsion load had a different dynamic model than the model of the other agents, it could be modeled as a heterogeneous agent.

Disadvantages of Partitioning Strategy I:

1) The alternate paths of vital loads were neglected in the multi-agent system. However, the alternate path of the vital load is critical to the survivability of navy ships. Without the alternate path, the vital load is not able to be switched to its alternate path to survive a fault on its normal path which is unacceptable.
2) Each identical agent was modeled using a second-order nonlinear system. The parameters of the agent model were identified from simulation data of a simplified notional all-electric ship power system model in PSCAD/EMTDC software. Simulation results indicated that the reduced-order agent model could track the actual system very well in the steady state, but not in the transient state.
3) A quantization method was used to convert the continuous agent control signal into the switch status signals of loads in each agent, which reduced the accuracy of the multi-agent system cooperative controller. If the rated power

of each load was very large (more than 150 kW), the quantization method would cause the cooperative controller to be unstable.

4) Since loads in the agent were modeled as constant resistive loads without considering dynamics of DC and AC motors, the accuracy of the cooperative controller was low.

Although the partitioning strategy has some disadvantages, some improvements can be done to make the performance of this partitioning strategy better. The improvements are stated as follows.

1) The alternate supply paths of vital loads can be integrated into the multi-agent system by adding constraints to the switch status of vital loads. The load supply path switch status is shown in Figure 4.6. For a vital load, the bus transfer constraint is added, which is shown in (4-2).

$$\begin{aligned} \sigma_{14}(t) + \sigma_{34}(t) \le 1 \\ \sigma_{13}(t) + \sigma_{33}(t) \le 1 \end{aligned} \tag{4-2}$$

where, $\sigma_{13}(t)$, $\sigma_{33}(t)$, $\sigma_{14}(t)$, and $\sigma_{34}(t)$ are the switch statuses of the supply paths for the two vital loads. The constraint means that the two supply paths of one vital load cannot serve the load at the same time.

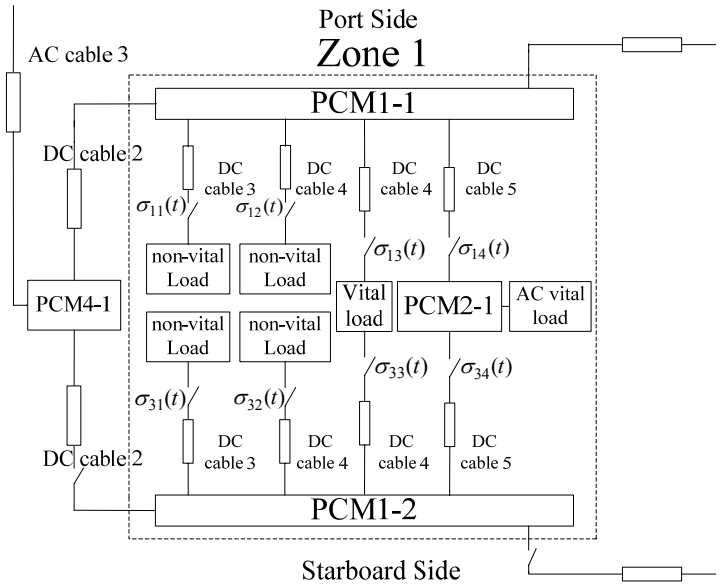

Figure 4.6 One DC zone with normal paths and alternate paths for vital loads

2) To improve the accuracy of the reduced-order agent model, an adaptive reduced-order agent was developed. The adaptive reduced-order agent model updated its parameters in real-time based on the measurements of voltages and currents from the power system. The gradient method was used to update the parameters.

3) A propulsion load can be integrated into the multi-agent system by adding communication links between the propulsion load and other agents. The priority of the propulsion load can be changed based on the operation mode of ships. For example, when the operation mode of a ship is changed from battle mode to cruise mode, the priority of propulsion load would be increased and the priority of pulse loads would be decreased. The propulsion load could be modeled using a second-order linear system [46]. The

propulsion load model is different from agent models in DC zones. The diagram of the multi-agent system topology with a propulsion load agent is shown in Figure 4.7.

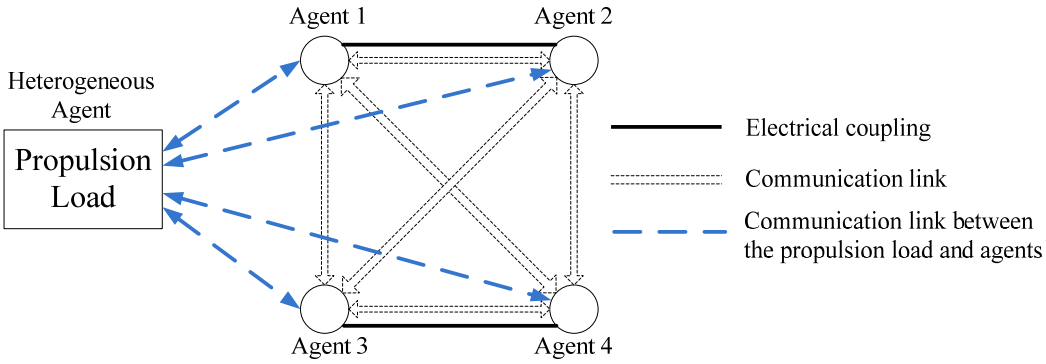

Figure 4.7 Topology of the multi-agent system with a propulsion load agent in Partitioning Strategy I

4.3.2 Partitioning Strategy II

In Partitioning Strategy II, two DC zones of the DC zone system of the notional all-electric ship power system were partitioned based on DC-DC converters in PCM1s, as shown in Figure 4.8. Each agent included one DC-DC converter, switches, and various priority loads. This partitioning strategy also neglected the detail load dynamics and the alternate supply paths of vital loads. A group of loads were aggregated into an agent model, and the load switches were aggregated into a control variable of the agent. Thus, the control signal of each agent was also quantized based on the rated power of each load to control the load switch status, which reduced the accuracy of the cooperative controller.

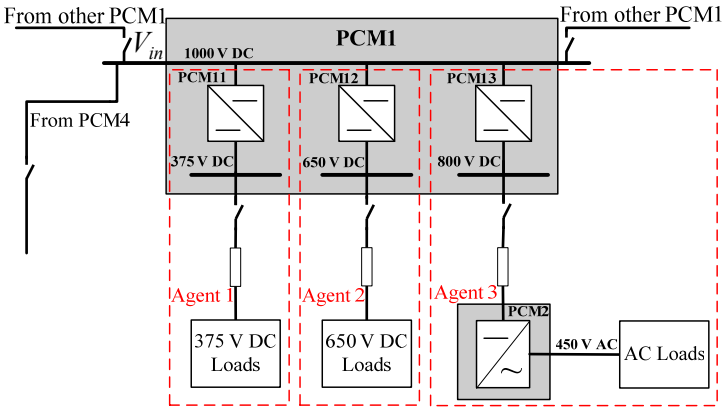

Figure 4.8 Diagram of Partitioning Strategy II for half a zone

Each agent included only one DC-DC converter and loads served by the converter. The agent was modeled using a second-order nonlinear system. In Partitioning Strategy I, each individual agent included three DC-DC converters with different voltage levels. Thus, the agent model in Partitioning Strategy II was more accurate than the agent model in Partitioning Strategy I. The dynamic performance of the cooperative controller directly depended on the accuracy of the dynamic agent model. Thus, the dynamic performance of the developed cooperative controller based on Partitioning Strategy II would be better than the performance of Partitioning Strategy I.

The agents in DC zones were homogeneous agents, and the propulsion loads were defined as heterogeneous agents. All the homogeneous agents had an identical second-order nonlinear model. The heterogeneous agents had a different type of dynamic model, which was modeled using a second-order linear system. The generator agent was also included in the multi-agent system and was modeled using a second-order linear system. The diagram of the multi-agent system is shown in Figure 4.9. Since an all-to-all communication network would make the network topology too complex, a

communication agent was introduced to reduce the connectivity of the network. There was one communication agent for each PCM1. The agents served by the same PCM1 only locally communicated with the communication agent. The communication agents and heterogeneous agents globally exchanged state information to achieve the group objective subject to the operating constraints of the system.

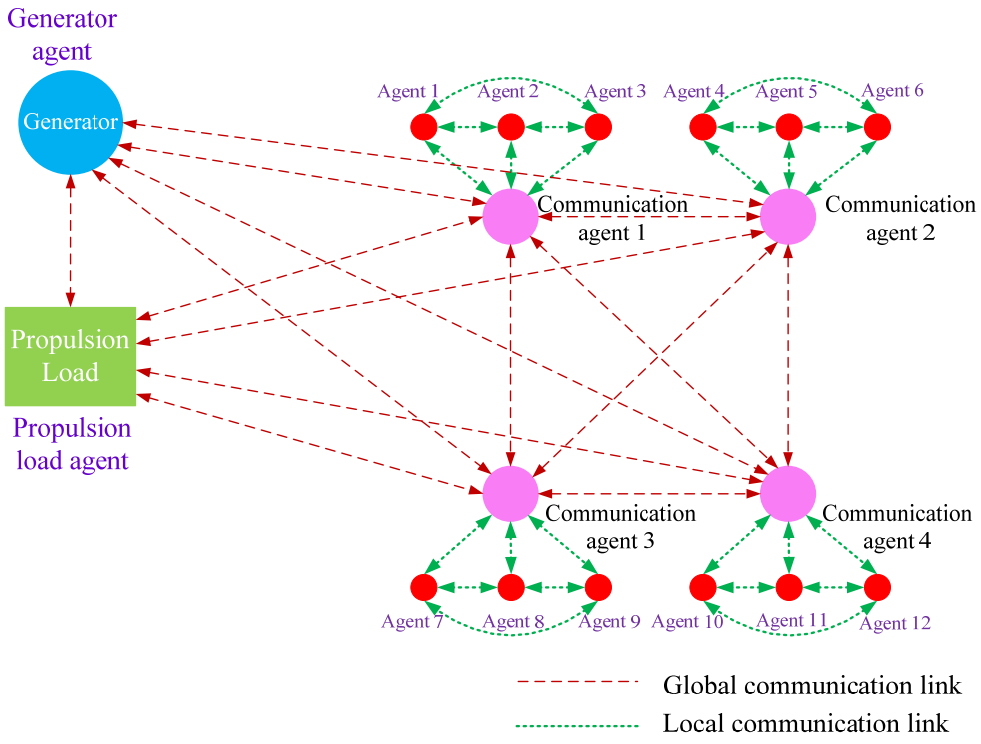

Figure 4.9 Topology of the multi-agent system using Partitioning Strategy II

Advantages of Partitioning Strategy II:

1) This partitioning strategy improved the accuracy of the reduced-order agent model. Each agent included one DC-DC converter, switches, and various

priority loads. The accuracy of the reduced-order agent model was better than that of the agent model in Partitioning Strategy I.

2) The agents in DC zones were homogeneous agents. The existing multi-agent system cooperative control strategies can be easily applied to achieve the real-time load management objective for the all-electric ship power system.
3) The propulsion loads were easily integrated into the multi-agent system, and were defined as heterogeneous agents due to their unique dynamic model.
4) The objective and constraints of real-time load management could be easily integrated into the multi-agent system.

Disadvantages of Partitioning Strategy II:

1) The topology of the multi-agent system in Partitioning Strategy II was more complex than the multi-agent system in Partitioning Strategy I. Communication agents were integrated in the multi-agent system to reduce the complexity of the communication network.
2) This partitioning strategy is valid only when the topology of PCM1 is parallel, as shown in Figure 4.8. If the topology of PCM1 is serial, as shown in Figure 4.10, the partitioning strategy is invalid.
3) The alternate path of the vital load was neglected.
4) All the loads in the agents were modeled using resistors and aggregated together. The switch status control signals were generated based on the quantization of the agent control signal, which decreased the accuracy of the cooperative controller.

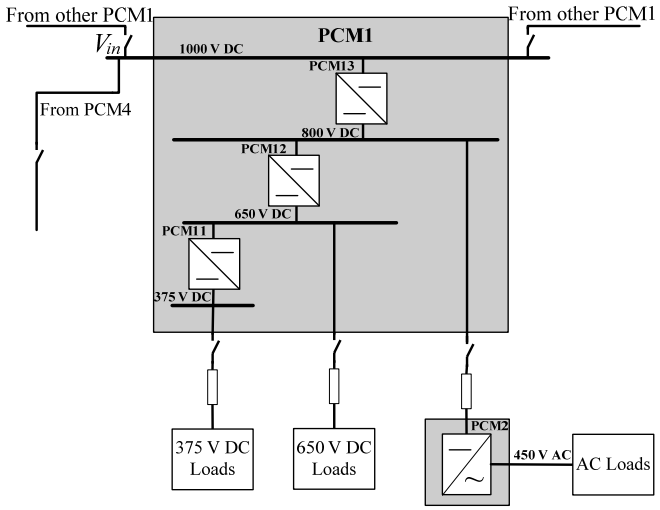

Figure 4.10 Serial topology of PCM1

4.3.3 Partitioning Strategy III

In Partitioning Strategy III, the DC zone system of the notional all-electric ship power system model was partitioned based on individual electrical components, such as loads and power converters. The loads were modeled using load agents; transformers, cables, and power converters were modeled using interactive agents; generators were modeled using generator agents. The various agents used different types of dynamic models. As a result, the partitioned system is a heterogeneous multi-agent system. In each DC zone, the system was partitioned based on individual electrical components such as DC-DC converters and individual loads, as shown in Figure 4.11.

The topology of the multi-agent system in one DC zone is shown in Figure 4.12. Each DC zone consisted of two communication agents, six DC-DC converter agents, and a group of load agents. Communication agents were used to reduce the communication complexity of the multi-agent system. Each communication agent communicated with

three DC-DC converter agents in the same PCM1, and all of the communication agents in the system as an all-to-all communication network to achieve the real-time load management objective. Further each DC-DC converter agent communicated with the group of load agents connected to that converter as an all-to-all communication network, as shown in Figure 4.12. The alternate paths of vital loads were also integrated into the multi-agent system.

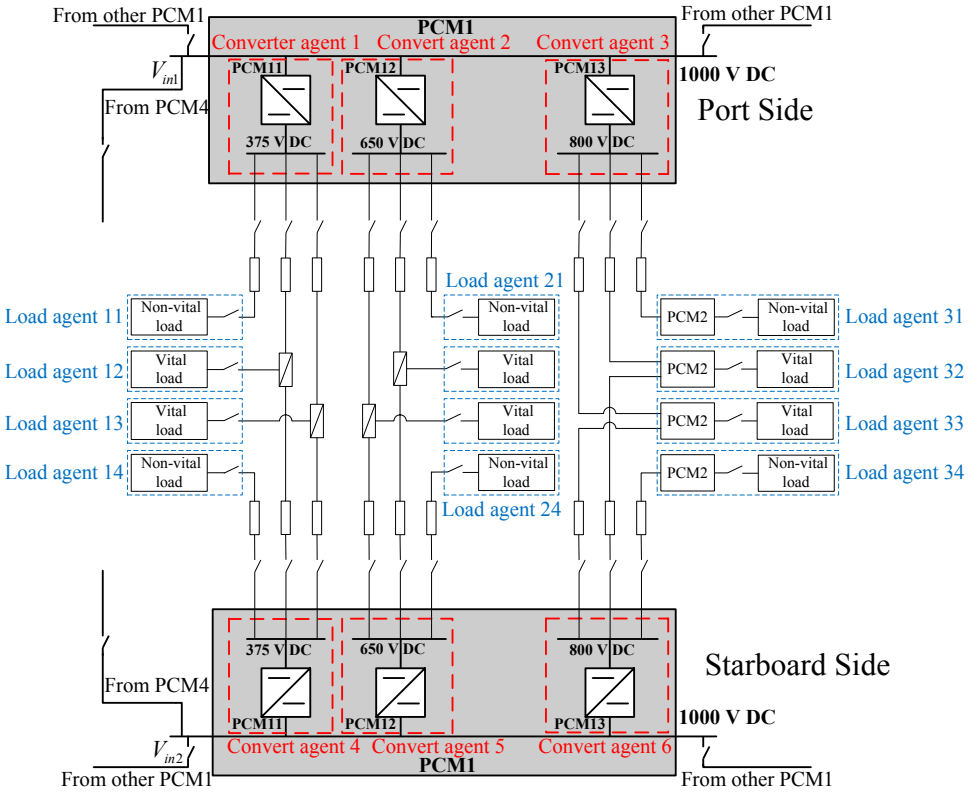

Figure 4.11 Diagram of a DC zone partitioning using Partition Strategy III

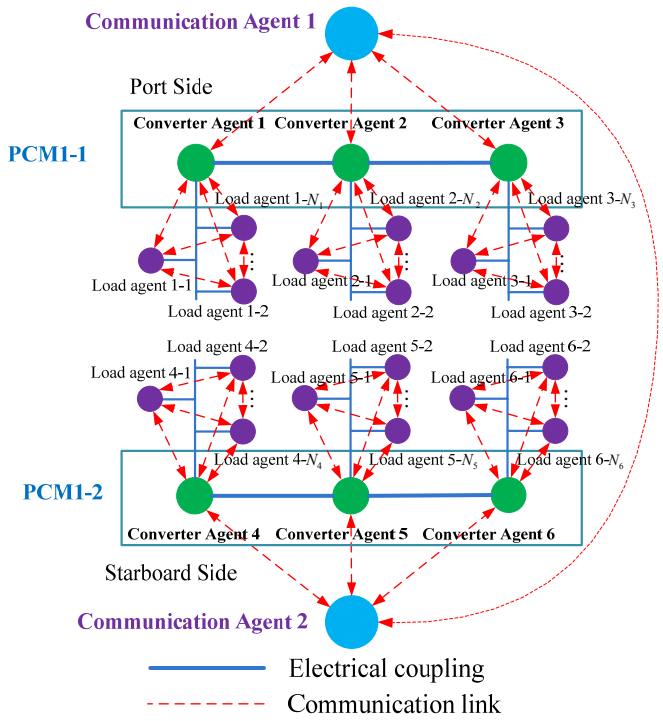

Figure 4.12 Topology of the multi-agent system in one DC zone using Partition Strategy III

The load agent was used to model loads such as constant power loads, DC motors, induction motors, propulsion loads, pulse loads, etc. A diagram of the load agent is shown in Figure 4.13. Induction motors served by PCM2 were also defined as a load agent, as shown in Figure 4.14. The constant power load agent was modeled using a linear circuit, as shown in Figure 4.15. Motor loads and propulsion loads were modeled using second-order systems. The charging circuit for pulse loads were also modeled using the linear circuit shown in Figure 4.15.

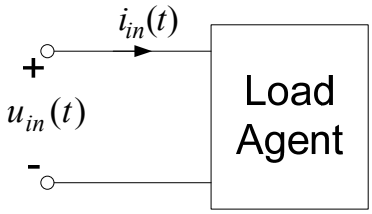

Figure 4.13 Diagram of the load agent for Partitioning Strategy III

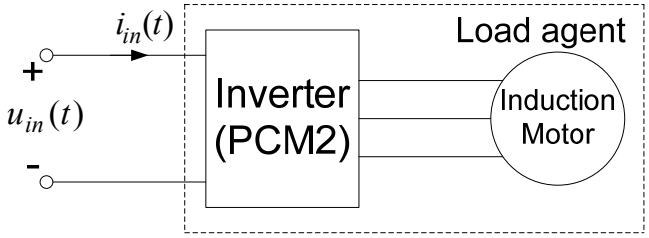

Figure 4.14 Diagram of the induction motor with PCM2 for Partitioning Strategy III

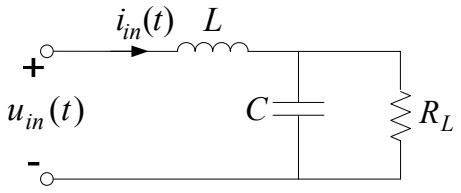

Figure 4.15 Diagram of the equivalent circuit used to model a constant load agent for Partitioning Strategy III

The interactive agent was used to model transformers, DC-DC converters, etc. The diagram of the interactive agent is shown in Figure 4.16. Since PCM4 included a transformer and an uncontrolled rectifier, it was modeled using an interactive agent. The second-order linear circuit used to model the interactive agent is shown in Figure 4.17.

Figure 4.16 Diagram of the interactive agent for Partitioning Strategy III

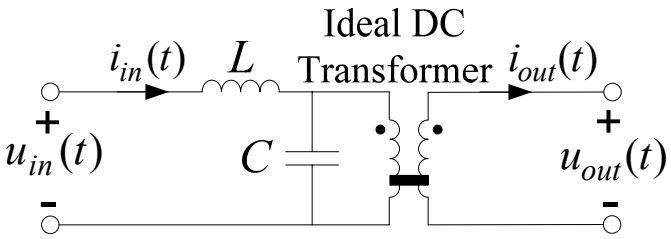

Figure 4.17 Diagram of the equivalent circuit used to model the interactive agent for Partitioning Strategy III

Advantages of Partitioning Strategy III:

1) The system was partitioned based on individual electrical components, which provided more flexibility to integrate system dynamics into the multi-agent system. The individual electrical components, such as loads, transformers, DC-DC converters, generators, cables, and propulsion loads, were modeled as agents. Each agent was modeled using different types of dynamic systems. Since the detail dynamics of individual loads were integrated into agent models, the accuracy of the multi-agent system was greatly improved.
2) The alternate supply paths of vital loads were integrated into the multi-agent system.

3) Various operational constraints of the system were integrated into the multi-agent system.
4) Since loads were not aggregated in Partitioning Strategy III, the cooperative controller could ensure that vital loads were served before non-vital loads.

Disadvantages of Partitioning Strategy III:

1) Since the heterogeneous cooperative control theory is not well developed in current literature, a cooperative controller for heterogeneous multi-agent systems for power systems needed to be designed and developed to achieve real-time load management for all-electric ship power systems.
2) Since the topology of the heterogeneous multi-agent system was more complex than the multi-agent system topologies used in Partitioning Strategies I and II, the integration of the real-time load management objectives into the heterogeneous multi-agent system was very challenging.

4.3.4 Summary of comparisons of the three partitioning strategies

A summary of the comparison of the three partitioning strategies discussed in the earlier sections is shown in Table 4.1 [89]. Partitioning Strategy III provided more flexibility to integrate various agents with different dynamic models in the multi-agent system, which improved the accuracy of the agent model and cooperative controller. Moreover, alternate supply paths of vital loads were integrated into this heterogeneous multi-agent system. Furthermore, various operational constraints of the system could be integrated into the multi-agent system to ensure that a feasible solution for real-time load management could be obtained. Due to these reasons, Partitioning Strategy III was

selected as the partitioning strategy to design a heterogeneous multi-agent system framework to solve the real-time load management problem for all-electric ship power systems. The following section in this chapter provides details on a novel heterogeneous multi-agent system design for real-time load management in all-electric ship power systems.

Table 4.1 Comparison of the three partitioning strategies

Partitioning Strategy	I	II	III
Multi-agent system topology	Homogeneous	Homogeneous	Heterogeneous
Cooperative controller design	Simple	Simple	Complex
Alternate path of the vital load	Neglected	Neglected	Included
Loads in the agent model	Aggregated	Aggregated	Included
Load dynamics	Neglected	Neglected	Included
Agent model accuracy	Low	Medium	High
Computational Complexity	Low	Medium	High
Real-time step size	Large	Medium	Small
Steady state accuracy	High	High	High
Transient state accuracy	Low	Medium	High

4.4 Multi-Agent System Framework for the All-Electric Ship Power System

In this section, a heterogeneous multi-agent system framework developed for all-electric ship power systems to achieve real-time load management is presented. A one-line diagram of a simplified notional all-electric ship power system model is shown in Figure 4.18. The system consists of one MTG, one ATG, two transformers, one propulsion load, one pulse load, and two DC zones. The total generation capacity is 40 MW. The component definitions are shown in Table 2.1.

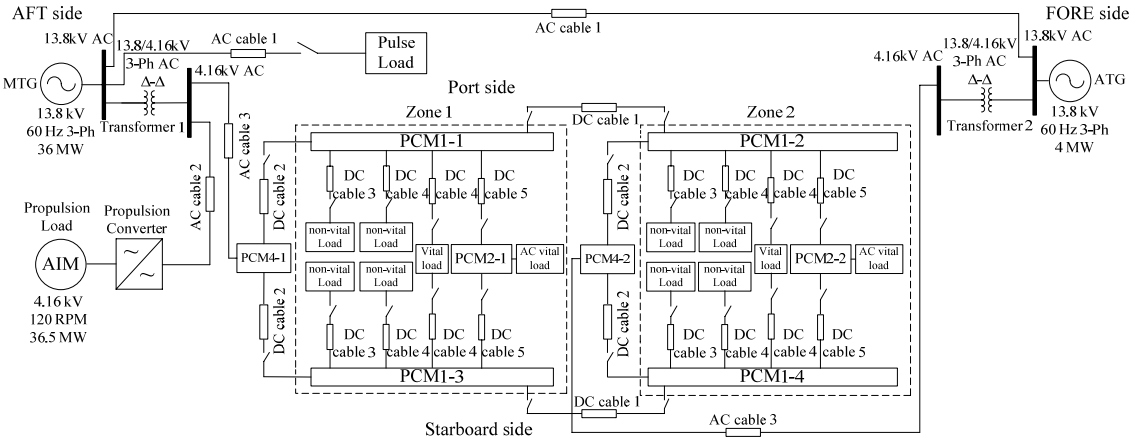

Figure 4.18 One-line diagram of a simplified notional all-electric ship power system model for the multi-agent system design

4.4.1 Multi-agent system overview

The diagram of the multi-agent system distributed control concept for real-time load management in all-electric ship power systems is shown in Figure 4.19(a). An all-electric ship power system is partitioned into a group of electrical subsystems; the switch status or set-point of loads in each electrical subsystem is controlled by a distributed controller. Each agent measures voltage, current, or power demand information from the corresponding electrical subsystem and communicates with other agents in the multi-agent system. Based on the measured information and communication with other agents, a distributed controller can optimally determine the switch status or set-point of loads in the electrical subsystem. The simulation step size of the all-electric ship power system model is chosen as $\Delta\tau$, and the simulation step size of the multi-agent system is Δt_i; the decision time step and measurement step size of each agent are Δt_i; the communication time step between different agents is also Δt_i.

The multi-agent system for a 2-zone simplified notional all-electric ship power system, as shown in Figure 4.19(b), includes two subsystems – MVAC system and DC zone system. The MVAC and DC zone multi-agent systems were designed separately to simplify the real-time load management problem. To coordinate the MVAC and DC zone multi-agent systems, an AC-DC communication agent was designed to exchange information between the two multi-agent systems to achieve real-time load management. The AC-DC communication agent provides the available power information to the DC zone system and the load demand information of the DC zone system to a system losses agent.

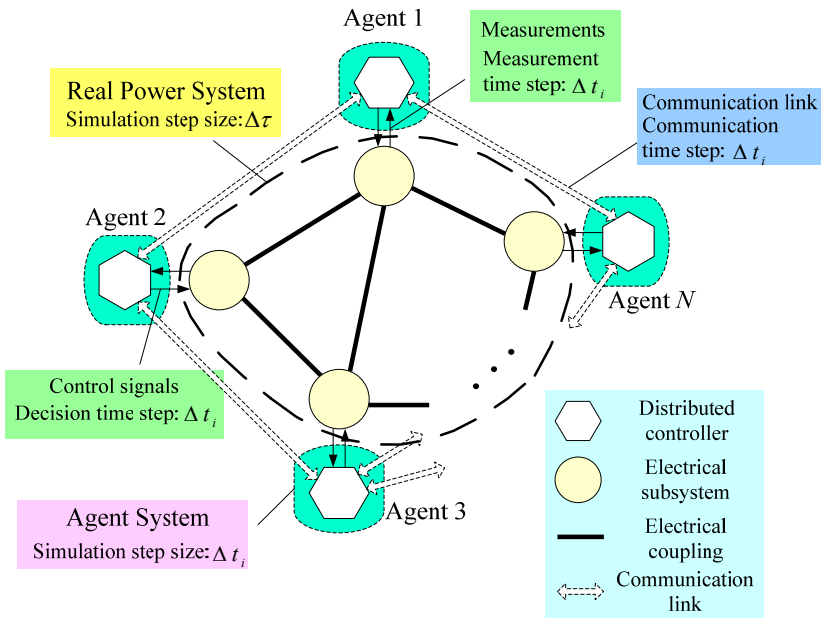

(a)

Figure 4.19 Diagrams of the multi-agent system distributed control concept. **(a)** Diagram of a general multi-agent distributed control system for real-time load management in all-electric ship power systems, **(b)** Diagram of a multi-agent system for a simplified 2-zone notional all-electric ship power system model

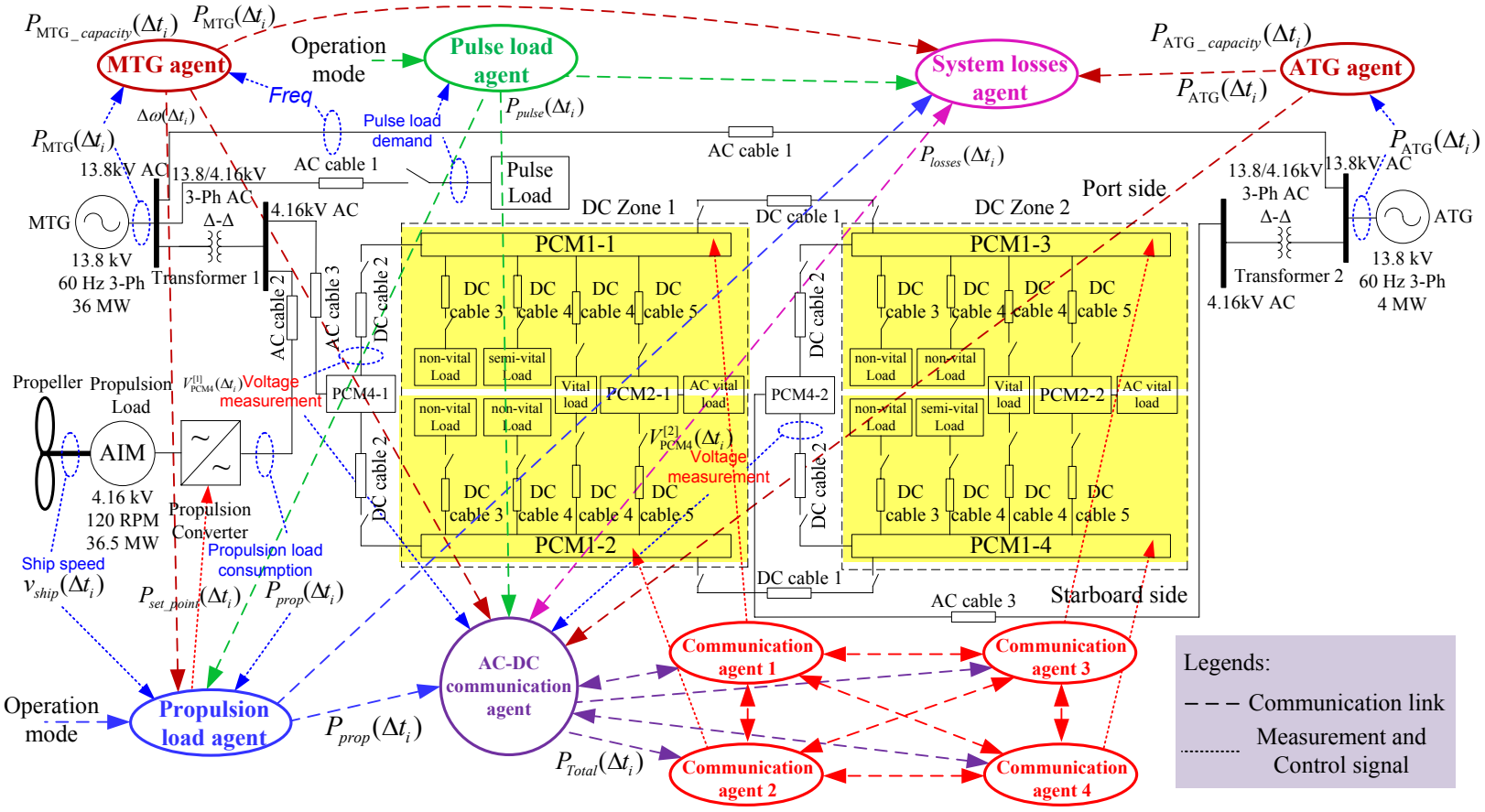

(b)

Figure 4.19 Continued

In the MVAC multi-agent system, generator agents, propulsion load agents, pulse load agents, and a system losses agent were designed to coordinate propulsion loads and pulse loads in the MVAC multi-agent system to achieve real-time load management. The generator agent measures the generator output and obtains the generator capacity information. MTG agent also measures the MTG frequency, which is calculated by propulsion load agents to implement the frequency regulation. The propulsion load agent obtains: 1) the pulse load demand from the pulse load agent, 2) the propulsion load demand from other propulsion load agents, 3) input voltage of the propulsion load; 4) system frequency deviation from the MTG agent, and 5) the ship's operation mode. In cruise mode, the speed controller of the marine propulsion system is used to drive the ship to its cruising speed smoothly; in battle mode, the power controller of the marine propulsion system is used to compensate for the impact of pulse loads, when utilized, on the power quality of the all-electric ship power system. The system losses agent obtains the propulsion load demand, pulse load demand, MTG and ATG power outputs, and DC zone load demand to calculate the total losses of the MVAC system based on the system topology.

In the DC zone multi-agent system, a 4-zone all-electric ship power system was partitioned using Partitioning Strategy III into a group of subsystems. The DC zone multi-agent system includes communication agents, converter agents, and load agents, which coordinately achieve the real-time load management objective for the DC zone system. Each DC zone includes six converter agents, two communication agents, and a group of load agents. The converter agents compose a converter-layer multi-agent

system, and each converter agent served a group of load agents, which compose a load-layer multi-agent system. Each communication agent communicates with three converter agents served by the same DC distribution bus, and exchanges information with other communication agents. Each converter or load agent measures local information and communicates with other load, converter or communication agents to make decisions using a cooperative controller. The total available power to the DC zone multi-agent system is calculated by the AC-DC communication agent, which also obtains the generation capacity information, propulsion load demand, pulse load demand, and system losses from the MVAC multi-agent system.

Since the MVAC and DC zone multi-agent systems are separate subsystems, the two multi-agent systems are coordinated to achieve the real-time load management for an all-electric ship power system. The AC-DC communication agent is a bridge that connects the MVAC and DC zone multi-agent systems. The AC-DC communication agent communicates with the MVAC multi-agent system to calculate the available power to the DC zone multi-agent system. Moreover, the AC-DC communication agent provides the DC zone load demand information to the system losses agent in the MVAC multi-agent system.

4.4.2 MVAC multi-agent system

4.4.2.1 Overview of the MVAC multi-agent system

The objectives of the MVAC multi-agent system are summarized in (4-3)-(4-9). The goal of the objective function, as shown in (4-3), was to minimize the mismatch between generation and load. The voltage and frequency constraints were determined

based on the power quality requirements for shipboard power systems defined by IEEE-STD-45 [17]. The frequency and voltage deviation tolerances were 3% and 5% in steady state, respectively; the frequency and voltage deviation tolerances were 4% and 16% in transient state, respectively; and the transient recovery time was 2 seconds. The first two constraints in (4-4) and (4-5) are steady state frequency and voltage constraints. The equations (4-6)-(4-9) are transient state frequency and voltage constraints, which mean that a sudden change in voltage or frequency that goes outside the steady state tolerance and returns to and remains within the limits within a recovery time [17].

The constraint shown in (4-9) is cable dynamic constraint. The dynamic cable constraint considers a time horizon *T*, and the total violation time of the cable ampacity constraint should be no larger than the maximum allowed time T_1, as shown in (4-9). When $I_{\text{pulse}}(\Delta t_i) > I_{\text{pulse}}^{\text{Ampacity}}$, $0.5 \cdot [1 + \text{sgn}(I_{\text{pulse}}(\Delta t_i) - I_{\text{pulse}}^{\text{Ampacity}})]$ is equal to 1. The value of the integral term, $\int_{t-T}^{t} 0.5 \cdot \left[1 + \text{sgn}(I_{\text{pulse}}(\Delta t_i) - I_{\text{pulse}}^{\text{Ampacity}})\right] dt$, begins to increase. If the value of the integral term is larger than T_1, the pulse load needs to be disconnected immediately to satisfy the dynamic cable constraint.

$$\min \quad \left(\sum_{k \in G} [P_{G_k}(\Delta t_i)] - \left[\sum_{j \in L} [s_j(\Delta t_i) P_{L_j}(\Delta t_i)] + P_{losses}(\Delta t_i) \right] \right)^2 \tag{4-3}$$

$$\text{s. t.} \quad \left| \Delta \omega_j(\Delta t_i) \right| \le 3\% \tag{4-4}$$

$$\left| \Delta V_{\text{prop1}_j}(\Delta t_i) \right| \le 5\%, \quad \left| \Delta V_{\text{prop2}_j}(\Delta t_i) \right| \le 5\% \tag{4-5}$$

$$\int_{t-T}^{t} 0.5 \cdot \left[1 + \text{sgn}\left(\left|\Delta \omega(\Delta t_i)\right| - 3\%\right)\right] dt \le 2 \text{ sec} \tag{4-6}$$

$$\int_{t-T}^{t} 0.5 \cdot \left[1 + \mathrm{sgn}\left(\left|\Delta V_{\mathrm{prop1}}(\Delta t_i)\right| - 5\%\right)\right] dt \le 2 \text{ sec} \tag{4-7}$$

$$\int_{t-T}^{t} 0.5 \cdot \left[1 + \mathrm{sgn}\left(\left|\Delta V_{\mathrm{prop2}}(\Delta t_i)\right| - 5\%\right)\right] dt \le 2 \text{ sec} \tag{4-8}$$

$$\int_{t-T}^{t} 0.5 \cdot \left[1 + \mathrm{sgn}(I_{\mathrm{pulse}}(\Delta t_i) - I_{\mathrm{pulse}}^{\mathrm{Ampacity}})\right] dt \le T_1 \tag{4-9}$$

where, $\mathrm{sgn}(x)$ is a sign function (if $x > 0$, $\mathrm{sgn}(x) = 1$; if $x = 0$, $\mathrm{sgn}(x) = 0$; if $x < 0$, $\mathrm{sgn}(x) = -1$); T is an integral time, which is positive constant; Δt_i is the decision time step of the real-time load management; $P_{G_k}(\Delta t_i)$ is the output power of generator k; G is the generator set in the MVAC system; $s_j(\Delta t_i)$ is the load switch status of load j; $P_{L_j}(\Delta t_i)$ is the power demand of load j; L is the load set in the system; $P_{losses}(\Delta t_i)$ is the total losses in the MVAC system, which is discussed in section 4.4.2.5, and the expression of system losses $P_{losses}(\Delta t_i)$ is shown in (4-19); $\Delta\omega$ is the frequency of the MTG generator; ΔV_{prop1} and ΔV_{prop2} are the input voltages of propulsion loads 1 and 2, respectively; $I_{\mathrm{pulse}}(\Delta t_i)$ is the input current to the pulse load; $I_{\mathrm{pulse}}^{\mathrm{Ampacity}}$ is the ampacity of the cable serving the pulse load; and T_1 is maximum allowed violation time of the cable amapcity constraint. In (4-3)-(4-9), ΔV_{prop1}, ΔV_{prop2}, $I_{\mathrm{pulse}}(\Delta t_i)$, $P_{G_k}(\Delta t_i)$, and $\Delta\omega$ are measured from the all-electric ship power system; $P_{losses}(\Delta t_i)$ is calculated based on steady state method, as shown in (4-19).

The objective of the MVAC multi-agent system is to coordinate pulse loads and propulsion loads while satisfying the operational constraints of the system and considering load priorities. The diagram of the MVAC multi-agent system is shown in

Figure 4.20. The MVAC multi-agent system consists of MTG agents, ATG agents, propulsion load agents, a pulse load agent, and a system losses agent. This diagram illustrates that different agents exchange state information through communication links to achieve the group goal. Moreover, the operation mode of the ship is obtained by propulsion load agents and the pulse load agent to determine load priorities and to choose the appropriate controller (power or speed controller) to achieve the real-time load management objective. The MVAC system is a tightly coupled power system and the system frequency has nearly the same value at different locations; therefore, the frequency is measured by MTG agent 1 to implement the frequency regulation using propulsion load agents.

Since real-time load management aims to regulate load demand in a power system to achieve dynamic balancing while satisfying the operational constraints of the system, the power set-points of the generators are not control variables in the real-time load management problem. In the MVAC multi-agent system, MTG and ATG agents only measure local information and communicate with other agents, but do not make decisions to regulate generators; on the other hand, propulsion load agents and pulse load agents not only measure local information and communicate with other agents, but they also make decisions to control individual load demands.

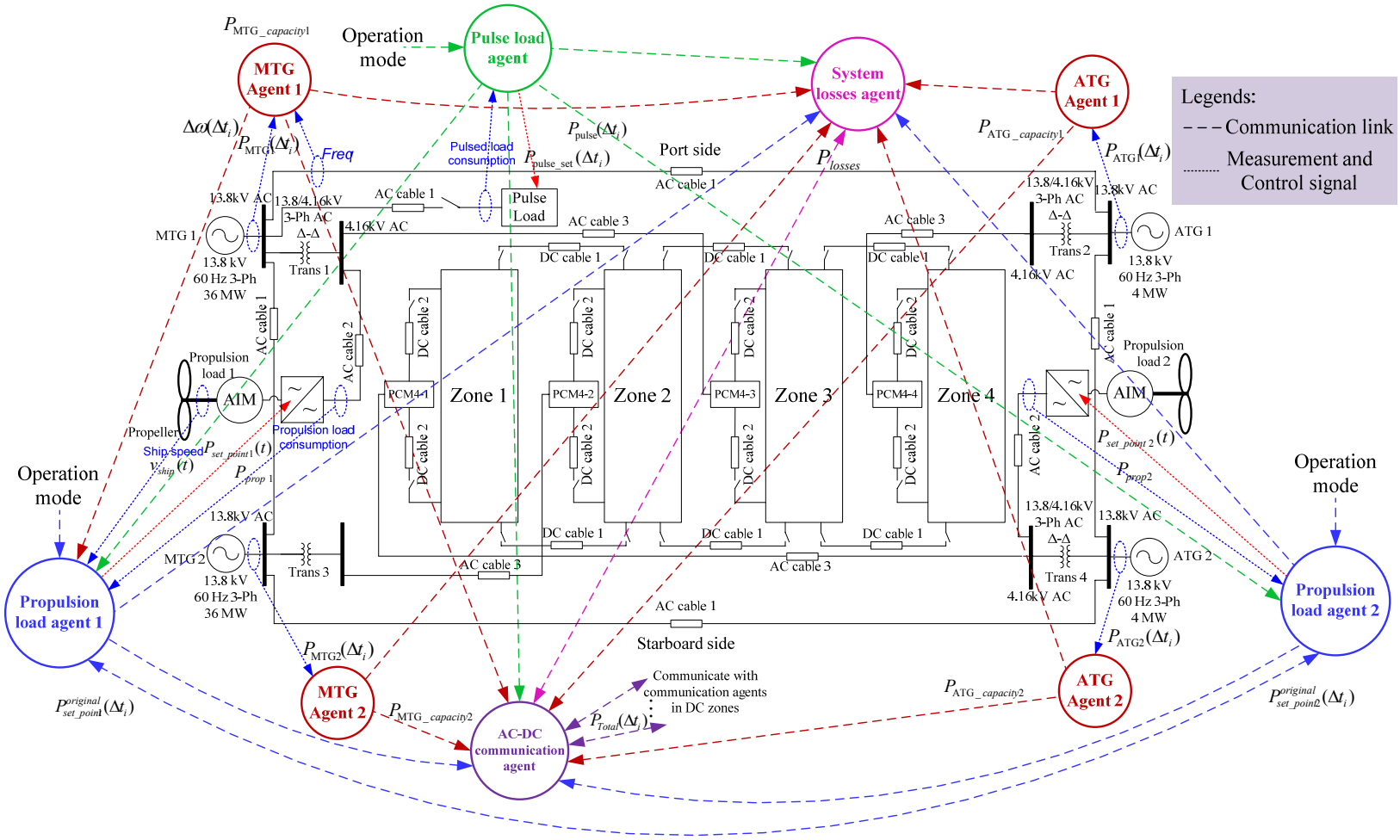

Figure 4.20 Diagram of the MVAC multi-agent system for the notional all-electric ship power system

4.4.2.2 Generator agent in the MVAC multi-agent system

The generator agent measures its output power and obtains the generation capacity information from the individual generator. MTG agent 1 also measures the generator's frequency, which is obtained by propulsion load agents and used to reduce the impact of pulse loads on the power quality of the system. The measurement interval for the generation output is 200 milliseconds, since the generation output is obtained by the system losses agent to calculate the system losses in steady state. The communication interval between generator agents and the system losses agent is 200 milliseconds. The measurement interval for the MTG frequency is 10 milliseconds because this frequency signal is used to implement the propulsion load compensation. The generator agent sends the generation capacity information to the AC-DC communication agent which calculates the available power to the DC zone system, and this communication interval is also 10 milliseconds. As noted earlier, the MTG and ATG agents only measure local information and communicate with other agents; they do not regulate generator outputs in the real-time load management problem. The mathematical models of generator agents are discussed in Appendix A.1.

4.4.2.3 Propulsion load agent in the MVAC multi-agent system

The goal of the propulsion load agent is to coordinate the propulsion load and pulse load in the MVAC system to reduce the frequency oscillations caused by pulse load changes. The frequency constraints of the system are shown as $|\Delta\omega| \le 3\%$ and $\int_{t-T}^{t} 0.5 \cdot \left[1 + \mathrm{sgn}\left(\left|\Delta\omega(\Delta t_i)\right| - 3\%\right)\right] dt \le 2\,\mathrm{sec}$. A frequency regulation controller was designed in a propulsion load agent to reduce the frequency oscillations in the MVAC system.

Moreover, the propulsion load agent integrates the propulsion load input voltage constraints, as shown in (4-5), (4-7), and (4-8), to make the input voltage of each propulsion load in the normal range.

As shown in Figure 4.20, two propulsion loads are served by the notional all-electric ship power system. The power set-point of propulsion load 1 is determined by propulsion load agent 1; the power set-point of propulsion load 2 is determined by propulsion load agent 2. The decision time step of the propulsion load agent is 10 milliseconds. The communication time step between the propulsion load agent and system losses agent is 200 milliseconds; the communication time step between propulsion load agents and all other agents is 10 milliseconds. The measurement time step is also 10 milliseconds.

The diagram of the propulsion load agent 1 is shown in Figure 4.21. The inputs of the propulsion load agent included: 1) input voltage of the propulsion load, 2) ship operation mode, 3) ship speed reference $v_{\text{ref}}(t)$, 4) actual ship speed $v_{\text{ship}}(t)$, 5) the original power set-point of propulsion load 1 $P_{\text{set\_point1}}^{\text{original}}(t)$, 6) pulse load demand $P_{\text{pulse}}(t)$, 7) the original power set-point of propulsion load 2 $P_{\text{set\_point2}}^{\text{original}}(t)$, and 8) the frequency deviation of MTG 1 $\Delta\omega$. The output signal of the propulsion load agent is the new power set-point of propulsion load 1, which is used to regulate the power demand of the propulsion load. The mathematical model of the propulsion load agent 1 is discussed in Appendix A.2. The PI controllers 1 and 2 are also discussed in Appendix A.2.

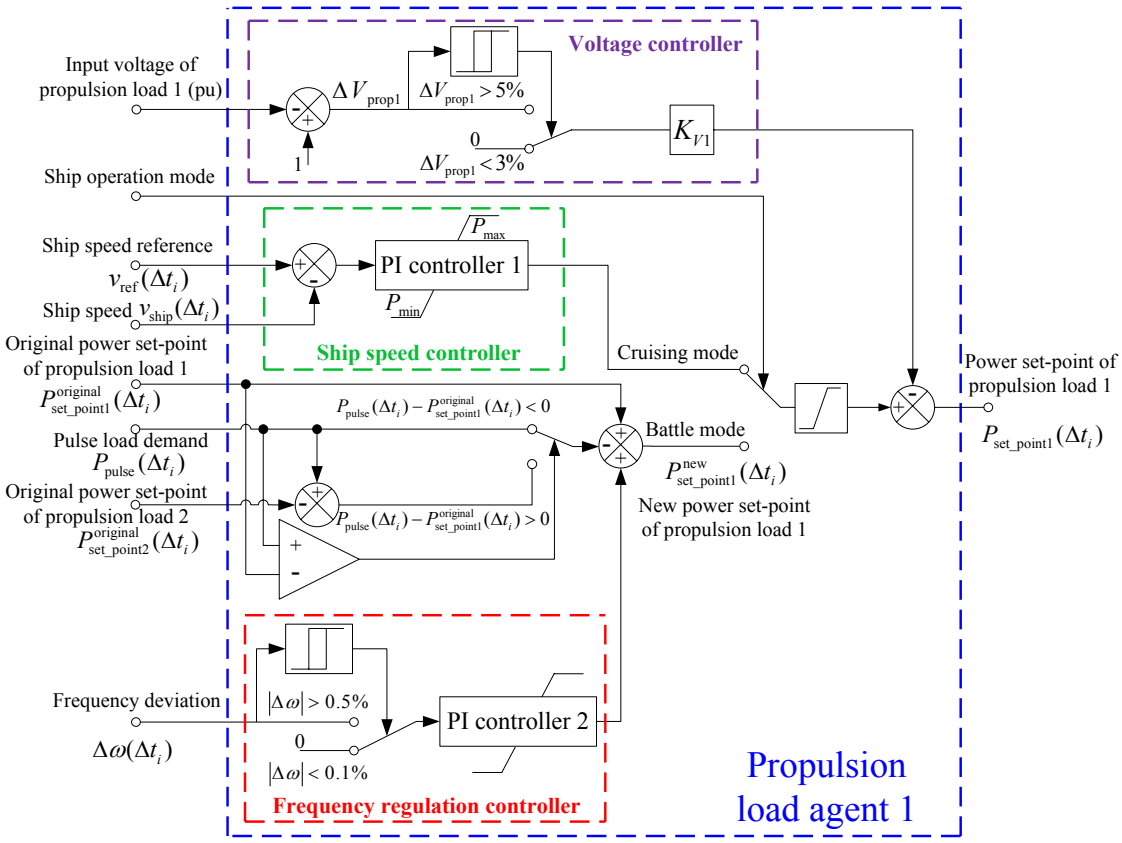

Figure 4.21 Diagram of propulsion load agent 1 in the MVAC multi-agent system

In order to compensate for the load changes caused by pulse loads, propulsion loads are reduced temporarily to achieve the real-time balancing of the generation and load in the system. If the magnitude of the pulse load is less than the load demand of propulsion load 1, only propulsion load 1 is used to compensate for pulse load demand, and the power set-point of propulsion load 2 is not changed. If the magnitude of the pulse load is larger than the load demand of propulsion load 1, the power set-point of propulsion load 2 is reduced first, and then the propulsion load 1 is still used to compensate for the pulse load demand.

In the MVAC multi-agent system, propulsion load agent 1 is responsible for the frequency regulation. The diagram of propulsion load agents 1 and 2 in MVAC multi-agent system is shown in Figure 4.22. Propulsion load agents 1 and 2 exchange their original power set-points to determine whether propulsion load 2 needs to be disturbed while a pulse load is being served. The voltage controller in the propulsion load agent is activated to reduce the propulsion load demand when the input voltage of the propulsion load is less than 95% of the nominal value. When the input voltage is larger than 97% of the nominal value, the voltage controller is deactivated. The hysteresis component eliminates high frequency switching of the voltage controller.

In cruise mode, propulsion loads have the highest priority. If the power system does not have enough available power, non-vital service loads and pulse loads need to be disconnected from the system. The power set-point of the propulsion load is determined by the ship speed controller, and the ship speed is gradually regulated to the desired speed by the speed controller. The input signals of the ship speed controller are the ship speed reference $v_{\text{ref}}(t)$ and the actual ship speed $v_{\text{ship}}(t)$; the output signal is the power set-point of the propulsion load.

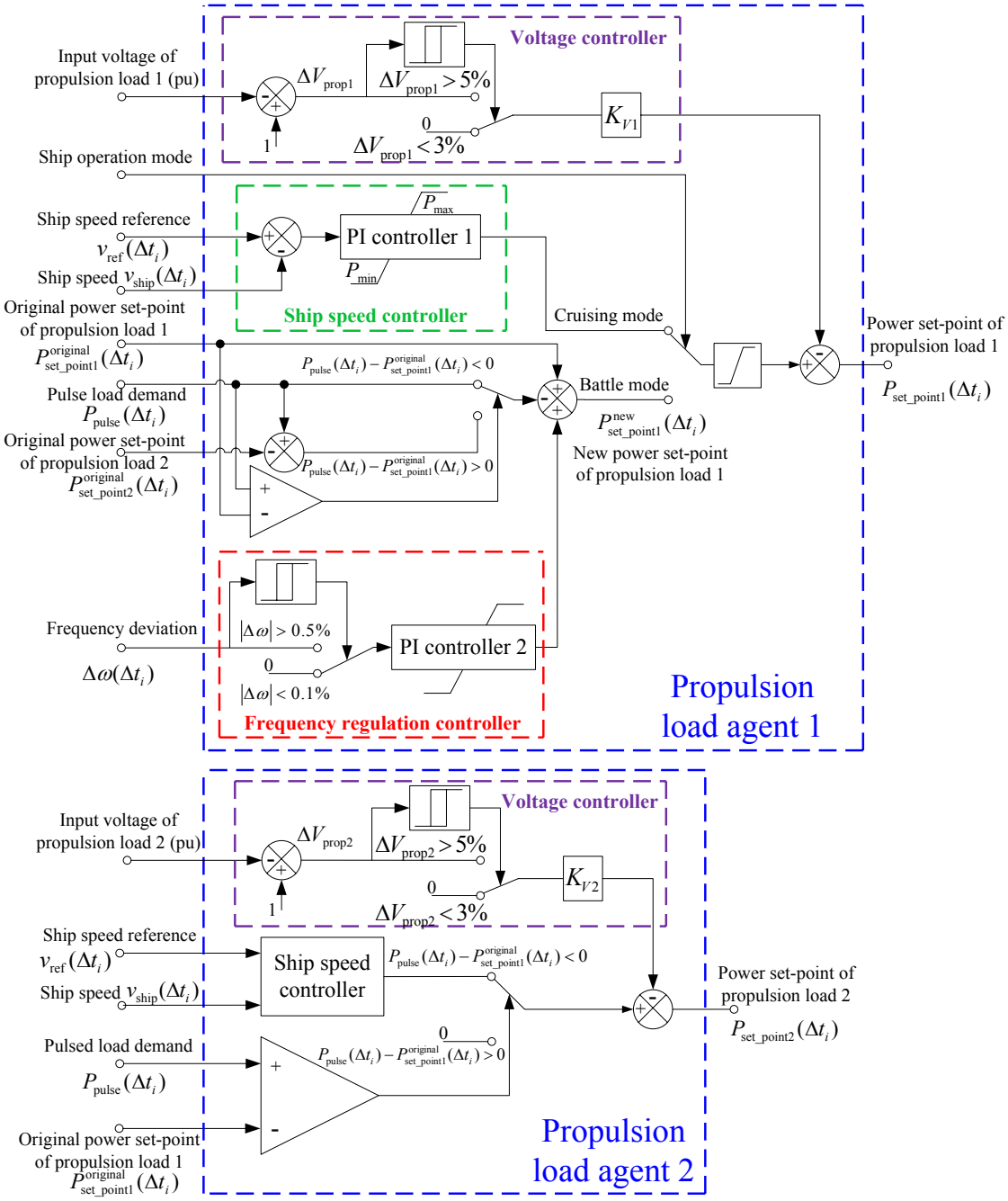

Figure 4.22 Diagram of propulsion load agents 1 and 2 in the MVAC multi-agent system

In battle mode, pulse loads have the highest priority, and propulsion loads are reduced temporarily to compensate for the pulse load demand. When the ship's

operation mode is changed from cruise mode to battle mode, the marine propulsion system is switched from speed control mode to power control mode, as shown in Figure 4.21. The frequency regulation controller was implemented to compensate for the frequency oscillations caused by pulse loads. The frequency regulation controller is activated when the frequency deviation is more than 0.5% of the nominal value; the controller is deactivated when the frequency deviation is less than 0.1% of the nominal value. This hysteresis component eliminates the high frequency switching of the controller.

4.4.2.4 Pulse load agent in the MVAC multi-agent system

The dynamic constraint of the cable serving the pulse load was included in the pulse load agent. Since a pulse load draws a large amount of current from the system in a short time frame, the cable ampacity constraint can be violated for a short period of time while serving a pulse load. The dynamic cable constraint considers a time horizon *T*, and the total violation time of the cable ampacity constraint should be no larger than the maximum allowed time T_1, as shown in $\int_{t-T}^{t} 0.5 \cdot \left[1 + \mathrm{sgn}(I_{\mathrm{pulse}}(\Delta t_i) - I_{\mathrm{pulse}}^{\mathrm{Ampacity}})\right] dt \le T_1$. If the total violation time is larger than T_1, the pulse load needs to be disconnected immediately to satisfy the dynamic cable constraint.

The diagram of a pulse load agent is shown in Figure 4.23. The inputs of the pulse load agent are the ship's operation mode, power set-point of the pulse load, and input voltage and current of the pulse load. The outputs are the pulse load demand and the actual power set-point of the pulse load. In cruise mode, pulse loads have lower priorities than propulsion loads, which may not be served when the system does not have

enough available power. In battle mode, pulse loads have higher priorities than propulsion loads, and propulsion loads and service loads need to be decreased to mitigate frequency and voltage oscillations caused by pulse loads. The mathematical model of the pulse load agent is discussed in Appendix A.3.

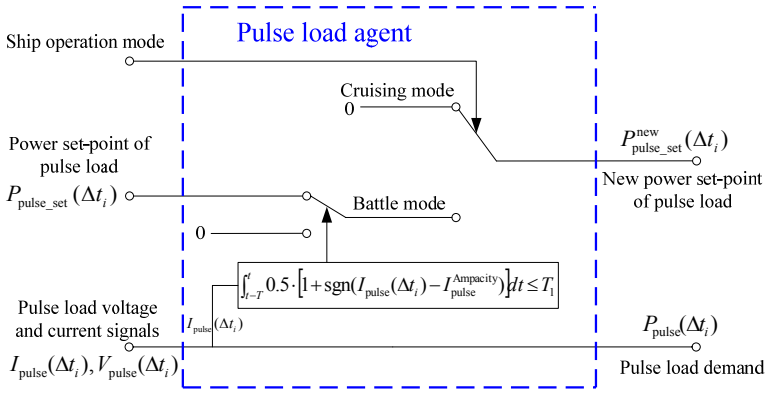

Figure 4.23 Diagram of a pulse load agent in the MVAC multi-agent system

The pulse load agent measures the pulse load demand, which is sent to the propulsion load agent to reduce the impact of the pulse load on the power quality of the all-electric ship power system. The measurement time step is 10 milliseconds. The communication time step between pulse load agent and system losses agent is 200 milliseconds; the communication time step with propulsion load agents and AC-DC communication agent is 10 milliseconds.

4.4.2.5 System losses agent in the MVAC multi-agent system

In this section, the system losses agent for the MVAC system is introduced using a simplified all-electric ship power system, as shown in Figure 4.24. The simplified system includes one MTG, one ATG, two transformers, AC cables, a propulsion load, a

pulse load, and two partial DC zones. PCM4-1 serves port side DC distribution buses, and PCM4-2 serves starboard side DC distribution buses. The time step of power measurement is chosen as Δt_i.

The system losses agent obtains MTG and ATG power outputs ($P_{\text{MTG}}(\Delta t_i)$ and $P_{\text{ATG}}(\Delta t_i)$), propulsion load demand ($P_{\text{prop}}(\Delta t_i)$), pulse load demand ($P_{\text{pulse}}(\Delta t_i)$),power demand at each PCM4 ($P_{\text{PCM4--1}}(\Delta t_i)$ and $P_{\text{PCM4--2}}(\Delta t_i)$), and the MVAC system topology information to calculate system losses in the MVAC system. It is assumed that the topology information is available for the system losses agent. The diagram of the system losses agent is shown in Figure 4.25. The communication interval between the system losses agent and other agents is chosen as 200 ms, since system losses are calculated based on a steady state method from [68]. The decision time step is also chosen as 200 ms.

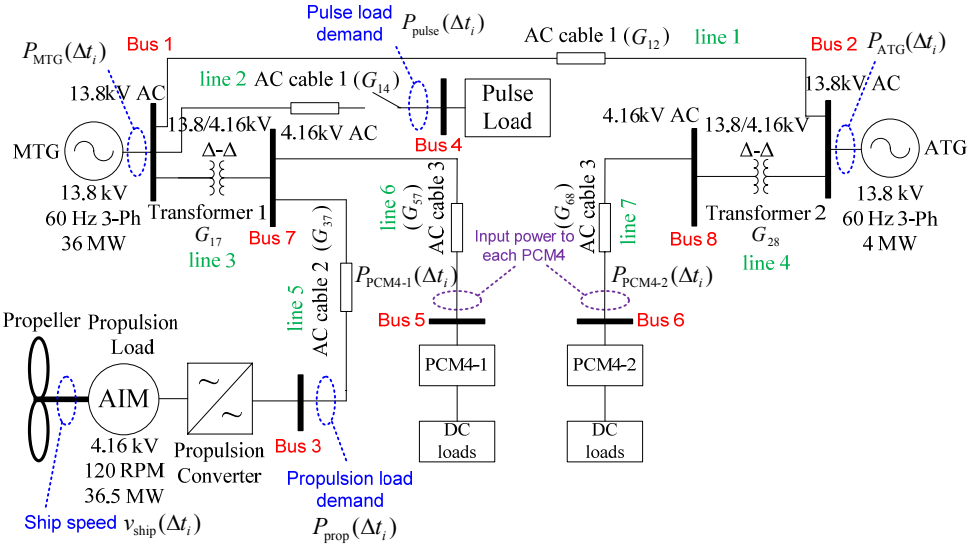

Figure 4.24 Diagram of a simplified MVAC system used for system losses calculation

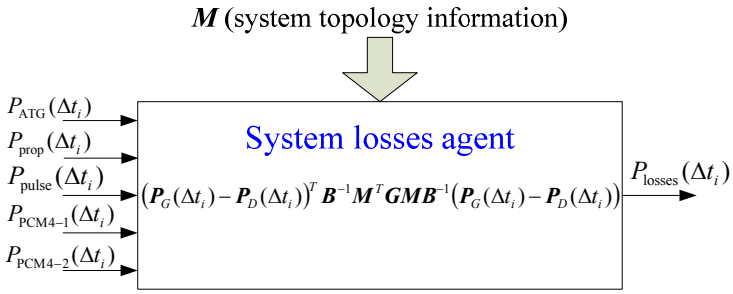

Figure 4.25 Diagram of the system losses agent in the MVAC multi-agent system

The total losses in the MVAC system are calculated using a DC power flow method. It is assumed that all the bus voltages are at nominal values. The line losses can be expressed as (4-10).

$$P_{L_{ij}} \approx G_{ij}(\delta_i - \delta_j)^2 \tag{4-10}$$

where, G_{ij} is the conductance of line *i-j*; δ_i and δ_j are voltage angles of bus *i* and *j*, respectively; $P_{L_{ij}}$ is the losses on line *i-j*. In the simplified MVAC system, bus 1 is chosen as slack bus, so the voltage angle of bus 1 is equal to 0. The angle difference across a line is computed as (4-11).

$$\boldsymbol{\psi} = \boldsymbol{M}\boldsymbol{\delta} \tag{4-11}$$

where, $\boldsymbol{\delta} = [\delta_2, \delta_3, \cdots, \delta_8]^T$ is the bus angle vector, $\boldsymbol{\psi}$ is the vector of angle differences across lines, and $\boldsymbol{M}$ is the line-bus incidence matrix, which is shown as (4-12).

$$\boldsymbol{M} = \begin{bmatrix} -1 & 0 & 0 & 0 & 0 & 0 & 0 \\ 0 & 0 & -1 & 0 & 0 & 0 & 0 \\ 0 & 0 & 0 & 0 & 0 & -1 & 0 \\ 1 & 0 & 0 & 0 & 0 & 0 & -1 \\ 0 & 1 & 0 & 0 & 0 & -1 & 0 \\ 0 & 0 & 0 & 1 & 0 & -1 & 0 \\ 0 & 0 & 0 & 0 & 1 & 0 & -1 \end{bmatrix} \tag{4-12}$$

Thus, the vector of angle differences across lines is expressed as (4-13).

$$\boldsymbol{\psi} = \boldsymbol{M\delta} = \begin{bmatrix} -1 & 0 & 0 & 0 & 0 & 0 & 0 \\ 0 & 0 & -1 & 0 & 0 & 0 & 0 \\ 0 & 0 & 0 & 0 & 0 & -1 & 0 \\ 1 & 0 & 0 & 0 & 0 & 0 & -1 \\ 0 & 1 & 0 & 0 & 0 & -1 & 0 \\ 0 & 0 & 0 & 1 & 0 & -1 & 0 \\ 0 & 0 & 0 & 0 & 1 & 0 & -1 \end{bmatrix} \cdot \begin{bmatrix} \delta_2 \\ \delta_3 \\ \delta_4 \\ \delta_5 \\ \delta_6 \\ \delta_7 \\ \delta_8 \end{bmatrix} = \begin{bmatrix} 0-\delta_2 \\ 0-\delta_4 \\ 0-\delta_7 \\ \delta_2-\delta_8 \\ \delta_3-\delta_7 \\ \delta_5-\delta_7 \\ \delta_6-\delta_8 \end{bmatrix} \tag{4-13}$$

The diagonal matrix of line conductances of the simplified MVAC system is determined by (4-14).

$$\boldsymbol{G} = \begin{bmatrix} G_{12} & 0 & 0 & 0 & 0 & 0 & 0 \\ 0 & G_{14} & 0 & 0 & 0 & 0 & 0 \\ 0 & 0 & G_{17} & 0 & 0 & 0 & 0 \\ 0 & 0 & 0 & G_{28} & 0 & 0 & 0 \\ 0 & 0 & 0 & 0 & G_{37} & 0 & 0 \\ 0 & 0 & 0 & 0 & 0 & G_{57} & 0 \\ 0 & 0 & 0 & 0 & 0 & 0 & G_{68} \end{bmatrix} \tag{4-14}$$

The total line losses [68] can be expressed as (4-15).

$$P_{losses} = \sum_{\text{all lines}} P_{L_{ij}} = \boldsymbol{\psi}^T \boldsymbol{G\psi} \tag{4-15}$$

In order to compute the bus angle vector, $\boldsymbol{\delta}(\Delta t_i)$, at time interval Δt_i, explicitly, a DC power flow analysis method [45], [68] is used to calculate the bus angle vector, which is expressed in (4-16).

$$\boldsymbol{\delta}(\Delta t_i) = \boldsymbol{B}^{-1}\left(\boldsymbol{P}_G(\Delta t_i) - \boldsymbol{P}_D(\Delta t_i)\right) \tag{4-16}$$

where, $\boldsymbol{P}_G(\Delta t_i)$ is the generation power vector of the simplified MVAC system, which is defined as $[P_{\text{ATG}}(\Delta t_i) \;\; 0 \;\; 0 \;\; 0 \;\; 0 \;\; 0 \;\; 0]^T$; $\boldsymbol{P}_D(\Delta t_i)$ is the load demand vector of the simplified MVAC system, which is defined as $[0 \; -P_{\text{prop}}(\Delta t_i) \; -P_{\text{pulse}}(\Delta t_i) \; -P_{\text{PCM 4–1}}(\Delta t_i) \; -P_{\text{PCM 4–2}}(\Delta t_i) \;\; 0 \;\; 0]^T$; $\boldsymbol{B}$ matrix is the susceptance matrix, which is the imaginary part of the admittance matrix $\boldsymbol{Y}$ of the system. By using (4-11) and (4-16), the total system losses at time interval Δt_i can be expressed as (4-17).

$$\begin{aligned} P_{losses}(\Delta t_i) &= \boldsymbol{\psi}(\Delta t_i)^T \boldsymbol{G}\boldsymbol{\psi}(\Delta t_i) = \boldsymbol{\delta}(\Delta t_i)^T \boldsymbol{M}^T \boldsymbol{G}\boldsymbol{M}\boldsymbol{\delta}(\Delta t_i) \\ &= \left(\boldsymbol{P}_G(\Delta t_i) - \boldsymbol{P}_D(\Delta t_i)\right)^T \boldsymbol{B}^{-1}\boldsymbol{M}^T\boldsymbol{G}\boldsymbol{M}\boldsymbol{B}^{-1}\left(\boldsymbol{P}_G(\Delta t_i) - \boldsymbol{P}_D(\Delta t_i)\right) \end{aligned} \tag{4-17}$$

The real power injection vector $\boldsymbol{P}_G(\Delta t_i) - \boldsymbol{P}_D(\Delta t_i)$ is expressed as (4-18).

$$\boldsymbol{P}_G(\Delta t_i) - \boldsymbol{P}_D(\Delta t_i) = [P_{\text{ATG}}(\Delta t_i) \; -P_{\text{prop}}(\Delta t_i) \; -P_{\text{pulse}}(\Delta t_i) \; -P_{\text{PCM 4–1}}(\Delta t_i) \; -P_{\text{PCM 4–2}}(\Delta t_i) \;\; 0 \;\; 0]^T \tag{4-18}$$

where, $P_{\text{ATG}}(\Delta t_i)$ is the ATG output power, $P_{\text{prop}}(\Delta t_i)$ is the propulsion load demand, $P_{\text{pulse}}(\Delta t_i)$ is the pulse load demand, and $P_{\text{PCM4–1}}(\Delta t_i)$ and $P_{\text{PCM4–2}}(\Delta t_i)$ are the input powers to PCM4-1 and PCM4-2, respectively.

4.4.2.6 Cooperation and coordination of agents in the MVAC multi-agent system

In the MVAC multi-agent system, decision variables for the real-time load management problem include power set-points of two propulsion loads, power set-points

of pulse loads, and the available power to the DC zone system. Power set-points of propulsion loads are determined by propulsion load agents; power set-points of pulse loads are determined by pulse load agents; and the available power to the DC zone system is determined by the AC-DC communication agent, which will be discussed later in section 4.4.4. MTG and ATG agents only communicate their power outputs with other agents, but do not regulate power outputs of the generators. The system losses agent calculates system losses in the MVAC system based on measurements communicated by other agents and sends the system losses information to the AC-DC communication agent. Thus, generator agents and the system losses agent do not control electrical components in the system.

A diagram illustrating the cooperation of agents in the MVAC multi-agent system via communication links is shown in Figure 4.26. The diagram indicates that the pulse load agent and propulsion load agents make decisions to control pulse load and propulsion loads based on communicated data and local measurements. The propulsion load agents decrease the set-points of propulsion loads when a pulse load is served in the system; the propulsion load agents increase the set-points of propulsion loads when a pulse load is disconnected from the system. The AC-DC communication agent calculates the available power to the DC zone system based on the information from the MVAC multi-agent system.

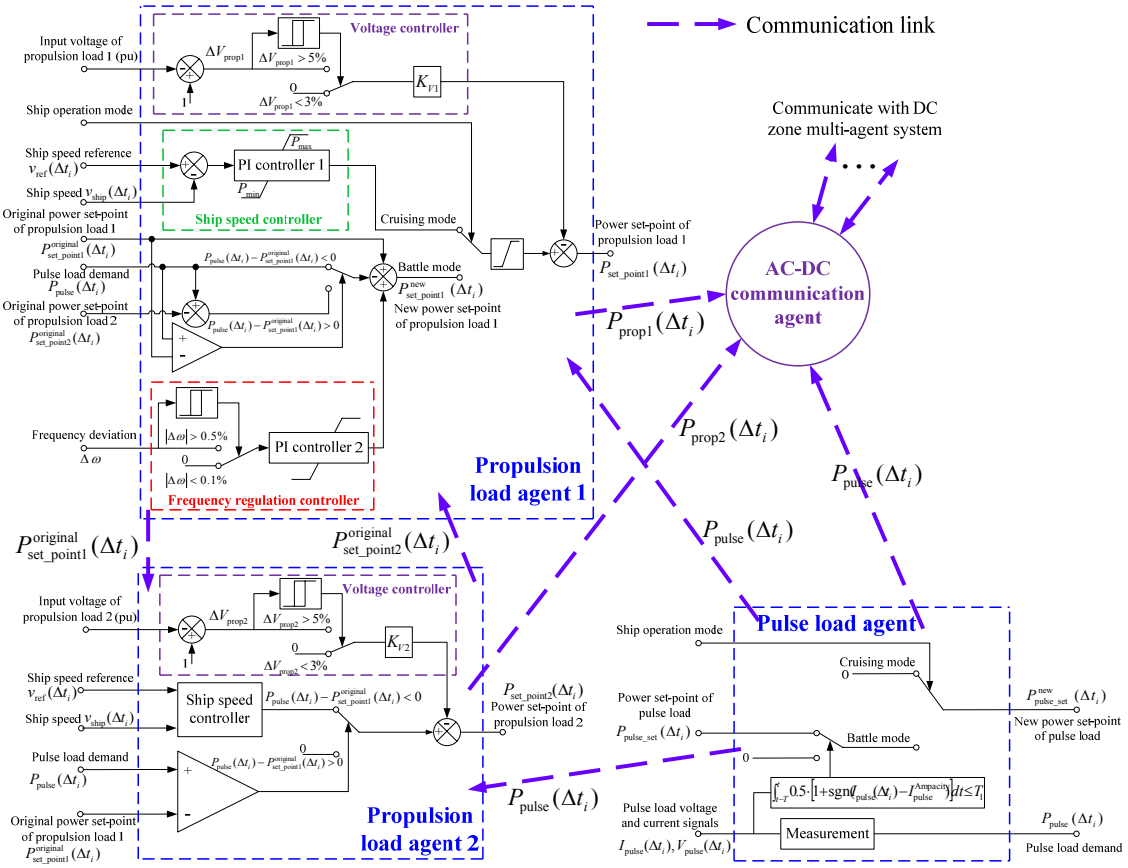

Figure 4.26 Diagram illustrating cooperation of agents in the MVAC multi-agent system

4.4.3 DC zone multi-agent system

4.4.3.1 Overview of the DC zone multi-agent system

The objective of the DC zone multi-agent system can be summarized in (4-19)-(4-25). The DC zone multi-agent system was designed based on the continuous dynamic system. The objective of the DC zone multi-agent system is to maximize the served loads considering load priorities, as shown in (4-19). Constraints include available power capacity constraints, as shown in (4-20), PCM4 capacity constraints, as shown in (4-21), and motor load voltage constraints, as shown in (4-22). (4-23)-(4-25) are system

constraints, which calculate the input power of each PCM4, input current of each converter agent, and input current of each load agent. The power losses of the cables in the DC zone system are neglected.

$$\text{Objective:} \quad \max \quad \sum_{k \in L} \left[P_k(\Delta t_i) \cdot s_k(\Delta t_i) \cdot W_k \right] \tag{4-19}$$

s.t. Available power source capacity constraint in DC zone multi-agent system:

$$\text{s.t.} \quad \sum_{k \in L} \left[P_k(\Delta t_i) \cdot s_k(\Delta t_i) \right] \le P_{Total}(\Delta t_i) \tag{4-20}$$

PCM4 capacity constraints:

$$P_{\text{PCM4}-j\,j}(\Delta t_i) \le P_{\text{PCM4}-j}^{\text{Capacity}}, \; j = 1, 2, 3, \text{and } 4 \tag{4-21}$$

Motor load voltage constraints:

$$V_m^{\min} \le \left| V_m(\Delta t_i) \right|, \; \forall m \in \{1, 2, \cdots, N_{motor}\} \tag{4-22}$$

System constraints:

$$\begin{aligned}
P_{\text{PCM4}-1\,j}(\Delta t_i) &= \textstyle\sum_{i=1}^{3} V_{in-i} x_i(t) + \sum_{i=7}^{9} V_{in-i} x_i(t) \\
P_{\text{PCM4}-2\,j}(\Delta t_i) &= \textstyle\sum_{i=4}^{6} V_{in-i} x_i(t) + \sum_{i=10}^{12} V_{in-i} x_i(t) \\
P_{\text{PCM4}-3\,j}(\Delta t_i) &= \textstyle\sum_{i=13}^{15} V_{in-i} x_i(t) + \sum_{i=19}^{21} V_{in-i} x_i(t) \\
P_{\text{PCM4}-4\,j}(\Delta t_i) &= \textstyle\sum_{i=16}^{18} V_{in-i} x_i(t) + \sum_{i=22}^{24} V_{in-i} x_i(t)
\end{aligned} \tag{4-23}$$

$$\begin{aligned}
&\dot{\hat{x}}_i(t) = \hat{y}_i(t) \\
&\dot{\hat{y}}_i(t) = -\hat{x}_i(t)/(L_i C_i) + d_i/(L_i C_i) \cdot \hat{i}_{out-i}(t) \\
&\hat{i}_{out-i}(t) = \textstyle\sum_{l=1}^{N_i} z_l(\Delta t_i); \; x_i(t) = \hat{x}_i(t)
\end{aligned} \tag{4-24}$$

$$P_k(\Delta t_i) = V_k(\Delta t_i) \cdot z_l \tag{4-25}$$

where, $P_k(\Delta t_i)$, $s_k(\Delta t_i)$, and W_k are the power demand, switch status, and weight-factor of load *k* in the DC zone system, respectively; *L* is the load set of the system; $P_{Total}(\Delta t_i)$ is the available power to the DC zone system, which is calculated based on the generation capacity, load demand in the MVAC system, and system losses; $P_{\mathrm{PCM4}-j}$ and $P_{\mathrm{PCM4}-j}^{\mathrm{Capacity}}$ are the input power and power capacity of PCM4- *j*, respectively; $V_m(\Delta t_i)$ and $V_m^{\min}$ are the input voltage and the minimum allowed voltage of motor load *m*, respectively; N_{motor} is the number of motor loads in the DC zone system; V_{in-i} and $x_i(t)$ are the input voltage and current of *i*th DC-DC converter; and $\hat{x}_i$, $\hat{y}_i$, and $\hat{i}_{out-i}$ are estimated values of the *i*th converter agent; and z_l is the input current of load *l*, which is determined by (4-48). The input and output signals of the DC zone multi-agent system are updated every Δt_i.

The notional DC zone system model was partitioned based on DC-DC converters in PCM1s and individual loads in DC zones. A diagram of the architecture of the DC zone multi-agent system and some MVAC components are shown in Figure 4.27. Each converter serves a group of constant loads and dynamic loads with various priorities. DC-DC converters are modeled as converter agents; and loads are modeled as load agents. The AC-DC communication agent communicates with communication agents and agents in MVAC multi-agent system. The diagram of the multi-agent system topology for the DC zone system is shown in Figure 4.28. In the 4-zone system, each DC zone includes six converter agents, two communication agents, and a group of load agents. The AC-DC communication agent is included in multi-agent system, which

coordinates the DC zone and MVAC multi-agent systems. The converter agents compose a converter-layer multi-agent system, and each converter agent serves a group of load agents, which compose a load-layer multi-agent system. Each communication agent communicates with three converter agents served by the same DC distribution bus, and exchanges information with other communication agents. Each converter or load agent measures local information and communicates with other load, converter or communication agents to make decisions using a cooperative controller.

The converter-layer multi-agent system topology of a 4-zone all-electric ship power system model is shown in Figure 4.29. The communication agents are defined to reduce the complexity of the communication network in the system. Each communication agent communicates with three converter agents in the same PCM1, and the eight communication agents compose an all-to-all communication network, which can communicate with each other. Using information passed via the communication links and local measurements, each converter agent makes decision to achieve the group goals. To increase the accuracy of the DC zone multi-agent system, the dynamics of loads in zones are included in DC zone multi-agent system.

A diagram of the *i*th converter agent and load-layer multi-agent system is shown in Figure 4.30. Converter agent *i* serves a group of load agents. The total number of load agents in the *i*th load-layer multi-agent system is N_i. The converter agent and its load agents compose an all-to-all communication network.

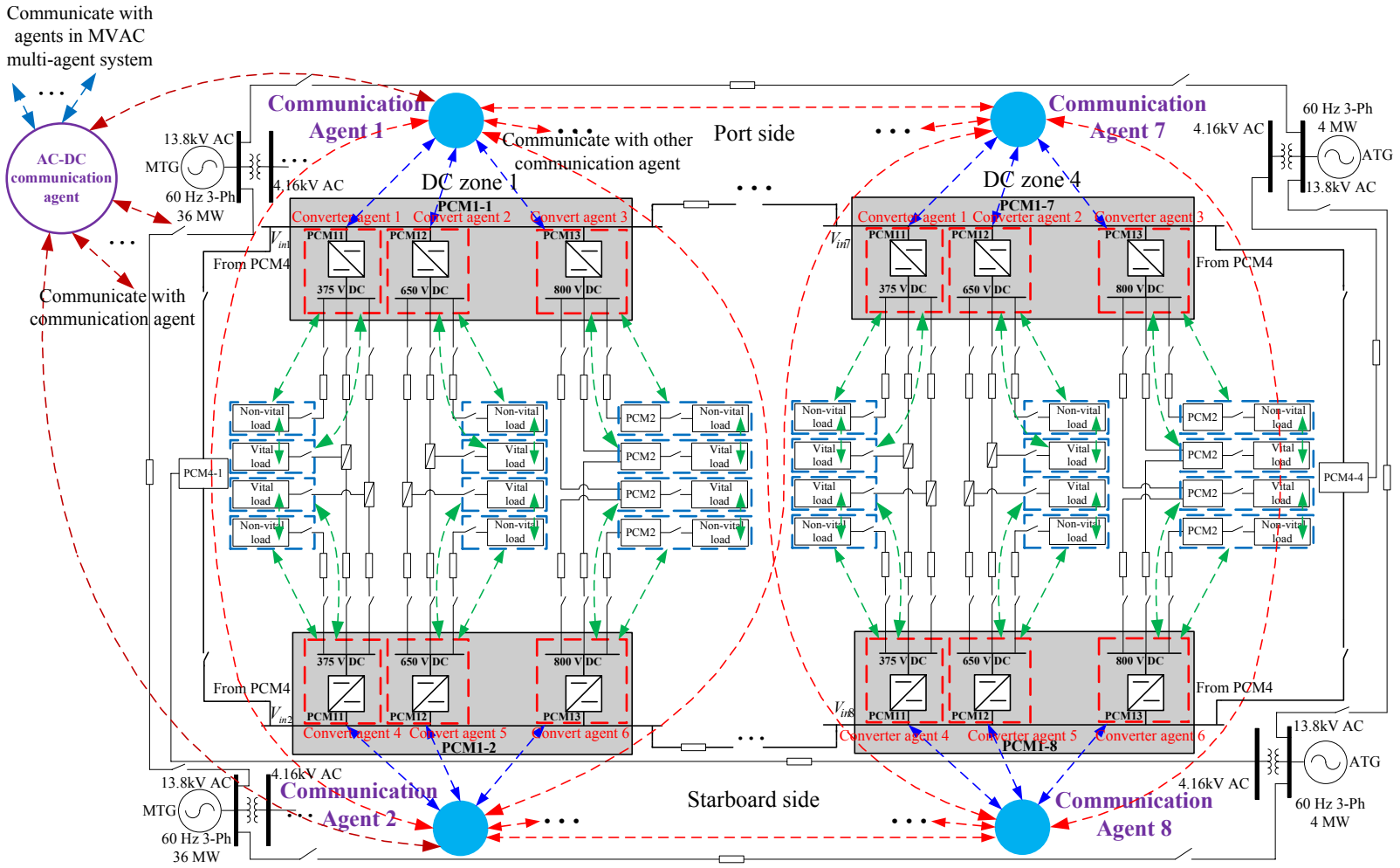

Figure 4.27 Diagram of the DC zone multi-agent system and some MVAC components

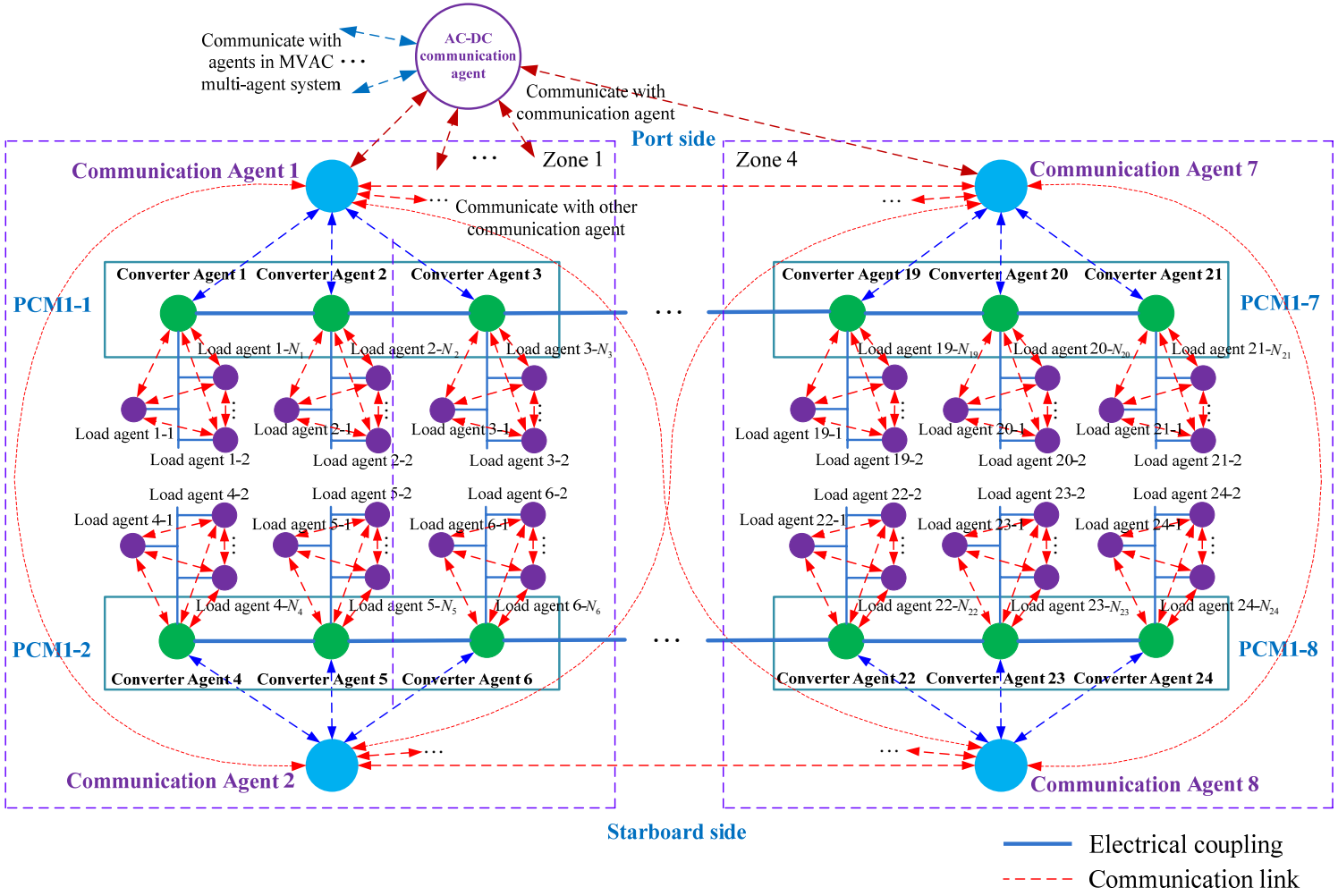

Figure 4.28 Diagram of the multi-agent system topology for the DC zone system of an all-electric ship power system

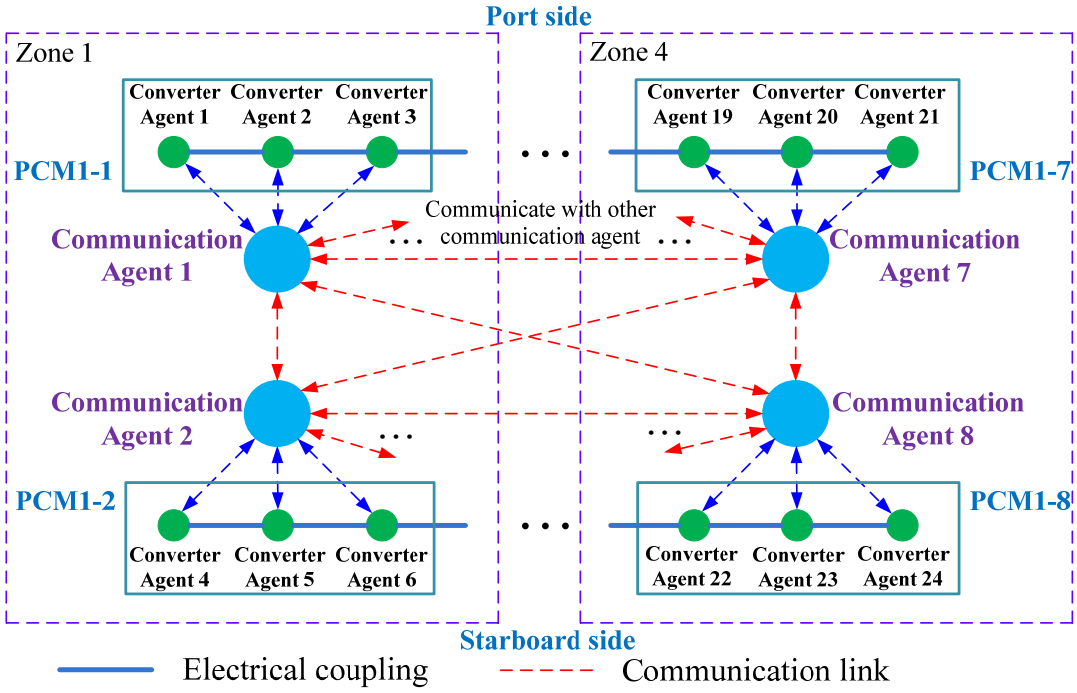

Figure 4.29 Diagram of the converter-layer multi-agent system topology for the DC zone system

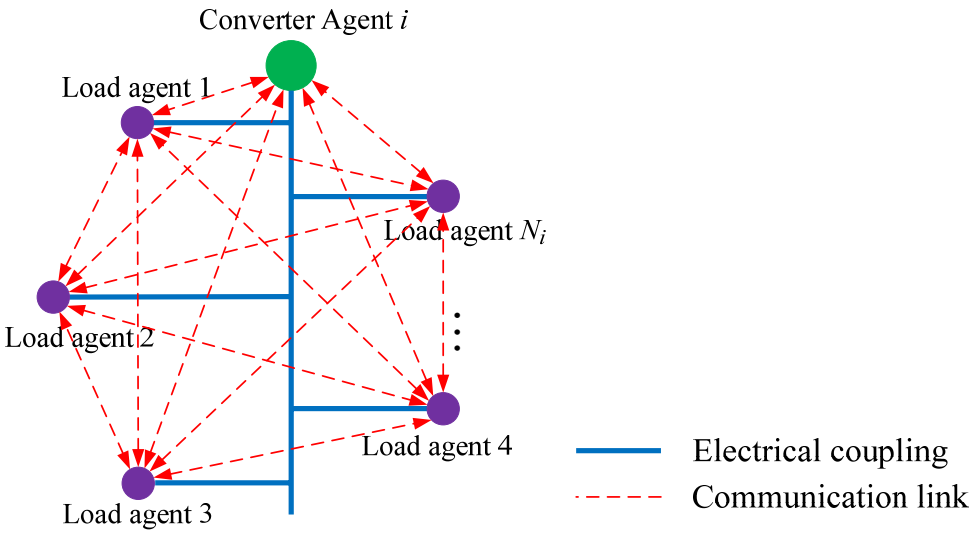

Figure 4.30 Diagram of the *i*th converter agent and load-layer multi-agent system topology for the DC zone system

4.4.3.2 Converter agent model in the converter-layer multi-agent system

A diagram of the DC-DC converter model is shown in Figure 4.31. The DC-DC converter includes a switch, a diode, a capacitor, an inductor, and a lump load. The loads served by the converter can be constant resistive loads, DC motors, or inverter-interfaced AC loads. The output voltage of the converter is controlled by a PI controller, and the continuous control signal is converted into a discrete signal using a pulse-width modulator to control the switch status of the switching device. To simplify the cooperative controller design, a simplified DC-DC converter model was used. In the simplified model, the PI controller and nonlinear parts of the DC-DC converter were neglected. The circuit diagram of the simplified DC-DC converter model used in this work is shown in Figure 4.32. The simplified converter model includes an ideal DC transformer, a capacitor, an inductor, and a lump load representing the loads served by the converter. The models and parameters of DC-DC converter agents are discussed in Appendix A.4.

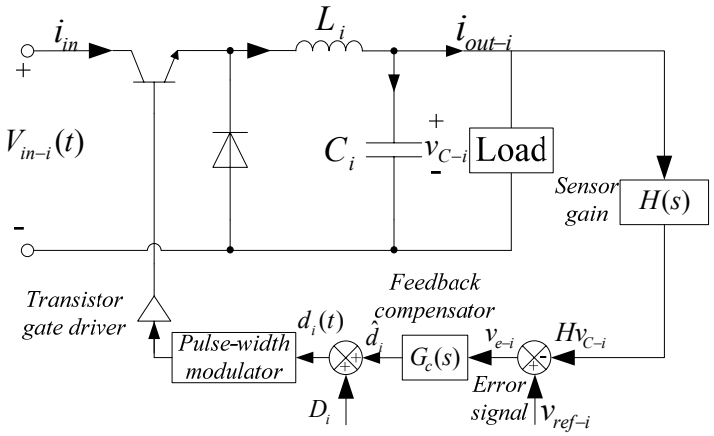

Figure 4.31 Diagram of DC-DC converter model with a voltage regulator

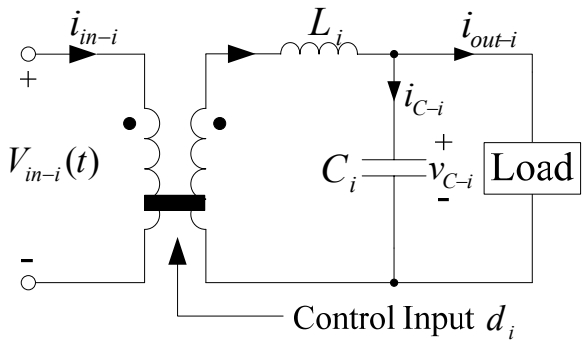

Figure 4.32 Diagram of the simplified DC-DC converter model

The state space equation of the *i*th simplified converter agent model is expressed in (4-26).

$$\begin{cases} \dot{i}_{in-i}(t) = (V_{in-i} \cdot d_i^2 - v_{C-i}(t) \cdot d_i) / L_i \\ \dot{v}_{C-i}(t) = 1/(C_i \cdot d_i) \cdot i_{in-i}(t) - 1/C_i \cdot i_{out-i}(t) \end{cases} \tag{4-26}$$

where, V_{in-i} and $i_{in-i}(t)$ are the input voltage and current of the *i*th converter agent, respectively; $v_{C-i}(t)$ and $i_{out-i}(t)$ are the output voltage and current of the converter agent, respectively; d_i is the duty ratio of the switch of the DC-DC converter; L_i and C_i are the inductor and the capacitor of the converter agent, respectively. V_{in-i} is the input voltage of PCM1, which is equal to the output voltage of PCM4. PCM4 is a rectifier with 1000 V DC output voltage. Therefore, the input voltage of each converter agent is approximately 1000 V DC. To transform the converter agent model into a double integrator system, a coordinate transformation is defined as (4-27).

$$\begin{aligned} x_i(t) &= i_{in-i}(t) \\ y_i(t) &= \left(V_{in-i} \cdot d_i^2 - d_i \cdot v_{C-i}(t)\right) / L_i \end{aligned} \tag{4-27}$$

The simplified converter agent model was transformed into (4-28).

$$\begin{cases} \dot{x}_i(t) = y_i(t) \\ \dot{y}_i(t) = u_{C-i}(t) \end{cases} \tag{4-28}$$

where, $u_{C-i}(t) = -\frac{x_i(t)}{L_i C_i} + \frac{d_i}{L_i C_i} \cdot i_{out-i}(t)$. The parameters L_i and C_i in the agent model are obtained from the DC-DC converter circuit model.

4.4.3.3 Converter-layer multi-agent system model

In a 4-zone system, twenty-four DC-DC converters serve various priority loads. The dynamic model of the converter-layer multi-agent system can be expressed as (4-29).

$$\begin{cases} \dot{\boldsymbol{x}}(t) = \boldsymbol{y}(t) \\ \dot{\boldsymbol{y}}(t) = \boldsymbol{u}_C(t) \end{cases} \tag{4-29}$$

where, $\boldsymbol{x} = [x_1, x_2, \cdots, x_{24}]^T$, $\boldsymbol{y} = [y_1, y_2, \cdots, y_{24}]^T$, and $\boldsymbol{u}_C = [u_{C1}, u_{C2}, \cdots, u_{C24}]^T$. The control variable of the *i*th converter agent u_{Ci}, determined by a cooperative controller, is used to calculate the available current of the *i*th converter agent $i_{out-i}(t)$ by using $i_{out-i}(t) = \left(L_i C_i \cdot u_{Ci}(t) + x_i(t)\right) / d_i$. Based on the definition in (4-27), the state variable x_i is the input current to the *i*th DC-DC converter. The input power to the converter is shown in (4-30).

$$P_{in-i}(t) = x_i(t) \cdot V_{in-i} \tag{4-30}$$

where, V_{in-i} is the input voltage to the *i*th DC-DC converter.

4.4.3.4 Objective of the converter-layer multi-agent system

The objective of the converter-layer multi-agent system is to maximize the number of loads served in the 4-zone system while satisfying the available power capacity constraints and PCM4 capacity constraints. The power losses of the cables in the DC zone system are neglected in the multi-agent system design. The objective of the converter-layer multi-agent system is expressed in (4-31). $\sum_{i=1}^{3} V_{in-i} x_i(t)$, $\sum_{i=4}^{6} V_{in-i} x_i(t)$, $\sum_{i=7}^{9} V_{in-i} x_i(t)$, $\sum_{i=10}^{12} V_{in-i} x_i(t)$, $\sum_{i=13}^{15} V_{in-i} x_i(t)$, $\sum_{i=16}^{18} V_{in-i} x_i(t)$, $\sum_{i=19}^{21} V_{in-i} x_i(t)$, and $\sum_{i=22}^{24} V_{in-i} x_i(t)$ represent the input power to PCM1-1 to PCM1-8, respectively. $\sum_{i=1}^{24} V_{in-i} x_i(t)$ represents the total power demand in the DC zone multi-agent system.

$$
\begin{aligned}
\max \quad & \sum_{i=1}^{24} V_{in-i} x_i(t) \\
\text{s.t.} \quad & \sum_{i=1}^{24} V_{in-i} x_i(t) \le P_{Total} \\
& \sum_{i=1}^{3} V_{in-i} x_i(t) + \sum_{i=7}^{9} V_{in-i} x_i(t) \le P_{\text{PCM4-1}}^{\text{Capacity}} \\
& \sum_{i=4}^{6} V_{in-i} x_i(t) + \sum_{i=10}^{12} V_{in-i} x_i(t) \le P_{\text{PCM4-2}}^{\text{Capacity}} \\
& \sum_{i=13}^{15} V_{in-i} x_i(t) + \sum_{i=19}^{21} V_{in-i} x_i(t) \le P_{\text{PCM4-3}}^{\text{Capacity}} \\
& \sum_{i=16}^{18} V_{in-i} x_i(t) + \sum_{i=22}^{24} V_{in-i} x_i(t) \le P_{\text{PCM4-4}}^{\text{Capacity}} \\
& \dot{\hat{x}}_i(t) = \hat{y}_i(t) \\
& \dot{\hat{y}}_i(t) = -\hat{x}_i(t)/(L_i C_i) + d_i/(L_i C_i) \cdot \hat{i}_{out-i}(t) \\
& \hat{i}_{out-i}(t) = \sum_{l=1}^{N_i} z_l(\Delta t_i);\ x_i(t) = \hat{x}_i(t)
\end{aligned}
\tag{4-31}
$$

where, P_{Total} is the available power to the 4-zone all-electric ship power system, which is determined by the AC-DC communication agent; $P_{\text{PCM4-1}}^{\text{Capacity}}$, $P_{\text{PCM4-2}}^{\text{Capacity}}$, $P_{\text{PCM4-3}}^{\text{Capacity}}$, and $P_{\text{PCM4-4}}^{\text{Capacity}}$ are power capacities of PCM4-1, PCM4-2, PCM4-3, and PCM4-4, respectively;

z_l is the input current of load agent *l* in the *i*th load-layer multi-agent system; N_i is the number of load agents in the *i*th load-layer multi-agent system; and $\hat{x}_i$, $\hat{y}_i$, and $\hat{i}_{out-i}$ are estimated values of the *i*th converter agent. The differential algebraic equations (DAEs) of the converter agent in (4-31) are used to estimate the input current of each converter agent. The dynamic system of converter agent is a second order system, and the output current of the converter $\hat{i}_{out-i}$ is calculated using input current of load agent z_l.

4.4.3.5 Artificial potential function of the converter-layer multi-agent system

In a multi-agent system, an artificial potential function is used to integrate the objective and constraints of a multi-agent system, which corresponds to an attractor term and repulsor term [73], [90]. The attractor term increases monotonically with the increase of the mismatch between the system state and desired state, which drives the system to the desired state. On the other hand, the repulsor term decreases when the system state leaves constraint regions. The artificial potential function reaches its minimum point when the system state reaches the desired state.

The artificial potential function, $E_C(t)$, of the converter-layer multi-agent system is designed based on the objective and constraints of the converter-layer multi-agent system as shown in (4-32).

$$E_C(t) = E_A(t) + E_{\text{PCM4-1}}(t) + E_{\text{PCM4-2}}(t) + E_{\text{PCM4-3}}(t) + E_{\text{PCM4-4}}(t) \tag{4-32}$$

The artificial potential function includes attractor term, $E_A(t)$, which drives the system state to the desired state and repulsor term, $E_{\text{PCM4-1}}(t) + E_{\text{PCM4-2}}(t) + E_{\text{PCM4-3}}(t) + E_{\text{PCM4-4}}(t)$, which repulses the system state from constraint regions. The attractor term,

$E_A(t)$, is expressed as (4-33). $E_A(t)$ ensures that the converter-layer multi-agent system maximizes the number of loads served in the DC zone system while satisfying the available power capacity constraint. If the total load demand in the DC zone system exceeds the available power, the exponential term increases monotonically to reduce the load demand by using a cooperative controller; if the total load demand in the DC zone system is less than the available power, the first term, $-C_1 \cdot \sum_{i=1}^{24} V_{in-i} x_i(t)$, makes $E_A(t)$ increase to increase the load demand in the DC zone system by using a cooperative controller.

$$E_A(t) = -C_1 \cdot \sum_{i=1}^{24} V_{in-i} x_i(t) + (C_1/C_2) \cdot \exp\left(C_2 \left(\sum_{i=1}^{24} V_{in-i} x_i(t) - P_{Total}\right)\right) \quad (4\text{-}33)$$

where, C_1 and C_2 are two positive constants; V_{in-i} and $x_i(t)$ are the input voltage and current to the *i*th DC-DC converter, respectively; and P_{Total} is the available power to the 4-zone all-electric ship power system. $E_{\mathrm{PCM4-1}}(t)$, $E_{\mathrm{PCM4-2}}(t)$, $E_{\mathrm{PCM4-3}}(t)$, and $E_{\mathrm{PCM4-4}}(t)$ are expressed in (4-34). $E_{\mathrm{PCM4-1}}(t)$, $E_{\mathrm{PCM4-2}}(t)$, $E_{\mathrm{PCM4-3}}(t)$, and $E_{\mathrm{PCM4-4}}(t)$ ensure that the PCM4 power capacity constraints are satisfied. If the power input of a PCM4 is no larger than its power capacity, the energy function is equal to 0; otherwise, the energy function has a positive value to drive the power input less than the power capacity using a cooperative controller.

$$
\begin{aligned}
E_{\text{PCM4–1}}(t) &= \begin{cases} 0 & \text{if } \sum_{j=1}^{3} V_{in-j} x_j(t) + \sum_{j=7}^{9} V_{in-j} x_j(t) \le P_{\text{PCM4–1}}^{\text{Capacity}} \\ K_1 \cdot \left(\sum_{j=1}^{3} V_{in-j} x_j(t) + \sum_{j=7}^{9} V_{in-j} x_j(t) - P_{\text{PCM4–1}}^{\text{Capacity}} \right)^2 & \text{else} \end{cases} \\
E_{\text{PCM4–2}}(t) &= \begin{cases} 0 & \text{if } \sum_{j=4}^{6} V_{in-j} x_j(t) + \sum_{j=10}^{12} V_{in-j} x_j(t) \le P_{\text{PCM4–2}}^{\text{Capacity}} \\ K_2 \cdot \left(\sum_{j=4}^{6} V_{in-j} x_j(t) + \sum_{j=10}^{12} V_{in-j} x_j(t) - P_{\text{PCM4–2}}^{\text{Capacity}} \right)^2 & \text{else} \end{cases} \\
E_{\text{PCM4–3}}(t) &= \begin{cases} 0 & \text{if } \sum_{j=13}^{15} V_{in-j} x_j(t) + \sum_{j=19}^{21} V_{in-j} x_j(t) \le P_{\text{PCM4–3}}^{\text{Capacity}} \\ K_3 \cdot \left(\sum_{j=13}^{15} V_{in-j} x_j(t) + \sum_{j=19}^{21} V_{in-j} x_j(t) - P_{\text{PCM4–3}}^{\text{Capacity}} \right)^2 & \text{else} \end{cases} \\
E_{\text{PCM4–4}}(t) &= \begin{cases} 0 & \text{if } \sum_{j=16}^{18} V_{in-j} x_j(t) + \sum_{i=22}^{24} V_{in-j} x_j(t) \le P_{\text{PCM4–4}}^{\text{Capacity}} \\ K_4 \cdot \left(\sum_{j=16}^{18} V_{in-j} x_j(t) + \sum_{i=22}^{24} V_{in-j} x_j(t) - P_{\text{PCM4–4}}^{\text{Capacity}} \right)^2 & \text{else} \end{cases}
\end{aligned}
\tag{4-34}
$$

where, K_1, K_2, K_3, and K_4 are positive constants; V_{in-j} and $x_j(t)$ are the input voltage and current to the *j*th DC-DC converter, respectively; and $P_{\text{PCM4–1}}^{\text{Capacity}}$, $P_{\text{PCM4–2}}^{\text{Capacity}}$, $P_{\text{PCM4–3}}^{\text{Capacity}}$, and $P_{\text{PCM4–4}}^{\text{Capacity}}$ are power capacities of PCM4-1, PCM4-2, PCM4-3, and PCM4-4, respectively.

4.4.3.6 Cooperative controller for the converter-layer multi-agent system

In order to achieve the real-time load management objectives, cooperative controllers are developed based on artificial potential functions of converter-layer multi-agent system, E_C, and load-layer multi-agent systems, E_L. In this work, the cooperative controllers are developed based on the flocking algorithm [73]. However, the objective of the DC zone multi-agent system is different from bird flocking. The objective of bird flocking is to achieve consensus and cooperation through communication and distributed control of multiple agents, which ensures that all agents in the group move to the same direction and maintain certain formations; on the other hand, the objective of the DC zone multi-agent system is to achieve consensus and cooperation through

communication and distributed control of multiple load and converter agents. The DC zone multi-agent system dynamically determines the control switch status or set-point of individual loads to achieve dynamic balancing subject to the operational constraints of the system.

The cooperative controller for the converter-layer multi-agent system is shown in (4-35).

$$\boldsymbol{u}_C(t) = -\frac{\partial E_C(t)}{\partial \boldsymbol{x}(t)} - \boldsymbol{L}\boldsymbol{y}(t) - k_1(\boldsymbol{y}(t) - \boldsymbol{y}^{ref}) \tag{4-35}$$

where, k_1 is a positive constant; $\boldsymbol{x}(t)$, $\boldsymbol{y}(t)$, and $\boldsymbol{u}_C(t)$ are vectors as given in (4-29); $\boldsymbol{y}^{ref}$ is a reference signal for vector $\boldsymbol{y}(t)$, which is chosen as 0 because $\boldsymbol{y}(t)$ equals to 0 in steady state; and $\boldsymbol{L}$ is the graph Laplacian, which is determined based on the topology of the converter-layer multi-agent system, as shown in Figure 4.29. The graph of the converter layer multi-agent system uses an all-to-all communication topology.

The graph Laplacian [91] is defined as (4-36).

$$\boldsymbol{L} = \boldsymbol{D} - \boldsymbol{A} \tag{4-36}$$

where, $\boldsymbol{A}$ and $\boldsymbol{D}$ are adjacency and diagonal matrices of the graph, respectively. The adjacency matrix [72], $\boldsymbol{A}$, is defined as (4-37).

$$\boldsymbol{A} = [a_{ij}] \in \boldsymbol{R}^{n \times n} \tag{4-37}$$

where, $a_{ij} = 1$, if $j \in Nb_i$, and $a_{ij} = 0$, otherwise. Nb_i is the set of neighbor agents of agent i, and n is the total agent number in the group. The degree matrix, $\boldsymbol{D}$, of the graph is defined as (4-38).

$$\boldsymbol{D} = \mathrm{diag}\left(\sum_{j \in Nb_1} a_{1j}, \cdots, \sum_{j \in Nb_n} a_{nj} \right) \tag{4-38}$$

The Laplacian matrix $\boldsymbol{L}$ is a *positive semidefinite matrix* and always has a right eigenvector of $\boldsymbol{1}_n = [1, 1, \cdots, 1]^T$ associated with eigenvalue $\lambda_1 = 0$. More details about the Laplacian matrix are given in [72], [91].

For the *i*th DC-DC converter agent, the cooperative controller is expressed as (4-39). This control signal is the *i*th element of the cooperative control vector, $\boldsymbol{u}_C(t)$, as given in (4-35). The partial derivative terms are gradient terms; $-\boldsymbol{L}_{row\_i}\boldsymbol{y}$ is the consensus term; and $-k_1(y_i - y_i^{ref})$ is the navigational feedback term.

$$\begin{aligned} u_{Ci}(\Delta t_i) &= -\frac{\partial E_C(t)}{\partial x_i(t)} - \boldsymbol{L}_{row\_i}\boldsymbol{y}(t) - k_1(y_i(t) - y_i^{ref}) \\ &= -\frac{\partial E_A(t)}{\partial x_i(t)} - \frac{\partial E_{\mathrm{PCM4-1}}(t)}{\partial x_i(t)} - \frac{\partial E_{\mathrm{PCM4-2}}(t)}{\partial x_i(t)} - \frac{\partial E_{\mathrm{PCM4-3}}(t)}{\partial x_i(t)} - \frac{\partial E_{\mathrm{PCM4-4}}(t)}{\partial x_i(t)} - \frac{\partial E_i(t)}{\partial x_i(t)} \\ &\quad - \boldsymbol{L}_{row\_i}\boldsymbol{y}(t) - k_1(y_i(t) - y_i^{ref}) \end{aligned} \tag{4-39}$$

where, y_i^{ref} is the reference signal for the *i*th converter agent model, which is equal to 0; and $\boldsymbol{L}_{row\_i}$ is a row vector, which is the *i*th row of the graph Laplacian.

The partial derivatives of E_A, $E_{\mathrm{PCM4-1}}$, $E_{\mathrm{PCM4-2}}$, $E_{\mathrm{PCM4-3}}$, $E_{\mathrm{PCM4-4}}$, and E_i to x_i are expressed in (4-40). The expressions of partial derivatives are used to implement the cooperative controller for the *i*th DC-DC converter agent.

$$\frac{\partial E_A(t)}{\partial x_i(t)} = -C_1 V_{in-i} + C_1 V_{in-i} \cdot \exp\left(C_2\left(\sum_{i=1}^{24} V_{in-i} x_i(t) - P_{Total}\right)\right)$$

$$\frac{\partial E_{\text{PCM4}-1}(t)}{\partial x_i(t)} = \begin{cases} 0 & \text{if } \sum_{j=1}^{3} V_{in-j} x_j(t) + \sum_{j=7}^{9} V_{in-j} x_j(t) \le P_{\text{PCM4}-1}^{Capacity} \\ 2K_1 V_{in-i} \cdot \left(\sum_{j=1}^{3} V_{in-j} x_j(t) + \sum_{j=7}^{9} V_{in-j} x_j(t) - P_{\text{PCM4}-1}^{Capacity}\right) & \text{else} \end{cases}$$

$i = 1, 2, 3, 7, 8, \text{and } 9$

$$\frac{\partial E_{\text{PCM4}-2}(t)}{\partial x_i(t)} = \begin{cases} 0 & \text{if } \sum_{j=4}^{6} V_{in-j} x_j(t) + \sum_{j=10}^{12} V_{in-j} x_j(t) \le P_{\text{PCM4}-2}^{Capacity} \\ 2K_2 V_{in-i} \cdot \left(\sum_{j=4}^{6} V_{in-j} x_j(t) + \sum_{j=10}^{12} V_{in-j} x_j(t) - P_{\text{PCM4}-2}^{Capacity}\right) & \text{else} \end{cases}$$

$i = 4, 5, 6, 10, 11, \text{and } 12$

$$\frac{\partial E_{\text{PCM4}-3}(t)}{\partial x_i(t)} = \begin{cases} 0 & \text{if } \sum_{j=13}^{15} V_{in-j} x_j(t) + \sum_{j=19}^{21} V_{in-j} x_j(t) \le P_{\text{PCM4}-3}^{Capacity} \\ 2K_3 V_{in-i} \cdot \left(\sum_{j=13}^{15} V_{in-j} x_j(t) + \sum_{j=19}^{21} V_{in-j} x_j(t) - P_{\text{PCM4}-3}^{Capacity}\right) & \text{else} \end{cases}$$

$i = 13, 14, 15, 19, 20, \text{and } 21$

$$\frac{\partial E_{\text{PCM4}-4}(t)}{\partial x_i(t)} = \begin{cases} 0 & \text{if } \sum_{j=16}^{18} V_{in-j} x_j(t) + \sum_{j=22}^{24} V_{in-j} x_j(t) \le P_{\text{PCM4}-4}^{Capacity} \\ 2K_4 V_{in-i} \cdot \left(\sum_{j=16}^{18} V_{in-j} x_j(t) + \sum_{j=22}^{24} V_{in-j} x_j(t) - P_{\text{PCM4}-4}^{Capacity}\right) & \text{else} \end{cases}$$

$i = 16, 17, 18, 22, 23, \text{and } 24$

$$\frac{\partial E_i(t)}{\partial x_i(t)} = \begin{cases} 2\lambda_i V_{in-i} \cdot \left(V_{in-i} x_i(t) - P_i^{\max}\right)^2 & \text{if } V_{in-i} x_i(t) > P_i^{\max} \\ 0 & \text{else} \end{cases}$$

(4-40)

Since the cooperative controller was designed based on the double integrator system, the signal was transformed into the original control signal to control the original converter agent model. Using (4-39), the cooperative controller for the original converter agent model is given in (4-41).

$$i_{out-i}(\Delta t_i) = \left(L_i C_i \cdot u_{Ci}(\Delta t_i) + x_i((\Delta t_i))\right)/d_i \tag{4-41}$$

where, L_i and C_i are the inductor and capacitor of the converter agent model, d_i is the duty ratio of the converter, and i_{out-i} is the available current of the *i*th DC-DC converter agent.

4.4.3.7 Load agent model in the load-layer multi-agent system

DC zones include three different kinds of loads: constant impedance loads, DC motor loads, and AC motor loads. DC zones include two types of loads – variable-type loads and fixed-type loads [6]. For the variable-type loads, the loads can be served from 0 to their maximum power rating. The variable-type loads represent a lump load in a panel consisting of groups of loads, which can be on and off independently. For the fixed-type loads, the loads can be either served at their maximum power rating or cannot be served at all. In the DC zone multi-agent system, all of the constant loads are modeled as variable-type loads; and all of the DC and AC motors are modeled as fixed-type loads.

In the cooperative controller for a load layer multi-agent system, the constant impedance loads are modeled using a second-order dynamic system, as shown in Figure 4.33. The constant impedance AC loads are served by PCM2, which is an inverter connecting to the 800 V DC voltage level. Thus, the constant impedance AC loads are modeled using the same dynamic model, as shown in Figure 4.33. The state space equation of the constant load *j* is expressed as (4-42).

$$\begin{cases} \dot{i}_{L_{1j}}(t) = 1/L_{L_{1j}} \cdot \left(v_{inL_{1j}} - v_{cL_{1j}}(t) \right) \\ \dot{v}_{cL_{1j}}(t) = i_{L_{1j}}(t)/C_{L_{1j}} - v_{cL_{1j}}(t)/C_{L_{1j}} \cdot \hat{u}_{L_{1j}}(\Delta t_i) \end{cases} \tag{4-42}$$

where, $v_{inL_{1j}}$ and $i_{L_{1j}}(t)$ are the input voltage and current of the *j*th constant load agent; $C_{L_{1j}}$ and $L_{L_{1j}}$ are the equivalent capacitor and inductor of the load agent; $\hat{u}_{L_{1j}}(\Delta t_i)$ is the control variable of the load agent, which is equal to $1/R_{L_{1j}}$. $\hat{u}_{L_{1j}}(\Delta t_i)$ is determined by a cooperative controller in the load-layer multi-agent system.

The control variable of the constant impedance load agent is defined as $\hat{u}_{L_{1j}}(\Delta t_i) = 1/R_{L_{1j}}(\Delta t_i)$; where, $R_{L_{1j}}(\Delta t_i)$ is the equivalent resistor of the constant load *j*. Since the constant impedance load is a variable-type load consisting a group of loads, the control variable of this load agent should be quantized based on the current ratings of these loads. In this dissertation, it is assumed that each constant load consists a group of identical loads which have 10 amperes of current rating.

The constant load agent model is a second-order nonlinear system, which was converted into a double integrator system using feedback linearization [92]. The constant load agent *j* is shown as (4-43).

$$\begin{cases} \dot{z}_{1j}(t) = q_{1j}(t) \\ \dot{q}_{1j}(t) = u_{L_{1j}}(t) \end{cases} \qquad j = 1, 2, \cdots, M_{i1} \tag{4-43}$$

where, $u_{L_{1j}}(t) = -z_{1j}(t)/(L_{L_{1j}}C_{L_{1j}}) + \left(v_{inL_{1j}} - L_{L_{1j}} \cdot q_{1j}(t)\right)/(L_{L_{1j}}C_{L_{1j}}) \cdot \hat{u}_{L_{1j}}(\Delta t_i)$, $q_{1j}(t) = 1/L_{L_{1j}} \cdot (v_{inL_{1j}} - v_{cL_{1j}}(t))$, $z_{1j}(t) = i_{1j}(t)$, and M_{i1} is the total number of constant load agents in the *i*th load-layer multi-agent system. Since $v_{inL_{1j}}$ is the input voltage of the constant load, which is well controlled by the PI controller in the DC-DC converter, it is assumed that

$v_{inL_{1j}}$ is constant in the load agent model. The models and parameters of constant load agents are discussed in Appendix A.5.

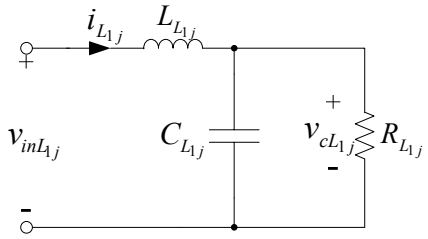

Figure 4.33 Diagram of a constant load agent model in DC zones

The diagrams of the DC motor and AC motor models are shown in Figure 4.34 and Figure 4.35, respectively. AC motors and DC motors are driven by machine drive systems, which regulate the power demands of dynamic loads. The dynamic load [46] is modeled using (4-44). The second order linear system is used to model the dynamic behavior of motor loads.

$$P_d(s) = \frac{K_d}{T_2 s^2 + T_1 s + 1} P_{\text{set-point}}(s) \tag{4-44}$$

where, K_d, T_1, and T_2 are the coefficients of the dynamic load model; $P_{\text{set-point}}$ is the power demand set-point of the dynamic load; and P_d is the actual power demand of the dynamic load.

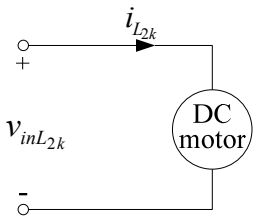

Figure 4.34 Diagram of a DC motor model used in the DC zone multi-agent system

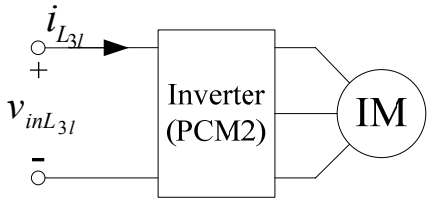

Figure 4.35 Diagram of an AC motor model used in the DC zone multi-agent system

The state space equation of the DC motor load agent model is expressed in (4-45).

$$\begin{cases} \dot{z}_{2k}(t) = q_{2k}(t) \\ \dot{q}_{2k}(t) = u_{L_{2k}}(t) \end{cases} \qquad k = 1, 2, \cdots, M_{i2} \tag{4-45}$$

where, $z_{2k}(t) = P_{d_{2k}}(t) \big/ v_{inL_{2k}}$, $v_{inL_{2k}}$ is the input voltage of the DC motor load agent, $u_{L_{2k}}(t) = -(1/T_{2_{2k}})z_{2k}(t) - (T_{1_{2k}}/T_{2_{2k}})q_{2k}(t) + (K_{d_{2k}}/T_{2_{2k}})\hat{u}_{2k}(\Delta t_i)$, $\hat{u}_{2k}(\Delta t_i) = P_{\text{set-point}_{2k}}(\Delta t_i) \big/ v_{inL_{2k}}$, and M_{i2} is the total number of DC motor load agents in the *i*th load-layer multi-agent system. The models and parameters of DC motor agents are discussed in Appendix A.6.

The state space equation of the AC motor load agent model is expressed in (4-46).

$$\begin{cases} \dot{z}_{3l}(t) = q_{3l}(t) \\ \dot{q}_{3l}(t) = u_{L_{3l}}(t) \end{cases} \qquad l = 1, 2, \cdots, M_{i3} \tag{4-46}$$

where, $z_{3l}(t) = P_{d_{3l}}(t) \big/ v_{inL_{3l}}$, $v_{inL_{3l}}$ is the input voltage of the AC motor load agent, $u_{L_{3l}}(t) = -(1/T_{2_{3l}})z_{3l}(t) - (T_{1_{3l}}/T_{2_{3l}})q_{3l}(t) + (K_{d_{3l}}/T_{2_{3l}})\hat{u}_{3l}(\Delta t_i)$, $\hat{u}_{3l}(\Delta t_i) = P_{\text{set-point}_{3l}}(\Delta t_i) \big/ v_{inL_{3l}}$,

and M_{i3} is the total number of AC motor load agents in the load-layer multi-agent system. The models and parameters of DC motor agents are discussed in Appendix A.7.

Since all of the motors are fixed-type loads which can be either served at the maximum power rating or cannot be served at all, the power set-point of each motor is either full rated power or 0, which means that the set-point of the motor agent can only be chosen as its power rating or 0. Genetic algorithms [93], [94] were used to identify the unknown parameters of agent models based on the data from the all-electric ship power system. The parameters of DC-DC converter agent models and load agent models are shown in Appendix A.4, Appendix A.6, and Appendix A.7.

Table 4.2 Load definitions in a typical DC zone with sample loads

Component name	Priority	Rating (kW)	Voltage (V)	Switch Board	Load type
constant load 1	semi-vital	115.4	375	port	variable
constant load 2	non-vital	72	375	port	variable
DC motor 1	non-vital	36	375	port	fixed
constant load 3	vital	151.4	375	starboard	variable
constant load 4	semi-vital	70	375	starboard	variable
DC motor 2	semi-vital	115.4	375	starboard	fixed
DC motor 3	semi-vital	115.4	650	port	fixed
DC motor 4	non-vital	36	650	port	fixed
constant load 5	semi-vital	115.4	650	port	variable
DC motor 5	semi-vital	115.4	650	starboard	fixed
DC motor 6	semi-vital	47.6	650	starboard	fixed
constant load 6	semi-vital	22	650	starboard	variable
constant load 7	non-vital	199	650	starboard	variable
AC motor 1	vital	181	450	port	fixed
constant load 8	vital	42.6	450	port	variable
AC motor 2	semi-vital	79.4	450	port	fixed
constant load 9	semi-vital	40	450	port	variable
constant load 10	non-vital	85	450	port	variable
constant load 11	semi-vital	119.6	450	starboard	variable
constant load 12	non-vital	177	450	starboard	variable
AC motor 3	non-vital	192.6	450	starboard	fixed
AC motor 4	non-vital	115.4	450	starboard	fixed

The load definitions of a typical DC zone with sample loads are shown in Table 4.2. Each DC zone includes various priority loads with different ratings and voltage levels. Only 800 V DC-DC converters serve AC loads. Some loads are served by port side DC distribution bus, and other loads are served by starboard DC distribution bus. The diagram of a typical DC zone with sample loads is shown in Figure 4.36.

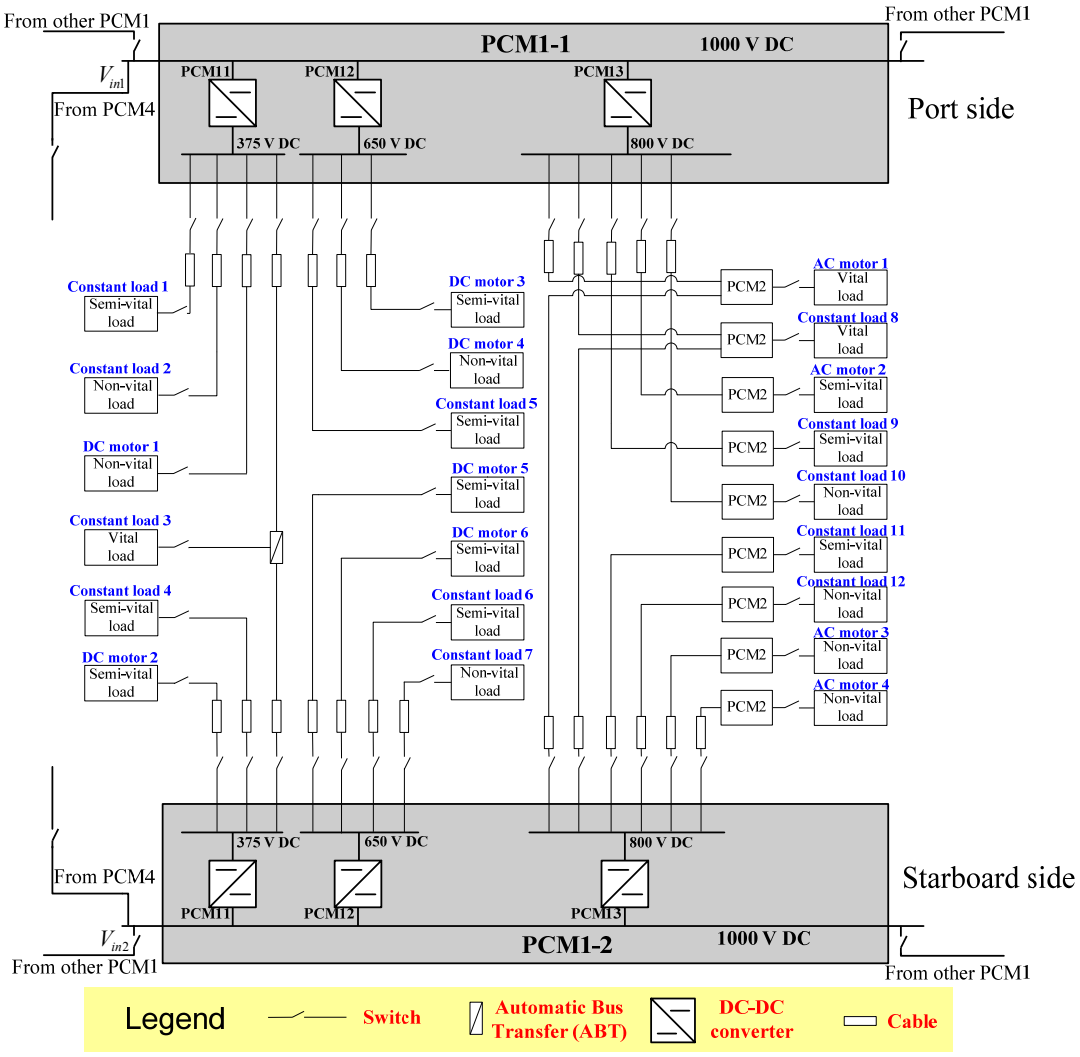

Figure 4.36 Diagram of a typical DC zone with sample loads

4.4.3.8 Load-layer multi-agent system model

The dynamic model for the *i*th load-layer multi-agent system is expressed in (4-47).

$$\begin{cases} \dot{\boldsymbol{z}}(t) = \boldsymbol{q}(t) \\ \dot{\boldsymbol{q}}(t) = \boldsymbol{u}_{\boldsymbol{L}}(t) \end{cases} \tag{4-47}$$

where, $\boldsymbol{z} = [z_{11}, z_{12}, \cdots, z_{1M_{i1}}, z_{21}, z_{22}, \cdots, z_{2M_{i2}}, z_{31}, z_{32}, \cdots, z_{3M_{i3}}]^T$; $\boldsymbol{q} = [q_{11}, q_{12}, \cdots, q_{1M_{i1}}, q_{21}, q_{22}, \cdots, q_{2M_{i2}}, q_{31}, q_{32}, \cdots, q_{3M_{i3}}]^T$; $\boldsymbol{u}_L = [u_{L_{11}}, u_{L_{12}}, \cdots, u_{L_{1M_{i1}}}, u_{L_{21}}, u_{L_{22}}, \cdots, u_{L_{2M_{i2}}}, u_{L_{31}}, u_{L_{32}}, \cdots, u_{L_{3M_{i3}}}]^T$; M_{i1} , M_{i2}, and M_{i3} are the total number of constant loads, DC motor loads, and AC motor loads in the *i*th load-layer multi-agent system, respectively; and the total number of agents in the *i*th load-layer multi-agent system is defined as N_i, which is equal to $M_{i1} + M_{i2} + M_{i3}$.

4.4.3.9 Objective of the load-layer multi-agent system

The objective of the load-layer multi-agent system is to maximize the loads served by the *i*th DC-DC converter considering the load priorities while satisfying available power capacity constraints and motor input voltage constraints. The objective of the *i*th load-layer multi-agent system is expressed as (4-48). The dynamic equations are used to estimate the input currents of constant loads, DC motor loads and AC motor loads in the load layer multi-agent system.

$$
\begin{aligned}
\min \quad & -[\textstyle\sum_{j=1}^{M_{i1}}(z_{1j}(t)\cdot W_{1j}\cdot s_{1j}(\Delta t_i))+\sum_{k=1}^{M_{i2}}(z_{2k}(t)\cdot W_{2k}\cdot s_{2k}(\Delta t_i))+\sum_{l=1}^{M_{i3}}(z_{3l}(t)\cdot W_{3l}\cdot s_{3l}(\Delta t_i))] \\
\text{s.t.} \quad & \textstyle\sum_{j=1}^{M_{i1}}(z_{1j}(t)\cdot s_{1j}(\Delta t_i))+\sum_{k=1}^{M_{i2}}(z_{2k}(t)\cdot s_{2k}(\Delta t_i))+\sum_{l=1}^{M_{i3}}(z_{3l}(t)\cdot s_{3l}(\Delta t_i))=i_{out-i}(\Delta t_i) \\
& V_{2k}^{\min}\le V_{2k}(t) \quad k=1,2,\cdots,M_{i2} \\
& V_{3l}^{\min}\le V_{3l}(t) \quad l=1,2,\cdots,M_{i3} \\
& \dot{\hat{z}}_{1j}(t)=\hat{q}_{1j}(t) \\
& \dot{\hat{q}}_{1j}(t)=-\hat{z}_{1j}(t)/(L_{L_{1j}}C_{L_{1j}})+(v_{inL_{1j}}-L_{L_{1j}}\cdot\hat{q}_{1j}(t))/(L_{L_{1j}}C_{L_{1j}})\cdot\hat{u}_{L_{1j}}(\Delta t_i) \\
& \dot{\hat{z}}_{2k}(t)=\hat{q}_{2k}(t) \\
& \dot{\hat{q}}_{2k}(t)=-(1/T_{2_{2k}})\hat{z}_{2k}(t)-(T_{1_{2k}}/T_{2_{2k}})\hat{q}_{2k}(t)+(K_{d_{2k}}/T_{2_{2k}})\hat{u}_{L_{2k}}(\Delta t_i) \\
& \dot{\hat{z}}_{3l}(t)=\hat{q}_{3l}(t) \\
& \dot{\hat{q}}_{3l}(t)=-(1/T_{2_{3l}})\hat{z}_{3l}(t)-(T_{1_{3l}}/T_{2_{3l}})\hat{q}_{3l}(t)+(K_{d_{3l}}/T_{2_{3l}})\hat{u}_{L_{3l}}(\Delta t_i) \\
& z_{1j}(t)=\hat{z}_{1j}(t);\ z_{2k}(t)=\hat{z}_{2k}(t);\ z_{3l}(t)=\hat{z}_{3l}(t) \\
& j=1,\cdots,M_{i1};\ k=1,\cdots,M_{i2};\ l=1,\cdots,M_{i3}
\end{aligned}
\tag{4-48}
$$

where, W_{1j}, W_{2k}, and W_{3l} are the weight factors of constant load agent *j*, DC motor load agent *k*, and AC motor load agent *l* in the *i*th multi-agent system, respectively; $s_{1j}(\Delta t_i)$, $s_{2k}(\Delta t_i)$, and $s_{3l}(\Delta t_i)$ are the switch statuses of constant load agent *j*, DC motor load agent *k*, and AC motor load agent *l* in the *i*th load-layer multi-agent system, respectively; $z_{1j}(t)$, $z_{2k}(t)$, and $z_{3l}(t)$ are the input currents of constant load agent *j*, DC motor load agent *k*, and AC motor load agent *l*, respectively; $V_{2k}(t)$ and $V_{3l}(t)$ are the input bus voltages of DC motor load agent *k* and AC motor load agent *l*; $V_{2k}^{\min}$ and $V_{3l}^{\min}$ are the minimum allowed bus voltages for DC motor load agent *k* and AC motor load agent *l*; $i_{out-i}(\Delta t_i)$ is the available output current of the *i*th converter, which is obtained from the converter-layer cooperative controller, as shown in (4-41); and $\hat{z}_{1j}(t)$, $\hat{q}_{1j}(t)$, $\hat{z}_{2k}(t)$,

$\hat{q}_{2k}(t)$, $\hat{z}_{3l}(t)$, and $\hat{q}_{3l}(t)$ are estimated values of load agents. The DAEs of load agents are used to estimate the input current of each load agent by using the input voltage and switch status or power set-point of each load.

4.4.3.10 Artificial potential function of the load-layer multi-agent system

The artificial potential function of the load-layer multi-agent system is shown as (4-49).

$$E_L(t) = E_{Lattractor}(t) \tag{4-49}$$

The attractor term, as shown in (4-50), is monotonically decreasing with the decrease of the mismatch between the system state and the desired state, which drives the system state to the desired state. The first term of $E_{Lattractor}(t)$ is used to match the load current to the available current of the *i*th load-layer multi-agent system; the second term of $E_{Lattractor}(t)$ is used to maximize the served loads in the *i*th load-layer multi-agent system considering load priorities.

$$\begin{aligned} E_{Lattractor}(t) = K_5 \cdot [\sum_{j=1}^{M_{i1}}(z_{1j}(t)\cdot s_{1j}) + \sum_{k=1}^{M_{i2}}(z_{2k}(t)\cdot s_{2k}) + \sum_{l=1}^{M_{i3}}(z_{3l}(t)\cdot s_{3l}) - i_{out-i}(t)]^2 \\ -[\sum_{j=1}^{M_{i1}}(z_{1j}(t)\cdot W_{1j}\cdot s_{1j}) + \sum_{k=1}^{M_{i2}}(z_{2k}(t)\cdot W_{2k}\cdot s_{2k}) + \sum_{l=1}^{M_{i3}}(z_{3l}(t)\cdot W_{3l}\cdot s_{3l})] \end{aligned} \tag{4-50}$$

where, K_5 is a positive constant, which determines the convergence speed of the cooperative controller; the definitions of other variables are the same as (4-48).

The repulsor term, $E_{Lrepulsor}(t)$, as shown in (4-51), is used to drive the input bus voltage of a motor load larger than its minimum allowed voltage. If the input bus voltage of a motor load is larger than its minimum allowed voltage, the value of $E_{Lrepulsor}(t)$ is 0;

otherwise, the value of $E_{Lrepulsor}(t)$ is a positive value. This replusor term only includes load input voltage variables, but does not include load input current variables.

$$
\begin{aligned}
E_{Lrepulsor}(t) &= \sum_{k=1}^{M_{i2}} E_{Lrepulsor}^{2k}(t) + \sum_{l=1}^{M_{i3}} E_{Lrepulsor}^{3l}(t) \\
E_{Lrepulsor}^{2k}(t) &= \begin{cases} \gamma_{2k} \cdot \left(V_{2k}(t) - V_{2k}^{\min}\right)^2 & \text{if } V_{2k}(t) < V_{2k}^{\min} \\ 0 & \text{otherwise} \end{cases} \\
E_{Lrepulsor}^{3l}(t) &= \begin{cases} \gamma_{3l} \cdot \left(V_{3l}(t) - V_{3l}^{\min}\right)^2 & \text{if } V_{3l}(t) < V_{3l}^{\min} \\ 0 & \text{otherwise} \end{cases}
\end{aligned}
\tag{4-51}
$$

where, γ_{2k} and γ_{3l} are positive constants; $E_{Lrepulsor}^{2k}(t)$ and $E_{Lrepulsor}^{3l}(t)$ are repulsor functions for DC motor *k* and AC motor *l*, respectively.

4.4.3.11 Cooperative controller for the load-layer multi-agent system

One challenge of the real-time load management problem is that the control variables include both continuous and binary variables, which means that this problem is a hybrid control problem. For the variable-type load, the load demand can be regulated from 0 to its maximum power rating at specified value; for the fixed-type load, the control variable is the switch status of the load, which is a binary variable. Since the cooperative controller is developed based on continuous system theory, the binary control variable will introduce errors in the multi-agent system. Thus, the parameters of the cooperative controller were determined carefully to ensure the stability of the cooperative controller.

The cooperative controller for the load-layer multi-agent system was designed based on the artificial potential function (4-49) through (4-51), which is shown as (4-52). This cooperative controller includes a gradient term, a consensus term, and a

navigational feedback term. The gradient term includes the partial derivative of $E_{Lattractor}(t)$ with respect to $\boldsymbol{z}(t)$ and the partial derivative of $E_{Lrepulsor}(t)$ with respect to $\boldsymbol{V}(t)$. This control vector, $\boldsymbol{u}_L(\Delta t_i)$, includes the control signals for constant loads, DC motors, and AC motors, which are shown in (4-55), (4-58), and (4-61), respectively.

$$\boldsymbol{u}_L(\Delta t_i) = -\frac{\partial E_{Lattractor}(t)}{\partial \boldsymbol{z}(t)} + \frac{\partial E_{Lrepulsor}(t)}{\partial \boldsymbol{V}(t)} - \boldsymbol{L}\boldsymbol{q}(t) - k_2(\boldsymbol{q}(t) - \boldsymbol{q}^{ref}) \tag{4-52}$$

where, k_2 is a positive constant; $\boldsymbol{V}$ is the voltage vector for all the load agents, which is equal to $\boldsymbol{V} = [V_{11}, V_{12}, \cdots, V_{1M_{i1}}, V_{21}, V_{22}, \cdots, V_{2M_{i2}}, V_{31}, V_{32}, \cdots, V_{3M_{i3}}]^T$; $\boldsymbol{z}$ is the input current vector for all the load agents, which is equal to $\boldsymbol{z} = [z_{11}, z_{12}, \cdots, z_{1M_{i1}}, z_{21}, z_{22}, \cdots, z_{2M_{i2}}, z_{31}, z_{32}, \cdots, z_{3M_{i3}}]^T$; $\boldsymbol{q}^{ref}$ is the reference signal, which is equal to 0 because $\boldsymbol{q}$ equals to 0 in steady state; $\boldsymbol{L}$ is the graph Laplacian, which is defined as (4-36). The adjacency matrix of the graph Laplacian is defined as (4-53).

$$\boldsymbol{A} = [a_{ij}] \in \boldsymbol{R}^{N_i \times N_i} \tag{4-53}$$

where, $a_{ij} = 1$, if $j \in Nb_k$, and $a_{ij} = 0$, otherwise. Nb_k is the set of neighbor agents of agent *k*, and N_i is the total agent number in the *i*th load-layer multi-agent system. The degree matrix of the graph is defined as (4-54).

$$\boldsymbol{D} = \text{diag}\left(\sum_{j \in Nb_1} a_{1j}, \cdots, \sum_{j \in Nb_{N_i}} a_{nj} \right) \tag{4-54}$$

Since the load-layer multi-agent system is an all-to-all communication network, all of the off-diagonal elements of the Laplacian have a value of -1 and all of the diagonal elements have a value of $N_i - 1$.

For the constant load agent *j*, the cooperative controller can be expressed as (4-55). This controller includes a gradient term, a consensus term, and a navigational feedback term. This expression is used to control constant load *j* in the load layer multi-agent system.

$$u_{L_{1j}}(\Delta t_i) = -\frac{\partial E_{Lattractor}(t)}{\partial z_{1j}(t)} - \boldsymbol{L}_{row\_j}\boldsymbol{q}(t) - k_2(q_{1j}(t) - q_{1j}^{ref}) \quad j = 1, 2, \cdots, M_{i1} \tag{4-55}$$

where, q_{1j}^{ref} is the reference signal for the *j*th constant load agent model, which is equal to 0; and L_{row_j} is the *j*th row of the graph Laplacian. The partial derivatives of $E_{Lattractor}(t)$ to $z_{1j}(t)$ is expressed as (4-56).

$$\begin{aligned}\frac{\partial E_{Lattractor}(t)}{\partial z_{1j}(t)} = 2K_5 \cdot (&\sum_{j=1}^{M_{i1}}\left(z_{1j}(t)\cdot s_{1j}(\Delta t_i)\right) + \sum_{k=1}^{M_{i2}}\left(z_{2k}(t)\cdot s_{2k}(\Delta t_i)\right) \\ &+ \sum_{l=1}^{M_{i3}}\left(z_{3l}(t)\cdot s_{3l}(\Delta t_i)\right) - i_{out-i}(t)) - W_{1j}\end{aligned} \tag{4-56}$$

Since the cooperative controller was designed based on the double integrator system, the signal should be transformed into the control signal to control the constant load agent model. Using (4-55), the cooperative controller for the constant load agent model is shown in (4-57).

$$\hat{u}_{L_{1j}}(\Delta t_i) = (L_{L_{1j}} C_{L_{1j}} \cdot u_{L_{1j}}(\Delta t_i) + z_{1j}(\Delta t_i))/(v_{inL_{1j}} - L_{L_{1j}} \cdot q_{1j}(\Delta t_i)) \quad j = 1, 2, \cdots, M_{i1} \tag{4-57}$$

where, $L_{L_{1j}}$ and $C_{L_{1j}}$ are the inductor and capacitor of the *j*th constant load agent model, and $v_{inL_{1j}}$ is the input voltage of the *j*th constant load agent model.

For the DC motor load agent *k*, the cooperative controller can be expressed as (4-58). This controller includes gradient term, consensus term, and navigational feedback term. This expression is used to control DC motors in the load layer multi-agent system.

$$u_{L_{2k}}(\Delta t_i) = -\frac{\partial E_{Lattractor}(t)}{\partial z_{2k}(t)} + \frac{\partial E_{Lrepulsor}(t)}{\partial V_{2k}(t)} - \boldsymbol{L}_{row\_k+M_{i1}}\boldsymbol{q}(t) - k_2(q_{2k}(t) - q_{2k}^{ref}) \quad k = 1, 2, \cdots, M_{i2} \tag{4-58}$$

where, q_{2k}^{ref} is the reference signal for the *k*th DC motor load agent model, which is equal to 0; and $\boldsymbol{L}_{row\_k+M_{i1}}$ is the $k+M_{i1}$ row of the graph Laplacian. The partial derivatives of $E_{Lattractor}(t)$ and $E_{Lrepulsor}(t)$ are expressed as (4-59).

$$\frac{\partial E_{Lattractor}(t)}{\partial z_{2k}(t)} = 2K_5 \cdot (\sum_{j=1}^{M_{i1}}\left(z_{1j}(t) \cdot s_{1j}(\Delta t_i)\right) + \sum_{k=1}^{M_{i2}}\left(z_{2k}(t) \cdot s_{2k}(\Delta t_i)\right) + \sum_{l=1}^{M_{i3}}\left(z_{3l}(t) \cdot s_{3l}(\Delta t_i)\right) - i_{out-i}(t)) - W_{2k}$$

$$\frac{\partial E_{Lreplusor}(t)}{\partial V_{2k}(t)} = \begin{cases} 2\gamma_{2k} \cdot \left(V_{2k}(t) - V_{2k}^{\min}\right) & \text{if } V_{2k} < V_{2k}^{\min} \\ 0 & \text{otherwise} \end{cases}$$

(4-59)

Using (4-58), the cooperative controller for the DC motor load agent model is shown in (4-60).

$$\hat{u}_{L_{2k}}(\Delta t_i) = (T_{2_{2k}} u_{L_{2k}}(\Delta t_i) + z_{2k} + T_{1_{2k}} q_{2k}(\Delta t_i)) / K_{d_{2k}} \quad k = 1, 2, \cdots, M_{i2} \tag{4-60}$$

where, $T_{1_{2k}}$, $T_{2_{2k}}$, and $K_{d_{2k}}$ are the coefficients of the *k*th DC motor load agent model.

For the AC motor load agent *l*, the cooperative controller can be expressed as (4-61). This controller includes gradient term, consensus term, and navigational feedback term. This expression is used to control AC motors in the load layer multi-agent system.

$$u_{L_{3l}}(\Delta t_i) = -\frac{\partial E_{Lattractor}(t)}{\partial z_{3l}(t)} + \frac{\partial E_{Lrepulsor}(t)}{\partial V_{3l}(t)} - \boldsymbol{L}_{row\_l+M_{i1}+M_{i2}}\boldsymbol{q}(t) - k_2(q_{3l}(t) - q_{3l}^{ref}) \quad l = 1, 2, \cdots, M_{i3} \tag{4-61}$$

where, q_{3l}^{ref} is the reference signal for the *l*th AC motor load agent model, which is equal to 0; and $\boldsymbol{L}_{row\_l+M_{i1}+M_{i2}}$ is the $l + M_{i1} + M_{i2}$ row of the graph Laplacian. The partial derivatives of $E_{Lattractor}$ and $E_{Lrepulsor}$ are expressed as (4-62).

$$\begin{aligned}
\frac{\partial E_{Lattractor}(t)}{\partial z_{3l}(t)} &= 2K_5 \cdot (\sum_{j=1}^{M_{i1}}\left(z_{1j}(t) \cdot s_{1j}(\Delta t_i)\right) + \sum_{k=1}^{M_{i2}}\left(z_{2k}(t) \cdot s_{2k}(\Delta t_i)\right) + \sum_{l=1}^{M_{i3}}\left(z_{3l}(t) \cdot s_{3l}(\Delta t_i)\right) \\
&\quad - i_{out-i}(t)) - W_{3l} \\
\frac{\partial E_{Lreplusor}(t)}{\partial V_{3l}(t)} &= \begin{cases} 2\gamma_{3l} \cdot \left(V_{3l}(t) - V_{3l}^{\min}\right) & \text{if } V_{3l}(t) < V_{3l}^{\min} \\ 0 & \text{otherwise} \end{cases}
\end{aligned} \tag{4-62}$$

Using (4-61), the cooperative controller for the AC motor load agent model is shown in (4-63).

$$\hat{u}_{L_{3l}}(\Delta t_i) = (T_{2_{3l}} u_{L_{3l}}(\Delta t_i) + z_{3l}(\Delta t_i) + T_{1_{3l}} q_{3l}(\Delta t_i)) / K_{d_{3l}} \quad l = 1, 2, \cdots, M_{i3} \tag{4-63}$$

where, $T_{1_{3l}}$, $T_{2_{3l}}$, and $K_{d_{3l}}$ are the coefficients of the *l*th AC motor load agent model.

Since each motor is a fixed-type load, the motor can either be served at full power or not served at all, which means that switch status is the only control variable for motors. In this dissertation, if $\hat{u}_{L_{2k}}(\Delta t_i)$ (or $\hat{u}_{L_{3l}}(\Delta t_i)$) is greater than 90% of its maximum value $P_{\text{rating}-2k} / v_{inL_{2k}}$ ($P_{\text{rating}-3l} / v_{inL_{3l}}$), the DC motor *k* (or AC motor *l*) is connected and the switch of the DC motor *k*, $s_{2k}(\Delta t_i)$, (or AC motor *l*, $s_{3l}(\Delta t_i)$) is '1'; if $\hat{u}_{L_{2k}}(\Delta t_i)$ (or $\hat{u}_{L_{3l}}(\Delta t_i)$) is less than 10% of its maximum value, the motor is

disconnected and the switch of the DC motor k, $s_{2k}(\Delta t_i)$, (or AC motor l, $s_{3l}(\Delta t_i)$) is '0'. $P_{\text{rating}-2k}$ and $P_{\text{rating}-3l}$ are power ratings of DC motor k and AC motor l, respectively.

4.4.4 Coordination of MVAC and DC zone multi-agent systems

The AC-DC communication agent was developed to coordinate the MVAC and DC zone multi-agent systems. This agent calculates the power available to the DC zone multi-agent system, and provides the DC zone load demand information at each time step to the system losses agent, which connects the MVAC and DC zone multi-agent systems to achieve real-time load management for the all-electric ship power system. Generator agents, propulsion load agents, pulse load agents, a system losses agent, and communication agents in DC zones communicate with the AC-DC communication agent to calculate the power available to the DC zone multi-agent system, as shown in Figure 4.37.

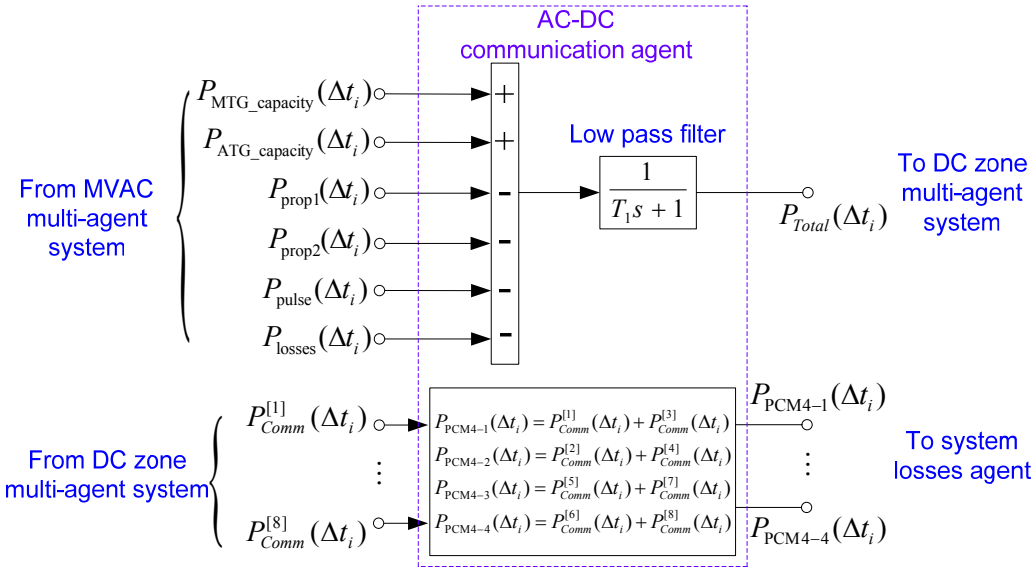

Figure 4.37 Block diagram of AC-DC communication agent which coordinates the MVAC and DC zone multi-agent systems

A low pass filter was designed to filter noise of the available power signal $P_{Total}(\Delta t_i)$ of the DC zone system. The time constant, T_1, of the filter is a positive constant with a value of 0.1. The AC-DC communication agent also obtains the input power to each PCM4, $P_{\text{PCM4–1}}(\Delta t_i)$, $P_{\text{PCM4–2}}(\Delta t_i)$, $P_{\text{PCM4–3}}(\Delta t_i)$, $P_{\text{PCM4–4}}(\Delta t_i)$, based on the DC zone system topology and data from the communication agents in the DC zone multi-agent system, which is shown in (4-64). The input power of each PCM4 is calculated using the following equation.

$$\begin{aligned} P_{\text{PCM4–1}}(\Delta t_i) &= P_{Comm}^{[1]}(\Delta t_i) + P_{Comm}^{[3]}(\Delta t_i) \\ P_{\text{PCM4–2}}(\Delta t_i) &= P_{Comm}^{[2]}(\Delta t_i) + P_{Comm}^{[4]}(\Delta t_i) \\ P_{\text{PCM4–3}}(\Delta t_i) &= P_{Comm}^{[5]}(\Delta t_i) + P_{Comm}^{[7]}(\Delta t_i) \\ P_{\text{PCM4–4}}(\Delta t_i) &= P_{Comm}^{[6]}(\Delta t_i) + P_{Comm}^{[8]}(\Delta t_i) \end{aligned} \tag{4-64}$$

where, $P_{Comm}^{[1]}(\Delta t_i)$ to $P_{Comm}^{[8]}(\Delta t_i)$ are the input power of PCM1-1 to PCM1-8, respectively. The AC-DC communication agent provides the load demand information of the DC zone system to the system losses agent to calculate system losses in the MVAC system as described in section 4.4.2.5.

The communication time step between the AC-DC communication agent and other agents was chosen as 10 milliseconds. The decision time step of the AC-DC communication agent was chosen as 10 milliseconds.

4.5 Summary

In this chapter, the bio-inspired multi-agent system concept and its applications in power system areas were discussed. Since a multi-agent system aims to cooperatively

achieve group objectives that are difficult to reach by a single agent or centralized controller, this technique has potential to solve complex problems in many engineering areas. To apply the load management multi-agent system technique to all-electric ship power systems, three different partitioning strategies for the DC zone system of the all-electric ship power system were studied to compare the advantages and disadvantages of each strategy. Partitioning Strategy III was chosen to use in the design of the multi-agent system cooperative controller for the DC zone system. This strategy partitioned the system based on the individual electrical components in the DC zone system with different types of dynamic models which, therefore, is a heterogeneous multi-agent system.

Since the all-electric ship power system consists of a MVAC system and a DC zone system, a separate MVAC and DC zone multi-agent system was developed. An AC-DC communication agent was developed to coordinate the two multi-agent systems to achieve real-time load management for the all-electric ship power system. In the MVAC system, generator agents, propulsion load agents, pulse load agents, and a system losses agent were developed to cooperatively coordinate propulsion loads and pulse loads in the MVAC system. In the DC zone system, a 4-zone system was partitioned based on DC-DC converters and individual loads. Communication agents were developed to reduce the complexity of the communication network of the two multi-agent systems. Each DC zone consists of two communication agents, six DC-DC converter agents, and a group of load agents. A converter-layer multi-agent system was developed to coordinate all of the DC-DC converters in the DC zone system and to

provide the available current information to the load-layer multi-agent system served by each DC-DC converter. The cooperative controllers were developed for the DC zone system based on artificial potential functions and reduced-order agent models to achieve the real-time load management objectives.

In the next chapter, the novel heterogeneous multi-agent system and the notional all-electric ship power system implemented in PSCAD software will be discussed. Case studies and performance analysis results will be discussed.

5. PSCAD SIMULATION OF MULTI-AGENT SYSTEM AND SIMULATION RESULTS

5.1 Introduction

This chapter discusses the implementation of the novel heterogeneous multi-agent system framework and a computer model of a notional 2-zone all-electric ship power system in the PSCAD/EMTDC dynamic simulation software. Simulation results of case studies and performance analysis are also discussed. The heterogeneous multi-agent system consists of a MVAC multi-agent system and a DC zone multi-agent system. These two multi-agent systems were designed separately and coordinated using an AC-DC communication agent. Thus, the MVAC and DC zone multi-agent systems were studied separately in case studies. Further the coordination of the two systems was studied to evaluate the dynamic performance of the real-time load management applied to the all-electric ship power system computer model.

In section 5.2, the computer model of a notional 2-zone all-electric ship power system for case studies and performance analysis is introduced. The simulation environment for the multi-agent system and power system model is also discussed. In section 5.3, case studies for the MVAC multi-agent system, DC zone multi-agent system, and coordination of the two multi-agent systems are presented to illustrate the dynamic performance of the new real-time load management technique. In section 5.4, results of performance analysis which evaluate the dynamic performance of the new technique for the MVAC and DC zone multi-agent systems are discussed. In section 5.5,

a summary of case studies and performance analysis is provided. Lastly, a summary is given in section 5.6.

5.2 PSCAD Simulation of All-Electric Ship Power System Computer Model and Simulation Environment

The one-line diagram of a notional 2-zone all-electric ship power system model is shown in Figure 5.1. The MVAC system consists of one MTG, one ATG, one propulsion load with 36.5 MW power rating, one pulse load, and two DC zones. The notional 2-zone all-electric ship power system model was implemented in PSCAD as a test system to validate the methodology and analyze the dynamic performance of the new real-time load management approach. The parameters of the electrical components in the all-electric ship power system are shown in Appendix B.1.

The PSCAD simulation environment of the multi-agent systems and all-electric ship power system model is shown in Figure 5.2. The multi-agent system measures the power demand and input voltage of individual loads from the electrical system and makes decisions to control switch status or power set-point of individual loads in operational real time Δt_i. The simulation time step of the multi-agent system is chosen as Δt_i, and the simulation time step of all-electric ship power system model is chosen as $\Delta\tau$. In this dissertation, the decision time step and measurement time step Δt_i are chosen as 10 milliseconds.

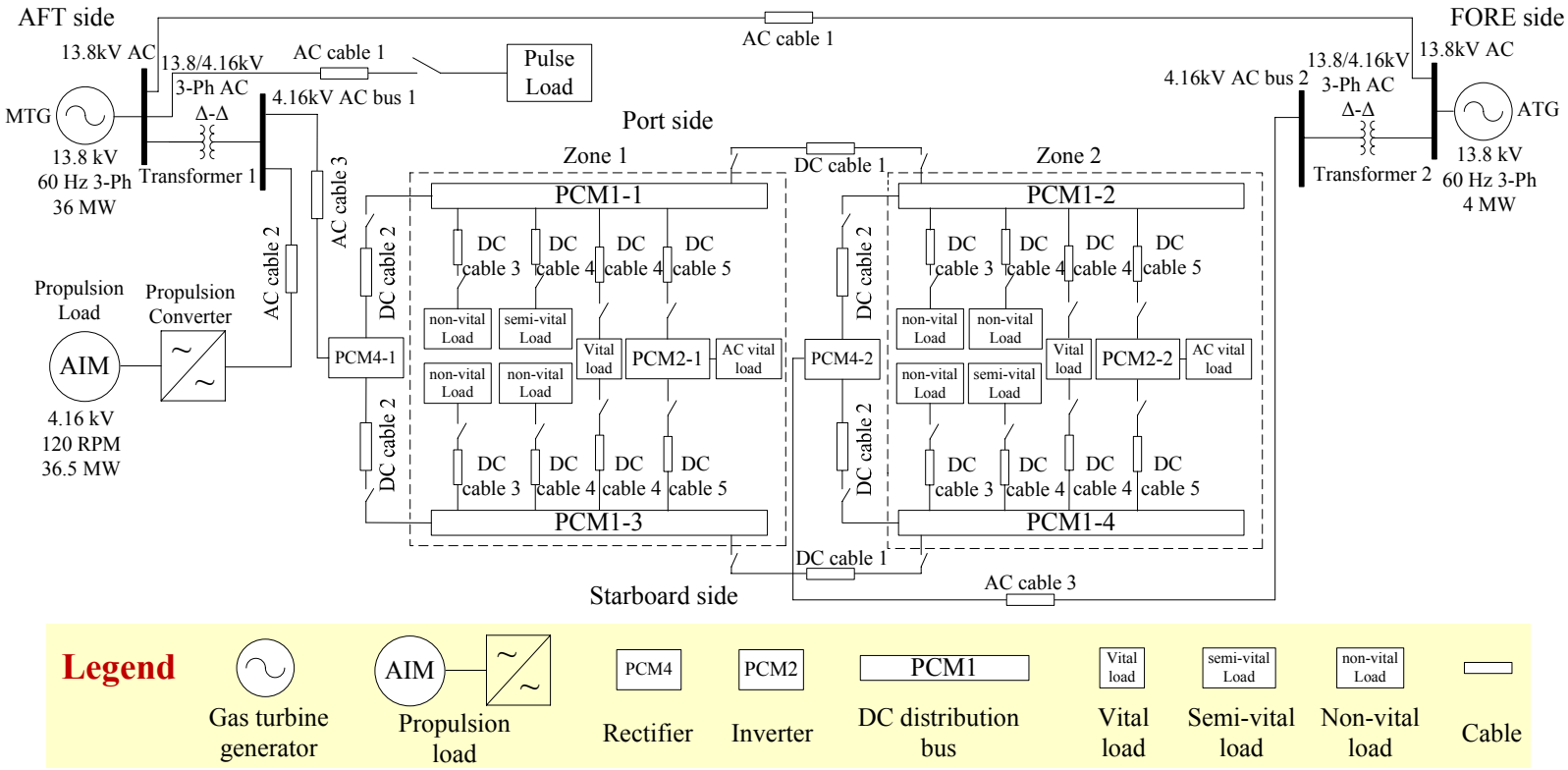

Figure 5.1 One-line diagram of a notional 2-zone all-electric ship power system computer model simulated in PSCAD software for case studies and performance analysis

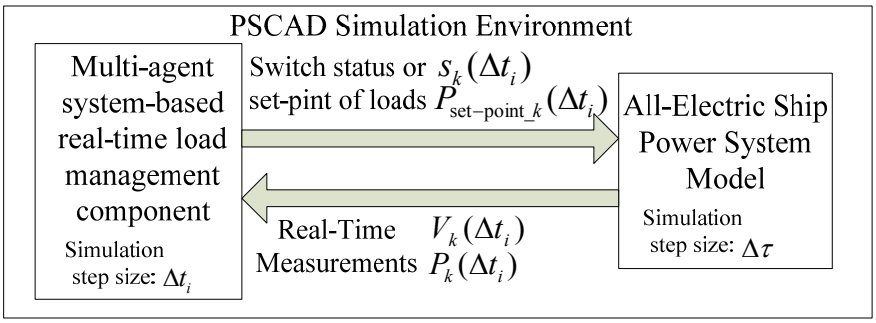

Figure 5.2 PSCAD simulation environment of the multi-agent system and all-electric ship power system model

5.3 Case Studies

In this section, various case studies are presented to illustrate the dynamic performance of the novel multi-agent system framework for real-time load management of all-electric ship power systems. In section 5.3.1, MVAC multi-agent system studies are presented to show the coordination of the propulsion load and pulse load to achieve real-time load management for the MVAC system. Three case studies with different pulse load characteristics are shown to illustrate the effectiveness of the MVAC multi-agent system to mitigate the frequency and voltage oscillations caused by pulse loads. In section 5.3.2, the DC zone multi-agent system studies are presented to show the coordination and cooperation of loads in DC zones to achieve real-time load management for the DC zone system. Two case studies are shown to illustrate the effectiveness of the DC zone multi-agent system. Further the coordination of the two multi-agent systems is discussed in section 5.3.3. A case study is presented to show the effectiveness of the novel multi-agent system framework to solve real-time load management for all-electric ship power systems.

5.3.1 MVAC multi-agent system case studies

In the MVAC multi-agent system studies, the diagram of the simplified notional all-electric ship power system simulation model for MVAC multi-agent system is shown in Figure 5.3, and the simulation step size $\Delta\tau$ was chosen as 40 microseconds in the PSCAD simulation. DC zone details were neglected and the DC zones were represented by constant lump loads. The MTG and ATG generators were in service. The total power generation capacity was 40 MW. It was assumed that the ship operated in cruise mode from 0 to 30 seconds at a cruising speed of 27 knots. The propulsion load demand at this cruising speed was 21 MW. At 30 seconds, the operation mode was switched from cruise mode to battle mode until the end of the simulation.

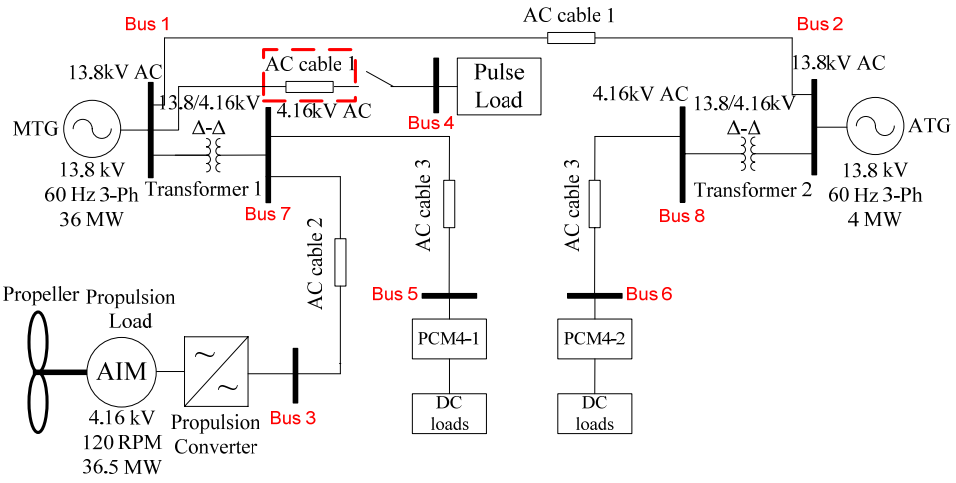

Figure 5.3 Diagram of a simplified notional all-electric ship power system simulation model for MVAC multi-agent system

The operational constraints of the MVAC multi-agent system included the propulsion load voltage constraint, MTG frequency constraint, and dynamic cable

ampacity constraint for the pulse load as discussed in section 4.4.2.1, which are shown in (5-1)-(5-5).

$$\left|\Delta\omega(\Delta t_i)\right| \le 3\% \tag{5-1}$$

$$\left|\Delta V_{\text{prop}}(\Delta t_i)\right| \le 5\% \tag{5-2}$$

$$\int_{t-T}^{t} 0.5\cdot\left[1+\text{sgn}\left(\left|\Delta\omega(\Delta t_i)\right|-3\%\right)\right]dt \le 2\text{ sec} \tag{5-3}$$

$$\int_{t-T}^{t} 0.5\cdot\left[1+\text{sgn}\left(\left|\Delta V_{\text{prop}}(\Delta t_i)\right|-5\%\right)\right]dt \le 2\text{ sec} \tag{5-4}$$

$$\int_{t-T}^{t} 0.5\cdot\left[1+\text{sgn}\left(I_{\text{pulse}}(\Delta t_i)-I_{\text{pulse}}^{\text{Ampacity}}\right)\right]dt \le T_1 \tag{5-5}$$

where, $\Delta\omega$ is the MTG generator frequency deviation, ΔV_{prop} is the propulsion load voltage deviation, $I_{\text{pulse}}^{\text{Ampacity}}$ is the ampacity of the cable serving the pulse load, and I_{pulse} is the input current of the pulse load. The constraints (5-1) and (5-2) are steady state frequency and voltage constraints, which mean that the frequency and voltage deviation should be no larger than 3% and 5% of nominal values in steady state, respectively [17]; and the constraints (5-3)-(5-5) are dynamic constraints, which mean that the system states can violate the steady state limits for a short period of time and return to and remain within the limits within a recovery time. The maximum allowed frequency and voltage transient recovery times were 2 seconds as given in [17].

The notional all-electric ship power system used to study the MVAC multi-agent system is discussed in detail in Appendix B.2. The parameters and mathematical models of the MTG and ATG agents, propulsion load agent, and pulse load agent are given in Appendices A.1-3. Since the system losses agent is only used to calculate the available

power for the DC zone system, the system losses agent was not included in the MVAC multi-agent system case studies.

In the case studies, the pulse loads had different ramp rates, pulse widths, and pulse magnitudes for each case study. Figure 5.4 shows a typical pulse load waveform. The ramp rate of a pulse load is defined as (5-6).

$$\text{ramp rate of pulse load} = P_{\text{pulse}} / \Delta t \tag{5-6}$$

where, P_{pulse} is the pulse load power rating, and Δt is the increase time of the pulse.

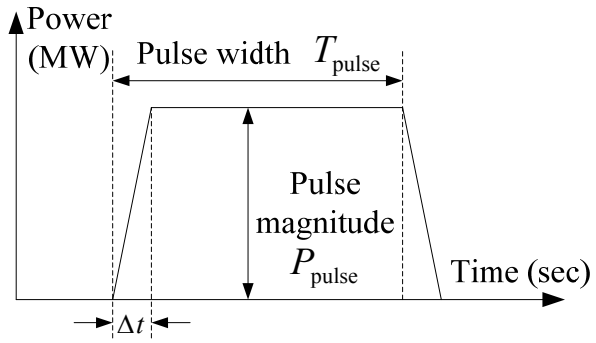

Figure 5.4 Diagram of a typical pulse load waveform

5.3.1.1 MVAC multi-agent system – case study I

In this case study, a pulse load with a 15 MW power magnitude and 2 seconds pulse width was used, and the ramp rate of the pulse load was 150 MW/sec. The pulse load was served at 30 seconds and the propulsion load demand was 21 MW. The steady state and dynamic state voltage constraints for the propulsion load and frequency constraints for the MTG generator were used to evaluate the performance of the new real-time load management technique.

The pulse load demand is shown in Figure 5.5. The actual power demand of the pulse load tracked the desired power demand very well. The cruising speed of the ship was 27 knots. The ship speed was increased from 0 to 27 knots in the first 20 seconds of the simulation with full propulsion power to accelerate the ship, which is shown in Figure 5.6. The ship speed reached steady state at 20 seconds. The ship speed decrease caused by the pulse load demand at 30 seconds is shown in Figure 5.7. The ship speed decrease was only 1.1 knots.

When the pulse load was served at 30 seconds, the ship speed was decreased because the propulsion load demand was reduced to compensate for the impact of the pulse load on the power quality of the all-electric ship power system. The power demand and set-point of the propulsion load are shown in Figure 5.8. From 0 to 20 seconds, the propulsion load demand was 35.5 MW to drive the ship speed to the desired speed quickly, and then the propulsion load demand decreased to 21 MW to maintain the ship's speed at 27 knots in steady state. When the pulse load was served at 30 seconds, the propulsion load was decreased to reduce the frequency and voltage oscillations caused by the pulse load. The output powers of the MTG and ATG generators are shown in Figure 5.9. The spikes in the output power signals were caused by disturbances of the pulse load, which caused small frequency oscillations. Due to the compensation of the propulsion load, the generator output powers were kept constant expect some transient times.

The frequency behavior of the MTG generator is shown in Figure 5.10. The frequency changes from 20 to 25 seconds were caused by the decrease of the propulsion

load demand. When the propulsion load reached steady state, the frequency gradually converged to 60 Hz. The maximum frequency deviation caused by the pulse load was 0.7 Hz, which was much less than the steady state frequency tolerance 1.8 Hz (3% of the nominal value). The output voltages of the MTG and ATG generators are shown in Figure 5.11. The maximum output voltage deviations of MTG and ATG generators were much less than the steady state voltage tolerance, which is 5% of the nominal value. The input voltage of the propulsion load is shown in Figure 5.12. The propulsion load input voltage was disturbed at 30 seconds due to the propulsion load compensation. The input voltage deviation of the propulsion load was less than the steady state voltage tolerance.

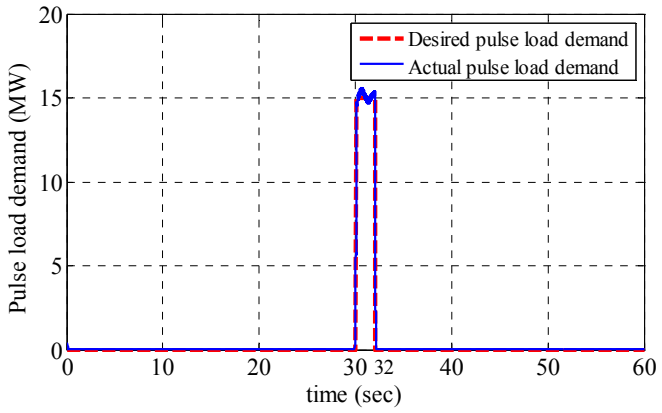

Figure 5.5 Desired and actual power demands of the pulse load in MVAC multi-agent system – case study I

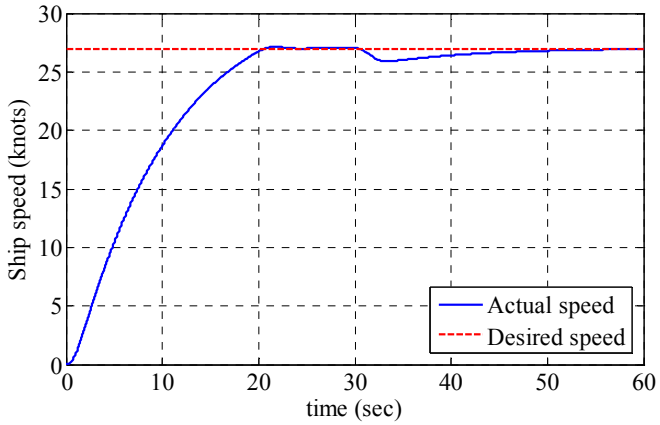

Figure 5.6 Desired ship speed and actual ship speed in MVAC multi-agent system – case study I

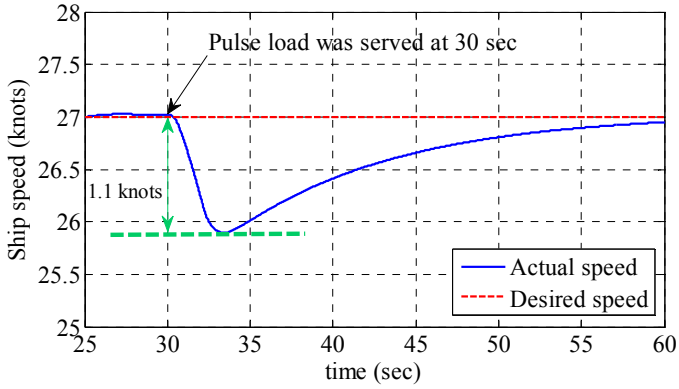

Figure 5.7 Ship speed decrease due to the pulse load in MVAC multi-agent system – case study I

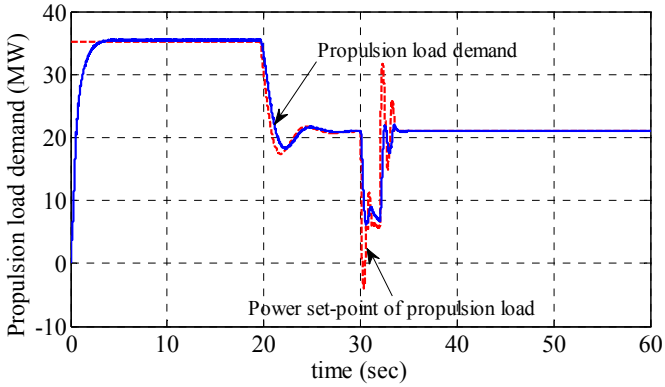

Figure 5.8 Power demand and set-point of the propulsion load in MVAC multi-agent system – case study I

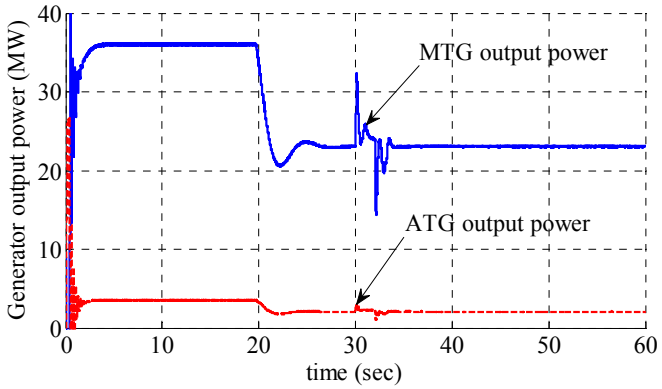

Figure 5.9 MTG and ATG output powers in MVAC multi-agent system – case study I

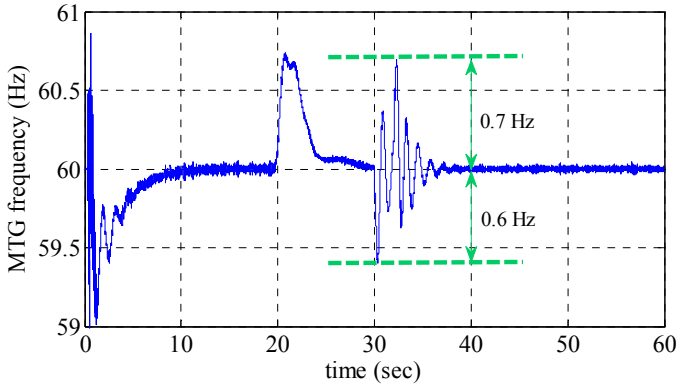

Figure 5.10 Frequency behavior of the MTG generator in MVAC multi-agent system – case study I

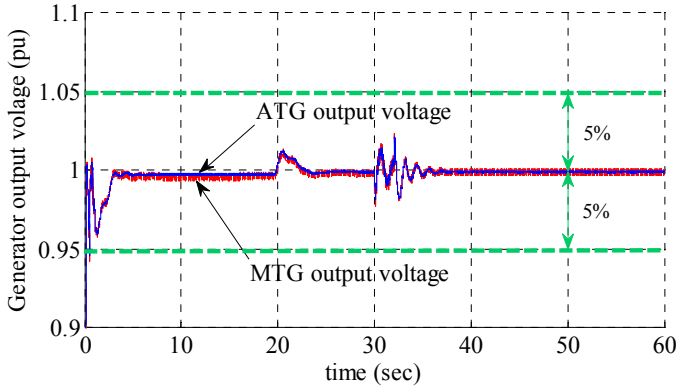

Figure 5.11 MTG and ATG output voltages in MVAC multi-agent system – case study I

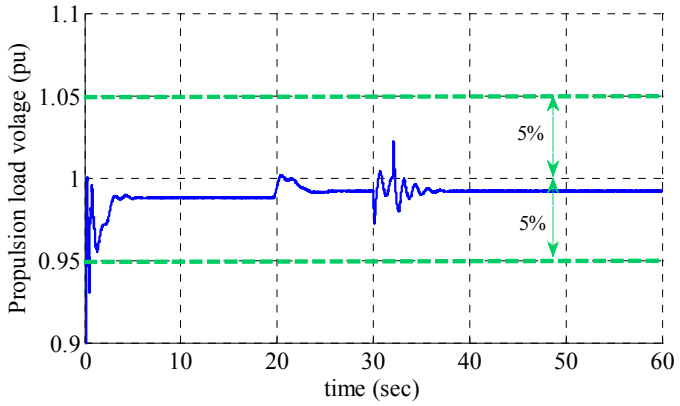

Figure 5.12 Propulsion load input voltage in MVAC multi-agent system – case study I

To show the advantages of the MVAC multi-agent system, the dynamic performance of the frequency of the MVAC system without the application of real-time load management was also studied. The frequency behavior of the MTG generator with and without real-time load management is shown in Figure 5.13. The maximum frequency deviation of the MTG generator without real-time load management was 2 Hz, which was larger than the steady state frequency tolerance 1.8 Hz. The steady state frequency constraint was violated if the real-time load management technique was not applied. The maximum frequency deviation of the MTG generator with real-time load management was much less than the deviation without real-time load management, which means that the new real-time load management technique reduced the frequency deviation when a pulse load was served.

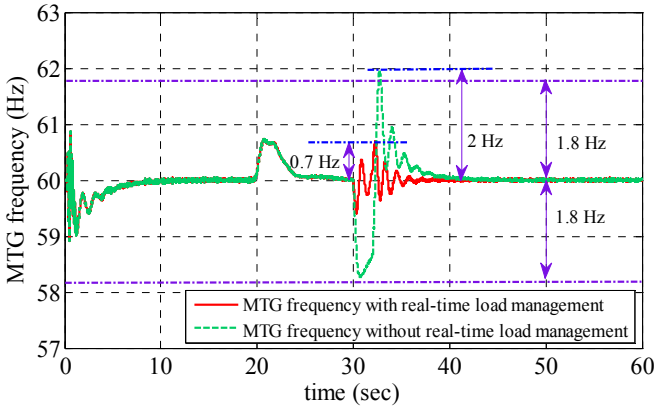

Figure 5.13 Frequency behavior of the MTG generator with and without the application of real-time load management in MVAC multi-agent system – case study I

In this case study, a pulse load with 15 MW pulse magnitude and 2 seconds pulse width was used to study the effectiveness of the new real-time load management technique. The propulsion load demand was 21 MW, which was larger than the pulse load demand. Thus, load changes caused by the pulse load were fully compensated by the propulsion load. The frequency deviation of the MTG generator and the voltage deviation of the propulsion load were less than the steady state tolerances. The simulation results indicated that the dynamic performance of the MVAC system was significantly improved by using this real-time load management technique.

5.3.1.2 MVAC multi-agent system – case study II

In this case study, another pulse load with a 35 MW rated power and 2 seconds pulse width was studied, and the ramp rate of the pulse load was 350 MW/sec. The pulse load was served at 30 seconds and the propulsion load demand was 21 MW. The cruising speed of the ship was 27 knots. The steady state and dynamic state voltage

constraints for the propulsion load and frequency constraints for the MTG generator were used to evaluate the performance of the new real-time load management technique.

The pulse load demand is shown in Figure 5.14. The actual pulse load demand tracked the desired value very well. The speed behavior of the ship is shown in Figure 5.15. The ship speed decrease at 30 seconds caused by the pulse load is shown in Figure 5.16. The ship speed decrease was 3.0 knots, which was greater than the speed decrease in MVAC multi-agent system – case study I.

The propulsion load demand is shown in Figure 5.17. When the pulse load was connected to the system at 30 seconds, the power set-point of the propulsion load was decreased quickly to decrease the propulsion load demand. When the pulse load was disconnected from the system at 32 seconds, the power set-point of the propulsion load was increased quickly to increase the propulsion load demand. The oscillations in the propulsion load demand were caused by the frequency regulation controller in the propulsion load agent, which could drive the system frequency to 60 Hz quickly.

The propulsion load demand in steady state was 21 MW, which was less than the rated power of the pulse load. Thus, the propulsion load could not fully compensate for the load changes caused by the pulse load, which caused significant frequency oscillations, as shown in Figure 5.18. The maximum frequency deviation caused by this pulse load was 2.4 Hz, which was much greater than the maximum frequency deviation of 0.7 Hz in MVAC system in the case study I. The frequency deviation of the MTG generator violated the steady state frequency tolerance 1.8 Hz, but the recovery time was

less than 0.3 second, which was less than the maximum allowed transient recovery time 2 seconds. Thus, the behavior of the MTG frequency was acceptable in this case.

The input voltage of the propulsion load is shown in Figure 5.19. The propulsion load input voltage was disturbed at 30 seconds due to the propulsion load compensation. The maximum voltage deviation was 7%, which was larger than the steady state voltage tolerance. The maximum voltage deviation was less than the transient voltage tolerance, which was equal to 16% of the nominal value. And the recovery time of the propulsion load voltage was 0.2 seconds, which was less than the maximum allowed transient recovery time 2 seconds. Thus, the behavior of the input voltage of the propulsion load was acceptable in this case.

Simulation results indicated that if the propulsion load demand was less than the power rating of the pulse load, the MVAC multi-agent system had limitations to mitigate frequency oscillations caused by the pulse load. The steady state tolerances of the propulsion load voltage and the MTG generator frequency were violated in this case, but the propulsion load voltage and the MTG generator frequency returned to and remained within the tolerances within a maximum allowed transient recovery time (2 seconds). In this case, the dynamic performance of the MVAC multi-agent system was still acceptable based on the power quality requirements for shipboard power systems in the IEEE-STD-45 [17].

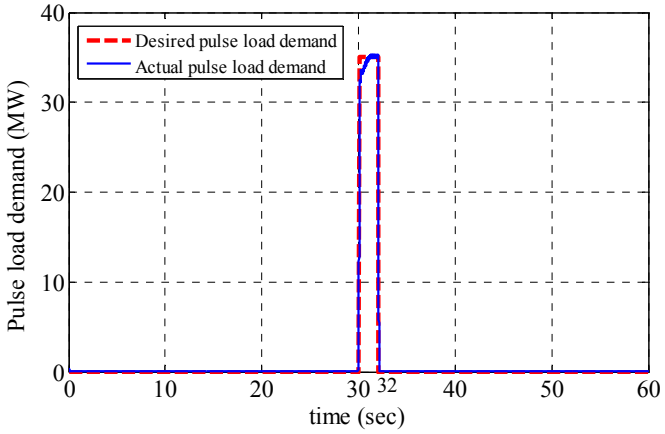

Figure 5.14 Desired and actual power demands of the pulse load in MVAC multi-agent system – case study II

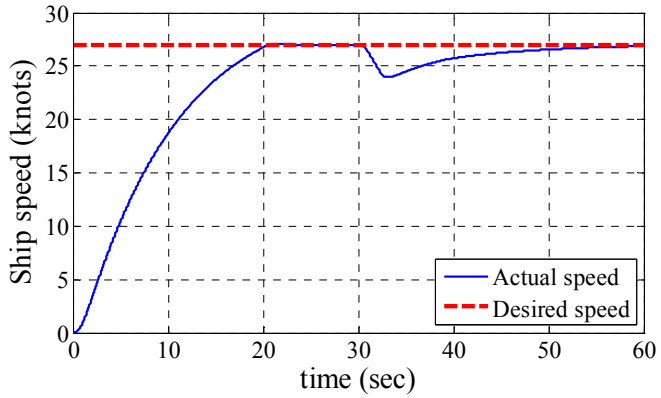

Figure 5.15 Desired ship speed and actual ship speed in MVAC multi-agent system – case study II

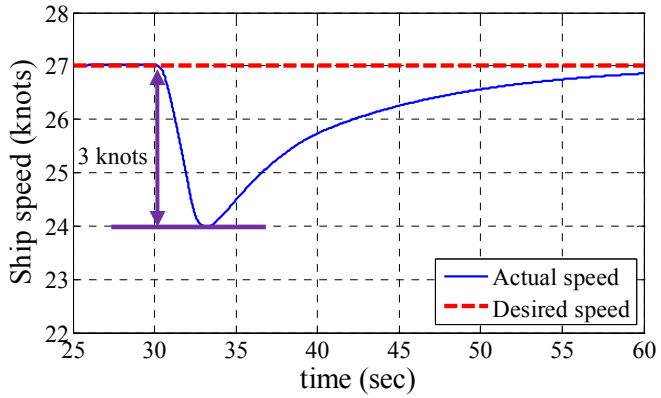

Figure 5.16 Ship speed decrease due to the pulse load in MVAC multi-agent system – case study II

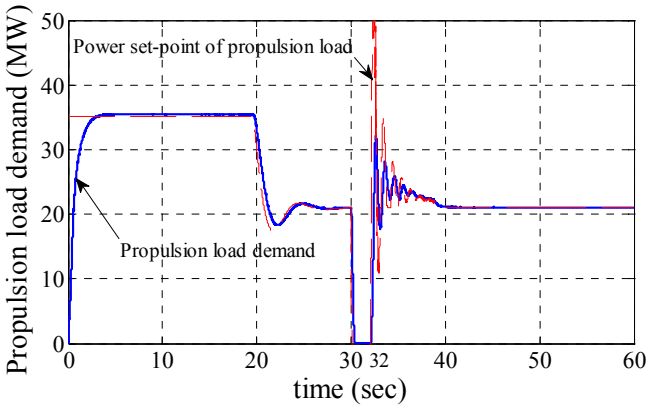

Figure 5.17 Power set-point and actual power demand of the propulsion load in MVAC multi-agent system – case study II

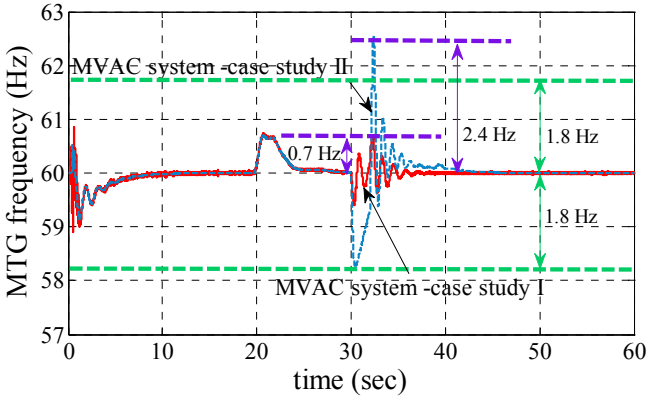

Figure 5.18 Frequency behavior of the MTG generator in MVAC multi-agent system – case studies I and II

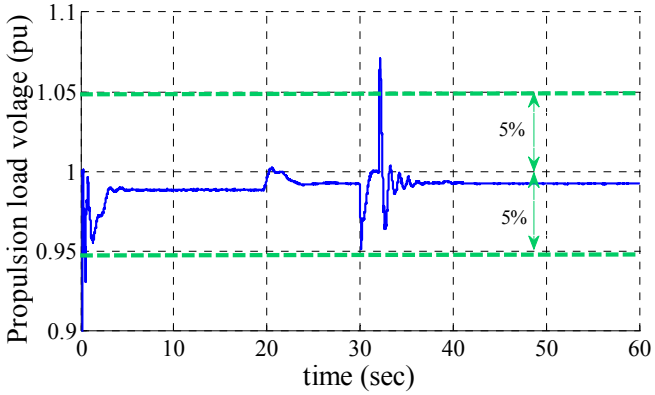

Figure 5.19 Propulsion load input voltage in MVAC multi-agent system – case study II

5.3.1.3 MVAC multi-agent system – case study III

In this case study, the behavior of the MVAC multi-agent system for the dynamic cable constraint for the pulse load is illustrated. The AC cable connecting the MTG generator bus and the pulse load is shown in Figure 5.3. It was assumed that the pulse load had two pulses, and the pulse magnitude was 35 MW with 8 seconds pulse width. The first pulse was from 30 to 38 seconds, and the second pulse was from 50 to 58 seconds. The ramp rate of the pulse load was 350 MW/sec.

The dynamic cable constraint that was used is shown in (5-7). The dynamic cable constraint considers a time horizon T, and the total violation time of the cable ampacity constraint should be no larger than the maximum allowed time T_1. If the total violation time is larger than T_1, the pulse load needs to be disconnected immediately to satisfy the dynamic cable constraint.

$$\int_{t-T}^{t} 0.5 \cdot \left[1 + \mathrm{sgn}(I_{\mathrm{pulse}}(\Delta t_i) - I_{\mathrm{pulse}}^{\mathrm{Ampacity}})\right] dt \le T_1 \tag{5-7}$$

where, T was chosen as 10 seconds; T_1 was chosen as 5 seconds; $I_{\mathrm{pulse}}^{\mathrm{Ampacity}}$ was chosen as 500 A; and $I_{\mathrm{pulse}}(\Delta t_i)$ was the current on the cable. If the dynamic constraint was violated, the switch to the pulse load would set open to satisfy the dynamic cable constraint.

For the case study, when the pulse load was served in the MVAC system at 30 seconds, the cable current was greater than 500 A. Thus, the pulse load could only be served for 5 seconds, as shown in Figure 5.20. At 35 seconds, the switch to the pulse load was set to open to satisfy the dynamic cable constraint. The second pulse happened

at 50 seconds. And the switch to the pulse load was set to open at 55 seconds to satisfy the dynamic cable constraint, as shown in Figure 5.20.

The dynamic cable constraint is illustrated in Figure 5.21. When the pulse load was served at 30 seconds, the value of $\int_{t-T}^{t} 0.5 \cdot \left[1 + \text{sgn}(I_{\text{pulse}}(\Delta t_i) - I_{\text{pulse}}^{\text{Ampacity}})\right] dt$ began to increase from 0 and the value hit the limit at 35 seconds, which caused the pulse load to be disconnected from the system. From 35 to 40 seconds, the pulse load was not allowed to be served. At 40 seconds, the value of $\int_{t-T}^{t} 0.5 \cdot \left[1 + \text{sgn}(I_{\text{pulse}}(\Delta t_i) - I_{\text{pulse}}^{\text{Ampacity}})\right] dt$ began to decrease from 5 and the value reached 0 at 45 seconds. The second pulse happened at 50 seconds, and the behavior of the second pulse was the same as the first one.

The propulsion load demand is shown in Figure 5.22. When the pulse load was connected to the system, the propulsion load demand was decreased to compensate for the power demand of the pulse load. In this case, the rated power of the pulse load was greater than the propulsion load demand. When the pulse load was served in the system, the propulsion load demand was decreased to 0 to compensate for the pulse load demand.

The frequency behavior of the MTG generator is shown in Figure 5.23. The frequency decrease caused by the connection of the pulse load was 1.3 Hz, as shown in Figure 5.23. This frequency decrease was less than the steady state frequency tolerance. When the switch to the pulse load was opened, the maximum frequency deviation was 2.1 Hz, as shown in Figure 5.23. The frequency deviation was greater than the steady state frequency tolerance, but the transient recovery time of the MTG generator

frequency was 0.2 seconds, which was less than the maximum allowed transient recovery time. Thus, the performance of the MTG frequency was acceptable in this case.

The input voltage of the propulsion load is shown in Figure 5.24. The maximum voltage deviation was 5.45% of the nominal value, which was greater than the steady state voltage tolerance. However, the recovery time of the voltage was 0.1 second, which was much less than the maximum allowed transient recovery time 2 seconds. Thus, the dynamic behavior of the propulsion load input voltage was acceptable in this case.

The ship speed is shown in Figure 5.25. Even though the propulsion load demand was decreased to 0 when the pulse load was served, the ship speed was decreased slowly due to the large inertia of the ship. When the pulse load was served from 30 to 35 seconds, the ship speed was decreased from 27 to 20 knots due to the decrease of the propulsion load demand. The speed was increased to 25 knots before the second pulse happened. Due to the second pulse, the ship speed was decreased to 19 knots at 55 seconds, as shown in Figure 5.26.

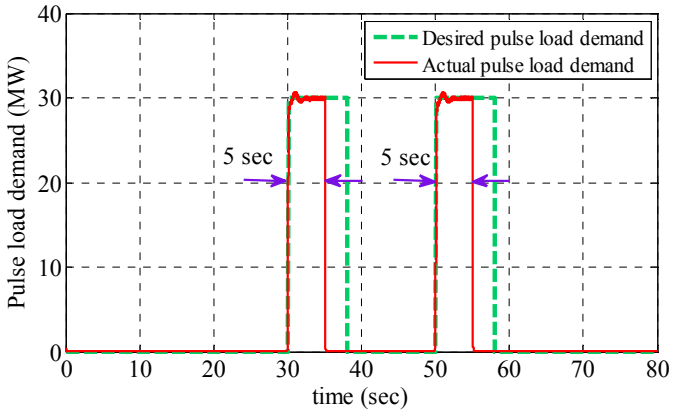

Figure 5.20 Pulse load demand in MVAC multi-agent system – case study III

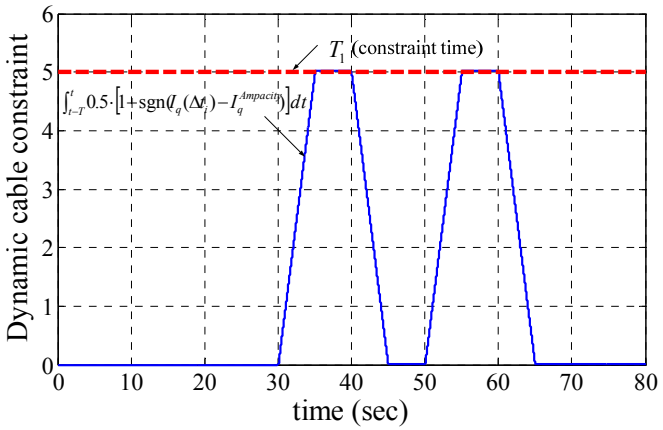

Figure 5.21 Diagram of the dynamic cable constraint in MVAC multi-agent system – case study III

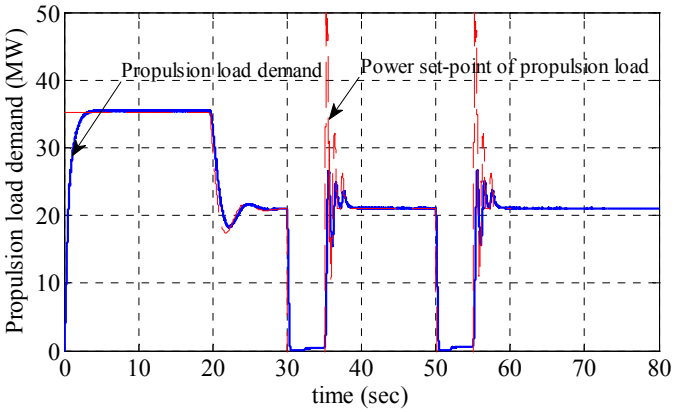

Figure 5.22 Propulsion load demand in MVAC multi-agent system – case study III

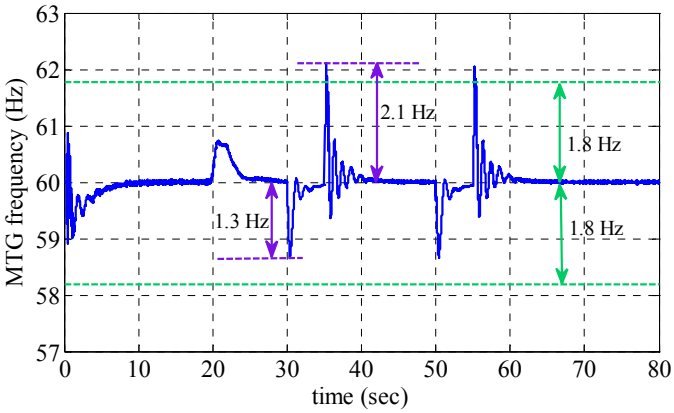

Figure 5.23 Frequency behavior of the MTG generator in MVAC multi-agent system – case study III

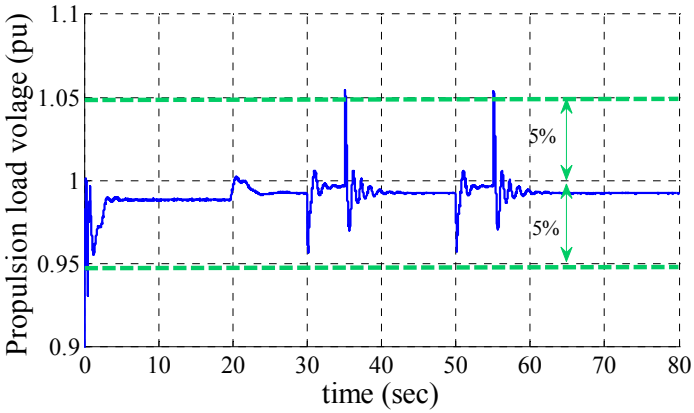

Figure 5.24 Propulsion load input voltage in MVAC multi-agent system – case study III

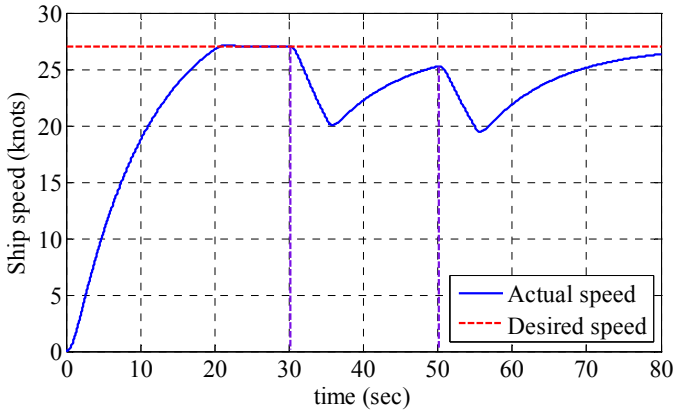

Figure 5.25 Desired ship speed and actual ship speed in MVAC multi-agent system – case study III

5.3.2 DC zone multi-agent system case studies

In the DC zone multi-agent system studies, the diagram of a simplified notional all-electric ship power system simulation model for DC zone multi-agent system is shown in Figure 5.26, and the simulation step size $\Delta\tau$ was chosen as 12 microseconds in the PSCAD simulation. The system consisted of two identical DC zones. The load definitions in one DC zone are shown in Table 5.1. It was assumed that only one ATG generator was in service, so the total generation capacity was 4 MW. It was also

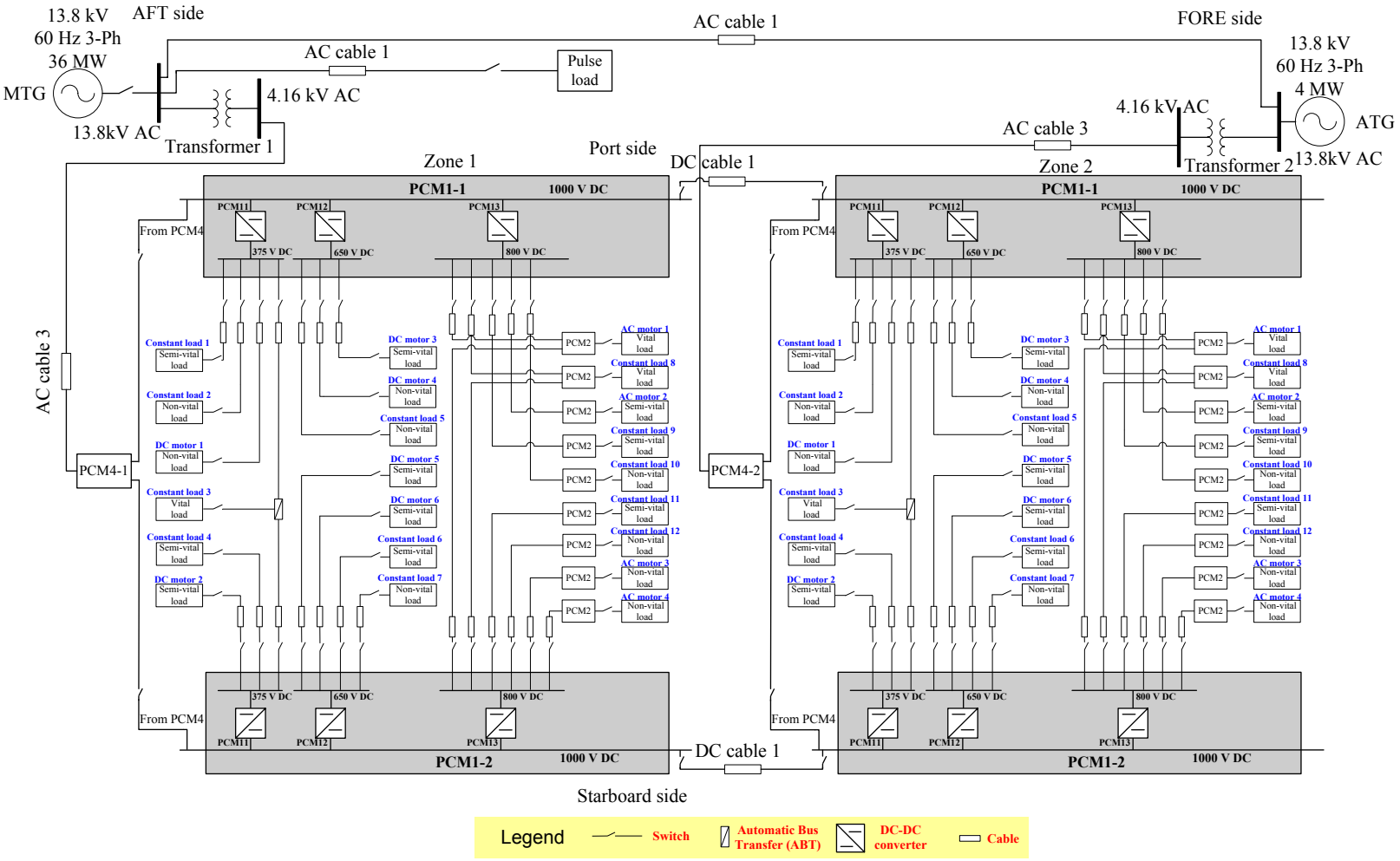

Figure 5.26 Diagram of a simplified notional all-electric ship power system simulation model for DC zone multi-agent system

assumed that the propulsion load was out of service and a pulse load was served in the MVAC system at certain times of simulation. The notional all-electric ship power system used to study the DC zone multi-agent system is discussed in details in Appendix B.3. The agents in DC zones are discussed in Appendices A.4-A.7.

Table 5.1 Load definitions in one DC zone for the DC zone multi-agent system case studies

Component name	Priority	Rating (kW)	Voltage (V)	Switch Board	Load type
constant load 1	semi-vital	115.4	375	port	variable
constant load 2	non-vital	72	375	port	variable
DC motor 1	non-vital	36	375	port	fixed
constant load 3	vital	151.4	375	starboard	variable
constant load 4	semi-vital	70	375	starboard	variable
DC motor 2	semi-vital	115.4	375	starboard	fixed
DC motor 3	semi-vital	115.4	650	port	fixed
DC motor 4	non-vital	36	650	port	fixed
constant load 5	semi-vital	115.4	650	port	variable
DC motor 5	semi-vital	115.4	650	starboard	fixed
DC motor 6	semi-vital	47.6	650	starboard	fixed
constant load 6	semi-vital	22	650	starboard	variable
constant load 7	non-vital	199	650	starboard	variable
AC motor 1	vital	181	450	port	fixed
constant load 8	vital	42.6	450	port	variable
AC motor 2	semi-vital	79.4	450	port	fixed
constant load 9	semi-vital	40	450	port	variable
constant load 10	non-vital	85	450	port	variable
constant load 11	semi-vital	119.6	450	starboard	variable
constant load 12	non-vital	177	450	starboard	variable
AC motor 3	non-vital	192.6	450	starboard	fixed
AC motor 4	non-vital	115.4	450	starboard	fixed

The operational constraints of the DC zone multi-agent system used in the case studies are shown in (5-8)-(5-11).

$$\sum_{i=1}^{12} V_{in-i} x_i(t) \le P_{Total} \tag{5-8}$$

$$\sum_{i=1}^{3} V_{in-i} x_i(t) + \sum_{i=7}^{9} V_{in-i} x_i(t) \le P_{\mathrm{PCM4-1}}^{\mathrm{Capacity}} \tag{5-9}$$

$$\sum_{i=4}^{6} V_{in-i} x_i(t) + \sum_{i=10}^{12} V_{in-i} x_i(t) \le P_{\mathrm{PCM4-2}}^{\mathrm{Capacity}} \tag{5-10}$$

$$V_k^{\min} \le V_k(t) \tag{5-11}$$

where, V_{in-i} and x_i are the input voltage and current of the *i*th DC-DC converter, respectively; P_{Total} is the power available to the DC zone system; $P_{\text{PCM4-1}}^{\text{Capacity}}$ and $P_{\text{PCM4-2}}^{\text{Capacity}}$ are the power capacity of PCM4-1 and PCM4-2, respectively; $V_k(t)$ and $V_k^{\min}$ are the input voltage and the minimum allowed input voltage of motor load *k*, respectively.

The two DC zones served 44 loads with various priorities and power ratings. The parameters of the converter agent model and motor agent model are shown in Tables 5.2 to 5.3. The equivalent inductor and capacitor of each constant load agent were chosen as 0.005 H and 0.0002 F, respectively. The parameters of the converter agent models as shown in (4-26) and motor agent models as shown in (4-45) and (4-46) are given in Tables 5.2 and 5.3. The parameters of the cooperative controllers as shown in (4-39), (4-55), (4-58) and (4-61) were chosen as follows.

$$k_1 = 10,\ k_2 = 100,\ K_1 = 7000,\ K_2 = 7000,\ K_5 = 10^5,\ C_1 = 300,\ C_2 = 10,$$

$$W_{\text{vital}} = 10^8, W_{\text{semi-vital}} = 10^7,\ W_{\text{non-vital}} = 1,\ \gamma_k = 100,\ P_{\text{PCM4-1}}^{\text{Capacity}} = 2\ \text{MW},\ P_{\text{PCM4-2}}^{\text{Capacity}} = 2\ \text{MW}$$

where, W_{vital}, $W_{\text{semi-vital}}$, and $W_{\text{non-vital}}$ are weight-factors of vital, semi-vital, and non-vital loads, respectively. The minimum allowed input voltage for each motor was chosen as 95% of its nominal voltage. In the case studies, each fixed-type load was either served at its maximum power rating or was not be served at all; each variable-type load was quantized based on 10 amperes current rating, which means that the load current could only be multiple of 10 amperes.

Table 5.2 Parameters of converter agents in the DC zone multi-agent system

Parameters	L (mH)	C (μF)	d
375 V DC converter	234	1000	0.375
650 V DC converter	228	1000	0.65
800 V DC converter	160	1000	0.8

Table 5.3 Parameters of motor load agents in the DC zone multi-agent system

Component name	K_d	T_1	T_2
DC motor 1	1	0.2203	0.01
DC motor 2	1	0.3289	0.01
DC motor 3	1	0.3648	0.01
DC motor 4	1	0.2203	0.01
DC motor 5	1	0.3648	0.01
DC motor 6	1	0.3123	0.01
AC motor 1	1	0.1789	0.002
AC motor 2	1	0.2763	0.0116
AC motor 3	1	0.3394	0.0105
AC motor 4	1	0.3	0.02

5.3.2.1 DC zone system – case study I

In this case study, a pulse load with a 1.2 MW power rating and 5 seconds pulse width was served in the MVAC system. Ramp rate of the pulse load was 10 MW/sec. The pulse load demand is shown in Figure 5.27. The pulse load was served from 3 to 8 seconds, which changed the power available to the DC zone system.

The available power and total load demand of the DC zone system are shown in Figure 5.28. At 3 seconds, the power available to the DC zone system was decreased due to the connection of the pulse load; the total load demand of the DC zone system was also decreased immediately to track the available power. At 8 seconds, the power available to the DC zone system was increased due to the disconnection of the pulse load; the total load demand in the DC zone system was increased slowly to track the

available power, since the load demand of AC and DC motor loads was increased gradually when these loads were connected.

The frequency behavior of the ATG generator is shown in Figure 5.29. The frequency oscillations at 3 and 8 seconds were caused by the sudden load changes in the DC zone system. At 8 seconds, large oscillations appeared due to the mismatch of the available power and the total load demand in the DC zone system. The DC zone system included AC and DC motors, which take several seconds to reach steady state. Moreover, the DC zone multi-agent system is also a dynamic system, which takes several seconds to reach steady state after large disturbances. The maximum frequency deviation was 0.75 Hz, which was also less than the steady state frequency tolerance. Thus, the dynamic behavior of the ATG frequency was good enough based on the frequency requirements in IEEE-STD-45.

The output power of the ATG generator is shown in Figure 5.30. When the power demand of the pulse load was increased or decreased, the output power of the ATG generator included some oscillations. Input power of PCM4-1 and PCM4-2 is shown in Figure 5.31, which indicates that the input power of each PCM4 was always less than its 2 MW power capacity by using the cooperative controller. The output voltages of DC-DC converters of port side PCM1 in DC zone 1 are shown in Figure 5.32. Since output voltages of DC-DC converters are controlled by local voltage regulators, the voltages were well maintained at nominal values - except when load changes happened. The motor input voltage constraints were also satisfied, since the voltage decrease was much less than 5% of the nominal value.

The power demand of some individual loads served by port side PCM1 in DC zone 1 is shown in Figure 5.33. When the power available to the DC zone system decreased due to the pulse load connection, the switches to some fixed-type non-vital loads were opened and the set-points of some variable-type non-vital loads were decreased, which decreased the total load demand in the DC zone system to track the available power; when the power available to the DC zone system increased due to the disconnection of the pulse load, these disturbed fixed-type non-vital loads were reconnected to the system and the set-points of these variable-type non-vital loads were increased, which increased the total load demand in the DC zone system to track the available power.

As shown in Figure 5.33, AC motor 1 was always served due to its higher priority; constant load 1 was a variable-type semi-vital load, which was disturbed for a short period of time when the power available to the DC zone system was decreased; and DC motor 1 was a fixed-type non-vital load, which was disconnected when the available power decreased and reconnected when the available power increased.

The power demand of some individual loads served by starboard side PCM1 in DC zone 1 is shown in Figure 5.34. When the power available to the DC zone system was decreased, the power demand of constant loads 4, 7, and 12 was decreased to reduce the total load demand in the DC zone system. Constant load 3 was a vital load, which was always served. DC motor 2 was a semi-vital load, which was always served.

Input voltages of PCM4-1 and PCM4-2 are shown in Figure 5.35. The voltage oscillations at 3 and 8 seconds were caused by pulse load changes. At 3 and 8 seconds,

the voltage deviations were less than 5% of the nominal value, which is the steady state voltage tolerance in IEEE-STD-45 [17]. The output voltage of the ATG generator also included voltage oscillations when the pulse load was connected or disconnected, as shown in Figure 5.36. The ATG voltage also satisfied the voltage requirements in IEEE-STD-45.

In this case study, a pulse load in the MVAC system was served, which changed the available power to the DC zone system. The heterogeneous multi-agent system cooperative controller was used to control each fixed-type or variable-type load to achieve dynamic balancing subject to PCM4 capacity constraints and motor input voltage constraints. The simulation results indicated that the total load demand in the DC zone system tracked the available power quickly, and the PCM4 capacity constraints and motor input voltage constraints were always satisfied in operational real time. The higher priority loads were served before lower priority loads.

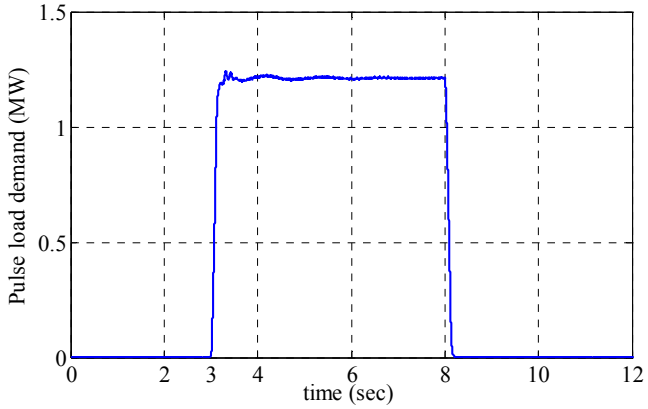

Figure 5.27 Power demand of the pulse load in the MVAC system in DC zone multi-agent system – case study I

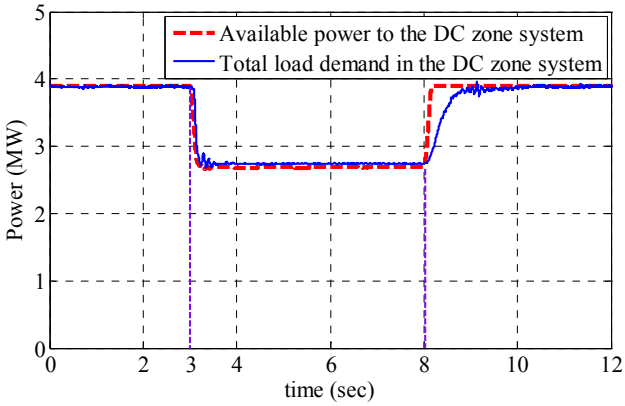

Figure 5.28 Available power and actual power demand of the DC zone system in DC zone multi-agent system – case study I

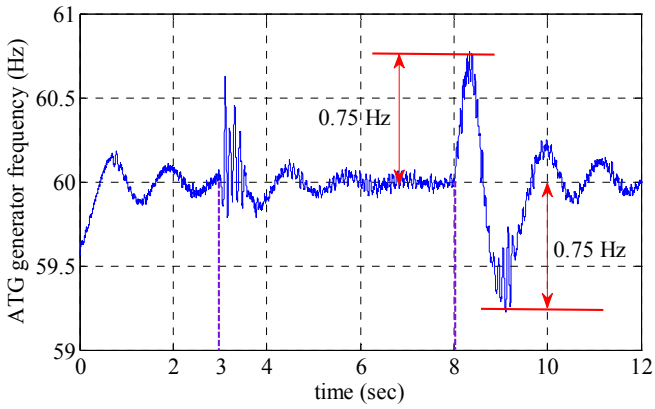

Figure 5.29 Frequency behavior of the ATG generator during disturbances of the pulse load in DC zone multi-agent system – case study I

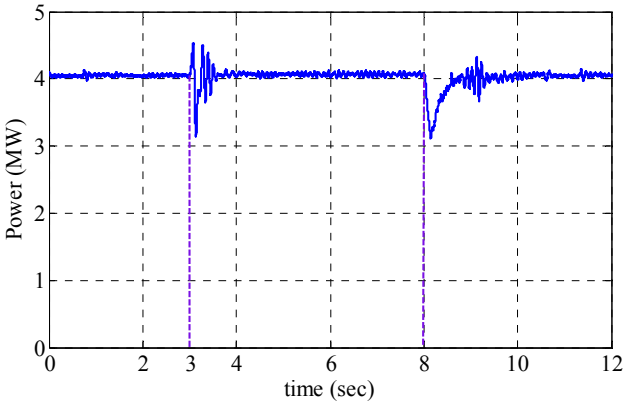

Figure 5.30 Output power of the ATG generator in DC zone multi-agent system – case study I

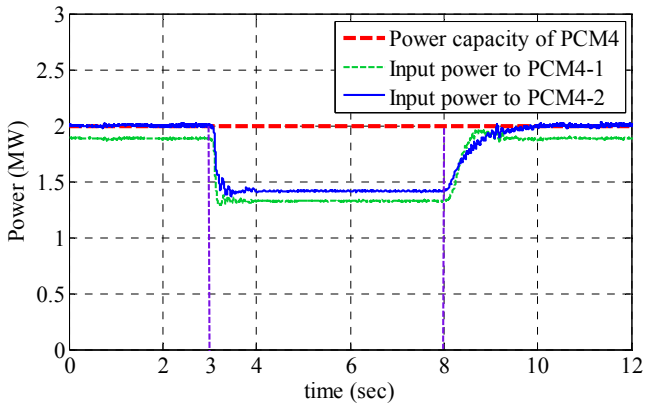

Figure 5.31 Input powers to PCM4-1 and PCM4-2 in DC zone multi-agent system – case study I

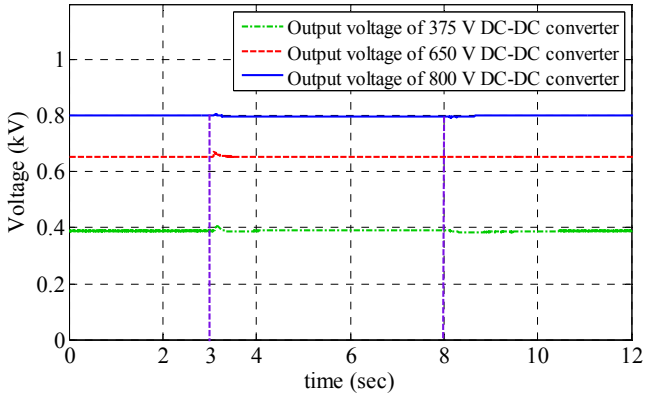

Figure 5.32 Output voltages of DC-DC converters of port side PCM1 in DC zone 1 in DC zone multi-agent system – case study I

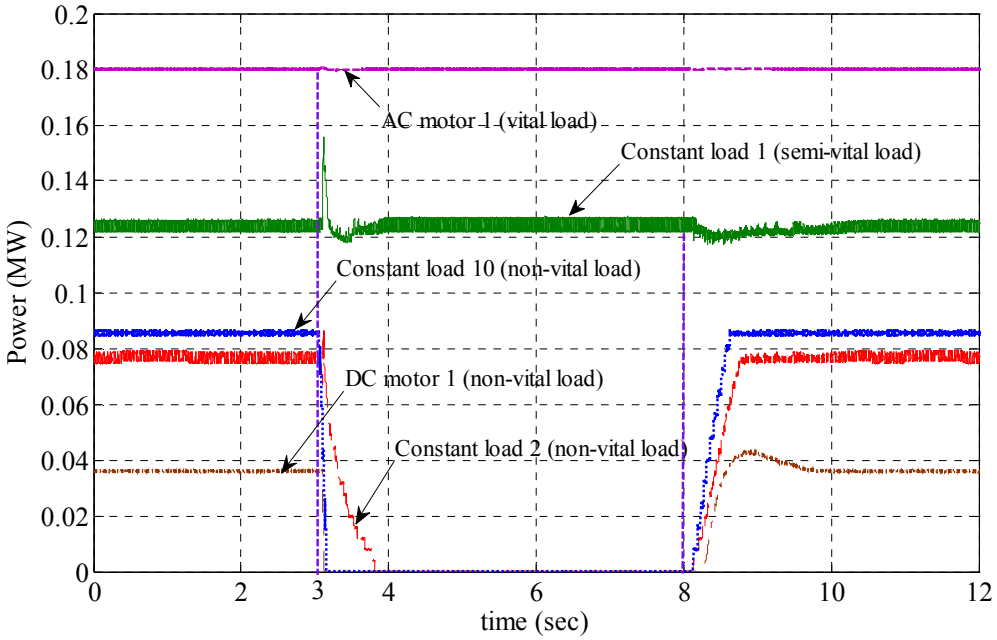

Figure 5.33 Power demand of some individual loads on port side of DC zone 1 in DC zone multi-agent system – case study I

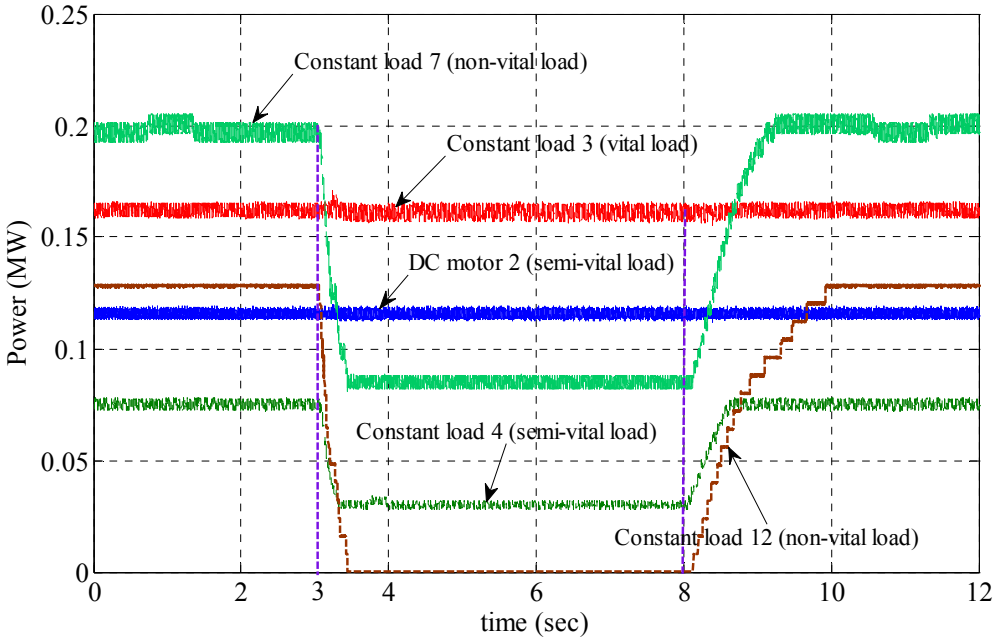

Figure 5.34 Power demand of some individual loads on starboard side of DC zone 1 in DC zone multi-agent system – case study I

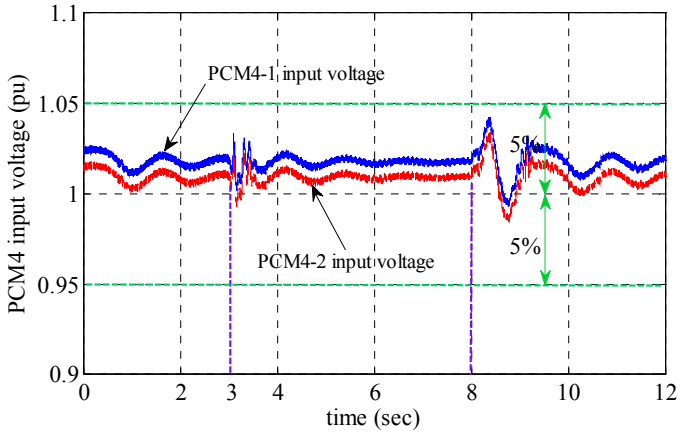

Figure 5.35 Input voltages of PCM4-1 and PCM4-2 in DC zone multi-agent system – case study I

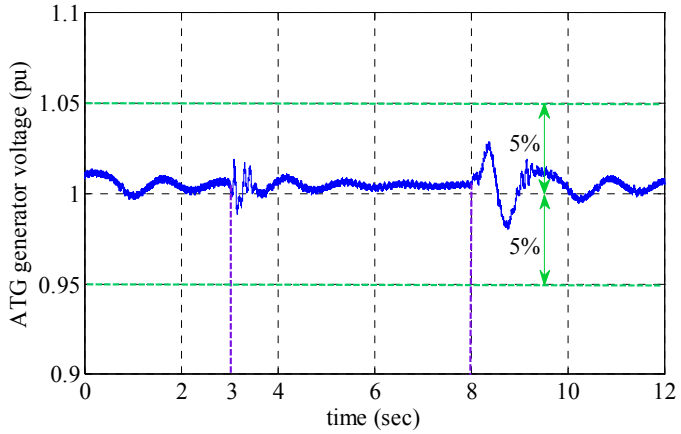

Figure 5.36 The output voltage of the ATG generator during disturbances of the pulse load in DC zone multi-agent system – case study I

5.3.2.2 DC zone multi-agent system – case study II

In DC zone – case study I, only pulse load demand was varied to change the power available to the DC zone system. In this case study, both pulse load demand and individual load demand in the DC zones were varied to study the dynamic performance of the new real-time load management method. The pulse load had a 5 seconds pulse with 0.8 MW magnitude. The ramp rate of the pulse load was 10 MW/sec. The pulse

load was served from 3 to 8 seconds, as shown in Figure 5.37. In DC zone 2, the switch status of five loads was changed to vary the total load demand in the DC zone system, as shown in Table 5.4. Each load was served at its maximum power rating when the load switch was closed; otherwise, the load was not served.

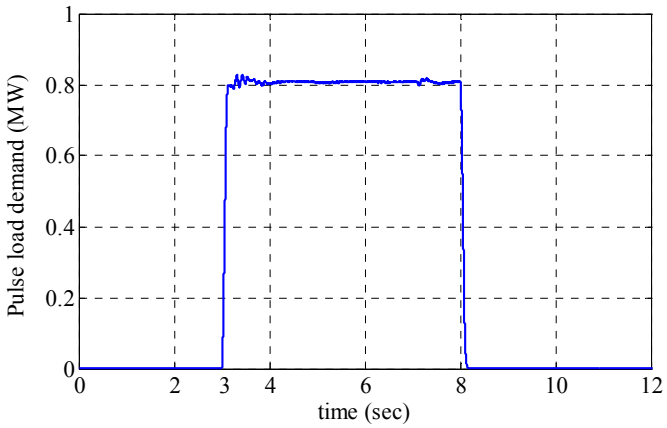

Figure 5.37 Power demand of the pulse load in the MVAC system in DC zone multi-agent system – case study II

Table 5.4 Switch status of five loads in DC zone 2

Component name	Switch closed	Switch open
DC motor 1	4 – 9 sec	0 – 4 sec; 9 – 12 sec
DC motor 4	5 – 11 sec	0 – 5 sec; 11 – 12 sec
AC motor 3	3 – 10 sec	0 – 3 sec; 10 – 12 sec
Constant load 4	2 – 7 sec	0 – 2 sec; 7 – 12 sec
Constant load 10	1 – 8 sec	0 – 1 sec; 8 – 12 sec

The available power and total load demand of the DC zone system are shown in Figure 5.38. The total load demand tracked the available power very well. When the pulse load was not served, the available power was greater than the total load demand. Since all the loads served by PCM4-1 already reached their maximum power and the

input power to PCM4-2 reached the power capacity of the PCM4, as shown in Figure 5.39, the total load demand in the DC zone system reached the maximum power.

The total load demand changes happened at 2 and 7 seconds, as shown in Figure 5.38, caused by load changes in DC zone 2. At 2 seconds, constant load 4 served by starboard side PCM1 in DC zone 2 was connected to the system, which caused the total load demand oscillations. At 7 seconds, constant load 4 served by starboard side PCM1 in DC zone 2 was disconnected. Since the total load demand should be less than the available power, some other loads were disturbed when the constant load 4 was connected.

The frequency behavior of the ATG generator is shown in Figure 5.40. The frequency oscillations were caused by the sudden load changes in the system. The maximum frequency deviation was 0.9 Hz, which was much less than the steady state frequency tolerance (3% of the nominal value) as given in IEEE-STD-45. The output voltages of DC-DC converters of port side PCM1 in DC zone 1 are shown in Figure 5.41. Each motor input voltage decrease was much less than 5% of the nominal value.

The power demand of some individual loads in DC zone 1 is shown in Figures 5.42 and 5.43. When load changes happened in DC zone 2, the power demand in DC zone 1 was also dynamically changed by using the real-time load management method to achieve the dynamic balancing while satisfying operational constraints of the system and considering load priorities.

In this case study, both pulse load demand and DC zone load demand were varied to study the dynamic performance of the new multi-agent system-based real-time

load management method. The developed cooperative controller dynamically regulated the power set-point of variable-type loads and the switch status of fixed-type loads to achieve dynamic balancing when load changes happened. The operational constraints of the system were also satisfied in operational real time.

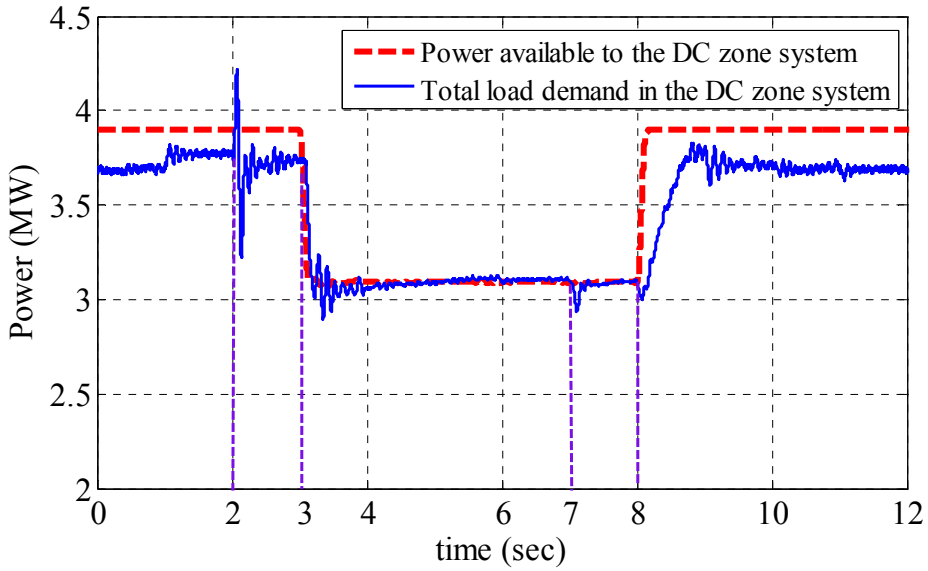

Figure 5.38 Total load demand and available power of the DC zone system in DC zone multi-agent system – case study II

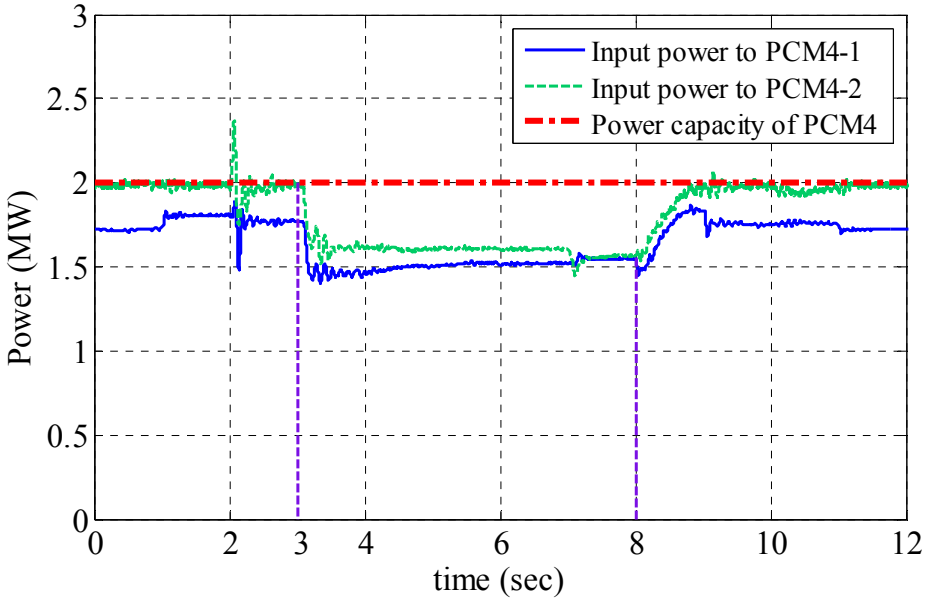

Figure 5.39 Input power of PCM4-1 and PCM4-2 in DC zone multi-agent system – case study II

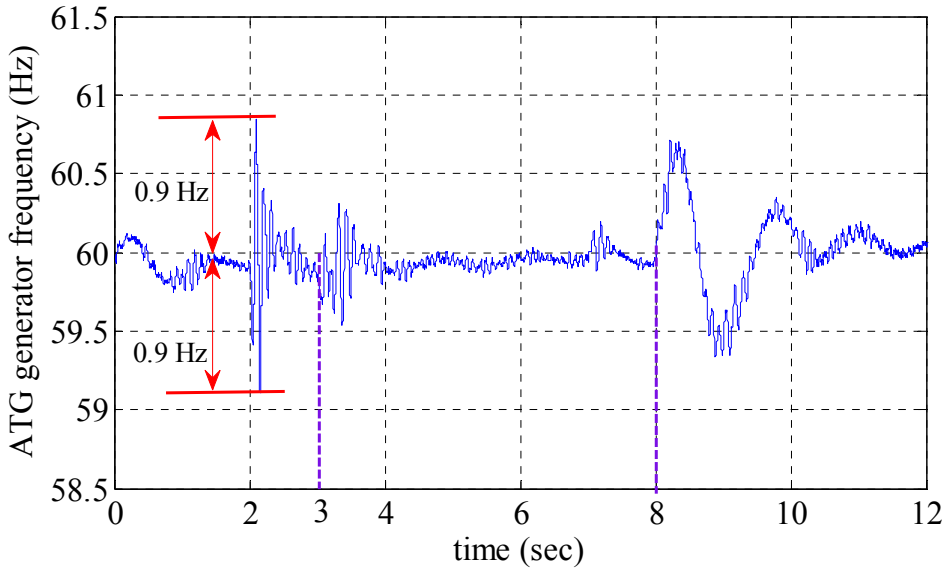

Figure 5.40 Frequency behavior of the ATG generator in DC zone multi-agent system – case study II

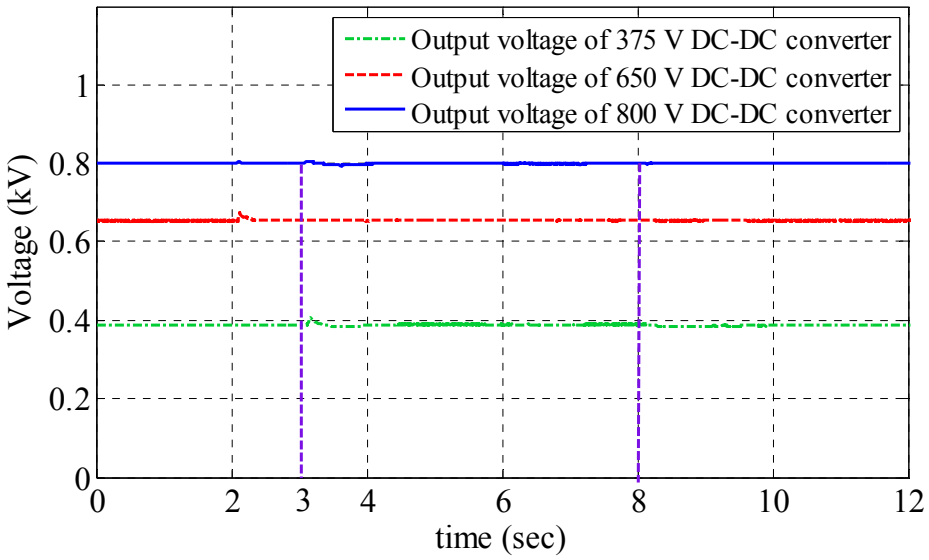

Figure 5.41 Output voltages of port side PCM1 in DC zone 1 in DC zone multi-agent system – case study II

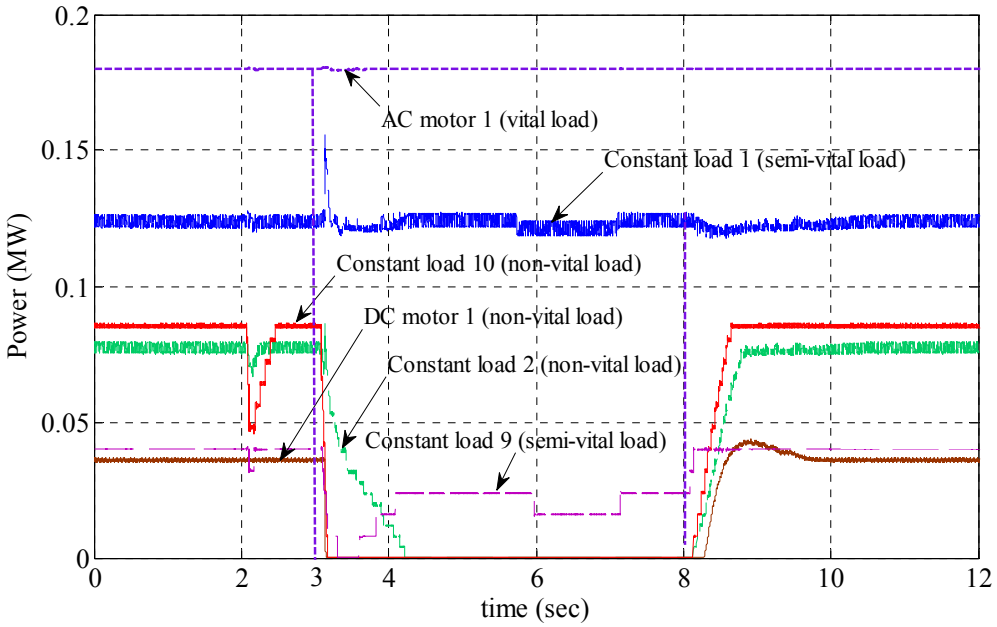

Figure 5.42 Power demand of some individual loads on port side of DC zone 1 in DC zone multi-agent system – case study II

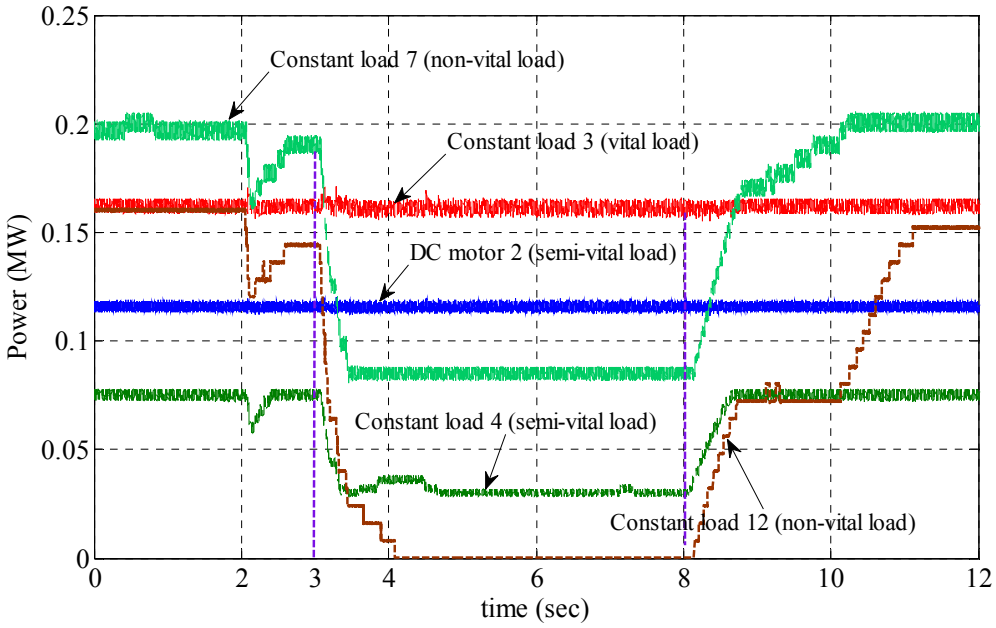

Figure 5.43 Power demand of some individual loads on starboard side of DC zone 1 in DC zone multi-agent system – case study II

5.3.3 Coordination of MVAC and DC zone multi-agent systems – coordination case study

In the study for coordination of the MVAC and DC zone multi-agent systems, the simulation step size was chosen as 15 microseconds in the PSCAD simulation. The diagram of a simplified notional all-electric ship power system simulation model for coordination of MVAC and DC zone multi-agent systems is shown in Figure 5.44. The simulation duration was 50 seconds. Two DC zones were included in the simulation. Both the MTG and ATG generators were in service. The total generation capacity was 40 MW. It was assumed that the ship operated in cruise mode from 0 to 30 seconds. At 30 seconds, the operation mode was switched from cruise mode to battle mode until the end of the simulation at 50 seconds. It was also assumed that the cruising speed of the

ship was 27 knots. The propulsion load demand at this cruising speed was 21 MW. A pulse load was served from 30 to 35 seconds. The magnitude and ramp rate of the pulse load were 36 MW and 100 MW/sec, respectively, which is shown in Figure 5.45. This pulse magnitude was extremely large, which was 90% of the total generation capacity.

The operational constraints for the MVAC multi-agent system included (5-1)-(5-5) and operational constraints for the DC zone multi-agent system included (5-8)-(5-11). The parameters of the MVAC and DC zone multi-agent systems in the coordination case study were the same as the parameters in MVAC case studies as shown in section 5.3.1 and DC zone case studies as shown in section 5.3.2. The notional all-electric ship power system used to study the coordination of the two multi-agent systems is discussed in details in Appendix B.4.

When the pulse load was served from 30 to 35 seconds, the ship speed was decreased from 27 to 20 knots, as shown in Figure 5.46. The propulsion load demand, as shown in Figure 5.47, was decreased to compensate for the load changes in the system caused by the pulse load.

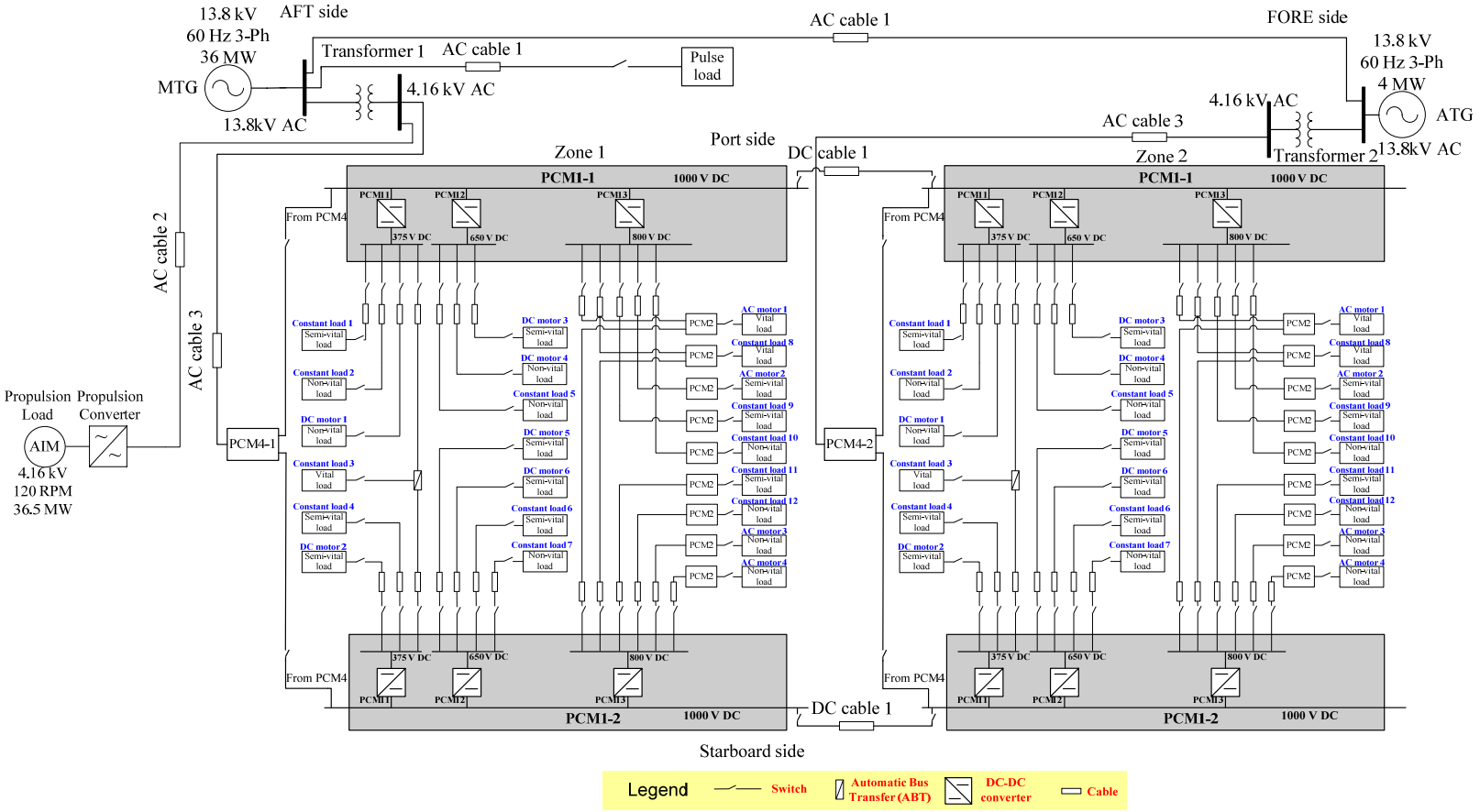

Figure 5.44 Diagram of a simplified notional all-electric ship power system simulation model for coordination of MVAC and DC zone multi-agent systems

The frequency behavior of the MTG generator is shown in Figure 5.48. The frequency drop caused by the connection of the pulse load was 1.9 Hz, which was less than the transient frequency deviation tolerance 2.4 Hz (4% of the normal value). When the pulse load was disconnected from the system, the frequency deviation was 2.9 Hz, which was greater than the transient frequency deviation tolerance. The transient recovery time of the MTG frequency was less than the maximum allowed transient recovery time, which is 2 seconds. Thus, the frequency of the MTG generator did not satisfy the frequency requirements in IEEE-STD-45.

When the pulse load was served, the available power to the DC zone system was also decreased, as shown in Figure 5.49. When the available power signal was decreased, the actual load demand was also reduced using the DC zone multi-agent system to follow the available power signal. At 35 seconds, the pulse load was disconnected, which increased the available power to the DC zone system, as shown in Figure 5.49. The actual load demand was regulated to follow the available power signal gradually. Input powers to PCM4-1 and PCM4-2 are shown in Figure 5.50. The PCM4 power capacity constraint was always satisfied.

In this case study, the coordination study of MVAC and DC zone multi-agent systems is presented. A 36 MW pulse load was served to verify the effectiveness of the real-time load management technique in this extreme case. When the pulse load was served, the propulsion load and lower priority service loads in DC zones were interrupted immediately to compensate the impact of the pulse load on the power quality

of the all-electric ship power system. The ship speed was decreased by around 7 knots due to the interruption of the pulse load.

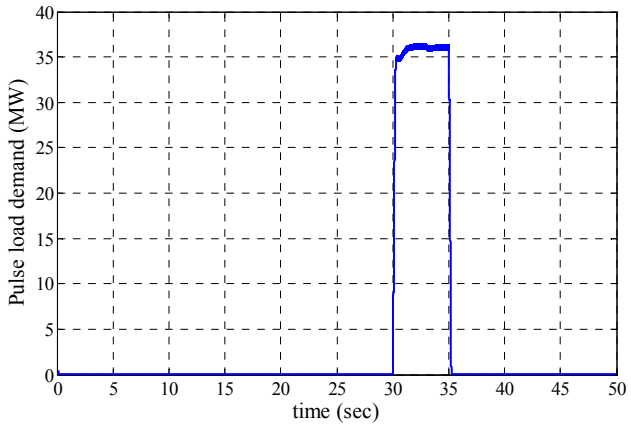

Figure 5.45 Power demand of the pulse load in the coordination case study

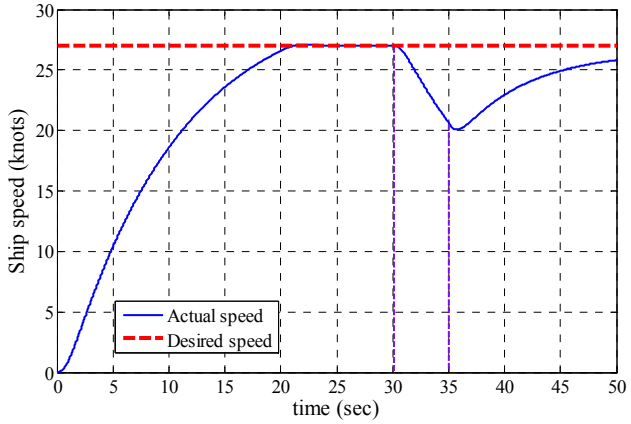

Figure 5.46 Desired ship speed and actual ship speed in the coordination case study

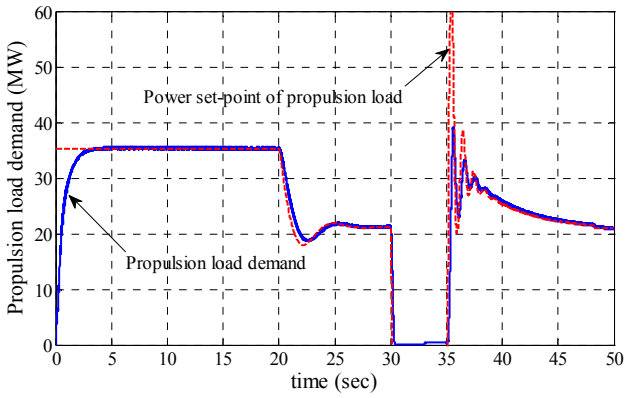

Figure 5.47 Propulsion load demand in the coordination case study

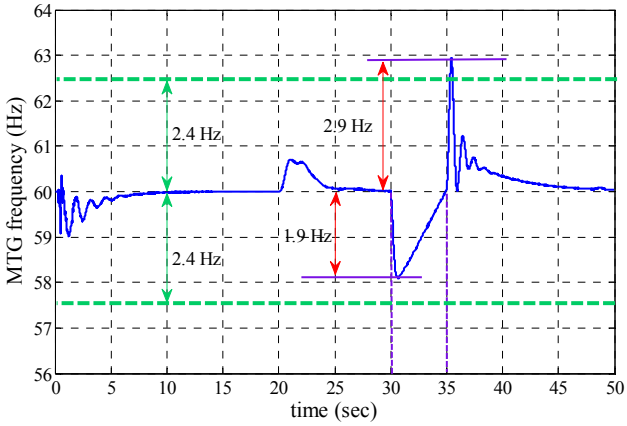

Figure 5.48 Frequency behavior of the MTG generator in the coordination case study

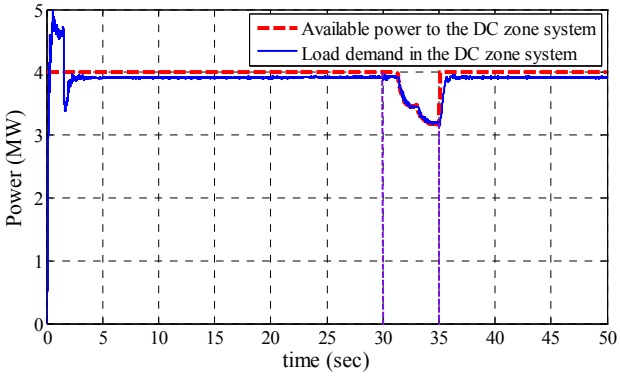

Figure 5.49 Available power and actual power demand of the DC zone system in the coordination case study

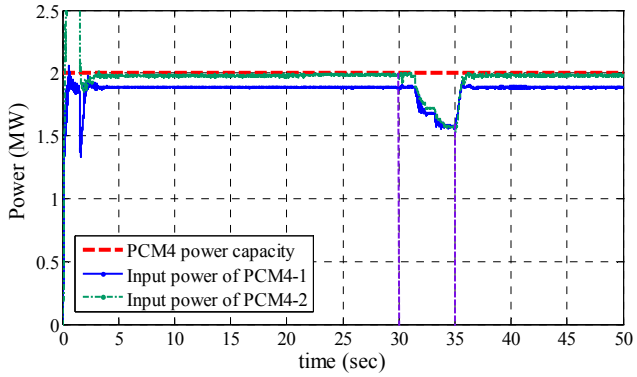

Figure 5.50 Input powers to PCM4-1 and PCM4-2 in the coordination case study

5.4 Performance Analysis

To evaluate the dynamic performance of the developed multi-agent system framework, two metrics [95] were used as defined in (5-12).

$$\begin{aligned} J_1 &= t_1 - t_0 \\ J_2 &= \left\| y(t) \right\|_\infty = \sup_{t \ge t_0} \left| y(t) - y_{desired} \right| \end{aligned} \tag{5-12}$$

The first metric, J_1, was used to evaluate the convergence time of a system state, which is shown in Figure 5.51(a). ε is an error tolerance. This metric was used to measure the convergence time of a system state after a disturbance happens. As shown in Figure 5.51(a), after the disturbance happens at t_0, the trajectory moves outside the tolerance boundary and the trajectory gradually converges inside the tolerance boundary at t_1. The second metric, J_2, was used to evaluate the maximum deviation of a system state from its desired value, which is shown in Figure 5.51(b). $\left\| y(t) \right\|_\infty$ is the infinity norm of signal $y(t)$. As shown in Figure 5.51(b), the trajectory includes oscillations after a system

disturbance, and this metric is used to measure the maximum deviation of the oscillation signal.

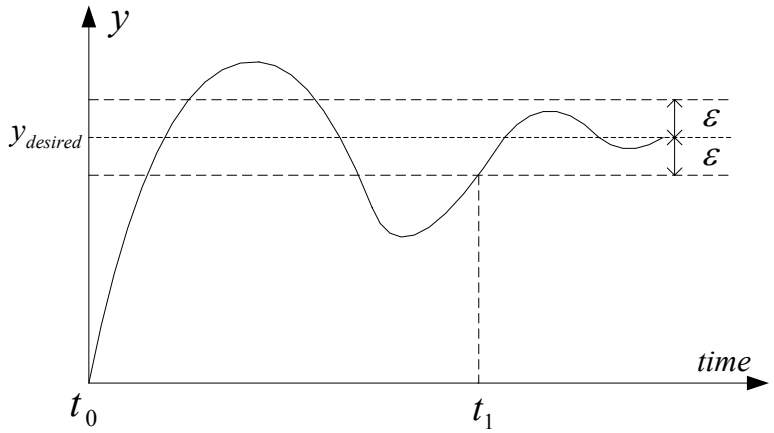

(a)

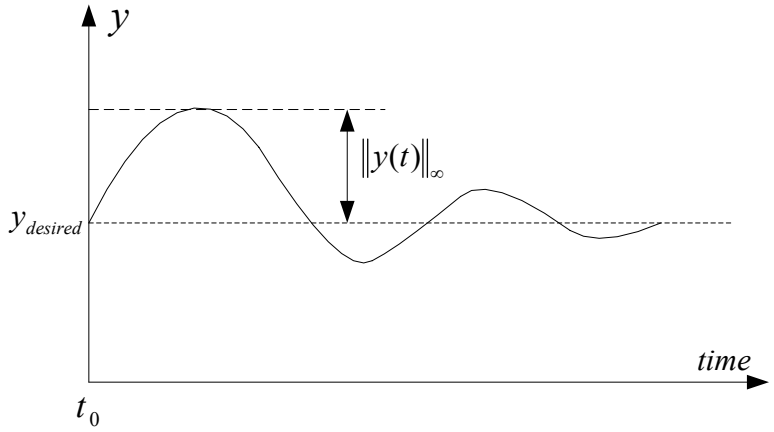

(b)

Figure 5.51 Performance metrics for the multi-agent system. **(a**) Performance metric for convergence time, **(b)** Performance metric for maximum deviation

5.4.1 Performance analysis – MVAC multi-agent system

In the MVAC multi-agent system performance analysis, the diagram of the simplified notional all-electric ship power system simulation model for MVAC multi-

agent system is shown in Figure 5.3, which is the same as the system used in MVAC multi-agent system case studies in section 5.3.1. Three scenarios were used to evaluate the dynamic performances of the MVAC multi-agent system using the two metrics. In the scenario, it was assumed that the MTG and ATG generators were both available, so the total generation capacity was 40 MW. DC zone details were neglected and each DC zones was represented by a constant resistive load. The simulation step size was 40 microseconds and the simulation duration was 60 seconds. The notional all-electric ship power system used for the performance analysis for the MVAC multi-agent system is discussed in detail in Appendix B.2. The parameters and mathematical models of the MTG and ATG agents, propulsion load agent, and pulse load agent are given in Appendices A.1-A.3. The operational constraints of the MVAC system used in the three scenarios are shown in (5-1)-(5-5).

In Scenario I, the propulsion load demand was 21 MW and the cruising speed was 27 knot. Twelve pulse loads with different power ratings and pulse widths were used. The power ratings of pulse loads were in the range of 5 to 15 MW. In this scenario, the propulsion load could fully compensate for the pulse load demand and the dynamic behaviors of the MVAC multi-agent system were studied. In Scenario II, the propulsion load demand was decreased to 10.5 MW and the cruising speed was 22 knots. The power ratings of pulse loads were also in the range of 5 to 15 MW. In this scenario, the propulsion load could not fully compensate for the pulse load demand and the dynamic behaviors of the MVAC multi-agent system were studied. In Scenario III, the power ratings of pulse loads were 35 MW, which were extremely high compared with the total

generation capacity. In this scenario, the pulse load demand was very close to the generation capacity, and the performance of the MVAC multi-agent system was explored in extreme cases.

5.4.1.1 MVAC multi-agent system – Scenario I

Twelve case studies were simulated in this scenario. The pulse load was served at 30 seconds. The power ratings, pulse widths, and ramp rates of the pulse load in this scenario are summarized in Table 5.5. The propulsion load demand was 21 MW in steady state to maintain the cruising speed at 27 knots. The power ratings of pulse loads were 5, 10, or 15 MW, which were less than the propulsion load demand. Thus, the propulsion load could fully compensate for the pulse load demand in this scenario.

Table 5.5 Summary of the pulse load in MVAC multi-agent system – Scenario I

Case No.	Pulse magnitude (MW)	Pulse width (sec)	Ramp rate (MW/sec)	Propulsion load demand (MW)
1	5	1	100	21
2	5	2	100	21
3	5	3	100	21
4	5	5	100	21
5	10	1	100	21
6	10	2	100	21
7	10	3	100	21
8	10	5	100	21
9	15	1	150	21
10	15	2	150	21
11	15	3	150	21
12	15	5	150	21

In cases 1-4, the power rating of each pulse load were 5 MW and the pulse widths were 1, 2, 3, and 5 seconds, respectively. In case 1, the pulse load and propulsion load demands are shown in Figure 5.52. In this case, the pulse width was 1 second and

the pulse load was served from 30 to 31 seconds. In case 2, the pulse load and propulsion load demands are shown in Figure 5.53. In this case, the pulse width was 2 seconds and the pulse load was served from 30 to 32 seconds. In case 3, the pulse load and propulsion load demands are shown in Figure 5.54. In this case, the pulse width was 3 seconds and the pulse load was served from 30 to 33 seconds. In case 4, the pulse load and propulsion load demands are shown in Figure 5.55. In this case, the pulse width was 5 seconds and the pulse load was served from 30 to 35 seconds.

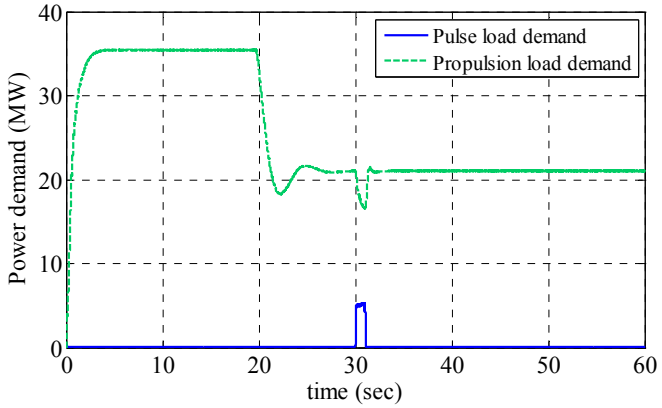

Figure 5.52 Pulse load and propulsion load demands in case 1 of MVAC multi-agent system – Scenario I

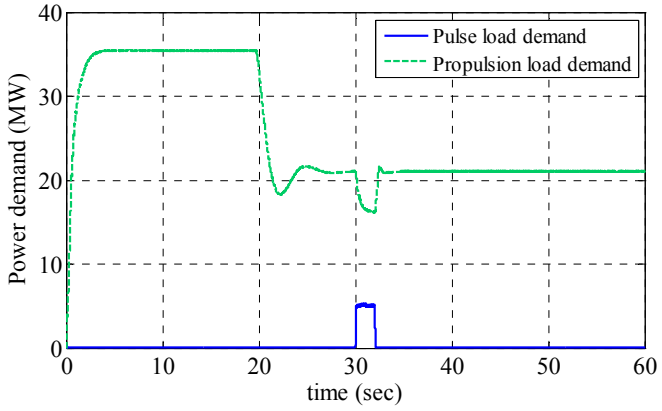

Figure 5.53 Pulse load and propulsion load demands in case 2 of MVAC multi-agent system – Scenario I

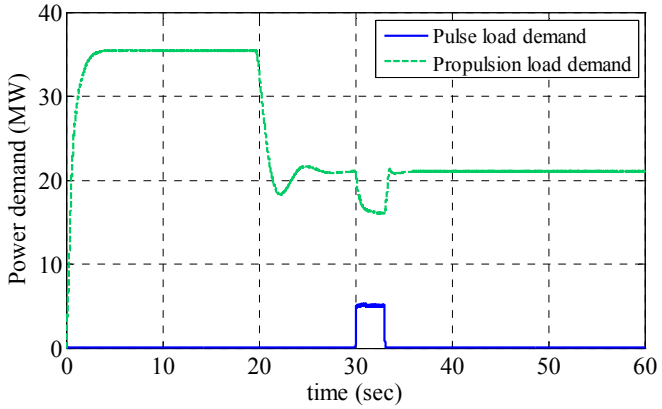

Figure 5.54 Pulse load and propulsion load demands in case 3 of MVAC multi-agent system – Scenario I

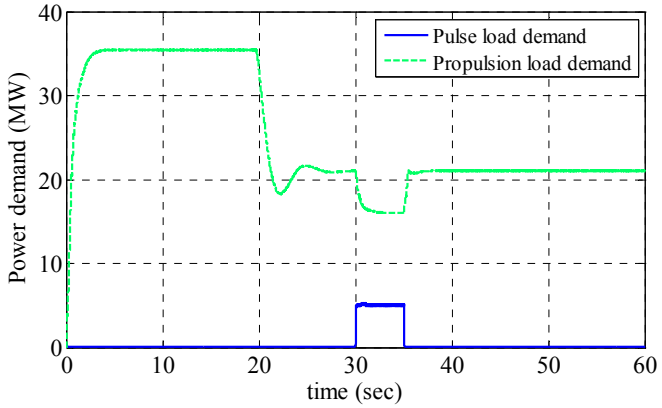

Figure 5.55 Pulse load and propulsion load demands in case 4 of MVAC multi-agent system – Scenario I

Comparison of the MTG generator frequency with 5 MW pulse loads with different pulse widths is shown in Figure 5.56. In this scenario, we mainly focus on the system frequency when the pulse load was connected or disconnected, so the frequency signal was plotted from 25 to 40 seconds. The connection and disconnection of the pulse load caused frequency oscillations. The deviation magnitude of each frequency signal was much less than the steady state frequency tolerance, which was 1.8 Hz. The ship speeds of cases 1 to 4 are shown in Figure 5.57. In this scenario, we mainly focus on the

ship speed decrease after the disturbance of the pulse load, so the ship speed was plot from 25 to 60 seconds. When the pulse load was served at 30 seconds, the ship speed began to decrease slowly until the pulse load was disconnected from the system.

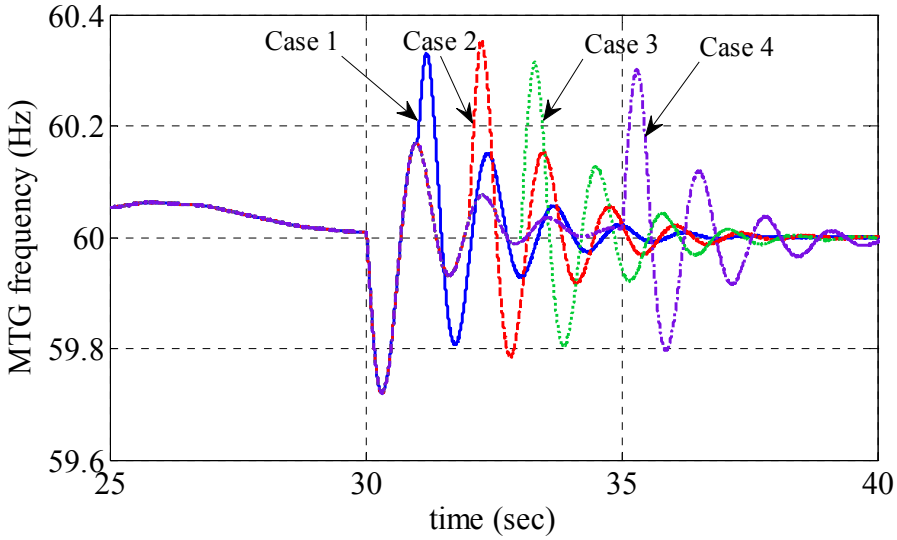

Figure 5.56 Comparison of the MTG generator frequency with 5 MW pulse loads with different pulse widths in MVAC multi-agent system – Scenario I

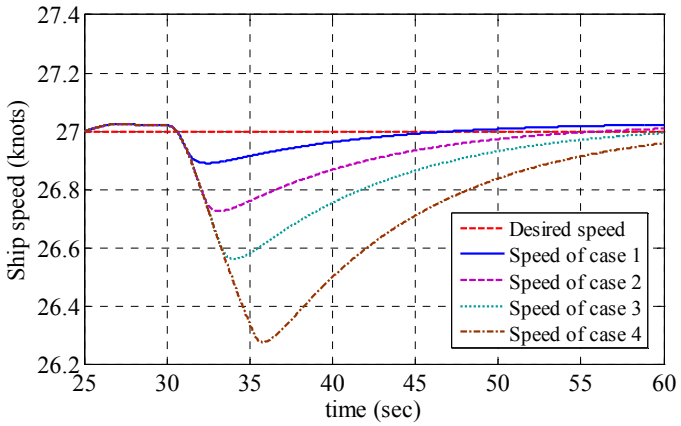

Figure 5.57 Comparison of ship speed with 5 MW pulse loads with different pulse widths in MVAC multi-agent system – Scenario I

In cases 5-8, the power rating of each pulse load was 10 MW and the pulse widths were 1, 2, 3, and 5 seconds, respectively. In case 5, the pulse load and propulsion load demands are shown in Figure 5.58. In this case, the pulse width was 1 second and the pulse load was served from 30 to 31 seconds. In case 6, the pulse load and propulsion load demands are shown in Figure 5.59. In this case, the pulse width was 2 seconds and the pulse load was served from 30 to 32 seconds. In case 7, the pulse load and propulsion load demands are shown in Figure 5.60. In this case, the pulse width was 3 seconds and the pulse load was served from 30 to 33 seconds. In case 8, the pulse load and propulsion load demands are shown in Figure 5.61. In this case, the pulse width was 5 seconds and the pulse load was served from 30 to 35 seconds.

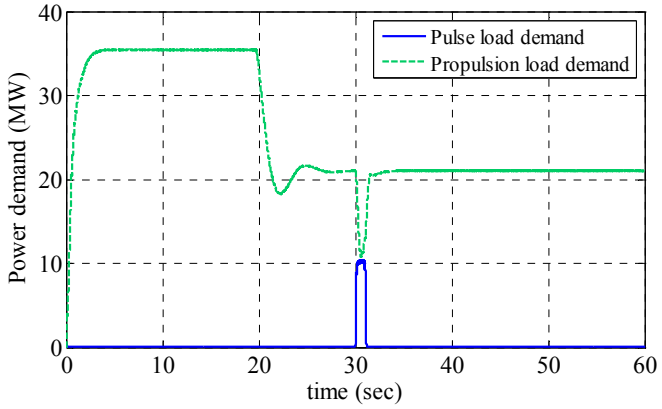

Figure 5.58 Pulse load and propulsion load demands in case 5 of MVAC multi-agent system – Scenario I

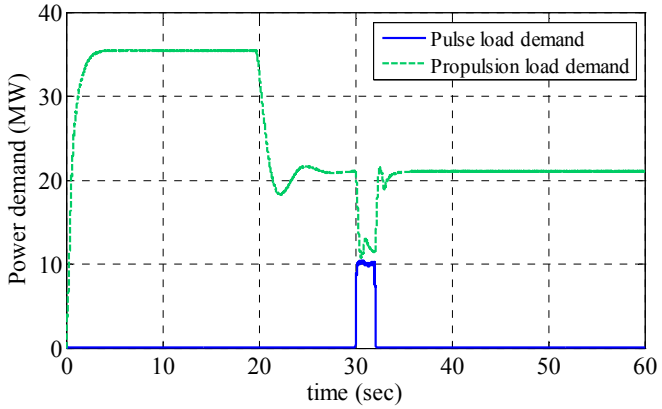

Figure 5.59 Pulse load and propulsion load demands in case 6 of MVAC multi-agent system – Scenario I

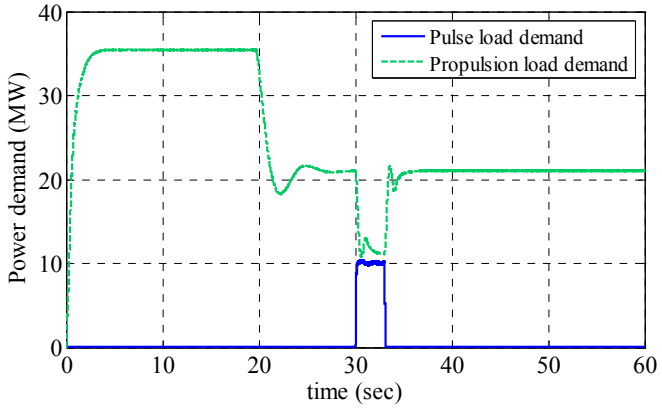

Figure 5.60 Pulse load and propulsion load demands in case 7 of MVAC multi-agent system – Scenario I

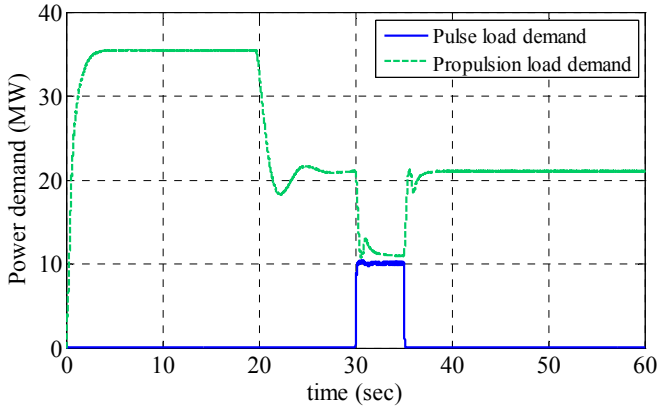

Figure 5.61 Pulse load and propulsion load demands in case 8 of MVAC multi-agent system – Scenario I

Comparison of the MTG generator frequency with 10 MW pulse loads with different pulse widths is shown in Figure 5.62. The connection and disconnection of the pulse load caused frequency oscillations. The deviation magnitude of each frequency signal was much less than the steady state frequency tolerance, which was 1.8 Hz. The ship speeds of cases 5 to 8 are shown in Figure 5.63. When the pulse load was served at 30 seconds, the ship speed began to decrease slowly until the pulse load was disconnected from the system.

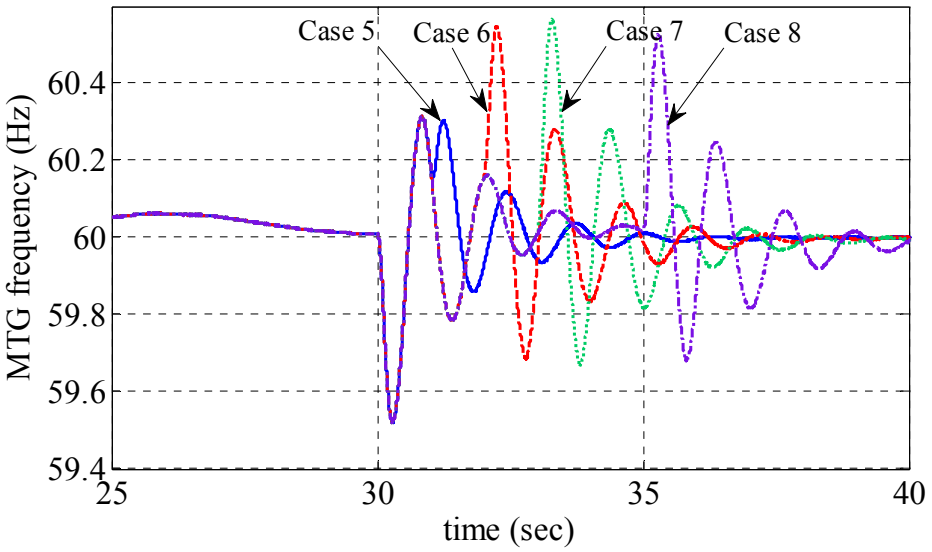

Figure 5.62 Comparison of the MTG generator frequency with 10 MW pulse loads with different pulse widths in MVAC multi-agent system – Scenario I

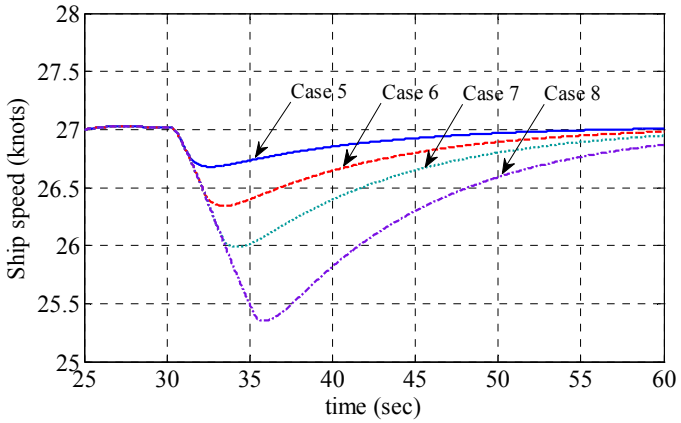

Figure 5.63 Comparison of ship speed with 10 MW pulse loads with different pulse widths in MVAC multi-agent system – Scenario I

In cases 9-12, the power rating of each pulse load was 15 MW and the pulse widths were 1, 2, 3, and 5 seconds, respectively. In case 9, the pulse load and propulsion load demands are shown in Figure 5.64. In this case, the pulse width was 1 second and the pulse load was served from 30 to 31 seconds. In case 10, the pulse load and propulsion load demands are shown in Figure 5.65. In this case, the pulse width was 2 seconds and the pulse load was served from 30 to 32 seconds. In case 11, the pulse load and propulsion load demands are shown in Figure 5.66. In this case, the pulse width was 3 seconds and the pulse load was served from 30 to 33 seconds. In case 12, the pulse load and propulsion load demands are shown in Figure 5.67. In this case, the pulse width was 5 seconds and the pulse load was served from 30 to 35 seconds.

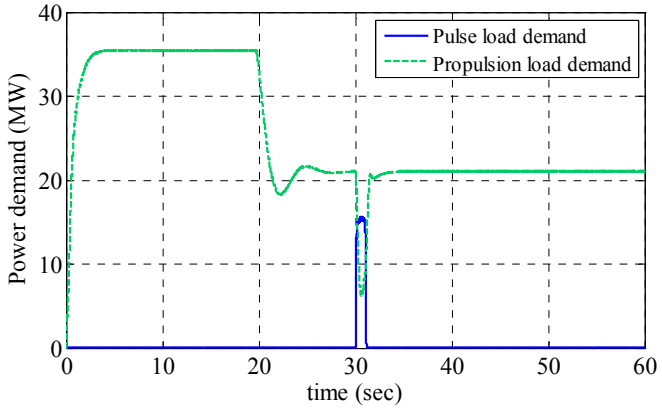

Figure 5.64 Pulse load and propulsion load demands in case 9 of MVAC multi-agent system – Scenario I

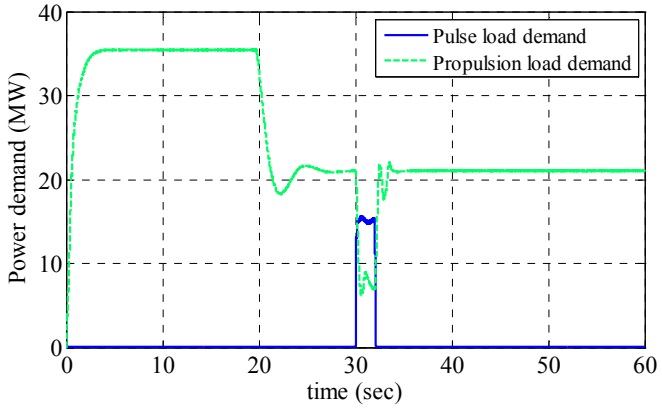

Figure 5.65 Pulse load and propulsion load demands in case 10 of MVAC multi-agent system – Scenario I

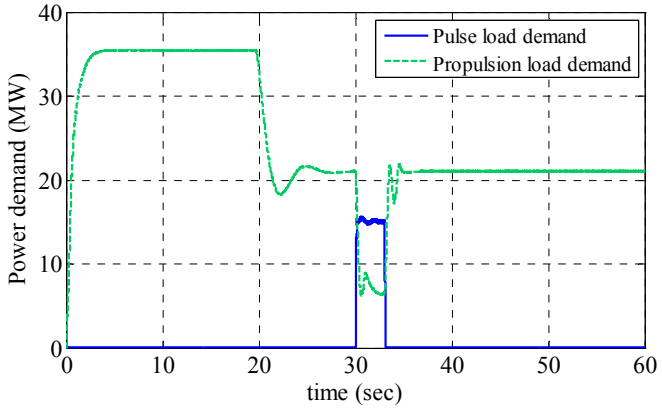

Figure 5.66 Pulse load and propulsion load demands in case 11 of MVAC multi-agent system – Scenario I

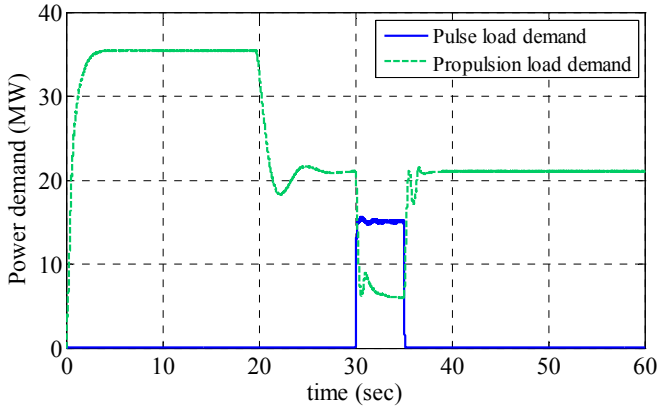

Figure 5.67 Pulse load and propulsion load demands in case 12 of MVAC multi-agent system – Scenario I

Comparison of the MTG generator frequency with 15 MW pulse loads with different pulse widths is shown in Figure 5.68. The connection and disconnection of the pulse load caused frequency oscillations. The deviation magnitude of each frequency signal was less than the steady state frequency tolerance, which was 1.8 Hz. The ship speeds of cases 9 to 12 are shown in Figure 5.69. When the pulse load was served at 30 seconds, the ship speed began to decrease slowly until the pulse load was disconnected from the system.

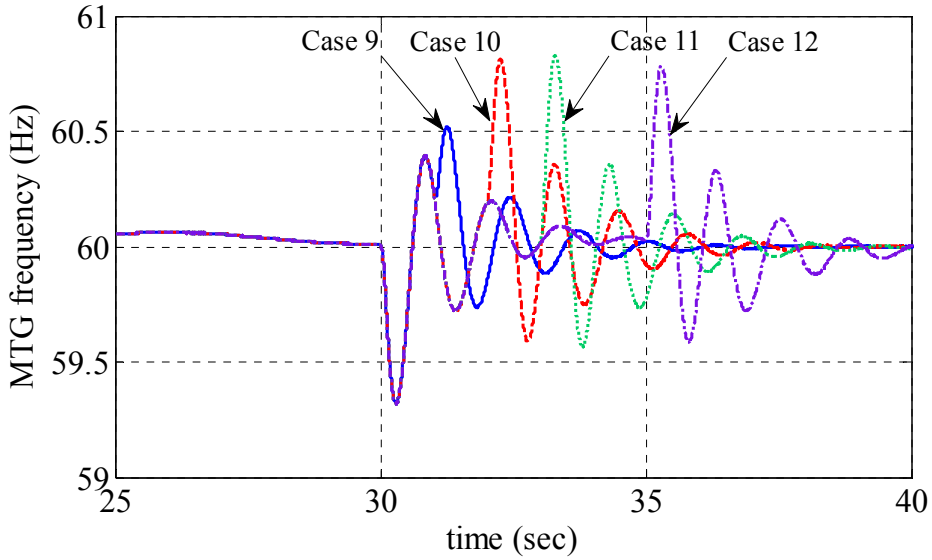

Figure 5.68 Comparison of the MTG generator frequency with 15 MW pulse loads with different pulse widths in MVAC multi-agent system – Scenario I

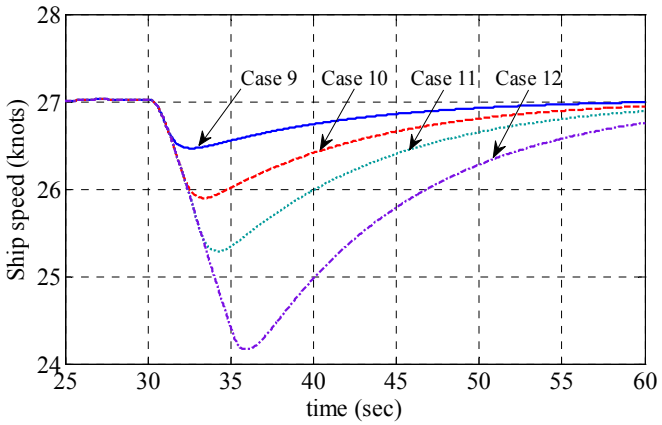

Figure 5.69 Comparison of ship speed with 15 MW pulse loads with different pulse widths in MVAC multi-agent system – Scenario I

The performance metrics, J_1 and J_2, were used to evaluate the dynamic performance of the MTG generator frequency for pulse loads with different power ratings and pulse widths.

Metric 1 analyzed the convergence time of the frequency signal when a pulse load was connected and disconnected in the MVAC multi-agent system. The frequency error tolerance ε of metric 1 was chosen as 3% of the nominal frequency because the steady state frequency tolerance is 3% of the nominal value as discussed in IEEE-STD-45 [17]. The convergence time of the system frequency should always be less than 2 seconds. To compute the value of metric 1, J_1, the MTG frequency signal is used. When the frequency deviation is larger than 3% of the nominal frequency, the time instant, t_0, is obtained; when the frequency deviation returns less than 3% of the nominal frequency, the time instant, t_1, is obtained. The value of metric 1, J_1, is equal to $t_1 - t_0$. Metric 2 was used to evaluate the maximum frequency deviation from the nominal value. To compute the value of metric 2, J_2, the maximum deviation of the MTG generator is obtained first. The value of metric 2, J_2, is equal to the maximum deviation of the MTG generator. In all-electric ship power systems, the frequency deviation of the system frequency should always be less than 4% of the nominal value [17].

The results are summarized in Table 5.6. The results indicated that when pulse magnitude was increased, the magnitude of the MTG frequency deviation was also increased shown in Figure 5.56, Figure 5.62, and Figure 5.68. The value of metric 2, J_2, is increased with the increase of the pulse magnitude, which is much less than 3% of the nominal frequency. The MTG frequency deviation was always less than the steady state frequency tolerance, and the value of metric 1 was equal to 0 in each case study in

Scenario I. Therefore, the behavior of the MTG frequency in each case satisfied the frequency requirements of IEEE-STD-45 very well in this scenario.

Table 5.6 Summary of the frequency performance of the MTG generator in MVAC multi-agent system – Scenario I

Case No.	Pulse magnitude (MW)	Pulse width (sec)	Ramp rate (MW/sec)	Metric 1 (sec)	Metric 2 (Hz)
1	5	1	100	0	0.332
2	5	2	100	0	0.351
3	5	3	100	0	0.314
4	5	5	100	0	0.302
5	10	1	100	0	0.478
6	10	2	100	0	0.545
7	10	3	100	0	0.568
8	10	5	100	0	0.527
9	15	1	150	0	0.680
10	15	2	150	0	0.816
11	15	3	150	0	0.834
12	15	5	150	0	0.782

5.4.1.2 MVAC multi-agent system – Scenario II

Twelve case studies were simulated in this scenario. The pulse load was served at 30 seconds. The definitions of pulse loads were the same as MVAC multi-agent system – Scenario I, which are shown in Table 5.5. The propulsion load demand was 10.5 MW in steady state to maintain the cruising speed of the ship at 22 knots. The power ratings of pulse loads were 5, 10, and 15 MW. The propulsion load could fully compensate for the pulse load demand when the power rating of the pulse load was 5 or 10 MW, but could not fully compensate for the pulse load demand when the power rating of the pulse load was 15 MW.

In cases 1-4, the power rating of each pulse load were 5 MW and the pulse widths were 1, 2, 3, and 5 seconds, respectively. In case 1, the pulse load and propulsion

load demands are shown in Figure 5.70. In this case, the pulse width was 1 second and the pulse load was served from 30 to 31 seconds. In case 2, the pulse load and propulsion load demands are shown in Figure 5.71. In this case, the pulse width was 2 seconds and the pulse load was served from 30 to 32 seconds. In case 3, the pulse load and propulsion load demands are shown in Figure 5.72. In this case, the pulse width was 3 seconds and the pulse load was served from 30 to 33 seconds. In case 4, the pulse load and propulsion load demands are shown in Figure 5.73. In this case, the pulse width was 5 seconds and the pulse load was served from 30 to 35 seconds.

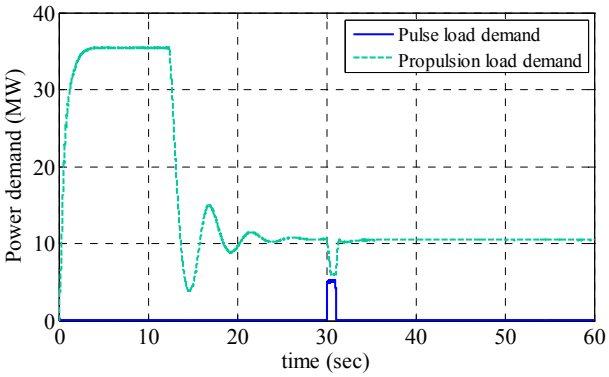

Figure 5.70 Pulse load and propulsion load demands in case 1 of MVAC multi-agent system – Scenario II

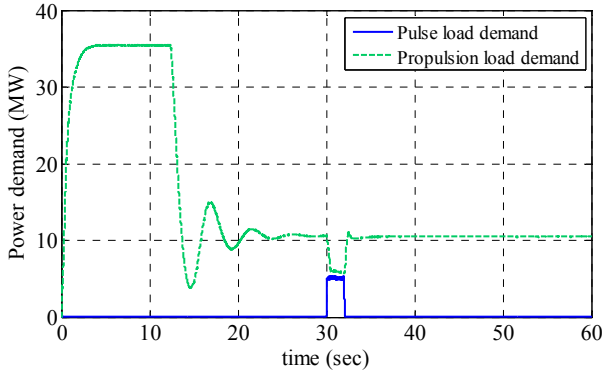

Figure 5.71 Pulse load and propulsion load demands in case 2 of MVAC multi-agent system – Scenario II

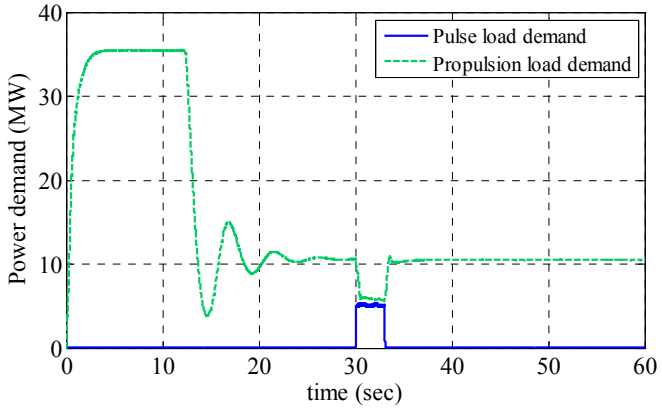

Figure 5.72 Pulse load and propulsion load demands in case 3 of MVAC multi-agent system – Scenario II

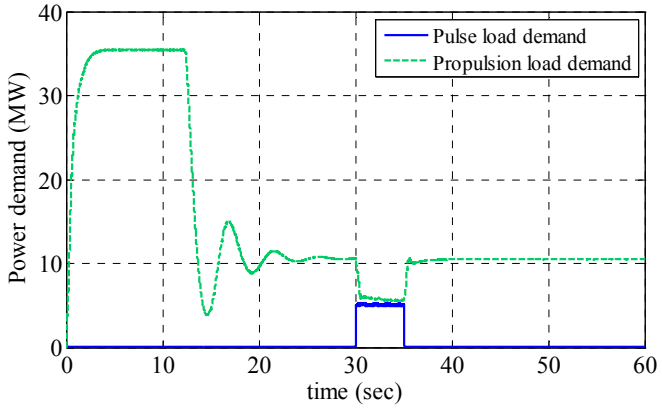

Figure 5.73 Pulse load and propulsion load demands in case 4 of MVAC multi-agent system – Scenario II

Comparison of the MTG generator frequency with 5 MW pulse loads with different pulse widths is shown in Figure 5.74. In this scenario, we mainly focus on the system frequency when the pulse load was connected or disconnected, so the frequency signal was plotted from 25 to 40 seconds. The connection and disconnection of the pulse load caused frequency oscillations. The deviation magnitude of each frequency signal was much less than the steady state frequency tolerance, which was 1.8 Hz.

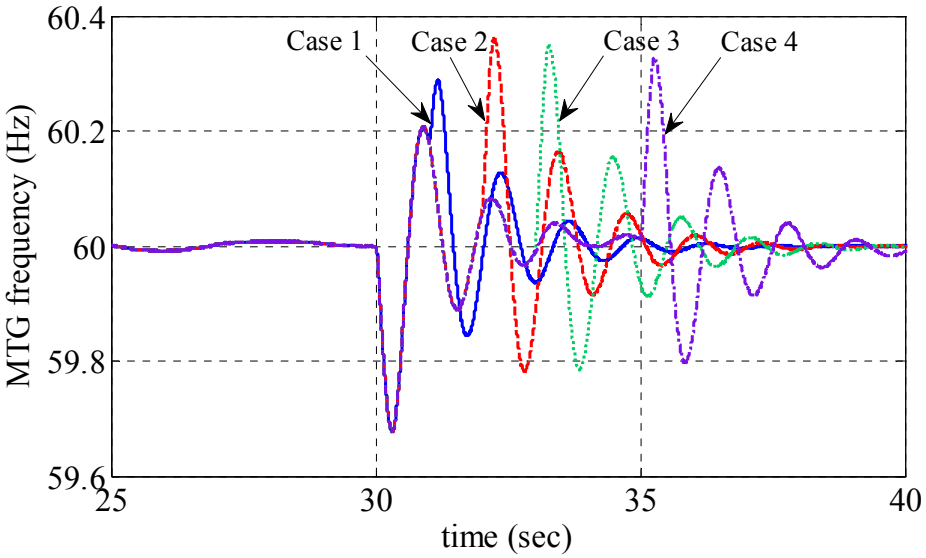

Figure 5.74 Comparison of the MTG generator frequency with 5 MW pulse loads with different pulse widths in MVAC multi-agent system – Scenario II

In cases 5-8, the power rating of each pulse load were 10 MW and the pulse widths were 1, 2, 3, and 5 seconds, respectively. In case 5, the pulse load and propulsion load demands are shown in Figure 5.75. In this case, the pulse width was 1 second and the pulse load was served from 30 to 31 seconds. In case 6, the pulse load and propulsion load demands are shown in Figure 5.76. In this case, the pulse width was 2 seconds and the pulse load was served from 30 to 32 seconds. In case 7, the pulse load and propulsion load demands are shown in Figure 5.77. In this case, the pulse width was 3 seconds and the pulse load was served from 30 to 33 seconds. In case 8, the pulse load and propulsion load demands are shown in Figure 5.78. In this case, the pulse width was 5 seconds and the pulse load was served from 30 to 35 seconds.

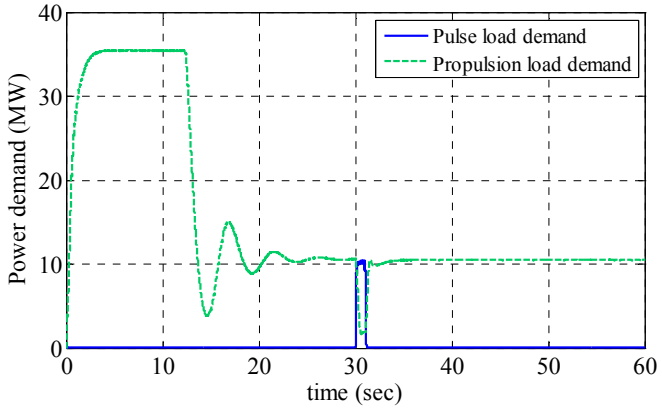

Figure 5.75 Pulse load and propulsion load demands in case 5 of MVAC multi-agent system – Scenario II

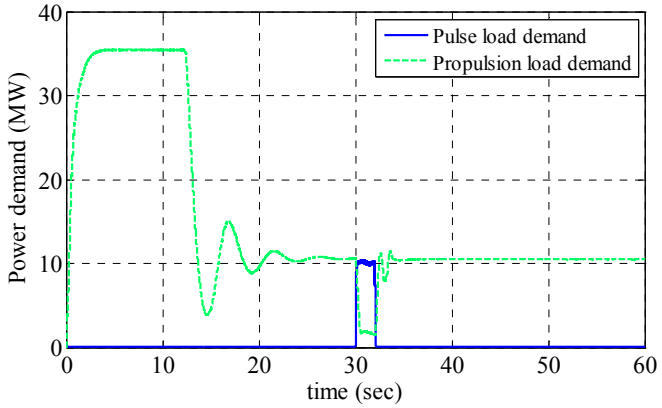

Figure 5.76 Pulse load and propulsion load demands in case 6 of MVAC multi-agent system – Scenario II

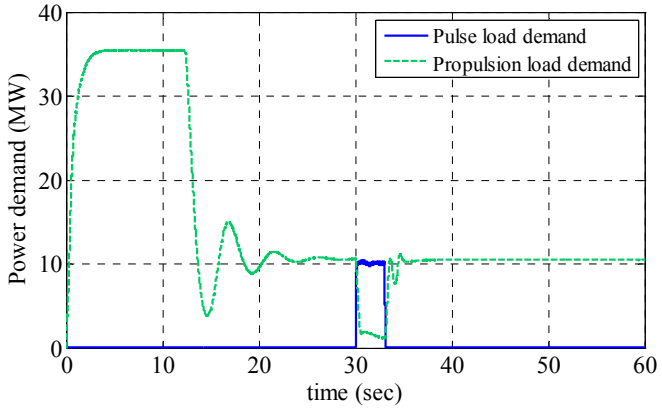

Figure 5.77 Pulse load and propulsion load demands in case 7 of MVAC multi-agent system – Scenario II

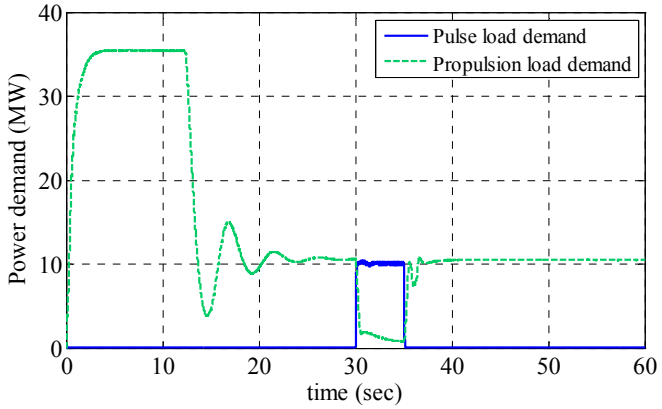

Figure 5.78 Pulse load and propulsion load demands in case 8 of MVAC multi-agent system – Scenario II

Comparison of the MTG generator frequency with 10 MW pulse loads with different pulse widths is shown in Figure 5.79. The connection and disconnection of the pulse load caused frequency oscillations. The deviation magnitude of each frequency signal was much less than the steady state frequency tolerance, which was 1.8 Hz.

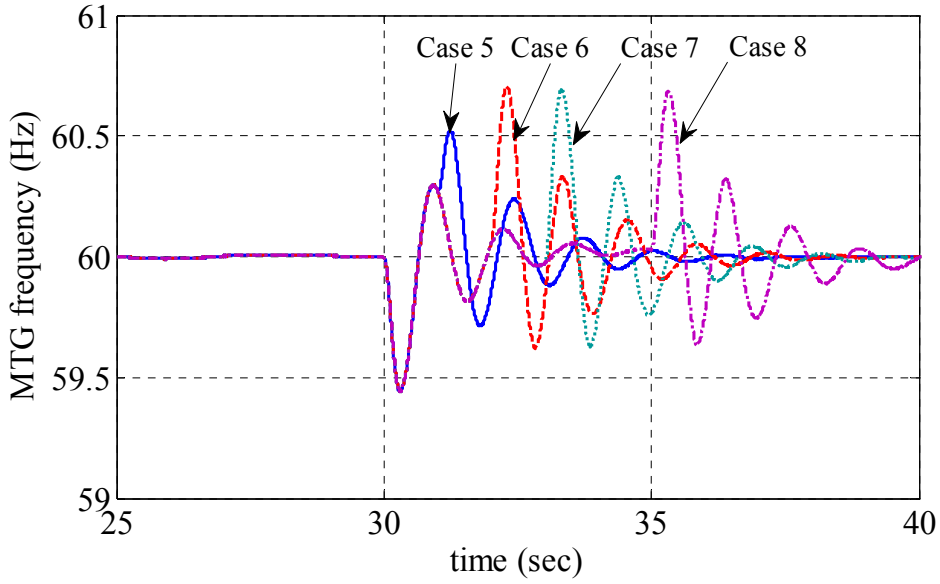

Figure 5.79 Comparison of MTG generator frequency with 10 MW pulse loads with different pulse widths in MVAC multi-agent system – Scenario II

In cases 9-12, the power rating of each pulse load was 15 MW and the pulse widths were 1, 2, 3, and 5 seconds, respectively. In case 9, the pulse load and propulsion load demands are shown in Figure 5.80. In this case, the pulse width was 1 second and the pulse load was served from 30 to 31 seconds. In case 10, the pulse load and propulsion load demands are shown in Figure 5.81. In this case, the pulse width was 2 seconds and the pulse load was served from 30 to 32 seconds. In case 11, the pulse load and propulsion load demands are shown in Figure 5.82. In this case, the pulse width was 3 seconds and the pulse load was served from 30 to 33 seconds. In case 12, the pulse load and propulsion load demands are shown in Figure 5.83. In this case, the pulse width was 5 seconds and the pulse load was served from 30 to 35 seconds.

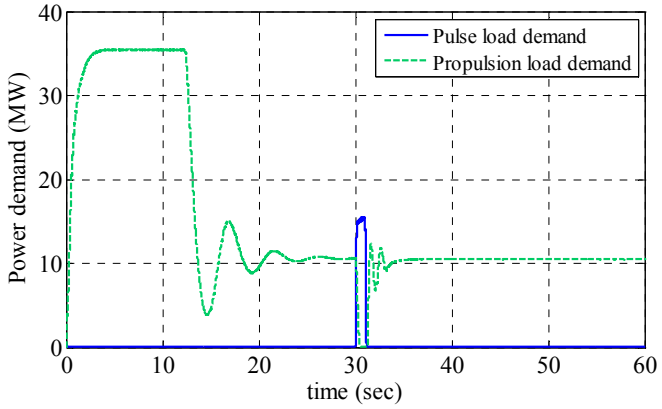

Figure 5.80 Pulse load and propulsion load demands in case 9 of MVAC multi-agent system – Scenario II

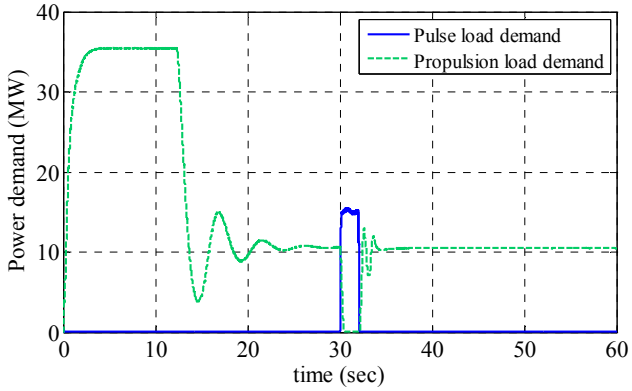

Figure 5.81 Pulse load and propulsion load demands in case 10 of MVAC multi-agent system – Scenario II

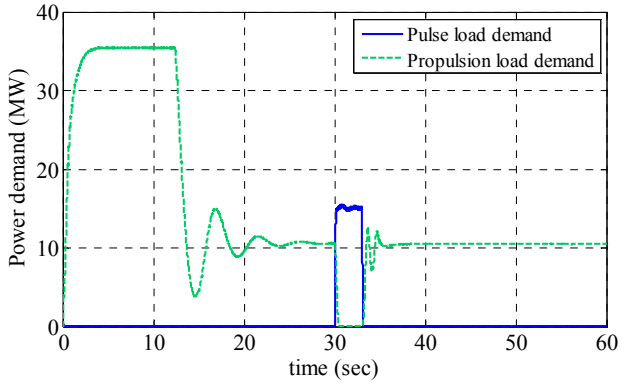

Figure 5.82 Pulse load and propulsion load demands in case 11 of MVAC multi-agent system – Scenario II

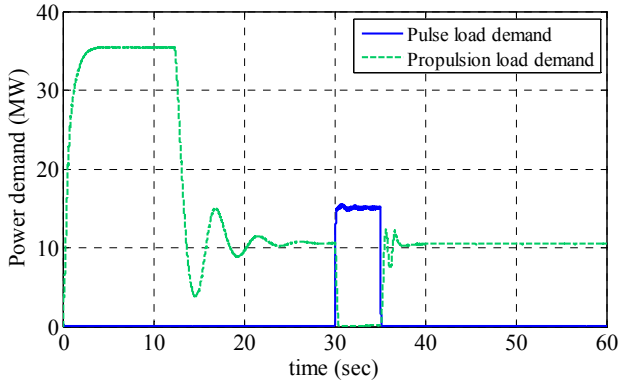

Figure 5.83 Pulse load and propulsion load demands in case 12 of MVAC multi-agent system – Scenario II

Comparison of the MTG generator frequency with 15 MW pulse loads with different pulse widths is shown in Figure 5.84. When the 15 MW pulse load was served, the propulsion load could not fully compensate for the pulse load demand because the total propulsion load demand was only 10.5 MW. Thus, the magnitude of each MTG frequency deviation in cases 9-12 in MVAC multi-agent system – Scenario II was greater than the frequency deviation in MVAC multi-agent system – Scenario I. As shown in Figure 5.84, the magnitude of each MTG frequency deviation in cases 9-12 in MVAC system – scenario II was still less than steady state frequency tolerance, which was equal to 1.8 Hz.

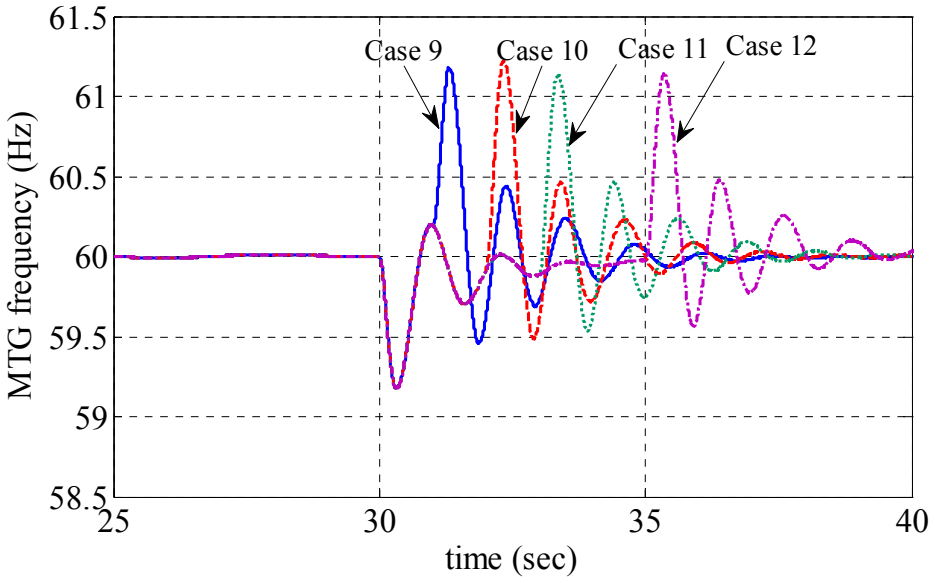

Figure 5.84 Comparison of MTG generator frequency with 15 MW pulse loads with different pulse widths in MVAC multi-agent system – Scenario II

The performance metrics, J_1 and J_2, were used to evaluate the dynamic performance of the MTG generator frequency for pulse loads with different power

ratings and pulse widths. The results in MVAC multi-agent system – Scenario II are summarized in Table 5.7. Metric 1 analyzed the convergence time of the frequency signal when a pulse load was connected and disconnected in the MVAC system. The frequency error tolerance ε of metric 1 was chosen as 3% of the nominal frequency because the steady state frequency tolerance is 3% of the nominal value as discussed in IEEE-STD-45. The convergence time of the system frequency should be less than 2 seconds. Metric 2 was used to evaluate the maximum frequency deviation from the nominal value. In all-electric ship power systems, the frequency deviation of the system frequency should be always less than 4% of the nominal value.

The results indicated that when pulse magnitude was increased, the magnitude of the MTG frequency deviation was increased as shown in Figure 5.74, Figure 5.79, and Figure 5.84. When the propulsion load could not fully compensate for the pulse load demand, the frequency oscillations would be more significant. The value of metric 2, J_2, is increased with the increase of the pulse magnitude, which is much less than 3% of the nominal frequency. In cases 9-12, the pulse load magnitude is larger than propulsion load demand, and the value of metric 2, J_2, is around 1.2, which is larger than the value in Scenario I. The MTG frequency deviation was always less than the steady state frequency tolerance, which was equal to 1.8 Hz, and the value of metric 1 was equal to 0 in each case study in MVAC multi-agent system – Scenario II. Therefore, the behavior of the MTG frequency in each case satisfied the frequency requirements of IEEE-STD-45 very well in this scenario.

Table 5.7 Summary of the frequency performance of the MTG generator in MVAC multi-agent system – Scenario II

Case No.	Pulse magnitude (MW)	Pulse width (sec)	Ramp rate (MW/sec)	Metric 1 (sec)	Metric 2 (Hz)
1	5	1	100	0	0.323
2	5	2	100	0	0.364
3	5	3	100	0	0.351
4	5	5	100	0	0.329
5	10	1	100	0	0.465
6	10	2	100	0	0.707
7	10	3	100	0	0.692
8	10	5	100	0	0.687
9	15	1	150	0	1.180
10	15	2	150	0	1.221
11	15	3	150	0	1.139
12	15	5	150	0	1.138

5.4.1.3 MVAC multi-agent system – Scenario III

Eight extreme cases were simulated to study dynamic behaviors of the MVAC multi-agent system in this scenario. The pulse load was served at 30 seconds. The definitions of the pulse load and propulsion load in each case are shown in Table 5.8. In this scenario, the power rating of the pulse load was 35 MW, which was always larger than the propulsion load demand.

Table 5.8 Summary of the pulse load and propulsion load in MVAC multi-agent system – Scenario III

Case No.	Pulse magnitude (MW)	Pulse width (sec)	Ramp rate (MW/sec)	Propulsion load demand (MW)
1	35	1	350	10.5
2	35	2	350	10.5
3	35	3	350	10.5
4	35	5	350	10.5
5	35	1	350	21
6	35	2	350	21
7	35	3	350	21
8	35	5	350	21

In cases 1-4, the power rating of each pulse load was 35 MW and the pulse widths were 1, 2, 3, and 5 seconds, respectively. The propulsion load demand in each case was 10.5 MW. In steady state, the cruising speed of the ship was 22 knots. In case 1, the pulse load and propulsion load demands are shown in Figure 5.85. In this case, the pulse width was 1 second and the pulse load was served from 30 to 31 seconds. In case 2, the pulse load and propulsion load demands are shown in Figure 5.86. In this case, the pulse width was 2 seconds and the pulse load was served from 30 to 32 seconds. In case 3, the pulse load and propulsion load demands are shown in Figure 5.87. In this case, the pulse width was 3 seconds and the pulse load was served from 30 to 33 seconds. In case 4, the pulse load and propulsion load demands are shown in Figure 5.88. In this case, the pulse width was 5 seconds and the pulse load was served from 30 to 35 seconds.

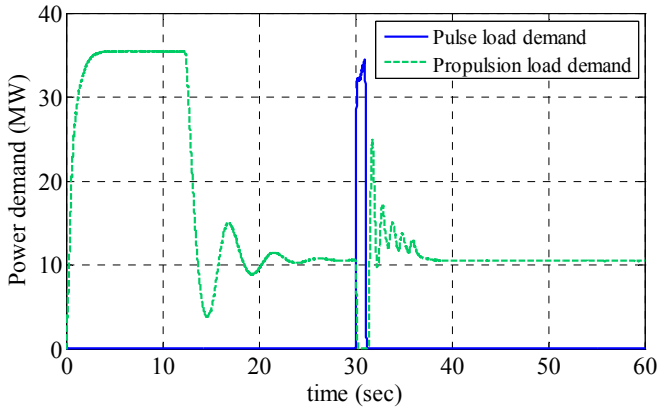

Figure 5.85 Pulse load and propulsion load demands in case 1 of MVAC multi-agent system – Scenario III

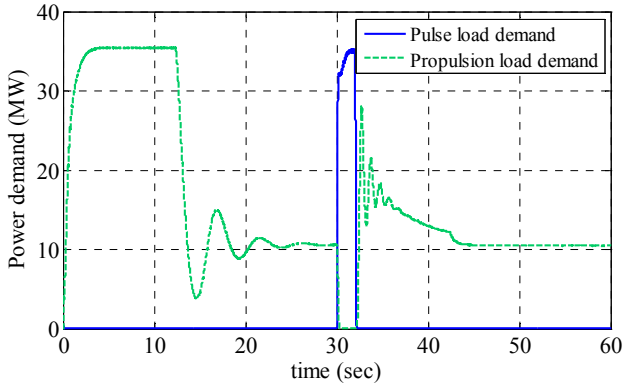

Figure 5.86 Pulse load and propulsion load demands in case 2 of MVAC multi-agent system – Scenario III

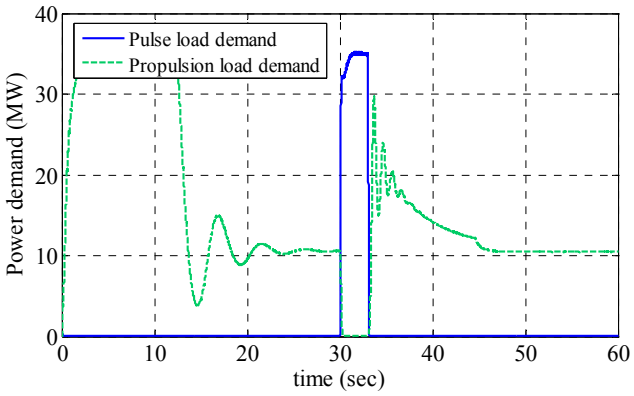

Figure 5.87 Pulse load and propulsion load demands in case 3 of MVAC multi-agent system – Scenario III

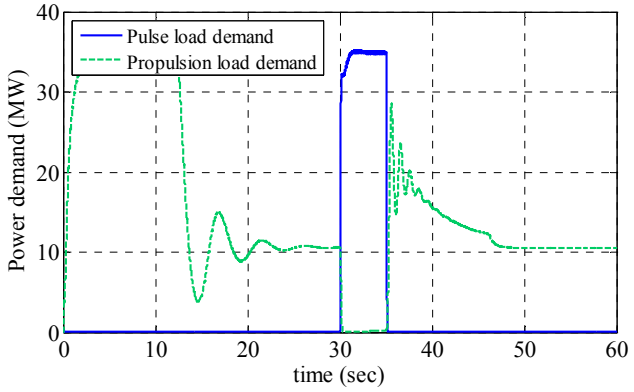

Figure 5.88 Pulse load and propulsion load demands in case 4 of MVAC multi-agent system – Scenario III

Comparison of the MTG frequency in cases 1-4 is shown in Figure 5.89. When the pulse load was connected, the maximum frequency decrease in each case was 4% of the nominal value, which was equal to the transient frequency tolerance. The recovery time of the MTG frequency in each case was less than the maximum allowed transient recovery time, which was 2 seconds. Therefore, when the pulse load was connected to the system, the dynamic behavior of the MTG frequency in each case was acceptable based on IEEE-STD-45 [17]. When the pulse load was disconnected from the system, the magnitude of the frequency deviation in each case was greater than the transient frequency tolerance. Thus, the dynamic behaviors of the MTG frequency in cases 1-4 did not satisfy the frequency requirements of IEEE-STD-45.

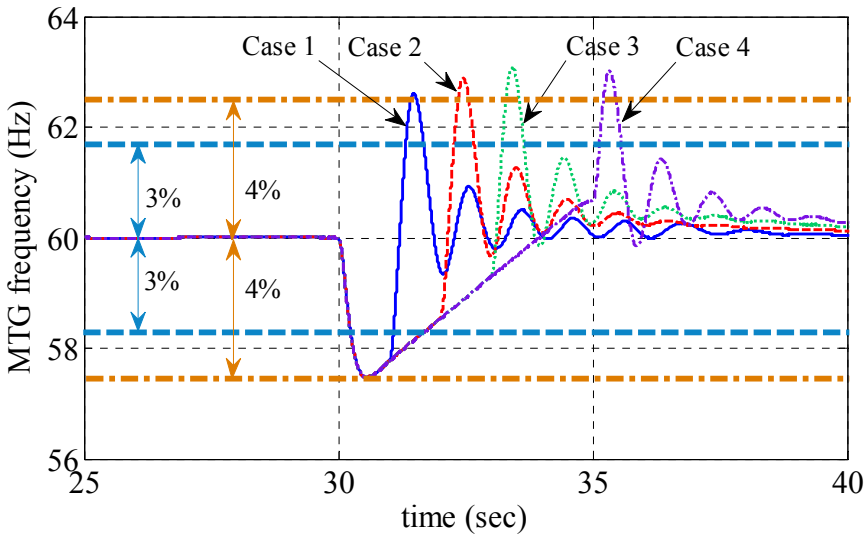

Figure 5.89 Comparison of the MTG generator frequency with 10.5 MW propulsion load and 35 MW pulse loads with different pulse widths in MVAC multi-agent system – Scenario III

In cases 5-8, the power rating of each pulse load was 35 MW and the pulse widths were 1, 2, 3, and 5 seconds, respectively. The propulsion load demand in each

case was 21 MW. In steady state, the cruising speed of the ship was 27 knots. In case 5, the pulse load and propulsion load demands are shown in Figure 5.90. In this case, the pulse width was 1 second and the pulse load was served from 30 to 31 seconds. In case 6, the pulse load and propulsion load demands are shown in Figure 5.91. In this case, the pulse width was 2 seconds and the pulse load was served from 30 to 32 seconds. In case 7, the pulse load and propulsion load demands are shown in Figure 5.92. In this case, the pulse width was 3 seconds and the pulse load was served from 30 to 33 seconds. In case 8, the pulse load and propulsion load demands are shown in Figure 5.93. In this case, the pulse width was 5 seconds and the pulse load was served from 30 to 35 seconds.

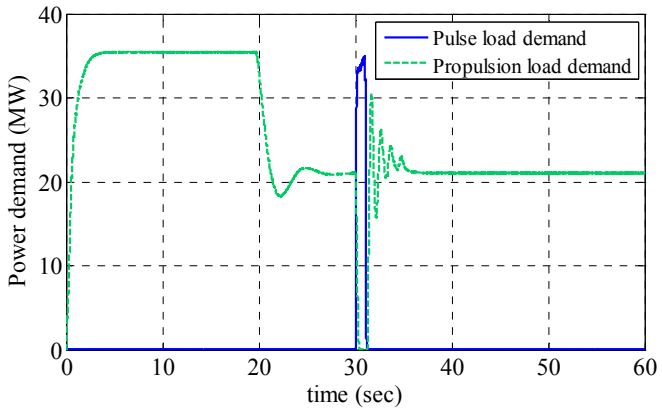

Figure 5.90 Pulse load and propulsion load demands in case 5 of MVAC multi-agent system – Scenario III

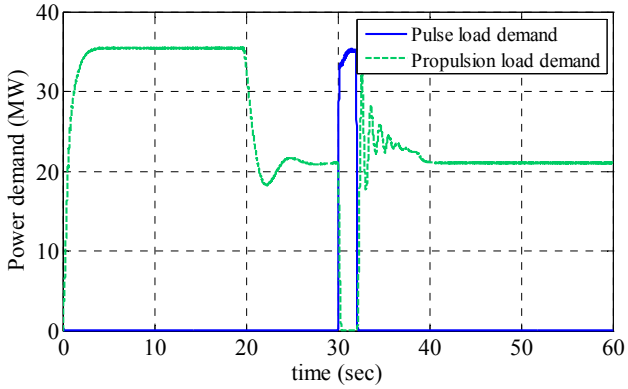

Figure 5.91 Pulse load and propulsion load demands in case 6 of MVAC multi-agent system – Scenario III

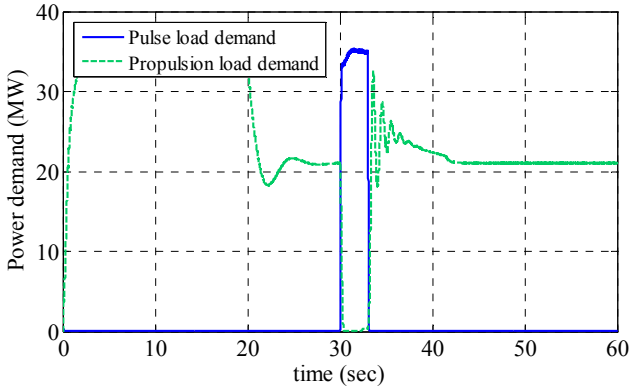

Figure 5.92 Pulse load and propulsion load demands in case 7 of MVAC multi-agent system – Scenario III

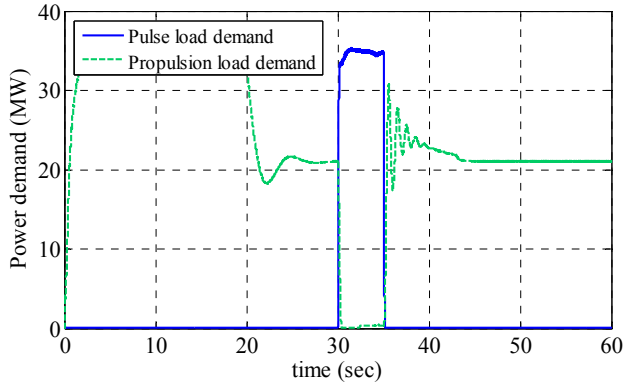

Figure 5.93 Pulse load and propulsion load demands in case 8 of MVAC multi-agent system – Scenario III

Comparison of the MTG frequency in cases 5-8 is shown in Figure 5.94. When the pulse load was connected, the maximum frequency decrease in each case was 3% of the nominal value, which was equal to the steady state frequency tolerance. The transient recovery time of the MTG frequency in each case was 0. Therefore, when the pulse load was connected to the system, the dynamic behavior of the MTG frequency in each case was acceptable based on IEEE-STD-45. When the pulse load was disconnected from the system, the magnitude of the frequency deviation in case 7 was greater than the transient frequency tolerance, and the magnitudes of the frequency deviations in case 5, 6, and 8 were less than the transient frequency tolerance. The transient recovery time of each case was less than the maximum allowed transient recovery time. The dynamic behaviors of the MTG frequency in case 7 did not satisfy the frequency requirements in IEEE-STD-45. The dynamic behaviors of the MTG frequency in case 5, 6, and 8 satisfied the frequency requirements of IEEE-STD-45.

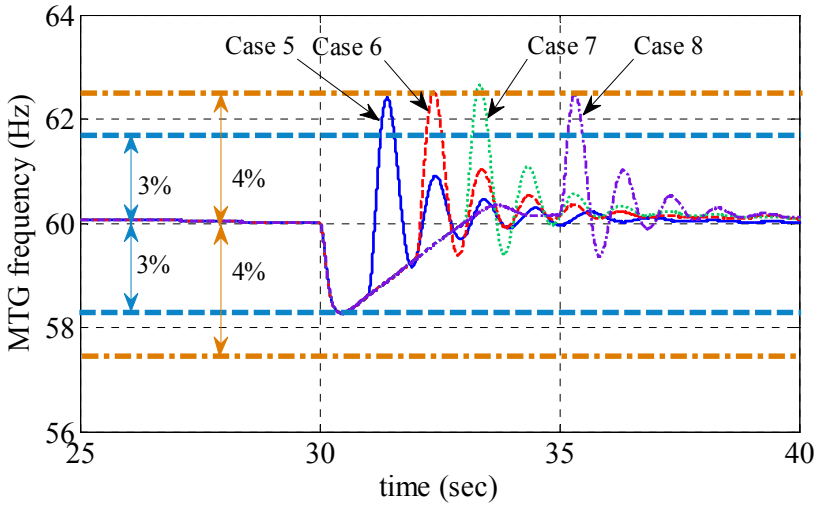

Figure 5.94 Comparison of the MTG generator frequency with 21 MW propulsion load and 35 MW pulse loads with different pulse widths in MVAC system – Scenario III

The performance metrics, J_1 and J_2, were used to evaluate the dynamic performance of the MTG generator frequency for pulse loads with different power ratings and pulse widths. The results in MVAC multi-agent system – Scenario III are summarized in Table 5.9. Metric 1 analyzed the convergence time of the frequency signal when a pulse load was connected and disconnected in the MVAC system. The frequency error tolerance ε of metric 1 was chosen as 3% of the nominal frequency. The convergence time of the system frequency should be less than 2 seconds. Metric 2 was used to evaluate the maximum frequency deviation from the nominal value. In all-electric ship power systems, the frequency deviation of the system frequency should be always less than 4% of the nominal value, which is equal to 2.4 Hz.

The results in Table 5.9 indicated that when the load demand of the propulsion load was increased, the magnitude of the MTG frequency deviation was also increased as shown in Figure 5.89 and Figure 5.94. Since the pulse load demand in each case was much greater than the propulsion load demand, the propulsion load could not fully compensate for the pulse load demand.

In cases 1-4, the propulsion load demand was 10.5 MW, which was less than the pulse load demand. When the pulse load was connected to the system, the steady state frequency tolerance was violated and the transient recovery time was less than the maximum allowed transient recovery time in each case; when the pulse load was disconnected from the system, the transient frequency tolerance was violated in each case. In each case, the value of metric 2, J_2, is larger than 4% of the nominal frequency

as shown in Table 5.9. Thus, the dynamic behaviors of the MTG generator in cases 1-4 did not satisfy the frequency requirements in IEEE-STD-45.

In cases 5-8, the propulsion load demand was 21 MW, which was less than the pulse load demand. When the pulse load was connected to the system, the steady state frequency tolerance was satisfied and the transient recovery time was 0 in each case; when the pulse load was disconnected from the system, the transient frequency tolerance was violated only in case 7. In case 7, the value of metric 2, J_2, is 2.65 Hz, which is larger than 4% of the nominal frequency as shown in Table 5.9. Thus, the dynamic behaviors of the MTG generator in cases 5, 6, and 8 satisfy the frequency requirements of IEEE-STD-45, but the dynamic behavior of the MTG generator in case 7 did not satisfy the frequency requirements of IEEE-STD-45.

Table 5.9 Summary of the frequency performance of the MTG generator in MVAC multi-agent system – Scenario III

Case No.	Metric 1 (sec) - pulse load connection	Metric 1 (sec) - pulse load disconnection	Metric 2 (Hz)
1	0.82	0.32	2.61
2	1.31	0.38	2.89
3	1.31	0.40	3.08
4	1.31	0.43	3.02
5	0	0.26	2.39
6	0	0.29	2.40
7	0	0.32	2.65
8	0	0.29	2.40

5.4.2 Performance analysis – DC zone multi-agent system

In the DC zone multi-agent system studies, the diagram of a simplified notional all-electric ship power system simulation model for DC zone multi-agent system is

shown in Figure 5.26, and the simulation step size $\Delta\tau$ was chosen as 12 microseconds in the PSCAD simulation. The simulation duration was 12 seconds. In the DC zone multi-agent system performance analysis, two scenarios were used to evaluate the dynamic performance of the DC zone multi-agent system using metric 2. The system consisted of two identical DC zones. The load definitions in one DC zone are shown in Table 5.1. It was assumed that only one ATG generator was in service, so the total generation capacity was 4 MW. It was also assumed that the propulsion load was out of service and a pulse load was served in the MVAC system from 3 to 8 seconds. The notional all-electric ship power system used to study the DC zone multi-agent system is discussed in detail in Appendix B.3. The agents in DC zones are discussed in Appendices A.4-A.7. The operational constraints of the DC zone system used in the two scenarios are shown in (5-8)-(5-11). The parameters of the multi-agent system cooperative controller were the same as DC zone multi-agent system case studies in section 5.3.2. The parameters of converter agents and load agents were also the same as DC zone multi-agent system case studies in section 5.3.2.

In Scenario I, four cases were used to study the impact of the ramp rate of pulse loads on the dynamic performance of the DC zone multi-agent system. In each case, the pulse load had the same power magnitude, but had different ramp rates. In Scenario II, five cases were used to study the impact of the power magnitude of pulse loads on the dynamic performance of the DC zone multi-agent system. In each case, the pulse load had the same ramp rate, but had different power magnitudes.

5.4.2.1 DC zone multi-agent system – Scenario I

It was also assumed that the pulse load was served from 3 to 8 seconds with a 1.2 MW magnitude. The ramp rate of the pulse load was chosen as 1, 2, 5, and 10 MW/sec to study the dynamic performance of the DC zone multi-agent system. The definitions of pulse loads in DC zone multi-agent system – Scenario I are summarized in Table 5.10. Since the generation capacity of the system was 4 MW, the available power to the DC zone system was decreased when the pulse load was served.

Table 5.10 Summary of the pulse load for the DC zone multi-agent system - Scenario I

Case No.	Pulse magnitude (MW)	Pulse width (sec)	Ramp rate (MW/sec)
1	1.2	5	1
2	1.2	5	2
3	1.2	5	5
4	1.2	5	10

In case 1, the power magnitude of the pulse load was 1.2 MW; the ramp rate of the pulse load was 1 MW/sec; the pulse width was 5 seconds. The power demand of the pulse load is shown in Figure 5.95. The available power and the total load demand of the DC zone system are shown in Figure 5.96. The frequency behavior of the ATG generator is shown in Figure 5.97. When the pulse load was connected in the system, the maximum frequency was 0.85 Hz; when the pulse load was disconnected in the system, the maximum frequency was 0.35 Hz.

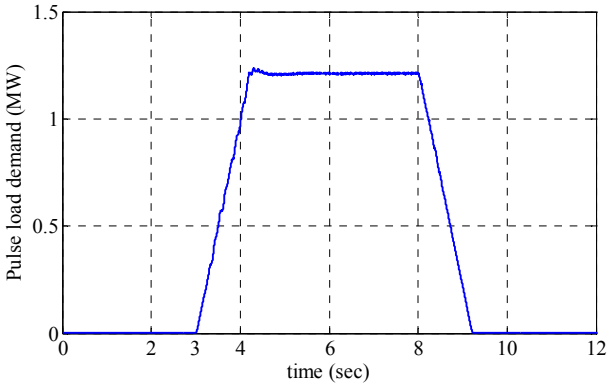

Figure 5.95 Power demand of the pulse load in case 1 of DC zone multi-agent system – Scenario I

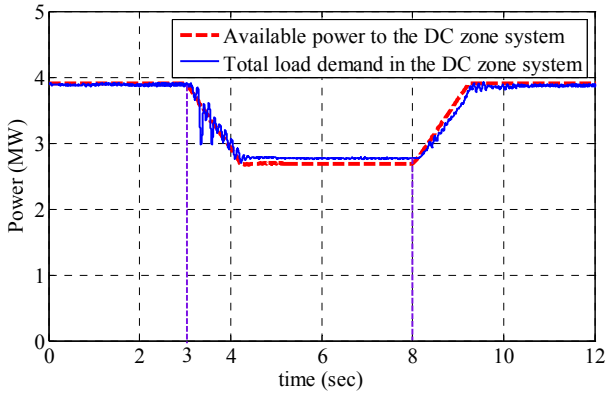

Figure 5.96 Total load demand and available power of the DC zone system in case 1 of DC zone multi-agent system – Scenario I

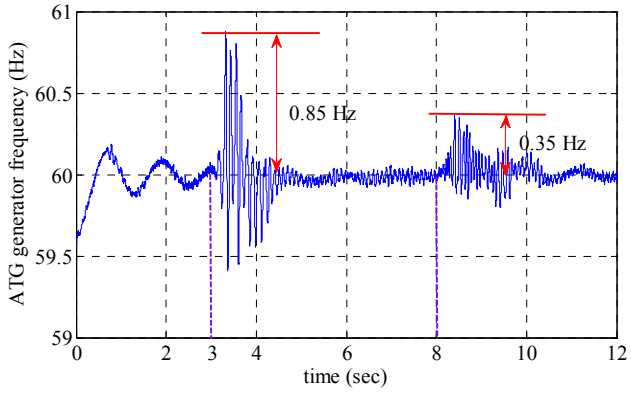

Figure 5.97 Frequency behavior of the ATG generator in case 1 of DC zone multi-agent system – Scenario I

In case 2, the power magnitude of the pulse load was 1.2 MW; the ramp rate of the pulse load was 2 MW/sec; the pulse width was 5 seconds. The power demand of the pulse load is shown in Figure 5.98. The available power and the total load demand of the DC zone system are shown in Figure 5.99. The frequency behavior of the ATG generator is shown in Figure 5.100. When the pulse load was connected in the system, the maximum frequency was 0.7 Hz; when the pulse load was disconnected in the system, the maximum frequency was 0.3 Hz.

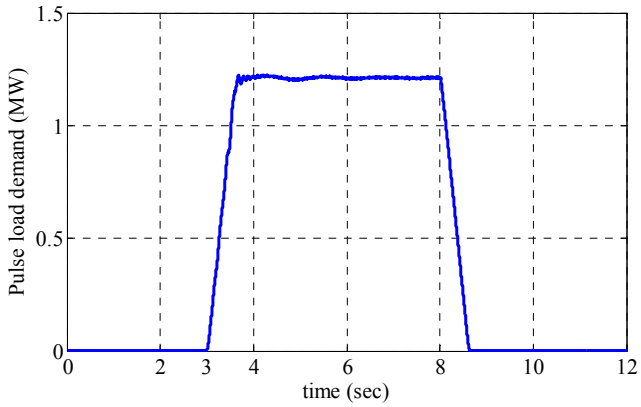

Figure 5.98 Power demand of the pulse load in case 2 of DC zone multi-agent system – Scenario I

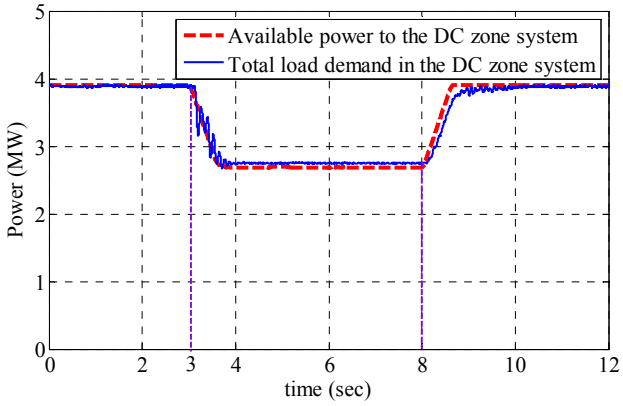

Figure 5.99 Total load demand and available power of the DC zone system in case 2 of DC zone multi-agent system – Scenario I

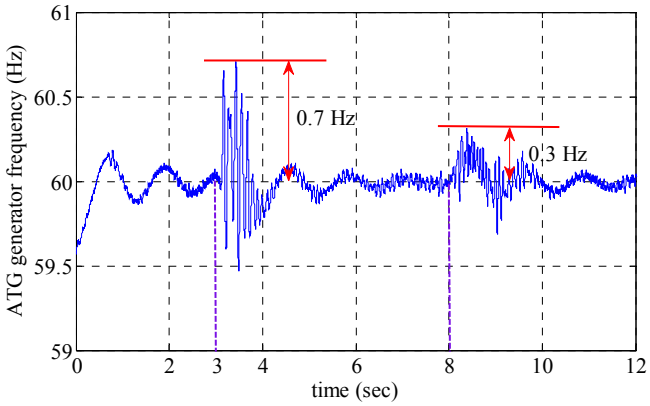

Figure 5.100 Frequency behavior of the ATG generator in case 2 of DC zone multi-agent system – Scenario I

In case 3, the power magnitude of the pulse load was 1.2 MW; the ramp rate of the pulse load was 5 MW/sec; the pulse width was 5 seconds. The power demand of the pulse load is shown in Figure 5.101. The available power and the total load demand of the DC zone system are shown in Figure 5.102. The frequency behavior of the ATG generator is shown in Figure 5.103. When the pulse load was connected in the system, the maximum frequency was 0.8 Hz; when the pulse load was disconnected in the system, the maximum frequency was 0.7 Hz.

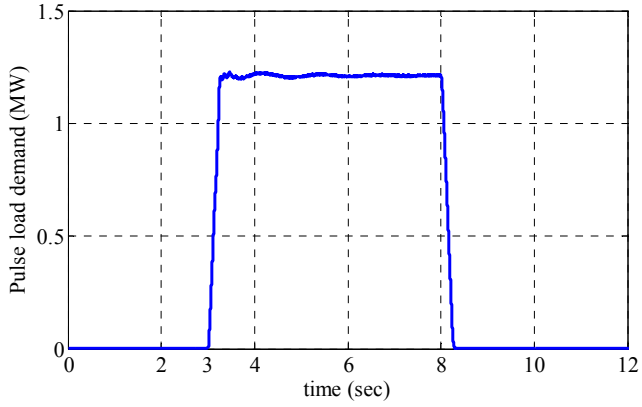

Figure 5.101 Power demand of the pulse load in case 3 of DC zone multi-agent system – Scenario I

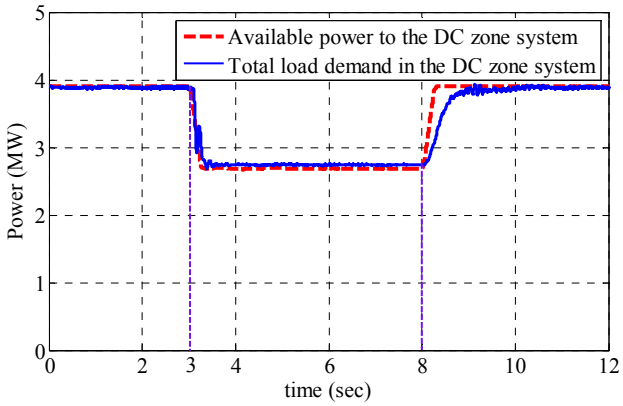

Figure 5.102 Total load demand and available power of the DC zone system in case 3 of DC zone multi-agent system – Scenario I

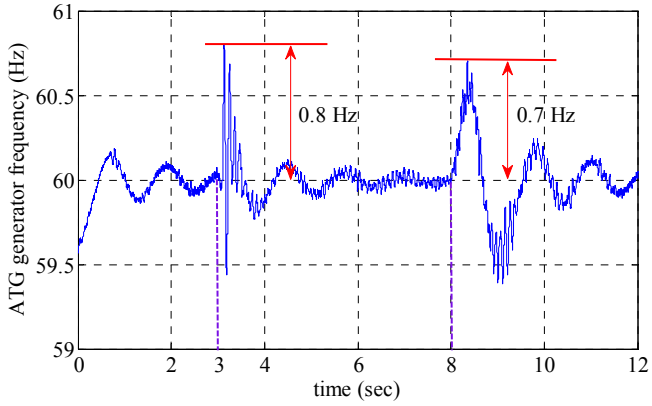

Figure 5.103 Frequency behavior of the ATG generator in case 3 of DC zone multi-agent system – scenario I

In case 4, the power magnitude of the pulse load was 1.2 MW; the ramp rate of the pulse load was 10 MW/sec; the pulse width was 5 seconds. The power demand of the pulse load is shown in Figure 5.104. The available power and the total load demand of the DC zone system are shown in Figure 5.105. The frequency behavior of the ATG generator is shown in Figure 5.106. When the pulse load was connected in the system,

the maximum frequency was 0.6 Hz; when the pulse load was disconnected in the system, the maximum frequency was 0.75 Hz.

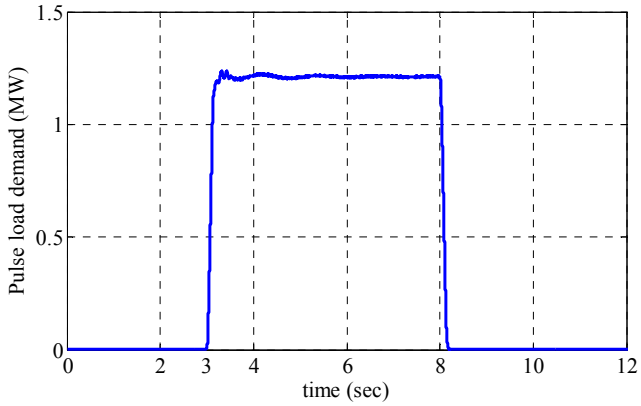

Figure 5.104 Power demand of the pulse load in case 4 of DC zone multi-agent system – Scenario I

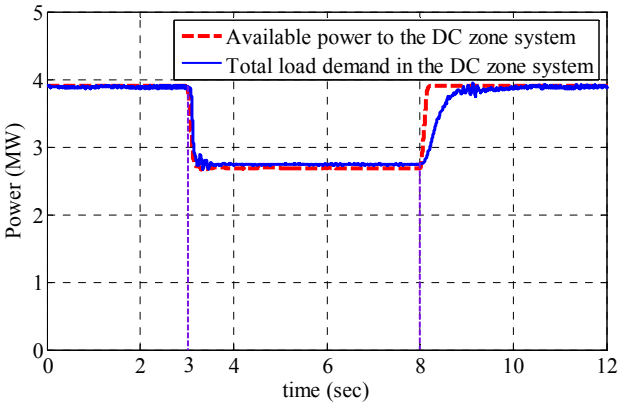

Figure 5.105 Total load demand and available power of the DC zone system in case 4 of DC zone multi-agent system – Scenario I

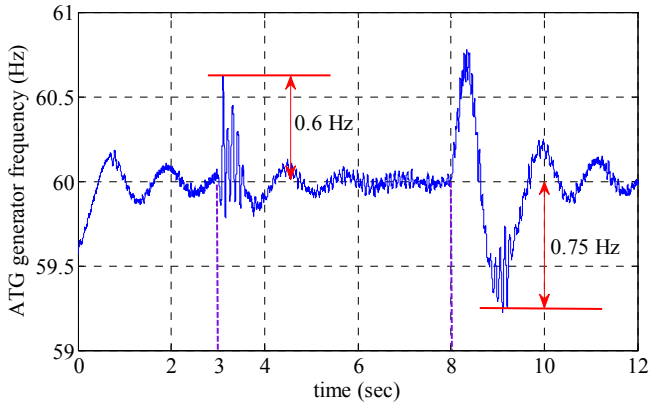

Figure 5.106 Frequency behavior of the ATG generator in case 4 of DC zone multi-agent system – Scenario I

The performance metric, J_2, was used to evaluate the dynamic performance of the ATG generator frequency for pulse loads with different ramp rates. The results in DC zone multi-agent system – Scenario I are summarized in Table 5.11. Metric 2 was used to evaluate the maximum frequency deviation from the nominal value. In all-electric ship power systems, the transient frequency deviation should be always less than 4% of the nominal value; the maximum allowed frequency deviation in steady state is 3% of the nominal value.

The results in Table 5.11 indicated that the magnitude of the ATG frequency deviation in each case was much less than the maximum allowed frequency deviation in steady state, which is equal to 3% of the nominal value. Thus, the dynamic behaviors of the ATG generator frequency in cases 1-4 satisfy the frequency requirements in IEEE-STD-45. When the pulse load is connected, the value of metric 2, J_2, is almost the same in each case; when the pulse load is disconnected, the value of metric 2, J_2, in cases 1

and 2 is smaller than the value in cases 3 and 4, which means that the maximum frequency deviation is increased with the increase of the ramp rate of the pulse load.

Table 5.11 Summary of the frequency behavior of the ATG generator in DC zone multi-agent system – Scenario I

Case No.	Metric 2 (Hz) - pulse load connection	Metric 2 (Hz) - pulse load disconnection
1	0.85	0.35
2	0.70	0.30
3	0.80	0.70
4	0.60	0.75

5.4.2.2 DC zone multi-agent system – Scenario II

It was also assumed that the pulse load was served from 3 to 8 seconds and the ramp rate of the pulse load was 10 MW/sec in each case. The power magnitude of the pulse load was chosen as 0.4, 0.6, 0.8, 1.0, and 1.2 MW to study the dynamic performance of the DC zone system. The definitions of pulse loads in DC zone multi-agent system – Scenario II are summarized in Table 5.12. Since the generation capacity of the system was 4 MW, the available power to the DC zone system was decreased when the pulse load was served.

Table 5.12 Summary of the pulse load for the DC zone multi-agent system – Scenario II

Case No.	Pulse magnitude (MW)	Pulse width (sec)	Ramp rate (MW/sec)
1	0.4	5	10
2	0.6	5	10
3	0.8	5	10
3	1.0	5	10
5	1.2	5	10

In case 1, the power magnitude of the pulse load was 0.4 MW; the ramp rate of the pulse load was 10 MW/sec; the pulse width was 5 seconds. The power demand of the pulse load is shown in Figure 5.107. The available power and the total load demand of the DC zone system are shown in Figure 5.108. The frequency behavior of the ATG generator is shown in Figure 5.109. When the pulse load was connected in the system, the maximum frequency was 0.91 Hz; when the pulse load was disconnected in the system, the maximum frequency was 0.25 Hz.

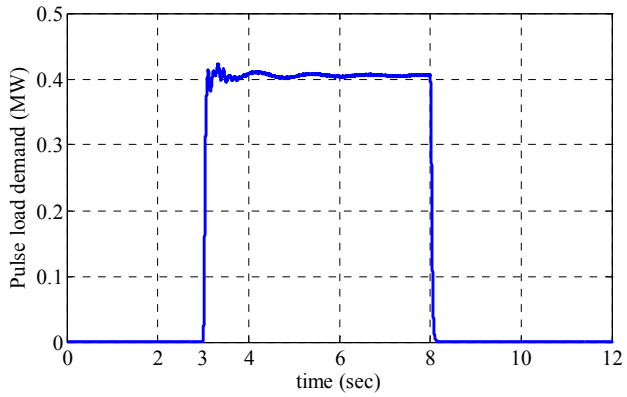

Figure 5.107 Power demand of the pulse load in case 1 of DC zone multi-agent system – Scenario II

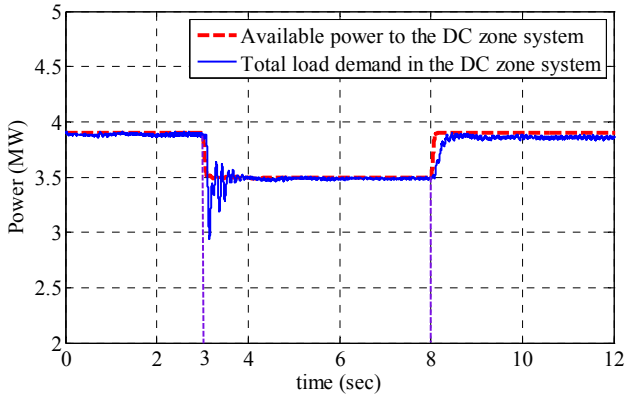

Figure 5.108 Total load demand and available power of the DC zone system in case 1 of DC zone multi-agent system – Scenario II

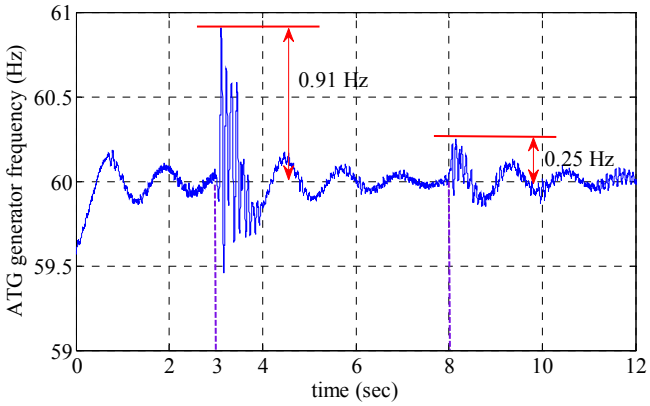

Figure 5.109 Frequency behavior of the ATG generator in case 1 of DC zone multi-agent system – Scenario II

In case 2, the power magnitude of the pulse load was 0.6 MW; the ramp rate of the pulse load was 10 MW/sec; the pulse width was 5 seconds. The power demand of the pulse load is shown in Figure 5.110. The available power and the total load demand of the DC zone system are shown in Figure 5.111. The frequency behavior of the ATG generator is shown in Figure 5.112. When the pulse load was connected in the system, the maximum frequency was 0.81 Hz; when the pulse load was disconnected in the system, the maximum frequency was 0.36 Hz.

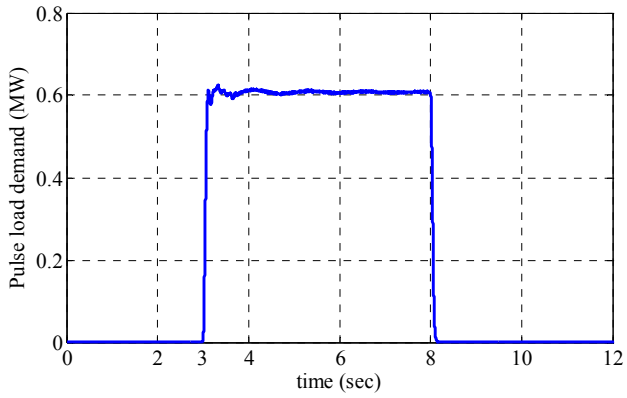

Figure 5.110 Power demand of the pulse load in case 2 of DC zone multi-agent system – Scenario II

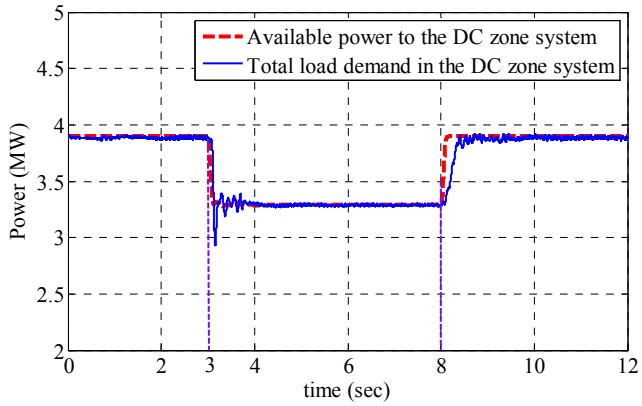

Figure 5.111 Total load demand and available power of the DC zone system in case 2 of DC zone multi-agent system – Scenario II

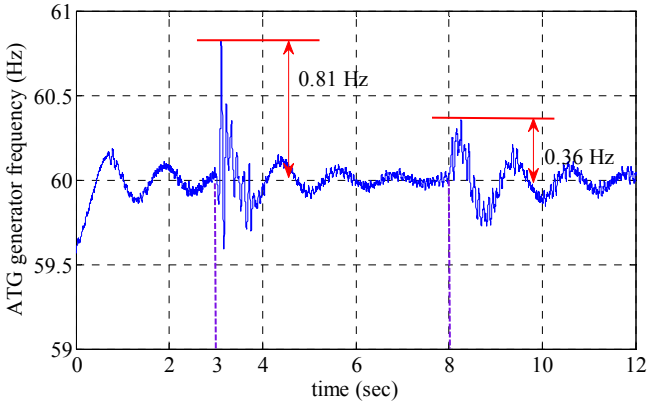

Figure 5.112 Frequency behavior of the ATG generator in case 2 of DC zone multi-agent system – Scenario II

In case 3, the power magnitude of the pulse load was 0.8 MW; the ramp rate of the pulse load was 10 MW/sec; the pulse width was 5 seconds. The power demand of the pulse load is shown in Figure 5.113. The available power and the total load demand of the DC zone system are shown in Figure 5.114. The frequency behavior of the ATG generator is shown in Figure 5.115. When the pulse load was connected in the system,

the maximum frequency was 0.71 Hz; when the pulse load was disconnected in the system, the maximum frequency was 0.49 Hz.

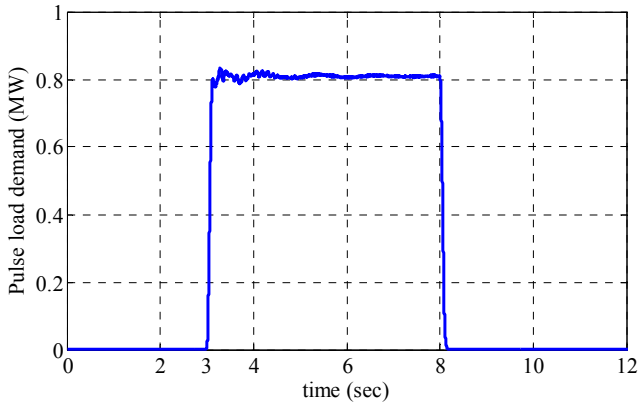

Figure 5.113 Power demand of the pulse load in case 3 of DC zone multi-agent system – Scenario II

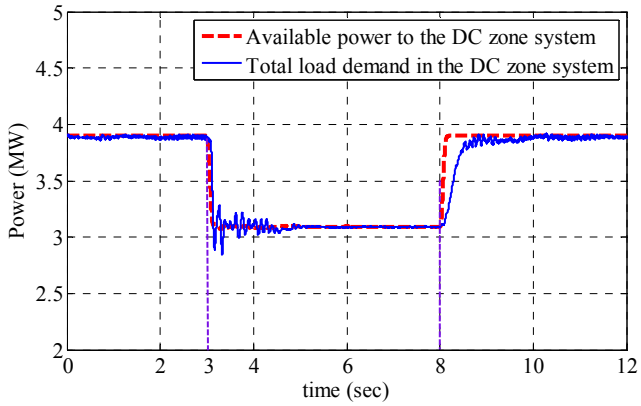

Figure 5.114 Total load demand and available power of the DC zone system in case 3 of DC zone multi-agent system – Scenario II

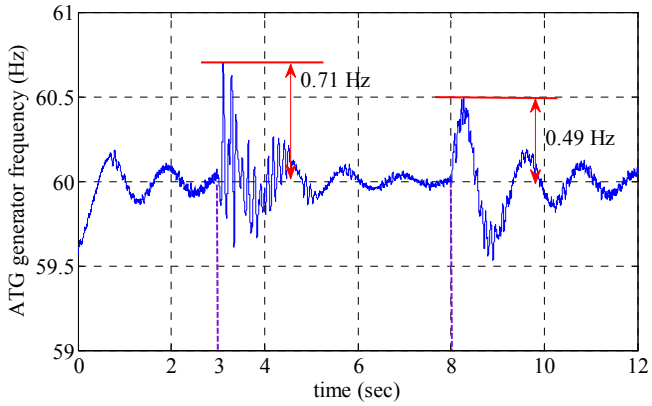

Figure 5.115 Frequency behavior of the ATG generator in case 3 of DC zone multi-agent system – Scenario II

In case 4, the power magnitude of the pulse load was 1.0 MW; the ramp rate of the pulse load was 10 MW/sec; the pulse width was 5 seconds. The power demand of the pulse load is shown in Figure 5.116. The available power and the total load demand of the DC zone system are shown in Figure 5.117. The frequency behavior of the ATG generator is shown in Figure 5.118. When the pulse load was connected in the system, the maximum frequency was 0.64 Hz; when the pulse load was disconnected in the system, the maximum frequency was 0.85 Hz.

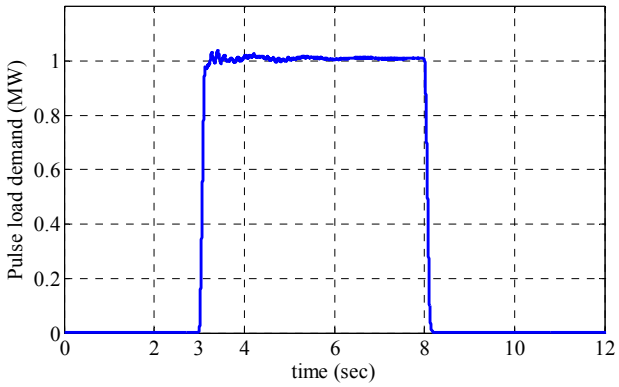

Figure 5.116 Power demand of the pulse load in case 4 of DC zone multi-agent system – Scenario II

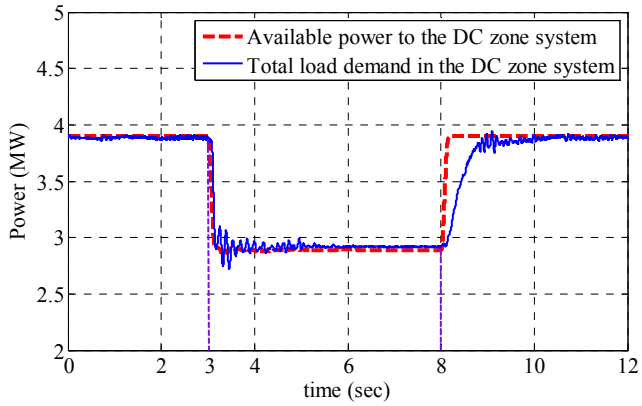

Figure 5.117 Total load demand and available power of the DC zone system in case 4 of DC zone multi-agent system – Scenario II

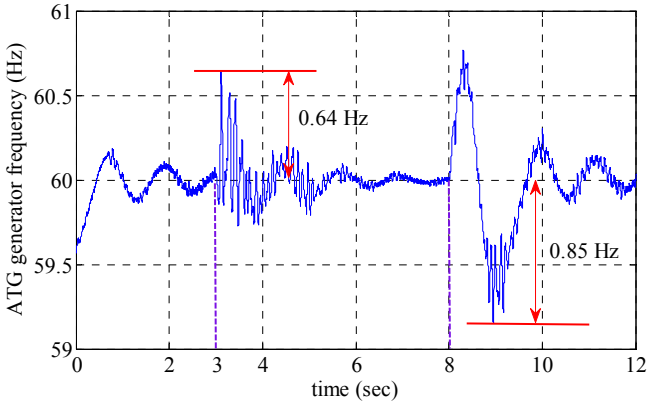

Figure 5.118 Frequency behavior of the ATG generator in case 4 of DC zone multi-agent system – Scenario II

In case 5, the power magnitude of the pulse load was 1.2 MW; the ramp rate of the pulse load was 10 MW/sec; the pulse width was 5 seconds. This case is the same as case 4 of DC zone multi-agent system – Scenario I as shown in section 5.4.2.1. When the pulse load was connected in the system, the maximum frequency was 0.6 Hz; when the pulse load was disconnected in the system, the maximum frequency was 0.75 Hz.

The performance metric, J_2, was used to evaluate the dynamic performance of the ATG generator frequency for pulse loads with various power magnitudes. The results in DC zone multi-agent system – Scenario II are summarized in Table 5.13. Metric 2 was used to evaluate the maximum frequency deviation from the nominal value. The results indicated that the magnitude of the ATG frequency deviation in each case was much less than the maximum allowed frequency deviation in steady state, which is equal to 3% of the nominal value. Thus, the dynamic behavior of the ATG generator frequency in cases 1-5 satisfies the frequency requirements in IEEE-STD-45. When the pulse load is connected, the value of metric 2, J_2, is almost the same in each case; when the pulse load is disconnected, the value of metric 2, J_2, is increased with the increase of the ramp rate of the pulse load.

Table 5.13 Summary of the frequency behavior of the ATG generator in DC zone multi-agent system – Scenario II

Case No.	Metric 2 (Hz) - pulse load connection	Metric 2 (Hz) - pulse load disconnection
1	0.91	0.25
2	0.81	0.36
3	0.71	0.49
4	0.64	0.85
5	0.60	0.75

5.5 Summary of Simulation Results

In the MVAC system case studies, various pulse loads with different power magnitudes and pulse widths were used to study the impact of the pulse load on the power quality of all-electric ship power systems. The real-time load management approach used the propulsion load to compensate the power demand of the pulse load to

reduce the frequency and voltage oscillations to meet operational constraints when load changes happened. The simulation results indicated that if the magnitude of the pulse load was less than the propulsion load demand, the propulsion load could fully compensate the load changes caused by the pulse load, which significantly reduced the frequency oscillations of the system. On the other hand, if the magnitude of the pulse load was greater than the propulsion load demand, the propulsion load could not fully compensate the load changes caused by the pulse load, which might result in some unacceptable frequency oscillations.

When the cruising speed of the ship was 27 knots, the propulsion load demand was 21 MW in steady state. In this case, if a 36 MW pulse load was served, the maximum frequency deviation was less than 4% of the nominal value and the recovery time of the system frequency was less than 2 seconds. When the cruising speed of the ship was 22 knots, the propulsion load demand was 10.5 MW in steady state. In this case, if a 36 MW pulse load was served, the maximum frequency deviation was greater than 4% of the nominal value, which means that the system frequency did not satisfy the frequency requirements as given in IEEE-STD-45. Thus, the real-time load management approach needs enough loads in service to compensate the load changes in the system.

In the DC zone system case studies, only one ATG generator was in service. A pulse load was also served to study the dynamic behavior of the system. When the pulse load was connected in the system, the total load demand of the DC zone system was decreased quickly to track the available power to the DC zone system by using the multi-agent system cooperative controller. On the other hand, when the pulse load was

disconnected from the system, the total load demand of the DC zone system was increased to track the available power to the DC zone system. Since the DC zone system includes some dynamic loads such as AC and DC motors, it takes 1 to 2 seconds for the load demand to reach steady state.

Performance analysis results of the MVAC multi-agent system indicated that if the propulsion load demand was larger than the magnitude of the pulse load, the propulsion load fully compensated the impact of the pulse load and the maximum system frequency deviation was reduced using the real-time load management approach, which was less than the maximum allowed frequency deviation. If the propulsion load demand was less than the magnitude of the pulse load, the propulsion load could not fully compensate the impact of the pulse load, which caused large frequency deviation. In some extreme cases, when the pulse load magnitude was 35 MW, the dynamic performance of the system frequency did not satisfy the frequency requirements in IEEE-STD-45.

In the performance analysis of the DC zone multi-agent system, pulse loads with various magnitudes and ramp rates were studied. When the pulse load was connected to the system, the maximum frequency deviation was almost the same in each case with various magnitudes or ramp rates of the pulse load. When the pulse load was disconnected, the maximum frequency deviation was increased with the increase of the magnitude or ramp rate of the pulse load. Performance analysis results of the DC zone multi-agent system indicated that the frequency deviation of the ATG generator was

much less than the steady state frequency tolerance, when various pulse loads with different power magnitudes and ramp rates were served.

5.6 Summary

In this chapter, the heterogeneous multi-agent system-based real-time load management and notional all-electric ship power system model were simulated in PSCAD to study the performance of the developed real-time load management approach. Case studies for the MVAC multi-agent system, DC zone multi-agent system, and the coordination of the two multi-agent systems were simulated in PSCAD to study the dynamic performances of the developed technique. In the MVAC multi-agent system case studies, the coordination of the propulsion load and pulse load were illustrated to show the effectiveness of the management of the propulsion load to reduce the frequency oscillations caused by the pulse load. The dynamic cable constraint was also illustrated to show that this constraint was satisfied for the pulse load agent by using the developed MVAC multi-agent system.

In the DC zone case studies, the dynamic performances of the DC zone multi-agent system were also studied. The results indicated that the actual load demand of the DC zone system tracked the available power very well, and the DC zone multi-agent system ensured that vital loads were served before semi-vital and non-vital loads. The coordination of the two multi-agent systems was also studied to show the dynamic performance of the proposed technique. The results showed that the objective of real-

time load management was achieved while satisfying the operational constraints of the system.

Performance analysis of the multi-agent system framework was conducted to evaluate the performance of the new multi-agent system-based real-time load management method. For the MVAC multi-agent system, various pulse loads with different power magnitudes and pulse widths were used to study the dynamic performance of the new method. The results indicated that a propulsion load could fully compensate for the load changes caused by a pulse load when the magnitude of the pulse load was less than the propulsion load demand. The frequency oscillations of the system were significantly reduced. However, if the magnitude of the pulse load was larger than the propulsion load demand, the propulsion load had some limitations to reduce the impact of the pulse load on the power quality of the system. The DC zone multi-agent system could reduce the load demand to track the available power reference quickly, when the available power to the DC zone system was decreased. On the other hand, when the available power was increased, the load demand took 1-2 seconds to track the available power reference.

6. CONCLUSIONS AND FUTURE WORK

6.1 Summary and Conclusions

In this dissertation, a novel bio-inspired multi-agent system framework developed for real-time load management of all-electric ship power systems was presented. The technique balances the generation and load of the system in operational real time while satisfying various operational constraints of the system and considering load priorities. The multi-agent system cooperatively achieved real-time load management based on cooperative controllers through local measurements and communication between different agents. In addition, pulse loads and propulsion loads were coordinated to compensate for the impact of pulse loads on the power quality of all-electric ship power systems.

The real-time load management multi-agent system for all-electric ship power systems includes MVAC and DC zone multi-agent systems. An AC-DC communication agent is used to coordinate these two systems. In the DC zone multi-agent system, the heterogeneous multi-agent system technique integrates multiple agents with different dynamic models to achieve the real-time load management objective and improve the accuracy of cooperative controllers. Moreover, an artificial potential function is used to drive the system state to the desired state while avoiding constraint regions by using an attractor term and repulsor term. The heterogeneous multi-agent system also takes load priorities into consideration, which ensures that vital loads are served before semi-vital and non-vital loads.

The MVAC multi-agent system coordinates generators, propulsion loads, and pulse loads in the MVAC system. The multi-agent system framework automatically regulates power set-points of propulsion loads to compensate for load changes caused by pulse loads based on the system frequency. The voltage controller in the propulsion load agents also regulates the propulsion load demand when the input voltage constraint of a propulsion load is violated. The pulse load agent regulates the pulse load to satisfy the dynamic cable constraint of the cable connecting the MTG generator and pulse load.

In order to apply the bio-inspired multi-agent system methodology in the DC zone system, the system was partitioned into subsystems, which were modeled using dynamic agent models. For the DC zone system of the all-electric ship power system, Partitioning Strategy III was used to partition the DC zone system into a group of electrical subsystems. Partitioning Strategy III partitioned the system based on individual electrical components. Since electrical components might have different dynamical models, a heterogeneous multi-agent system was developed. This partitioning strategy provides more flexibility to integrate detailed system dynamics and alternate paths of vital loads into the multi-agent system, which greatly improved the accuracy of the multi-agent system cooperative controller. In addition, various operational constraints of the system were integrated into the multi-agent system. A novel bio-inspired heterogeneous multi-agent system cooperative controller was developed based on Partitioning Strategy III for the DC zone multi-agent system.

The AC-DC communication agent connects the MVAC and DC zone multi-agent systems, which coordinates the two multi-agent systems to achieve the real-time load

management for all-electric ship power systems. Through communications with the two multi-agent agent systems, the AC-DC communication agent calculates the available power to the DC zone system and the total load demand of the DC zone system which is obtained by the system losses agent to calculate the total losses in the MVAC system.

The heterogeneous multi-agent system cooperative controller was implemented in the PSCAD software to evaluate the dynamic performance of the developed technique. Case studies for the MVAC multi-agent system, DC zone multi-agent system, and coordination of these two multi-agent systems indicated that the developed multi-agent system framework achieved generation and load balancing in real time while satisfying operational constraints of the system, such as PCM4 capacity constraints, and dynamic cable constraints.

In the MVAC multi-agent system case studies, the propulsion load and pulse load were coordinated to improve the frequency performance of the all-electric ship power system. When the pulse load was served, the propulsion load was disturbed temporarily to reduce the impact of the pulse load on the power quality of the system. Since the propulsion load was disturbed for a short period of time, the ship speed was slightly decreased due to the large inertia of the ship. In addition, the pulse load agent ensured that the dynamic cable constraint was always satisfied in operational real time. In an extreme case, when the magnitude of the pulse load was much larger than the propulsion load demand, the maximum frequency deviation was larger than 3% of nominal value, which was the steady state frequency deviation tolerance.

In the DC zone multi-agent system case studies, load changes in the DC zone system and pulse load changes in MVAC system were studied. By using the developed heterogeneous multi-agent system, the motor input voltage constraints, available power capacity constraint, and PCM4 capacity constraints were satisfied in operational real-time. In addition, the vital loads were served at a higher priority than semi-vital and non-vital loads. When the available power in the DC zone system was decreased, the actual load demand tracked the available power quickly and the frequency oscillation was in acceptable range. When the available power to the DC zone system was increased, the actual load demand took 1-2 seconds to track the available power since the dynamic loads in DC zones could not increase their load demands instantaneously. The frequency oscillation was in the acceptable range.

Performance analysis was performed using two metrics, J_1 and J_2. J_1 measures the convergence speed of a state trajectory; J_2 measures the maximum deviation of a state trajectory. Performance analysis results for the MVAC multi-agent system indicated that the propulsion load could fully compensate for the load changes caused by a pulse load when the magnitude of the pulse load was less than the propulsion load demand. The frequency and voltage oscillations were significantly reduced by the propulsion load compensation. However, if the magnitude of a pulse load was larger than the propulsion load demand, the propulsion load could not fully compensate for the load changes, which caused larger frequency and voltage oscillations in the system. The value of metric 1, J_1, was equal to 0, when the propulsion load could fully compensate the impact of the pulse load. In extreme cases, when the magnitude of the pulse load was

much larger than the propulsion load demand, the value of metric 1, J_1, had a positive value, which was still less than the maximum allowed value. The value of metric 2, J_2, increased with the increase of the magnitude of the pulse load. In some extreme cases, when the magnitude of the pulse load was much larger than the propulsion load demand, the value of metric 2, J_2, was larger than the tolerance value, which means that the frequency requirements in IEEE-STD-45were not satisfied.

In the DC zone multi-agent system performance analysis, the pulse load at various magnitudes and ramp rates was studied. When the pulse load was connected to the system, the value of metric 2, J_2, was almost the same in each case with different ramp rates or magnitudes of the pulse load. When the pulse load was disconnected from the system, the value of metric 2, J_2, increased with the increase of the magnitude or ramp rate of the pulse load. The value of metric 2, J_2, was always less than the tolerance value. Thus, the dynamic performance of the DC zone multi-agent system satisfied the requirements in IEEE-STD-45.

6.2 Contributions

The contributions of this dissertation are summarized as follows:

1) The developed heterogeneous multi-agent system framework is one of the first applications to address the real-time load management problem for all-electric ship power systems. This work is one of the first applications of the

multi-agent system cooperative control methodology to solve secondary control problems in power systems areas.

2) The developed heterogeneous multi-agent system framework successfully coordinates propulsion loads and pulse loads, which can greatly improve the power quality of all-electric ship power systems. Moreover, the heterogeneous multi-agent system framework integrates multiple agents in DC zones with different dynamic models, which can significantly improve the accuracy of cooperative controllers.
3) The multi-agent system cooperative controller was used for the first time to solve a hybrid control problem, which includes continuous control variables and switch control variables to control individual loads in all-electric ship power systems.
4) The developed multi-agent system-based real-time load management methodology has great potential to be extended to other types of isolated power systems, such as microgrids and islanded power systems in oil fields.

6.3 Future work

In the future work, the robust analysis of the multi-agent system-based cooperative controller could be studied. In the multi-agent system design, reduced-order converter and load agent models were used. The model simplifications introduced some errors in the multi-agent system. Moreover, continuous control variables and switch control variables are included in the real-time load management problem, which may

reduce the accuracy of the cooperative controller. The robust analysis could help to determine a region that the cooperative controller can work normally.

The developed bio-inspired multi-agent system methodology could also be applied to other isolated power systems such as microgrids. Microgrids can operate in grid-connected mode or islanded mode and can smoothly transient between these two modes. Moreover, microgrids employ a large number of intermittent energy resources such as wind and solar. These intermittent energy resources may change the generation capacity significantly depending on the weather [96], [97]. The developed real-time load management technique can be used to rebalance the generation and load in real time when the available generation power of microgrids changes. In addition, the dynamic balancing of generation and loads of microgrids needs to be achieved to mitigate system transients during switching to islanded mode [98]. Furthermore, microgrids in islanded mode include limited rotating inertia and fast system dynamics, and developed real-time load management technique can balance the load and generation in operational real time to improve frequency and voltage behaviors in microgrids.

REFERENCES

[1] T. X. Wang, and S. S. Choi, "Enhancement of voltage quality in isolated power systems," *IEEE Trans. Power Delivery*, vol. 22, no. 2, pp. 1160-1168, Apr. 2007.

[2] K. S. Smith, and L. Ran, "Voltage stability assessment of isolated power systems with power electronic converters," *IEE Proc. Gen. Trans. Distrib.*, vol. 141, no. 4, pp. 310-314, July 1994.

[3] P. Kundur, *Power System Stability and Control*, New York: McGraw-Hill, 1994.

[4] H .You, V. Vittal, and Z. Yang, "Self-healing in power systems: an approach using islanding and rate of frequency decline-based load shedding," *IEEE Trans. Power Systems*, vol. 18. no. 1, Feb. 2003.

[5] X. Feng, T. Zourntos, K. L. Butler-Purry, and S. Mashayekh, "Dynamic load management for NG IPS ships," in *Proc. IEEE PES General Meeting*, Minneapolis, MN, July 2010, pp. 4760-4767.

[6] K. L. Butler-Purry, N. D. R. Sarma, and I. V. Hicks, "Service restoration in naval shipboard power systems," *IEE Proc. Gener. Transm. Distrib.*, vol. 151, no. 1, pp. 95-102, Jan. 2004.

[7] Naval Sea Systems Command, Engineering Directorate, Electrical Engineering Group, *NAVSEA Design Practice and Criteria Manual for Electrical Systems for Surface Ships*, Chapter 300, 1992.

[8] S. K. Yee, J. M. Milanovic, and F. M. Hughes, "Overview and comparative analysis of gas turbine models for system stability studies," *IEEE Trans. Power Systems.*, vol. 23 no. 1, pp. 108-118, Feb. 2008.

[9] P. Mahat, Z. Chen, and B. Bak-Jensen, "Gas turbine control for islanding operation of distribution systems," in *Proc. IEEE Power and Energy Society General Meeting*, Calgary, Canada, July 2009, pp. 1-7.

[10] H.-M. Chou, F. A. Ituzaro, and K. L. Butler-Purry, "A PC-based test bed for NG IPS for ships in PSCAD™," in *Proc. IEEE Electric Ship Technologies Symposium*, Alexandria, VA, Apr. 2011, pp. 135-142.

[11] K. L. Butler-Purry, H.-M. Chou, R. Douglin, and F. Ituzaro, "Developing PSCAD simulation test bed of Notional Integrated Shipboard Power System," Texas Engineering Experiment Station, Texas A&M University, College Station, 2010.

[12] M. Steurer, M. Andrus, J. Langston, L. Qi, S. Suryanarayanan, S. Woodruff, and P. F. Ribeiro, "Investigating the impact of pulsed power charging demands on shipboard power quality," in *Proc. IEEE Electric Ship Technologies Symposium*, Arlington, VA, May 2007, pp. 315-321.

[13] S. L. Woodruff, L. Qi, and M. J. Sloderbeck, "Hardware-in-the-loop experiments on the use of propulsion motors to reduce pulse-load system disturbances," in *Proc. IEEE Electric Ship Technologies Symposium*, Arlington, VA, May 2007, pp. 455-461.

[14] Q. Shen, B. Ramachandran, S. K. Srivastava, M. Andrus, and D. A. Cartes, "Power and energy management in integrated power system," in *Proc. IEEE Electric Ship Technologies Symposium*, Alexandria, VA, Apr. 2011, pp. 414-419.

[15] J. J. A. Van Der Burgt, P. Van Gelder, and E. Van Dijk, "Pulsed power requirements for future naval ships," in *Proc. 12th IEEE International Pulsed Power Conference*, Monterey, CA, vol.2, June 1999, pp. 1357-1360.

[16] I. R. McNab, "Pulsed power for electric guns," *IEEE Trans. Magnetics*, vol. 33, no. 1, pp. 453-460, Jan. 1997.

[17] IEEE Std 45™-2002 , *IEEE Recommended Practice for Electrical Installations on Shipboard*, New York, NY: The Institute of Electrical and Electronics Engineers, Inc., 2002.

[18] NATO Standardisation Agreement STANAG 1008, *Characteristics of Shipboard Low Voltage Electrical Power Systems in Warships of the NATO Navies*, 9 ed, Brussels, Belgium: NATO Standardisation Agency, 2004.

[19] V. Salehi, B. Mirafzal, and O. Mohammed, "Pulse-load effects on ship power system stability," in *Proc. IEEE Industrial Electronics Society Annual Conference*, Glendale, AZ, Nov. 2010, pp. 3353-3358.

[20] S. Kulkarni and S. Santoso, "Impact of pulse loads on electric ship power system: with and without flywheel energy storage systems," in *Proc. IEEE Electric Ship Technologies Symposium*, Baltimore, MD, Apr. 2009, pp. 568-573.

[21] P. Mitra and G. K. Venayagamoorthy, "An adaptive control strategy for DSTATCOM applications in an electric ship power system," *IEEE Trans. Power Electronics*, vol. 25, no.1 , pp. 95-104, Jan. 2010.

[22] P. Mitra and G. K. Venayagamoorthy, "Artificial immune system based DSTATCOM control for an electric ship power system," in *Proc. IEEE Power Electronics Specialists Conference*, Rhodes, Greece, June 2008, pp. 718-723.

[23] P. Mitra and G. K. Venayagamoorthy, "Real time implementation of an artificial immune system based controller for a DSTATCOM in an electric ship power system," in *Proc. IEEE Industry Applications Society Annual Meeting*, Edmonton, Canada, Oct. 2008, pp. 1-8.

[24] B. Cassimere, C. R. Valdez, S. Sudhoff, S. Pekarek, B. Kuhn, D. Delisle, and E. Zivi, "System impact of pulsed power loads on a laboratory scale integrated fight through power (IFTP) system," in *Proc. IEEE Electric Ship Technologies Symposium*, Philadelphia, PA, July 2005, pp. 176-183.

[25] F. Scuiller, "Simulation of an energy storage system to compensate pulsed loads on shipboard electric power system," in *Proc. IEEE Electric Ship Technologies Symposium*, Alexandria, VA, Apr. 2011, pp. 396-401.

[26] J. M. Crider and S. D. Sudhoff, "Reducing impact of pulsed power loads on microgrid power systems," *IEEE Trans. Smart Grid*, vol. 1, no. 3, pp. 270-277, Dec. 2010.

[27] F. C. Beach and I. R. McNab, "Present and future naval applications for pulsed power," in *Proc. IEEE Pulsed Power Conference*, Monterey, CA, June 2005, pp. 1-7.

[28] M. Doyle, G. Sulich, and L. Lebron, "The benefits of electromagnetically launching aircraft," *Naval Engineers Journal*, vol. 112, no. 3, pp. 77–82, May 2000.

[29] S. D. Sudhoff, S. Pekarek, B. Kuhn, S. Glover, J. Sauer, and D. Delisle, "Naval combat survivability testbeds for investigation of issues in shipboard power electronics based power and propulsion systems," in *Proc. IEEE Power Engineering Society Summer Meeting*, Chicago, IL, July 2002, pp. 347-350.

[30] L. N. Domaschk, A. Ouroua, R. E. Hebner, O. E. Bowlin, and W. B. Colson, "Coordination of large pulsed loads on future electric ships," *IEEE Trans. Magnetics*, vol. 43, no. 1, pp. 450-455, Jan. 2007.

[31] M. Andrus and M. Steurer, "Controls for minimizing ship power system frequency fluctuations," in *Proc. American Society of Naval Engineers – Automation & Controls Symposium*, Dec. 2007.

[32] J. M. Apsley, A. Gonzalez-Villasenor, M. Barnes, A. C. Smith, S. Williamson, J. D. Schuddebeurs, P. J. Norman, C. D. Booth, G. M. Burt, and J. R. McDonald, "Propulsion drive models for full electric marine propulsion systems," *IEEE Trans. Industry Applications*, vol. 45, no. 2, pp. 676-684, Mar./Apr., 2009.

[33] M. Bash, R. R. Chan, J. Crider, C. Harianto, J. Lian, J. Neely, S. D. Pekarek, S. D. Sudhoff, and N. Vaks, "A medium voltage DC testbed for ship power system research," in *Proc. IEEE Electric Ship Technologies Symposium*, Baltimore, MD, Apr. 2009, pp. 560-567.

[34] J. M. Guerrero, J. C. Vasquez, J. Matas, L. G. de Vicuna, and M. Castilla, "Hierarchical control of droop-controlled AC and DC microgrids – a general approach toward standardization," *IEEE Trans. Industrial Electronics,* vol. 58, no. 1, pp. 158-172, Jan. 2011.

[35] A. Mehrizi-Sani and R. Iravani, "Potential-function based control of a microgrid in islanded and grid-connected modes," *IEEE Trans. Power Systems*, vol. 25, no. 4, pp. 1883-1891, Nov. 2010.

[36] U. Borup, F. Blaabjerg, and P. N. Enjeti, "Sharing of nonlinear load in parallel-connected three-phase converters," *IEEE Trans. on Industry Applications*, vol. 37, no.6, pp. 1817-1823, Nov./Dec. 2001.

[37] F. Katiraei and M. R. Iravani, "Power management strategies for a microgrid with multiple distributed generation units," *IEEE Trans. Power Systems,* vol. 21, no. 4, pp. 1821-1831, Nov. 2006.

[38] F. Gao and M. R. Iravani, "A control strategy for a distributed generation unit in grid-connected and autonomous modes of operation," *IEEE Trans. on Power Delivery*, vol. 23, no. 2, pp. 850-859, Apr. 2008.

[39] F. Katiraei, R. Iravani, N. Hatziargyriou, and A. Dimeas, "Microgrids management," *IEEE Power and Energy Magazine,* vol. 6, no. 3, pp. 54-65, May/June 2008.

[40] J. A. P. Lopes, C. L. Moreira, and A. G. Madureira, "Defining control strategies for MicroGrids islanded operation," *IEEE Trans. Power Systems*, vol. 21, no. 2, pp. 916-924, May 2006.

[41] K. Sedghisigarchi, A. Feliachi, A. Fernandes, and K. Schoder, "Gas turbine control and load sharing for shipboard power systems," in *Proc. IEEE Power Engineering Society General Meeting*, Tampa, FL, 2007, pp. 1-7.

[42] A. Madureira, C. Moreira, and J. A. P. Lopes, "Secondary load-frequency control for microgrids in islanded operation," in *Proc. Internationa Conference on Renewable Energy and Power Quality*, Zaragoza, Spain, 2005, pp. 1-4.

[43] V. Arcidiacono, R. Menis, and G. Sulligoi, "Improving power quality in all electric ships using a voltage and VAR integrated regulator," in *Proc. IEEE Electric Ship Technologies Symposium*, Arlington, VA 2007, pp. 322-327.

[44] V. Arcidiacono, S. Castellan, R. Menis, and G. Sulligoi, "Integrated voltage and reactive power control for all electric ship power systems," in *Proc. International Symposium on Power Electronics, Electrical Drives, Automation and Motion*, Taormina, Italy, May 2006, pp. 878-882.

[45] A. J. Wood and B. F. Wollenberg, *Power Generation, Operation, and Control*, 2nd ed., New York: Wiley-Interscience, 1996.

[46] X. Feng, K. L. Butler-Purry, T. Zourntos, and H.-M. Chou, "Multi-agent system-based real-time load management for NG IPS ships in high/medium voltage level," in *Proc. IEEE Power Systems Conference and Exposition*, Pheonix, AZ, Mar. 2011, pp. 1-8.

[47] A. L. Dimeas and N. D. Hatziargyriou, "Operation of a multiagent system for microgrid control," *IEEE Trans. Power Systems*, vol. 20, no. 3, pp. 1447-1455, Aug. 2005.

[48] K. H. Ng and G. B. Sheble, "Direct load control-A profit-based load management using linear programming," *IEEE Trans. Power Systems*, vol. 13, pp. 688-694, May 1998.

[49] A. I. Cohen and C. C. Wang, "An optimization method for load management scheduling," *IEEE Trans. Power Systems*, vol. 3, pp. 612-618, May 1988.

[50] H. R. Lu and L. Yao, "On-line load optimization for two way load management system," in *Proc. 2006 IEEE International Conference on Systems, Man and Cybernetics*, Taipei, Taiwan, Oct. 2006, pp. 3250-3255.

[51] J. Flitter, L. Markel, and P. Grimsrud, "A load management feasibility study for South Carolina Electric & Gas Co," *IEEE Trans. Power Apparatus and Systems*, vol. PAS-101, no. 10, pp. 3877-3884, Oct. 1982.

[52] S. H. Lee and C. L. Wilkins, "A practical approach to appliance load control analysis: a water heater case study," *IEEE Trans. Power Apparatus and Systems*, vol. PAS-102, no. 4, pp. 1007-1013, Apr. 1983.

[53] D. E. Nordell, "Forced duty cycling of air conditioning units for load management," *IEEE Trans. Power Systems*, vol. 2, no. 4, pp. 1110-1116, Nov. 1987.

[54] G. F. Strickler and S. K. Noell, "Residential air conditioner cycling-a case study," *IEEE Trans. Power Systems*, vol. 3, no. 1, pp. 207-212, Feb. 1988.

[55] J. Chen, F. N. Lee, A. M. Breipohl, and R. Adapa, "Scheduling direct load control to minimize system operation cost," *IEEE Trans. Power Systems*, vol. 10, no.4, pp. 1994-2001, Nov. 1995.

[56] K. D. Le, R. F. Boyle, M. D. Hunter, and K. D. Jones, "A procedure for coordinating direct-load-control strategies to minimize system production costs," *IEEE Trans. Power Apparatus and Systems*, vol. PAS-102, no. 6, pp. 1843-1849, June 1983.

[57] Y.-Y. Hsu and C.-C. Su, "Dispatch of direct load control using dynamic programming," *IEEE Trans. on Power Systems*, vol. 6, no.3, pp. 1056-1061, Aug. 1991.

[58] A. I. Cohen, J. W. Patmore, D. H. Oglevee, R. W. Berman, L. H. Ayers, and J. F. Howard, "An integrated system for residential load control," *IEEE Trans. Power Systems*, vol. 2, no.3, pp. 645-651, Aug. 1987.

[59] C. N. Kurucz, D. Brandt, and S. Sim, "A linear programming model for reducing system peak through customer load control programs," *IEEE Trans. Power Systems*, vol. 11, no.4, pp. 1817-1824, Nov. 1996.

[60] D.-C. Wei and N. Chen, "Air conditioner direct load control by multi-pass dynamic programming," *IEEE Trans. Power Systems*, vol. 10, no.1, pp. 307-313, Feb. 1995.

[61] K.-Y. Huang and Y.-C. Huang, "Integrating direct load control with interruptible load management to provide instantaneous reserves for ancillary services," *IEEE Trans. Power Systems*, vol. 19, no. 3, pp. 1626-1634, Aug. 2004.

[62] L. Yao, W. C. Chang, and R. L. Yen, "An iterative deepening genetic algorithm for scheduling of direct load control," *IEEE Trans. Power Systems*, vol. 20, no. 3, pp. 1414-1421, Aug. 2005.

[63] Z. Ding, D. A. Cartes, and S. Srivastava, "New load shedding scheme for islanded power systems," in *Proc. IEEE/SMC International Conference on System of Systems Engineering*, Los Angeles, CA, Apr. 2006, pp. 167-172.

[64] Z. Ding, S. Srivastava, and D. Cartes, "Expert system based dynamic load shedding scheme for shipboard power systems," in *Proc. 2006 IEEE IAS Annual Meeting*, Tampa, FL, Oct. 2006, pp. 1338-1344.

[65] Z. Ding, S. K. Srivastava, D. A. Cartes, and S. Suryanarayanan, "Dynamic simulation-based analysis of a new load shedding scheme for a notional destroyer-class shipboard power system," *IEEE Trans. Industry Applications*, vol. 45, no. 3, pp. 1166-1174, May-June 2009.

[66] A. Shrestha, E. L. Foulks, and R. W. Cox, "Dynamic load shedding for shipboard power systems using the non-intrusive load monitor," in *IEEE Electric Ship Technologies Symposium*, Baltimore, MD, Apr. 2009, pp. 412-419.

[67] K. L. Butler-Purry, T. Zourntos, and X. Feng, "A Bio-Inspired Multi-Agent Framework for Real-Time Load Management in NG IPS Ships Year 1 Report," Texas Engineering Experiment Station, Texas A&M University, College Station, Sep. 2009.

[68] A. S. Debs, *Modern Power Systems Control and Operation*, Norwell, MA: Kluwer Academic Publishers, 1988.

[69] W. K. Potts, "The chorus-line hypothesis of manoeuvre coordination in avian flocks," *Nature*, vol. 309, pp. 344-345, May 1984.

[70] S. V. Viscido, J. K. Parrish, and D. Grünbaum, "The effect of population size and number of influential neighbors on the emergent properties of fish schools," *Ecological Modelling*, vol. 183, no. 2-3, pp. 347-363, Apr. 2005.

[71] V. Gazi and B. Fidan, "Coordination and control of multi-agent dynamic systems: models and approaches," in *Swarm Robotics*, vol. 4433. Berlin, Germany: Springer-Verlag, pp. 71-102, 2007.

[72] R. Olfati-Saber, J. A. Fax, and R. M. Murray, "Consensus and Cooperation in Networked Multi-Agent Systems," *Proceedings of the IEEE*, vol. 95, no. 1, pp. 215-233, Jan. 2007.

[73] R. Olfati-Saber, "Flocking for multi-agent dynamic systems: algorithms and theory," *IEEE Trans. Automat. Contr.*, vol. 51, no. 3, pp. 401-420, Mar. 2006.

[74] R. Sepulchre, D. A. Paley, and N. E. Leonard, "Stabilization of planar collective motion: all-to-all communication," *IEEE Trans. Automat. Contr.*, vol. 52, no. 5, pp. 811-824, May 2007.

[75] N. Moshtagh and A. Jadbabaie, "Distributed geodesic control laws for flocking of nonholonomic agents," *IEEE Trans. Automat. Contr.*, vol. 52, no. 4, pp. 681-686, Apr. 2007.

[76] J. A. Fax and R. M. Murray, "Information flow and cooperative control of vehicle formations," *IEEE Trans. Automat. Contr.*, vol. 49, no. 9, pp. 1465-1476, Sep. 2004.

[77] R. Fierro, P. Song, A. K. Das, and V. Kumar, "Cooperative control of robot formations," in *Cooperative Control and Optimization*, R. Murphey and P. Pardalos, Eds. Dordrecht, The Netherlands: Kluwer, pp. 73-93, 2002.

[78] –, "Mobile Multirobot Systems," Cassino, Italy: Robotics Research Group of the DAEIMI, University of Cassino 2007. Available: http://webuser.unicas.it/lai/robotica/research.html

[79] Z. Qu, J. Wang, and R. A. Hull, "Cooperative control of dynamical systems with application to autonomous vehicles," *IEEE Trans. Automat. Contr.,* vol. 53, no. 4, pp. 894-911, May 2008.

[80] S. D. J. McArthur, E. M. Davidson, V. M. Catterson, A. L. Dimeas, N. D. Hatziargyriou, F. Ponci, and T. Funabashi, "Multi-agent systems for power engineering applications-Part I: concepts, approaches, and technical challenges," *IEEE Trans. Power Systems*, vol. 22, no. 4, pp. 1743-1752, Nov. 2007.

[81] S. D. J. McArthur, E. M. Davidson, V. M. Catterson, A. L. Dimeas, N. D. Hatziargyriou, F. Ponci, and T. Funabashi, "Multi-agent systems for power engineering applications-Part II: technologies, standards, and tools for building multi-agent systems," *IEEE Trans. Power Systems*, vol. 22, no. 4, pp. 1753-1759, Nov. 2007.

[82] T. Nagata and H. Sasaki, "A multi-agent approach to power system restoration," *IEEE Trans. Power Systems*, vol. 17, no. 2, pp. 457-462, May 2002.

[83] E. M. Davidson, S. D. J. McArthur, J. R. McDonald, T. Cumming, and I. Watt, "Applying multi-agent system technology in practice: automated management and

analysis of SCADA and digital fault recorder data," *IEEE Trans. Power Systems*, vol. 21, no. 2, pp. 559-567, May 2006.

[84] H. F. Wang, H. Li, and H. Chen, "Coordinated secondary voltage control to eliminate voltage violations in power system contingencies," *IEEE Trans. Power Systems*, vol. 18, no. 2, pp. 588-595, May 2003.

[85] H. Ni, G. T. Heydt, and L. Mili, "Power system stability agents using robust wide area control," *IEEE Trans. Power Systems*, vol. 17, no. 4, pp. 1123-1131, Nov. 2002.

[86] S. Sheng, K. K. Li, W. L. Chan, X. Zeng, and X. Duan, "Agent-based self-healing protection system," *IEEE Trans. Power Delivery*, vol. 21, no. 2, pp. 610-618, Apr. 2006.

[87] K. Huang, D. A. Cartes, and S. K. Srivastava, "A Multiagent-based algorithm for ring-structured shipboard power system reconfiguration," *IEEE Trans. Syst., Man, Cybern. - Part C: Appl. Rev.*, vol. 37, no. 5, pp. 1016-1021, Sep. 2007.

[88] J. A. Momoh, K. Alfred, and Y. Xia, "Framework for multi-agent system (MAS) detection and control of arcing of shipboard electric power systems," in *Proc. 15th International Conference on Intelligent System Applications to Power Systems*, Curitiba, Brazil, Nov. 2009, pp. 1-6.

[89] X. Feng, K. L. Butler-Purry, and T. Zourntos, "Analysis of various partitioning strategies for multi-agent system-based real-time load management for NG IPS ships," in *Proc. IEEE Electric Ship Technologies Symposium*, Alexandria, VA, Apr. 2011, pp. 173-180.

[90] N. E. Leonard and E. Fiorelli, "Virtual leaders, artificial potentials and coordinated control of groups," in *Proc. 40th IEEE Conference on Decision and Control*, Orlando, FL, vol. 3, Dec. 2001, pp. 2968-2973.

[91] R. Merris, "Laplacian matrices of graphs: a survey," *Linear Algebra and its Applications*, vol. 197-198, pp. 143-176, Jan.-Feb. 1994.

[92] H. K. Khalil, *Nonlinear Systems*, 3rd ed. Upper Saddle River, NJ: Prentice Hall, 2002.

[93] S. Cong, G. Li, and X. Feng, "Parameters identification of nonlinear DC motor model using compound evolution algorithm," in *Proc. World Congress on Engineering*, London, UK, July 2010, pp. 15-20.

[94] D. C. Aliprantis, S. D. Sudhoff, and B. T. Kuhn, "Genetic algorithm-based parameter identification of a hysteretic brushless exciter model," *IEEE Trans. Energy Conversion,* vol. 21, no. 1, pp. 148-154, Mar. 2006.

[95] I. J. Nagrath, *Control Systems Engineering*, 4th ed. Delhi: New Age International (P) Ltd., 2006.

[96] M. Milligan, K. Porter, E. Demeo, P. Denholm, H. Holttinen, B. Kirby, N. Miller, A. Mills, M. O'Malley, M. Schuerger and L. Soder, "Wind power myths debunked," *IEEE Power & Energy Magazine*, vol. 7, no. 6, pp. 89-99, Nov./Dec. 2009.

[97] W. Jewell, "Issues in utility interactive photovoltaic generation," *IEEE Power Engineering Review*, vol. 14, no. 4, pp. 19-21, Apr. 1994.

[98] N. Hatziargyriou, H. Asano, R. Iravani, and C. Marnay, "Microgrids: an overview of ongoing research, developement, and demonstration projects," *IEEE Power and Energy Magazine*, vol. 5, no. 4, pp. 78-94, July/Aug., 2007.

[99] B. Farhangi and K. L. Butler-Purry, "Transient study of DC zonal electrical distribution system in next generation shipboard integrated power systems using PSCAD," in *Proc. North American Power Symposium*, Starkville, MS, Oct. 2009, pp. 1-8.

APPENDIX A

MATHEMATICAL MODELS OF AGENTS

A.1 Generator Agent

The diagram of MTG agent 1 is shown in Figure A.1. The input signals of the MTG agent 1 are frequency deviation, status, and output power of MTG generator 1. The MTG generator 1 status $s_{\mathrm{MTG1}}(\Delta t_i)$ can be '0' or '1'. If MTG generator is in service, the status is '1'; otherwise, the status is '0'. Since the generation capacity of MTG generator is 36 MW, the gain of MTG agent 1 K_1 is chosen as 36. The generation capacity of MTG generator 1 is shown in (A-1).

$$P_{\mathrm{MTG\_capacity1}}(\Delta t_i) = K_1 \cdot s_{\mathrm{MTG1}}(\Delta t_i) \tag{A-1}$$

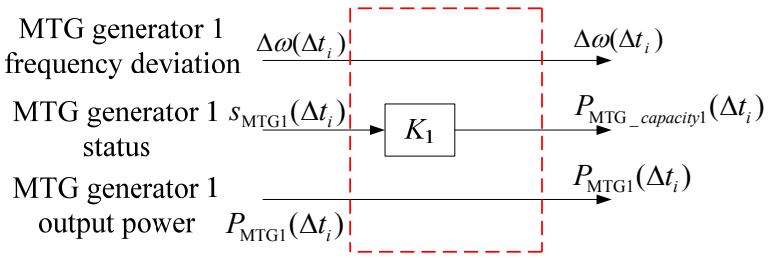

Figure A.1 Diagram of MTG agent 1 in the MVAC multi-agent system

Since only MTG agent 1 is used to measure the frequency, other generator agents do not measure the system frequency. The diagram of MTG agent 2 is shown in Figure A.2. The input signals of the MTG agent 2 are status, and output power of MTG generator 2. The gain of MTG agent 2 K_1 is also chosen as 36. The diagram of the ATG

agent is shown in Figure A.3. The input signal of the ATG agent status is $s_{\mathrm{ATG}}(\Delta t_i)$, and output power of the ATG generator. Since the generation capacity of ATG generator is 4 MW, the gain of the ATG agent K_2 is chosen as 4. The generation capacity of ATG generator is shown in (A-2).

$$P_{\mathrm{ATG\_capacity}}(\Delta t_i) = K_2 \cdot s_{\mathrm{ATG}}(\Delta t_i) \tag{A-2}$$

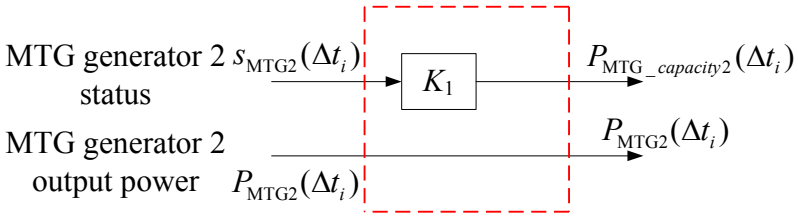

Figure A.2 Diagram of MTG agent 2 in the MVAC multi-agent system

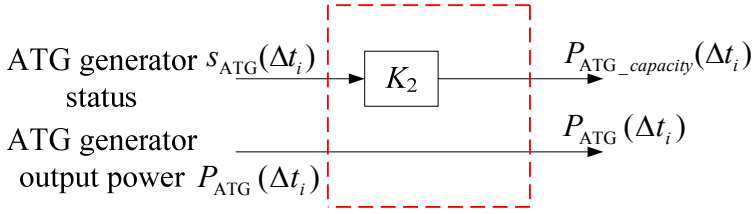

Figure A.3 Diagram of ATG agent in the MVAC multi-agent system

A.2 Propulsion Load Agent

The diagram of the ship speed controller in the propulsion load agent is shown in Figure A.4. The input signals of the speed controller are the actual ship speed and speed reference. The ship speed controller is shown in (A-3), which is the transfer function of PI controller 1 in Figure 4.21.

$$G_1(s) = k_{P1} + k_{I1}/s \tag{A-3}$$

where, k_{P1} and k_{I1} are the proportional and integral gains of the speed controller, which were chosen as 1 and 500, respectively; the maximum limit $P_{\max}$ and minimum limit $P_{\min}$ of the speed controller were chosen as 1.1 and 0 (p.u.), respectively.

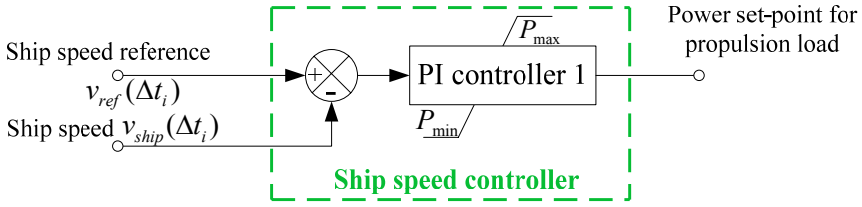

Figure A.4 Diagram of the ship speed controller in the propulsion load agent in the MVAC multi-agent system

The diagram of the frequency regulation controller in the propulsion load agent is shown in Figure A.5. The input signal of the controller is the frequency deviation of MTG generator 1. The frequency regulation controller in propulsion load agent 1 is shown in (A-4), which is the transfer function of PI controller 2 in Figure 4.21.

$$G_2(s) = k_{P2} + k_{I2}/s \tag{A-4}$$

where, k_{P2} and k_{I2} are the proportional and integral gains of the frequency regulation controller, which were chosen as 20 and 1, respectively; the maximum and minimum limits of the frequency regulation controller were chosen as 1.0 and 0 (p.u.), respectively. This controller is activated when the absolute value of the frequency deviation $\Delta\omega$ is larger than 0.5% of the nominal value; the controller is deactivated when $\Delta\omega$ is less than 0.1% of the nominal value. A hysteresis component was used to

implement this function. This hysteresis component can eliminate the high frequency switching of the controller, which improves the dynamic performance of the system.

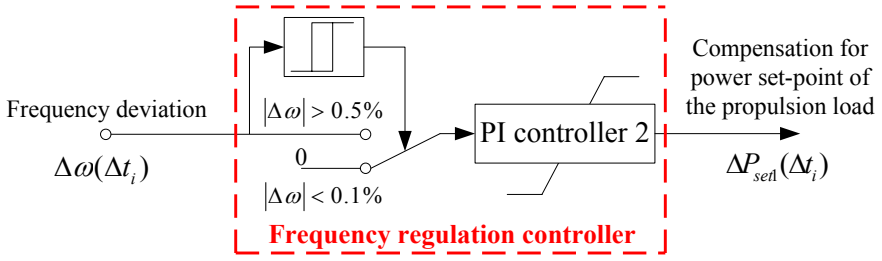

Figure A.5 Diagram of the frequency regulation controller in propulsion load agent 1 in the MVAC multi-agent system

The diagram of the voltage controller in the propulsion load agent is shown in Figure A.6. K_V is chosen as 10. If the input voltage of the propulsion load is less than 90% of the nominal value, the controller is activated to decrease the power set-point of the propulsion load to make the voltage return to nominal value; if the input voltage of the propulsion load is larger than 95% of the nominal value, the controller is deactivated. The hysteresis component is used to eliminate the high frequency switching of the voltage controller.

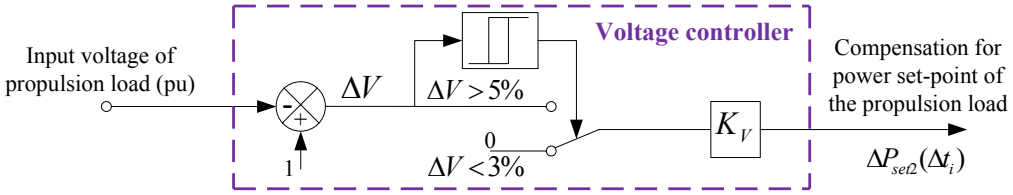

Figure A.6 Diagram of the voltage controller in the propulsion load agent in the MVAC multi-agent system

A.3 Pulse Load Agent

The implementation of the dynamic constraint of the cable serving the pulse load is shown in Figure A.7. $T_{Integral}$ is the total time of the violation of the cable ampacity constraint in a period time of T. If $T_{Integral}$ is no larger than the maximum allowed time T_1, the pulse load is still served; otherwise, the pulse load is disconnected immediately. The parameters of the pulse load agent are shown as $T = 10$ and $T_1 = 5$.

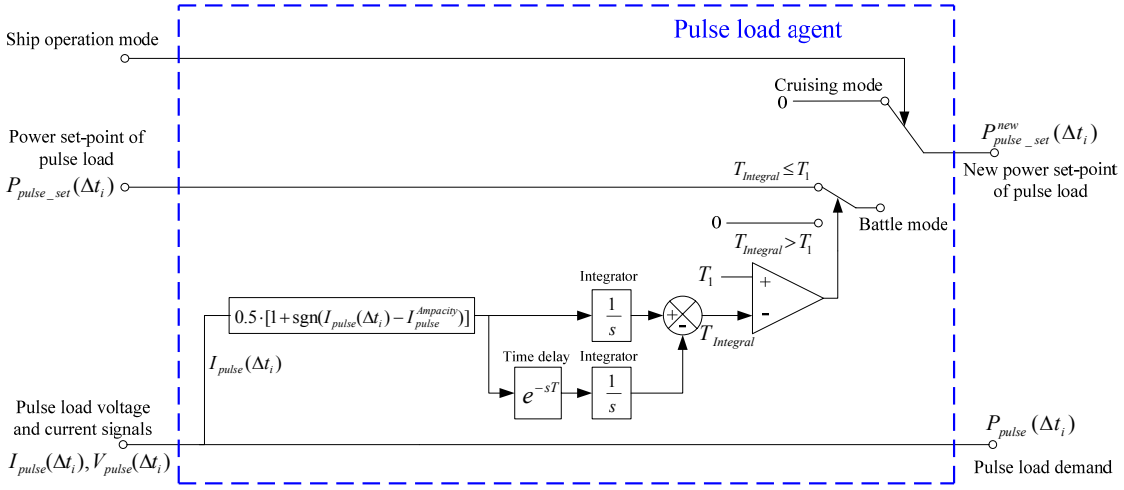

Figure A.7 Diagram of the pulse load agent in the MVAC multi-agent system

A.4 DC-DC Converter Agent

The model of DC-DC converter agent *i* is shown in (A-5).

$$\begin{cases} \dot{x}_i(t) = y_i(t) \\ \dot{y}_i(t) = u_{C-i}(t) \end{cases} \tag{A-5}$$

where, $u_{C-i}(t) = -\frac{x_i(t)}{L_i C_i} + \frac{d_i}{L_i C_i} \cdot i_{out-i}(t)$. The parameters L_i and C_i in the agent model are obtained from the DC-DC converter circuit model. $x_i(t)$ and $y_i(t)$ are defined as (A-6).

$$\begin{aligned} x_i(t) &= i_{in-i}(t) \\ y_i(t) &= \left(V_{in-i} \cdot d_i^2 - d_i \cdot v_{C-i}(t)\right) / L_i \end{aligned} \tag{A-6}$$

The DC-DC converter agent models have three different types – 375 V DC-DC converter agent, 650 V DC-DC converter agent, and 800 V DC-DC converter agent. The parameters of DC-DC converter agent models are shown in Table A.1.

Table A.1 Parameters of DC-DC converter agents in the DC zone multi-agent system

Parameters	L_i (mH)	C_i (μF)	d_i
375 V DC converter agent	234	1000	0.375
650 V DC converter agent	228	1000	0.65
800 V DC converter agent	160	1000	0.8

A.5 Constant Load Agent

The constant load agent *j* is shown as (A-7).

$$\begin{cases} \dot{z}_{1j}(t) = q_{1j}(t) \\ \dot{q}_{1j}(t) = u_{L_{1j}}(t) \end{cases} \qquad j = 1, 2, \cdots, M_{i1} \tag{A-7}$$

where, $u_{L_{1j}}(t) = -z_{1j}(t) / (L_{L_{1j}} C_{L_{1j}}) + \left(v_{inL_{1j}} - L_{L_{1j}} \cdot q_{1j}(t)\right) / (L_{L_{1j}} C_{L_{1j}}) \cdot \hat{u}_{L_{1j}}(\Delta t_i)$, $q_{1j}(t) = 1/L_{L_{1j}} \cdot (v_{inL_{1j}} - v_{cL_{1j}}(t))$, $z_{1j}(t) = i_{1j}(t)$, and M_{i1} is the total number of constant load agents in the *i*th load-layer multi-agent system. The equivalent inductor $L_{L_{1j}}$ and capacitor $C_{L_{1j}}$ of each constant load agent were chosen as 0.005 H and 0.0002 F, respectively.

A.6 DC Motor Agent

The DC motor load agent model is expressed in (A-8).

$$\begin{cases} \dot{z}_{2k}(t) = q_{2k}(t) \\ \dot{q}_{2k}(t) = u_{L_{2k}}(t) \end{cases} \qquad k = 1, 2, \cdots, M_{i2} \tag{A-8}$$

where, $z_{2k}(t) = P_{d_{2k}}(t) \big/ v_{inL_{2k}}$, $v_{inL_{2k}}$ is the input voltage of the DC motor load agent, $u_{L_{2k}}(t) = -(1/T_{2_{2k}})z_{2k}(t) - (T_{1_{2k}}/T_{2_{2k}})q_{2k}(t) + (K_{d_{2k}}/T_{2_{2k}})\hat{u}_{2k}(\Delta t_i)$, $\hat{u}_{2k}(\Delta t_i) = P_{\text{set-point}_{2k}}(\Delta t_i) \big/ v_{inL_{2k}}$, and M_{i2} is the total number of DC motor load agents in the *i*th load-layer multi-agent system. The parameters of DC motor agent models are shown in Table A.2.

Table A.2 Parameters of DC motor agents in one DC zone

Component name	K_d	T_1	T_2
DC motor 1	1	0.2203	0.01
DC motor 2	1	0.3289	0.01
DC motor 3	1	0.3648	0.01
DC motor 4	1	0.2203	0.01
DC motor 5	1	0.3648	0.01
DC motor 6	1	0.3123	0.01

A.7 AC Motor Agent

The AC motor load agent model is expressed in (A-9).

$$\begin{cases} \dot{z}_{3l}(t) = q_{3l}(t) \\ \dot{q}_{3l}(t) = u_{L_{3l}}(t) \end{cases} \qquad l = 1, 2, \cdots, M_{i3} \tag{A-9}$$

where, $z_{3l}(t) = P_{d_{3l}}(t) \big/ v_{inL_{3l}}$, $v_{inL_{3l}}$ is the input voltage of the AC motor load agent, $u_{L_{3l}}(t) = -(1/T_{2_{3l}})z_{3l}(t) - (T_{1_{3l}}/T_{2_{3l}})q_{3l}(t) + (K_{d_{3l}}/T_{2_{3l}})\hat{u}_{3l}(\Delta t_i)$, $\hat{u}_{3l}(\Delta t_i) = P_{\text{set-point}_{3l}}(\Delta t_i) \big/ v_{inL_{3l}}$,

and M_{i3} is the total number of AC motor load agents in the load-layer multi-agent system. The parameters of AC motor agent models are shown in Table A.3.

Table A.3 Parameters of AC motor agents in one DC zone

Component name	K_d	T_1	T_2
AC motor 1	1	0.1789	0.002
AC motor 2	1	0.2763	0.0116
AC motor 3	1	0.3394	0.0105
AC motor 4	1	0.3	0.02

APPENDIX B

SYSTEM PARAMETERS OF ALL-ELECTRIC SHIP POWER SYSTEM COMPUTER MODEL

B.1 All-Electric Ship Power System Computer Model for PSCAD Simulation

The one-line diagram of the notional all-electric ship power system model used in PSCAD simulation is shown in Figure B.1.

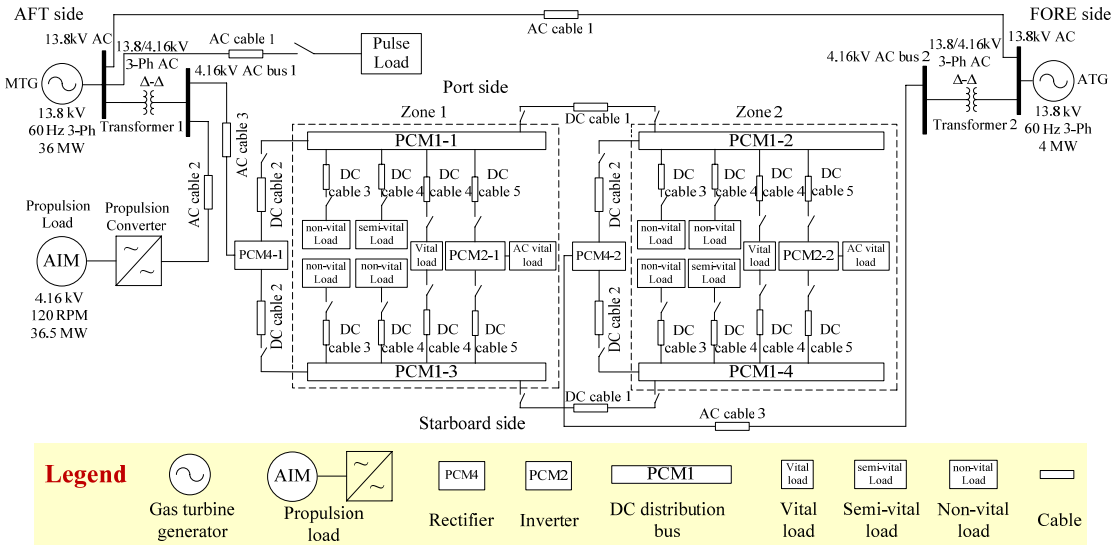

Figure B.1 One-line diagram of the simplified notional all-electric ship power system computer model for PSCAD simulation

B.1.1 Parameters of generators

The parameters of the MTG generator are shown in Table B.1 [11].

Table B.1 Parameters of the MTG generator in the notional all-electric ship power system

Name	Parameter	Value
Rated RMS Line-Line Voltage	$V_{gl\text{-}l}$	13.8 kV
Active Power	P_g	36 MW
Power Factor	*pf*	0.8
Frequency	*freq*	60 Hz
Armature Resistance at 95ºC	R_a	0.010Ω
Potier reactance	X_p	0.17
D axis unsaturated reactance	*Xd*	1.55
D axis unsaturated transient reactance	*Xd′*	0.22
D axis unsaturated sub-transient reactance	*Xd″*	0.14
D axis open circuit unsaturated transient time constant	*Tdo′*	8.95s
D axis open circuit unsaturated sub-transient time constant	*Tdo″*	0.036s
Q axis unsaturated reactance	*Xq*	0.76
Q axis unsaturated sub-transient reactance	*Xq″*	0.20
Q axis open circuit unsaturated sub-transient time constant	*Tqo″*	0.12 s
Inertia constant	*H*	1.49s

The parameters of the ATG generator are shown in Table B.2 [11].

Table B.2 Parameters of the ATG generator in the notional all-electric ship power system

Name	Parameter	Value
Rated RMS Line-Line Voltage	$V_{gl\text{-}l}$	13.8 kV
Active Power	P_g	4 MW
Power Factor	*pf*	0.8
Frequency	*freq*	60 Hz
Armature Resistance at 95ºC	R_a	0.199 Ω
Potier reactance	X_p	0.18
D axis unsaturated reactance	*Xd*	1.25
D axis unsaturated transient reactance	*Xd′*	0.24
D axis unsaturated sub-transient reactance	*Xd″*	0.17
D axis open circuit unsaturated transient time constant	*Tdo′*	4.11 s
D axis open circuit unsaturated sub-transient time constant	*Tdo″*	0.023 s
Q axis unsaturated reactance	*Xq*	0.62
Q axis unsaturated sub-transient reactance	*Xq″*	0.26
Q axis open circuit unsaturated sub-transient time constant	*Tqo″*	0.061 s
Inertia constant	*H*	1.06 s

The type of exciters used in the simulation is IEEE Alternator Supplied Rectifier Excitation System #1 (AC1A). The parameters of exciters of the MTG and ATG generators are shown in Table B.3 [11].

Table B.3 Parameters of the exciter in the notional all-electric ship power system

Name	Parameter	Value
Lead time constant	T_C	0
Lag time constant	T_B	0
Regulator gain	K_A	400 pu
Regulator time constant	T_A	0.02 s
Maximum regulator internal voltage	V_{AMAX}	14.5 pu
Minimum regulator internal voltage	V_{AMIN}	-14.5 pu
Maximum regulator output	V_{RMAX}	6.03 pu
Minimum regulator output	V_{RMIN}	-5.43 pu
Rate feedback gain	K_F	0.03
Rate feedback time constant	T_F	1 s
Exciter time constant	T_E	0.8 s
Exciter constant related to field	K_E	1 pu
Field circuit commutating reactance	K_C	0.2 pu
Demagnitizing factor	K_D	0.38 pu
Saturation at VE1	SE(VE1)	0.1 pu
Exciter voltage for SE1	VE1	4.18 pu
Saturation at VE2	SE(VE2)	0.03 pu
Exciter voltage for SE2	VE2	3.14 pu

B.1.2 Parameters of transformer

The parameters of transformers in the MVAC system of the all-electric ship power system are shown in Table B.4 [11].

Table B.4 Parameters of transformer in the MVAC system

Parameter	Value
Primary line-to-line voltage	13.8 kV
Secondary line-to-line voltage	4.16 kV
Winding type	D-D
3 phase transformer MVA	25 MVA
Base operation frequency	60 Hz
Positive sequence leakage reactance	0.1 pu
Cooper losses	0.001 pu
No load losses	0.001 pu
Saturation placed on:	Winding-2
Air Core Reactance	0.2 pu
In rush decay time constant	1.0 s
Knee voltage	1.25 pu
Time to release flux clipping	0.1 s
Magnetizing current	1%

B.1.3 Parameters of advanced induction motor (AMI) and propulsion converter

The parameters of the advanced induction motor in the all-electric ship power system are shown in Table B.5 [11].

Table B.5 Parameters of the advanced induction motor in the notional all-electric ship power system

Parameter	Value
Rated power	45 MVA
Rated voltage	12 kV
Base angular frequency	377
Stator / rotor turns ratio	2.637687
Angular moment of inertia ($J = 2H$)	1 sec
Mechanical damping	0.01 pu
Stator resistance	0.0034 pu
Wound rotor resistance	0.00607 pu
Magnetizing inductance	0.9 pu
Stator leakage inductance	0.0102 pu
Wound rotor leakage inductance	0.011 pu

The propulsion system and the hydrodynamics for the marine propulsion system have been discussed in detail in [10]. The diagram of propulsion converter is shown in Figure B.2. The parameters of the propulsion converter L_{dc} and C_{dc} are chosen as 1 mH and 10 mF, respectively.

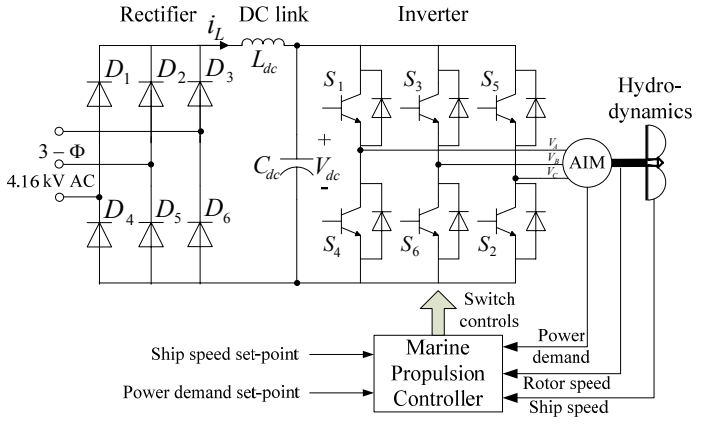

Figure B.2 Diagram of the propulsion converter and advanced induction motor

B.1.4 Parameters of the pulse load

The diagram of the pulse load charging circuit is shown in Figure B.3 [12], [13]. The inductor L_P and capacitor C_P in the charging circuit in the case studies were chosen as 1 mH and 10 mF, respectively. L_m was chosen as 0. R_P is the equivalent resistor of the pulse load, which is determined by the charging status of the pulse load. D_1 to D_6 are diodes in the rectifier. The load demand of the pulse load is shown as (B-1).

$$P_{pulse}(t) = \frac{V_{C_p}^2(t)}{R_p} \tag{B-1}$$

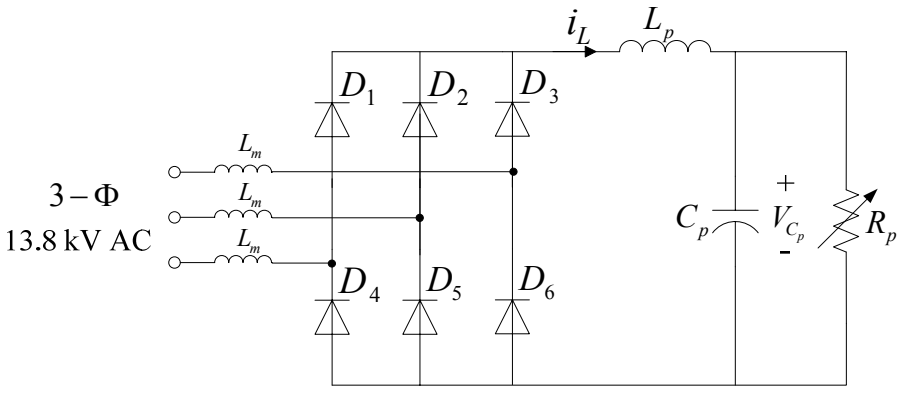

Figure B.3 Diagram of a pulse load charging circuit in the all-electric ship power system

B.1.5 Parameters of DC-DC converters in PCM1

A diagram of the DC-DC converter model in PCM1 is shown in Figure B.4. The DC-DC converter is controlled using a PI controller, which is expressed as (B-2).

$$G(s) = k_P + k_I / s \tag{B-2}$$

where, k_P and k_I are proportional and integral gains of the PI controller.

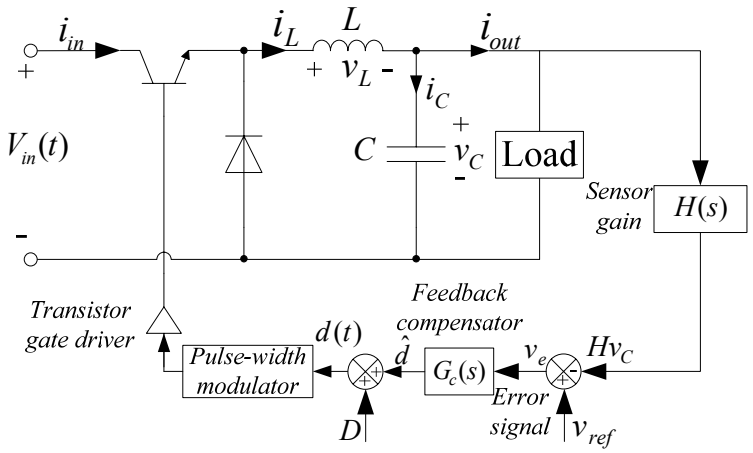

Figure B.4 Diagram of DC-DC converter model with a voltage controller

The parameters of DC-DC converters in PCM1 are summarized in Table B.6. L and C are the inductor and capacitor of the DC-DC converter, respectively. k_p and k_i are the proportional and integral gains of the DC-DC converter, respectively. d is the duty ratio of the DC-DC converter. The switching frequency of the converter was 5 kHz.

Table B.6 Parameters of DC-DC converters in PCM1

Parameter	375 V DC-DC converter	650 V DC-DC converter	800 V DC-DC converter
L	234 mH	228 mH	160 mH
C	1000 μF	1000 μF	1000 μF
k_p	0.1	1	0.05
k_i	0	0	0.01
d	0.375	0.650	0.800

B.1.6 Parameters of PCM2 and PCM4

The PCM2 is a three phase full-bridge inverter with bipolar sinusoidal pulsed width modulation, which has been implemented in [11], [99]. The detail parameters are

also shown in [11], [99]. The diagram of the PCM2 is shown in Figure B.5. R_A, R_B and R_C are equivalent loads. The parameter of PCM2 C_1 is chosen as 270 μF.

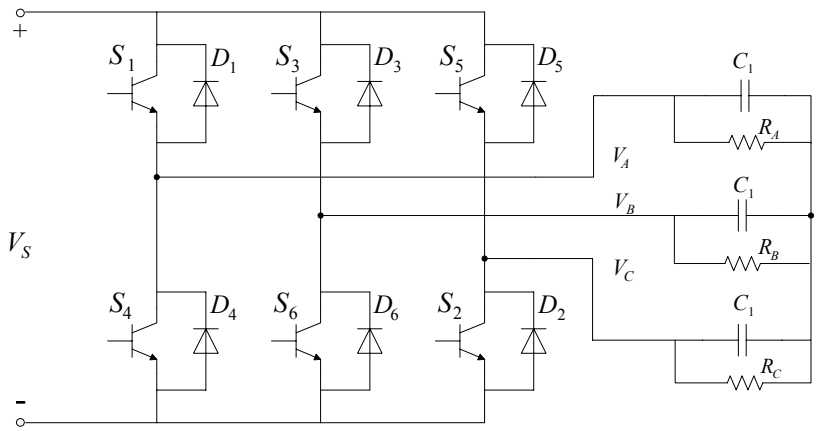

Figure B.5 Diagram of PCM2 in DC zones

PCM4 is an uncontrolled rectifier, which includes an AC transformer and an uncontrolled rectifier. The implementation and parameters of PCM4 are discussed in [11], [99]. The diagram of PCM4 is shown in Figure B.6. The parameters of PCM4 transformer are shown in Table B.7. The parameters of rectifier *L* and *C* are chosen as 1.1 mH and 102 mF, respectively.

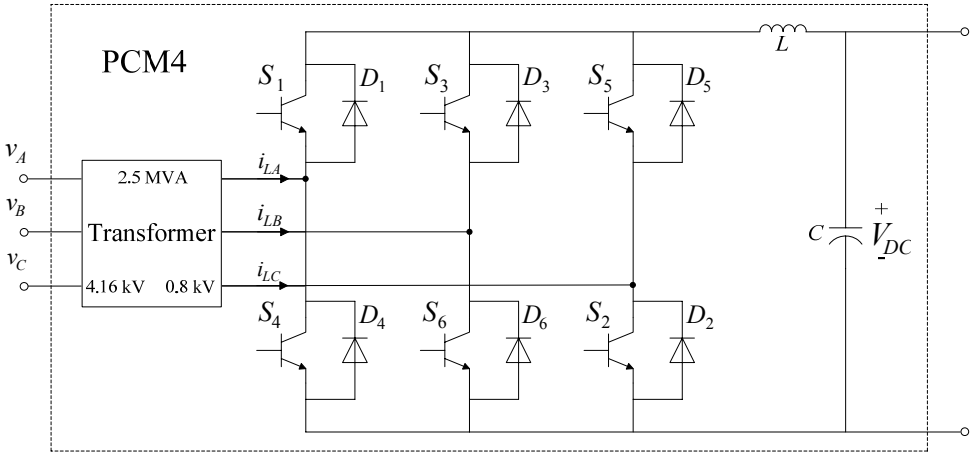

Figure B.6 Diagram of PCM4 in DC zones

Table B.7 Parameters of PCM4 transformer

Parameter	Value
Primary line-to-line voltage	4.16 kV
Secondary line-to-line voltage	0.8 kV
Winding type	D-D
3 phase transformer MVA	2.5 MVA
Base operation frequency	60 Hz
Positive sequence leakage reactance	0.06 pu
Cooper losses	0
No load losses	0
Saturation placed on:	Winding-2
Air Core Reactance	0.2 pu
In rush decay time constant	1.0 s
Knee voltage	1.25 pu
Time to release flux clipping	0.1 s

B.1.7 Parameters of cables

The simplified DC cable model used in the case studies is shown in Figure B.7.

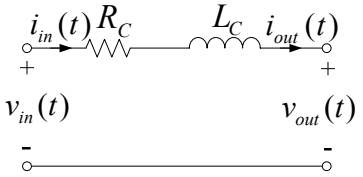

Figure B.7 Diagram of a simplified DC cable model in the all-electric ship power system

AC cables in the notional all-electric ship power system were also modeled as *RL* circuit. The parameters of the DC and AC cables are shown in Tables B.8 and B.9. The lengths of AC cables are shown in Table B.10.

Table B.8 Parameters of AC cables in the all-electric ship power system

Parameter	AC cable 1	AC cable 2	AC cable 3
R	6.314×10^{-5} Ω/meter	6.314×10^{-5} Ω/meter	6.314×10^{-5} Ω/meter
L	3.42×10^{-10} H/meter	3.42×10^{-10} H/meter	3.42×10^{-10} H/meter

Table B.9 Parameters of DC cables in the all-electric ship power system

Parameter	DC cable 1	DC cable 2	DC cable 3	DC cable 4	DC cable 5
R	10^{-5} Ω	10^{-5} Ω	10^{-4} Ω	5×10^{-5} Ω	2×10^{-5} Ω
L	10^{-7} H	10^{-7} H	10^{-4} H	5×10^{-7} H	2×10^{-7} H

Table B.10 AC cable lengths in the all-electric ship power system

Starting	End	Type of cable	Length (meter)
4.16 kV AC bus 1	PCM4-1	AC cable 3	15
4.16 kV AC bus 2	PCM4-2	AC cable 3	15
4.16 kV AC bus 1	Propulsion load	AC cable 2	15
MTG bus	Pulse load	AC cable 1	15
MTG bus	ATG bus	AC cable 1	100

B.1.8 Parameters of loads in DC zones

The constant DC loads are shown in Figure B.8. The parameters of constant DC loads are shown in Table B.11. The constant AC loads are shown in Figure B.9. The parameters of constant AC loads are shown in Table B.12. The DC motors are shown in Figure B.10. The parameters of DC motors are shown in Table B.13. The parameters for AC motors 1 and 3 in DC zones are shown in Table B.14 [11]. The parameters for AC motors 2 and 4 in DC zones are shown in Table B.15 [11].

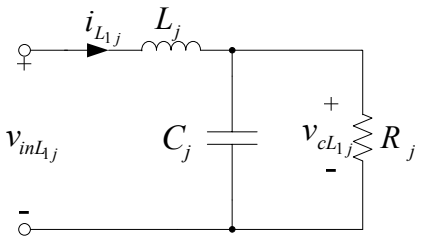

Figure B.8 Diagram of a constant DC load model in DC zones

Table B.11 Parameters of DC motors in DC zones

Parameter	R_j (Ω)	C_j(F)	L_j(H)
Constant load 1	1.219	0.0002	0.005
Constant load 2	1.953	0.0002	0.005
Constant load 3	0.929	0.0002	0.005
Constant load 4	2.009	0.0002	0.005
Constant load 5	3.661	0.0002	0.005
Constant load 6	19.205	0.0002	0.005
Constant load 7	2.123	0.0002	0.005

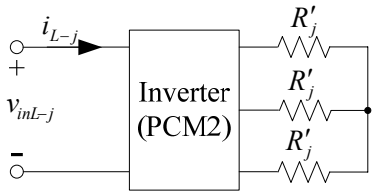

Figure B.9 Diagram of a constant AC load model in DC zones

Table B.12 Parameters of constant AC loads in DC zones

Parameter	R'_j
Constant load 8	4.754
Constant load 9	5.063
Constant load 10	2.383
Constant load 11	1.693
Constant load 12	1.144

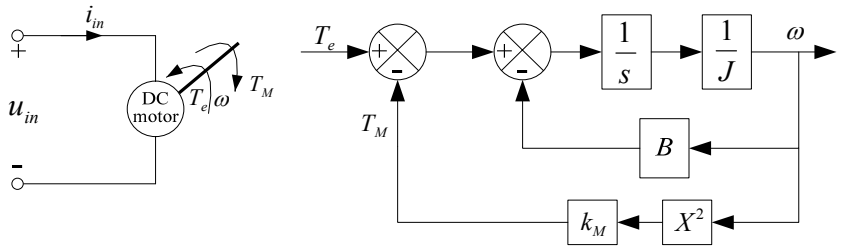

Figure B.10 Diagram of DC motor model in DC zones

Table B.13 Parameters of DC motors in DC zones

Parameter	Rated voltage (V)	Rated current (A)	J	B	k_M
DC motor 1	375	96	0.178	0.00355	0.88
DC motor 2	375	308	0.178	0.00355	1
DC motor 3	650	177	0.178	0.00355	1
DC motor 4	650	55	0.178	0.00355	0.88
DC motor 5	650	177	0.178	0.00355	1
DC motor 6	650	73	0.178	0.00355	0.88

Table B.14 Parameters of the AC motors 1 and 3 in DC zones

Parameter	Value
Rated line-to-line voltage (RMS)	0.45 kV
Frequency	60 Hz
Design ratio	1 pu
Power factor	0.884 pu
Efficiency	0.920 pu
Slip at full load	0.059 pu
Starting current at full volts	6.82 pu
Starting torque at full volts	2.59 pu
Maximum torque	3.28 pu
Number of poles	2
Polar moment of Inertia	3.0817 kg·m^2
mechanical damping	0.008 pu
Constant torque (load torque)	0.82 pu

Table B.15 Parameters of the AC motors 2 and 4 in DC zones

Parameter	Value
Rated line-to-line voltage (RMS)	0.45 kV
Frequency	60 Hz
Design ratio	0.6 pu
Power factor	0.816 pu
Efficiency	0.959 pu
Slip at full load	0.039 pu
Starting current at full volts	6.96 pu
Starting torque at full volts	1.73 pu
Maximum torque	3.33 pu
Number of poles	2
Polar moment of Inertia	3.0817 $kg \cdot m^2$
mechanical damping	0.008 pu
Constant torque (load torque)	0.82 pu

B.2 Simplified Notional All-Electric Ship Power System Model for MVAC Multi-Agent System Studies

The diagram of a simplified notional all-electric ship power system simulation model for the MVAC multi-agent system studies is shown in Figure B.11. The parameters of the MTG and ATG generators, transformers, propulsion load, and pulse load are given in Appendix B.1.1-Appendix B.1.4. The parameters of cables are given in Appendix B.1.7. This simplified notional system was used in the MVAC multi-agent system – case studies and performance analysis, as shown in sections 5.3.1 and 5.4.1.

In the notional system, it was assumed that the port side DC distribution buses were served by PCM4-1 and starboard side DC distribution buses were served by PCM4-2. In the MVAC system case studies, all the loads served by PCM4-1 or PCM4-2 were aggregated together and modeled using a constant load. The diagram of a PCM4 and its load is shown in Figure B.12. It was assumed that the lumped DC loads 1 and 2 were 2 MW in the simulation. The lumped DC loads were modeled using constant

resistors. The values of constant resistors $R_{PCM\,4\text{–}1}$ and $R_{PCM\,4\text{–}2}$ served by PCM4-1 and PCM4-2 were both chosen as 2 Ω.

The AC cable connecting bus 1 and bus 4 was used to test the dynamic cable constraints in the MVAC system. The cable connects to the MTG generator bus to the pulse load, which is shown in Figure B.11.

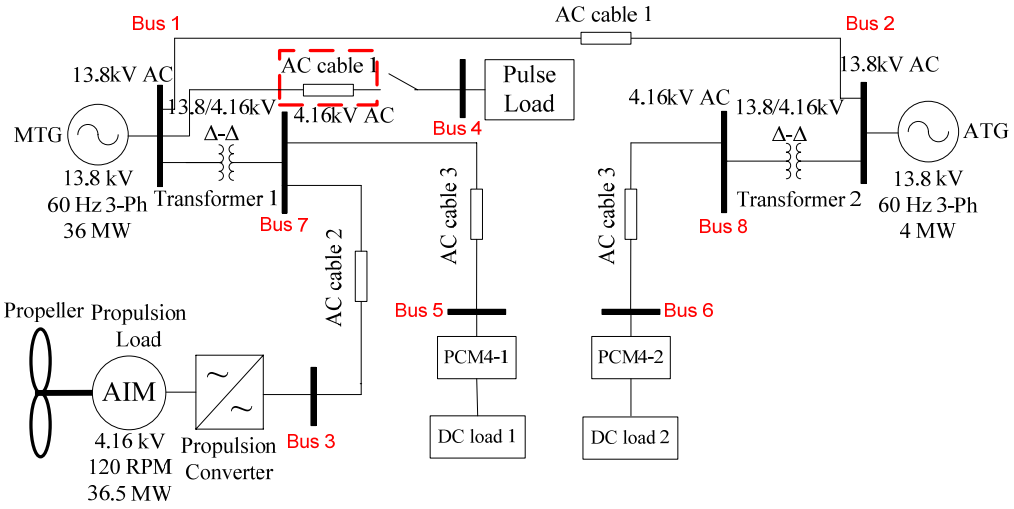

Figure B.11 Diagram of a simplified notional all-electric ship power system simulation model for MVAC multi-agent system studies

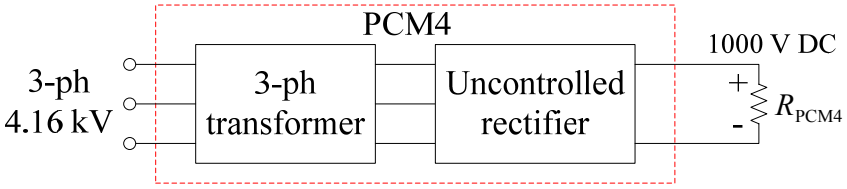

Figure B.12 Diagram of a PCM4 and its load used for MVAC multi-agent system case studies

B.3 Simplified Notional All-Electric Ship Power System Model for DC Zone Multi-Agent System Studies

The diagram of a simplified notional all-electric ship power system simulation model used for the DC zone multi-agent system studies is shown in Figure B.13. The system includes one ATG, two transformers, one pulse load, and two DC zones. The MTG generator was out of service in the DC zone multi-agent system case studies. The parameters of the ATG generator, transformers, and pulse load are given in Appendices B.1.1, B.1.2 and B.1.4, respectively. The models and parameters of PCM1, PCM2, and PCM4 in DC zones are given in Appendices B.1.5 and B.1.6. The parameters of the AC and DC cables are given in Appendix B.7. The models and parameters of loads in DC zones are given in Appendix B.1.8. This simplified notional system was used in the DC zone multi-agent system – case studies and performance analysis, as shown in sections 5.3.2 and 5.4.2.

B.4 Simplified Notional All-Electric Ship Power System Simulation Model for MVAC and DC Zone Multi-Agent Systems Coordination Case Study

The diagram of a simplified notional all-electric ship power system simulation model used for the coordination of MVAC and DC zone multi-agent systems case study is shown in Figure B.14. The system includes one MTG, one ATG, two transformers, one propulsion load, one pulse load, and two DC zones. The parameters of the MTG and ATG generators, transformers, propulsion load, and pulse load are given in Appendices B.1.1 to B.1.4, respectively. The models and parameters of PCM1, PCM2, and PCM4 in

DC zones are given in Appendices B.1.5 and B.1.6. The parameters of the AC and DC cables are given in Appendix B.7. The models and parameters of loads in DC zones are given in Appendix B.1.8. This simplified notional system was used in the coordination of MVAC and DC zone multi-agent systems case study, as shown in sections 5.3.3.

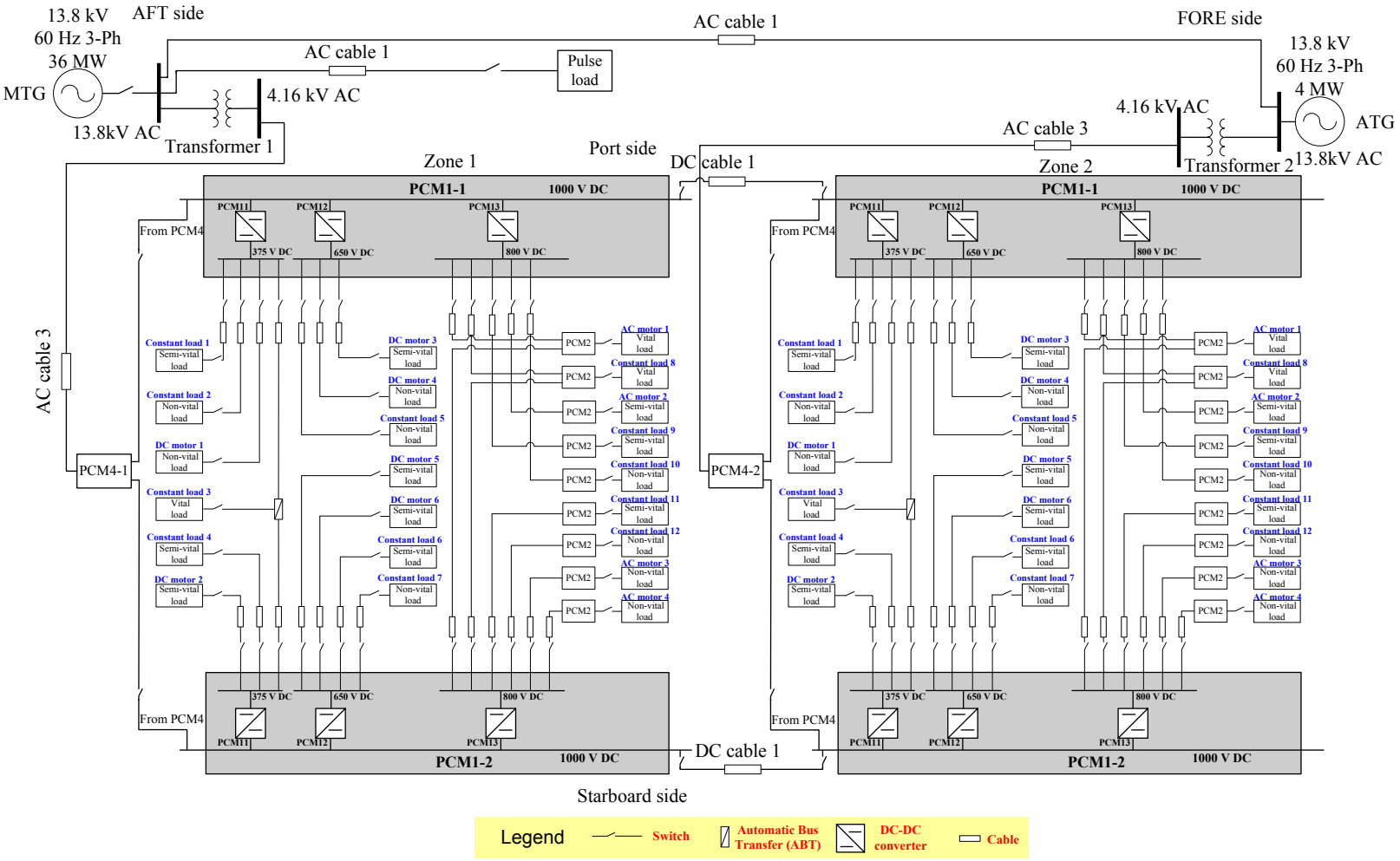

Figure B.13 Diagram of a simplified notional all-electric ship power system simulation model for DC zone multi-agent system studies

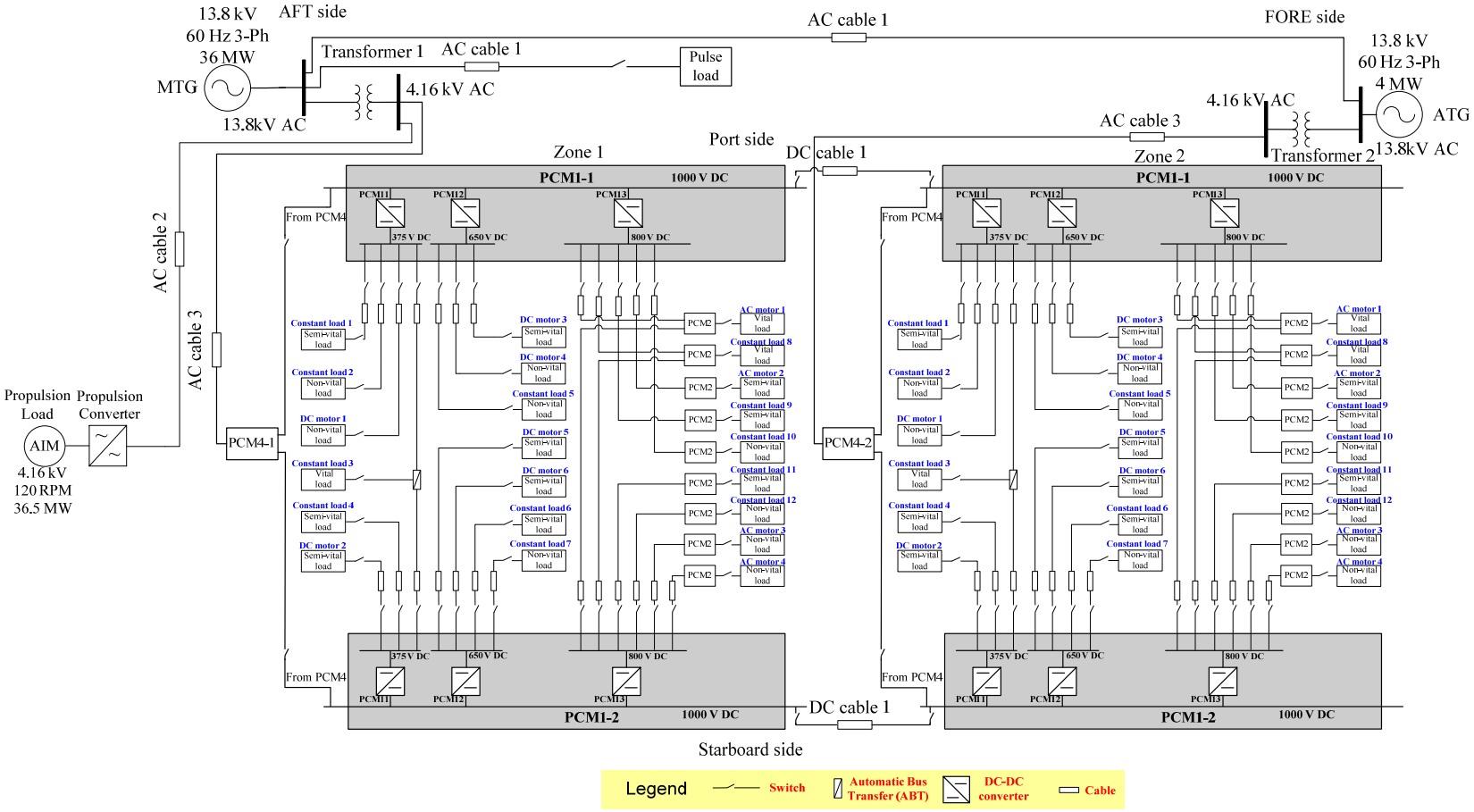

Figure B.14 Diagram of a simplified notional all-electric ship power system simulation model for coordination of MVAC and DC zone multi-agent systems case study

VITA

Xianyong Feng received his B.S. degree in Department of Electrical Engineering at Harbin Institute of Technology in July 2005. He received his M.S. degree in Department of Automation at University of Science and Technology of China in July 2008. He received his Ph.D. degree in Department of Electrical and Computer Engineering at Texas A&M University in May 2012. In December 2011, he joined ABB US Corporate Research Center at Raleigh, NC. His industrial experience also includes an internship in ExxonMobil Upstream Research Company in the summer of 2010. His research interests are in the areas of real-time load management for finite inertia power systems, microgrids, consensus and cooperative control, and applications of nonlinear system theory.

Xianyong Feng may be reached at Department of Electrical and Computer Engineering, Texas A&M University, 214 Zachry Engineering Center, College Station, Texas 77843-3128. His email is xianyongfeng@gmail.com.